Using Neutron Stars to Probe Fundamental Physics

Mia Kumamoto

A dissertation
submitted in partial fulfillment of the
requirements for the degree of

Doctor of Philosophy

University of Washington
2025

Reading Committee:
Sanjay Reddy, Chair
David Kaplan
Alejandro Garcia

Program authorized to offer degree:
Department of Physics

University of Washington

Abstract

Using Neutron Stars to Probe Fundamental Physics

Mia Kumamoto

Chair of the Supervisory Committee:

Sanjay Reddy

Institute for Nuclear Theory, Department of Physics

Neutron stars present some of the most extreme densities known to be found in the universe. At such densities, astrophysical study of these exotic objects requires high quality nuclear physics input in order to interpret. In this thesis, I will present my recent work addressing a range of questions requiring nuclear calculations that are pertinent to interpretation of astrophysical observations of neutron stars. In particular, I will discuss recent published work using neutron stars to constrain the parameter space of axion-gluon couplings, calculations of rates of neutrino interactions in the presence of strong astrophysical magnetic fields, and the effects that a dense medium of nucleons has on superfluidity at high density. Additionally, I will briefly discuss new progress on addressing whether the QCD axion can be constrained by neutron stars and calculating neutrino opacities in the neutron star merger environment in a computationally efficient formalism.

The axion is a well-motivated dark matter candidate and possible solution to the strong CP problem. The formation of an axion condensate can become energetically favorable at high baryon density and neutron star observables may be significantly altered, constraining such a scenario. When the mass of the axion is lighter than the QCD prediction by more than an order of magnitude, this transition occurs at densities accessibly in the crust of neutron stars. We provide a constraint on the parameter space of "exceptionally light" QCD axions by tuning a phenomenological model to match the range of predictions of a preliminary calculation in Chiral Effective Field Theory.

To access the QCD axion, modifications to nuclear forces in the presence of the axion condensate need to be better understood, in particular in light of large cutoff dependence we find in naively applied Chiral EFT. Isospin breaking effects are also amplified in the axion condensed phase, a component not fully incorporated in our simpler calculation. Presently unconstrained three nucleon forces also contribute to the energy at these densities. Finally, we will also comment on the relevance of chiral symmetry restoration for axion condensation.

In the presence of strong magnetic fields, the energy levels of charged particles are quantized. This quantization is expected to be present in neutron stars with strong magnetic field known as magnetars. When the energy levels of charged particles are quantized, the direct Urca process becomes available at lower densities than normally expected. The direct Urca process is responsible for rapidly cooling the

heaviest neutron stars, but without strong magnetic fields is strongly suppressed at densities accessible in most neutron stars. The quantization of the energy of charged particles introduces resonances in the density of states that amplify the emissivity in small regions of the neutron star, especially when the temperature is low.

At low density and high temperatures, the presence of magnetic fields also has important implications for the opacity of neutrinos. We find greatly amplified opacity for the lowest energy neutrinos in the presence of magnetic field strengths predicted to be found in neutron star merger ejecta. This enhanced opacity results from the large anomalous magnetic moment of the nucleons and modifications to the dispersion relations of electrons and protons.

For an unknown range of densities above nuclear density, it is expected that neutrons will become superfluid in the $^3P_2$ channel. At high density it is also expected that short range forces between nucleons are strongly repulsive. When including the one loop correction to the interaction between two nucleons, the Kohn-Luttinger mechanism introduces the possibility that this repulsive force may contribute to attraction in higher partial waves even if it is purely s-wave at tree level. We calculate the size of this effect with a variety of central and non-central potentials to assess the relevance of non-central interactions for induced $^3P_2$ pairing in dense matter.

For Cassiopeia and Fawn

With particular thanks to my advisor Sanjay Reddy
and my dear friends Ly, Heather, Emma, David,
Elliot, Sam, and Catherine

Contents

Chapter 1

Background

Neutron stars (NS) are some of the most extreme objects found in the universe and also some of the most mysterious. First proposed in 1934 by Baade and Zwicky [1], a NS is one possible endpoint in the life of a massive star that is heavy enough to undergo a core collapse supernova, but not heavy enough to collapse to a black hole. With the highest densities currently known to exist in the universe outside of a black hole, NSs probe the properties of matter at large baryon chemical potential and low temperature. The first observational evidence of the existence of NSs came in the 1960's with the first observation of a radio pulsar by Bell and Hewish [2] and the first observation of an x-ray binary by Giacconi, Gursky, Paolini, and Rossi [3]. More recently, the 2017 observation of gravitational wave event GW170817 [4] and subsequent electromagnetic observations [5–9] confirmed binary neutron star mergers as a source of gravitational waves and r-process nucleosynthesis and began a new era of multi-messenger observations of neutron stars. With more instruments planned to come online in the next few decades, the discovery potential continues to grow.

As the only known source of cold, dense nuclear matter, NSs can teach us a great deal about the high density, low temperature part of the QCD phase diagram and equilibrium or quasiequilibrium processes that require supranuclear densities to operate. In this introductory chapter, we will summarize the relevant features of NSs necessary to understand later chapters in which we will study properties of dense matter and the theories of exotic physics which NS observations can constrain. Chapter 2 presents work originally appearing in Ref. [10] regarding the condensation of axions lighter than the QCD prediction in neutron stars. Chap. 3 discusses ongoing work to constrain the QCD axion itself. Chapter 4 addresses interactions of neutrinos in the strong magnetic fields found in some isolated neutron stars, in the supernovae where they are born, and in the binary mergers where they die, originally published in Ref. [11]. Finally, Chap. 5 presents work from Ref. [12] to study the effect that short-range repulsive interactions can have on the superfluid gap in neutron stars via interactions with the medium.

1.1 Composition and structure

The outermost kilometer of a NS is made up of a solid crust of nuclei in a Coulomb lattice. In the outer crust, spherical nuclei are surrounded by free relativistic electrons. The boundary between the inner and outer crust occurs at the density where the chemical potential for neutrons exceeds their mass in vacuum. A nucleus found at this chemical potential is past the neutron drip line and would be unbound in vacuum, but in the inner crust of a NS, an excess of neutrons in nuclei comes into equilibrium with a background of unbound neutrons ("dripped" neutrons). In the inner crust, exotic neutron-rich nuclei are immersed in a background of free electrons and dripped neutrons and in the innermost regions of the inner crust, these nuclei become non-spherical ("nuclear pasta") [13]. Figure 1.2 shows a schematic diagram of the different pasta shapes found in the inner crust. The outer part of the core of the NS is a fluid of neutrons, protons, and charged leptons with muons appearing in the vicinity of saturation density ($n_{sat} = 0.16\,\mathrm{fm}^{-3}$) when the chemical potential for electrons exceeds the muon mass. It is not known whether the entire core is composed of hadronic matter or whether a quark phase might appear at high density. Figure 1.1 shows a diagram of these layers with approximate densities noted. While the maximum central density of a NS is not known, it is expected to be between $5n_{sat}$ and $10n_{sat}$.

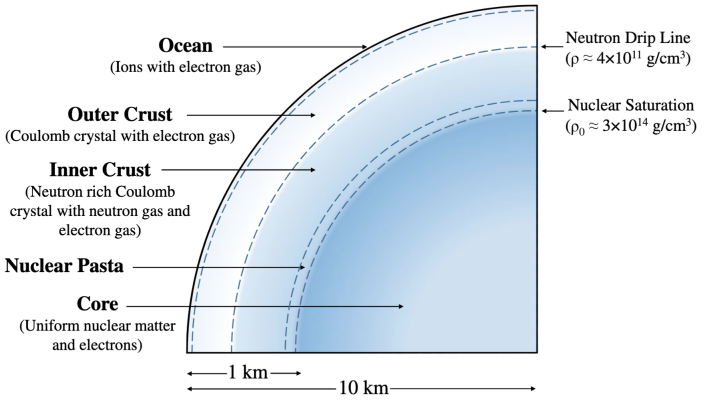

Figure 1.1: Schematic of the outer layers found in neutron stars. Figure from Ref. [14]

From the crust to the inner core, the Fermi energies of all the relevant particles range from tens to hundreds of MeV. Once a NS is at least a few seconds old, its temperature falls below an MeV and the system can be treated as cold [15]. After this initial cooling, any neutrinos produced by weak interactions have a mean free path greater than the size of the star and they escape. Since all of the energy and momentum scales are significantly less than the electroweak scale, the Fermi theory of beta decay is adequate to describe the weak interaction though a fully relativistic treatment should ideally include weak magnetism (for examples of the effects of weak magnetism, see Refs. [16, 17]).

For all constituents of the NS besides neutrinos, the inter-particle spacing and mean free path are a few fm and the Debye screening length is tens or hundreds of fm. Since the spacetime metric undergoes

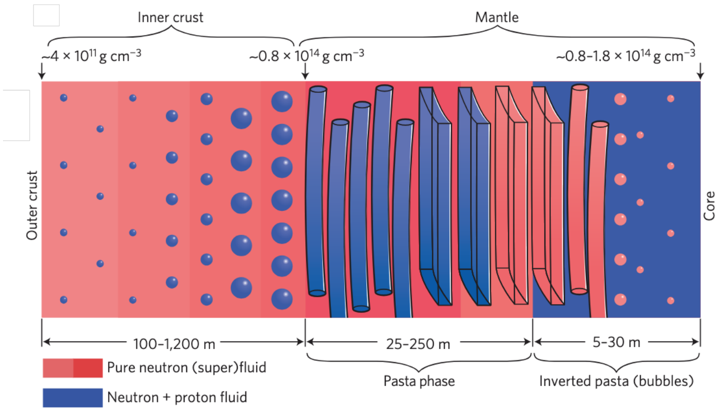

Figure 1.2: Different shapes of nuclei found in the inner crust of neutron stars. Figure from Ref. [18]

$\mathcal{O}(1)$ changes over distances of km, we calculate particle dynamics and composition assuming a locally flat spacetime metric. The exception where the behavior of a field needs to be calculated self-consistently with gravity occurs when the Compton wavelength is at least $\mathcal{O}(\text{km})$ and the field is unscreened.

Being the densest observed objects that are not black holes, the structure of a NS must be calculated using the TOV equations from general relativity.

$$\frac{\mathrm{d}p}{\mathrm{d}r} = -(p+\varepsilon)\frac{GM}{r^2}\left(1+\frac{4\pi r^3 p}{M}\right)\left(1-\frac{2GM}{r}\right)^{-1} \tag{1.1}$$

$$\frac{\mathrm{d}M}{\mathrm{d}r} = 4\pi r^2 \varepsilon \tag{1.2}$$

for $M(r)$ the enclosed mass within radius r, p the pressure, and ε the energy density. Practical numerical calculations are made easier by noting that the Schwarzschild radius of the Sun is $2GM_\odot/c^2 = 2.95\,\text{km}$ and performing all numerical calculations in units of solar masses and solar Schwarzschild radii.

Once a NS has gone through its initial proto-neutron star (PNS) evolution, the transport of heat and particles through the core is efficient and the entire core is in thermal and chemical equilibrium, modified by general relativity [19]. In a thermally equilibrated core, the redshifted temperature $\tilde{T} = T(r)e^{\nu(r)}$ is uniform throughout the core for $e^{2\nu(r)}$ the time-time component of the spacetime metric with the Schwarzschild boundary condition at the surface. In a chemically equilibrated NS, the redshifted baryon chemical potential $\tilde{\mu}_B = \mu_B(r)e^{\nu(r)}$ is a constant. The metric function $\nu(r)$ can be easily found from a solution to the TOV equations with the relation

$$\frac{\mathrm{d}\nu}{\mathrm{d}r} = -\frac{1}{p+\varepsilon}\frac{\mathrm{d}p}{\mathrm{d}r} \tag{1.3}$$

and the boundary condition at the surface

$$\nu(R_{\mathrm{NS}}) = \frac{1}{2}\log\left[1-\frac{2GM(R_{\mathrm{NS}})}{R_{\mathrm{NS}}}\right]. \tag{1.4}$$

While the core is isothermal because of its high thermal conductivity, large thermal gradients can occur in the crust due to their lower thermal conductivity [20]. How rapidly the temperature changes in the crust is a sensitive function of the composition of the outermost 100 or so meters of the crust, referred to as the envelope. Heat that will escape the star as blackbody radiation must first pass through the envelope. When the envelope is composed purely of iron, heat transport in the envelope is inefficient and the thermal gradient will be large while an envelope with light elements will have enhanced thermal conductivity and will be more isothermal [21–23], see Fig. 1.3.

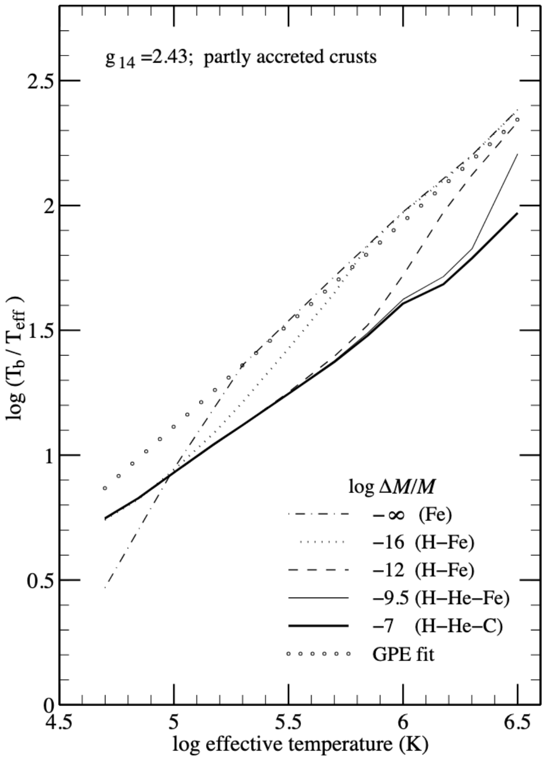

Figure 1.3: Temperature profiles of envelopes with varying composition. Plot from Ref. [21].

1.2 Microphysics of neutron star matter

Since the timescale for weak interactions is short compared to the life of the star, at temperatures below an MeV, the nucleons and leptons are in equilibrium with respect to the weak interaction and the relevant conserved charges are baryon number and electric charge. As such, we may define all of the chemical potentials in terms of the chemical potential associated with baryon number μ_B and the chemical potential associated with (negative) electric charge μ_e. The chemical potential of particle species i with baryon number B_i and charge Q_i is then given by

$$\mu_i = B_i\mu_B - Q_i\mu_e \,. \tag{1.5}$$

This relation carries over to quark matter and matter with strangeness so long as weak equilibrium is maintained.[1]

The densities present in NSs pose a particular challenge but also an opportunity. Cold laboratory experiments cannot significantly exceed nuclear density and heavy ion collisions, while achieving supranuclear densities, probe temperatures much higher than are found in NSs. Since QCD is non-perturbative in this regime and lattice QCD is only applicable at zero baryon chemical potential due to the famous sign problem, we must rely on effective field theory (EFT) methods to perform low energy nuclear physics calculations. Unfortunately, Chiral EFT (χEFT) has a breakdown scale that is reached between one and two times saturation density. Above this density, we must rely on nuclear models to do numerical simulations. Although this has the potential to be quite limiting in the robustness of any predictions and we must always guard against model-dependence, it also means that the properties of NSs directly probe densities that are currently inaccessible to both theory and terrestrial experiments.

The composition of the inner core of a NS is not known, with expectations that the central density of the heaviest NSs may be anywhere from $5n_{sat}$ to $10n_{sat}$. At these densities, it is possible that quarks deconfine and the inner core is a fluid of up, down, and strange quarks as well as a suppressed population of charged leptons. It is also possible that a population of hyperons or a meson condensate appears, although both of these scenarios result in a significant softening of the high density equation of state that is challenging to reconcile with observations of NSs with masses as large as $2M_\odot$. Such constraints can be avoided by invoking strong repulsion at high density (for example from three-body forces), but these scenarios remain speculative. As such, we must remain relatively agnostic on the composition of the inner core.

As NSs probe the properties of high density matter, they can also be used as detectors for any beyond Standard Model (BSM) theory that can be sourced by such matter. Light exotic fields with couplings to nucleons (like axions) are particularly attractive as small modifications to the energy per baryon of neutron star matter may be enough to source such a field. In Chapter 2, we will address the possibility of using neutron stars to constrain QCD axions and their lighter cousins “exceptionally light” QCD axions.

1.3 Neutron star equation of state

The first observed NSs were pulsars and NSs in accreting x-ray binaries with a main sequence companion. The rapid and regular pulse rate of radio pulsars (some reaching a frequency of hundreds of Hz [25]) and the short orbital periods of x-ray binaries indicated that the objects in these systems were incredibly compact [3, 26]. More recently, the regular pulse periods of radio pulsars have been used to measure NS masses in binary neutron star (BNS) systems by measuring the Shapiro delay of pulse signals as a function

---

[1] At the high temperatures found in proto-neutron stars and neutron star mergers, an imbalance between the rates of electron capture and beta decay causes this simple relation to fail. [24]

of orbital phase. Notably, observations of PSR J1614-2230, PSR J0348+0432, and PSR J0740+6620 confirmed the existence of neutrons stars with a mass $M \gtrsim 2\,M_\odot$ [27–29]. These observations, combined with nuclear theory predictions from χEFT that the low density equation of state (EOS) has relatively low pressure (it is "soft") suggest that the pressure of NS matter must rapidly rise (it becomes "stiff") above $2n_{sat}$. Without this rapid stiffening, it is not possible to achieve a maximum mass of $2\,M_\odot$ [30]. This is intriguing in light of the expectation that at high density QCD must become weakly coupled and approach the unitary gas limit of sound speed $c_s^2 = 1/3$ from below. This suggests that the sound speed of beta equilibrated matter must be non-monotonic, indicating a possible phase transition.

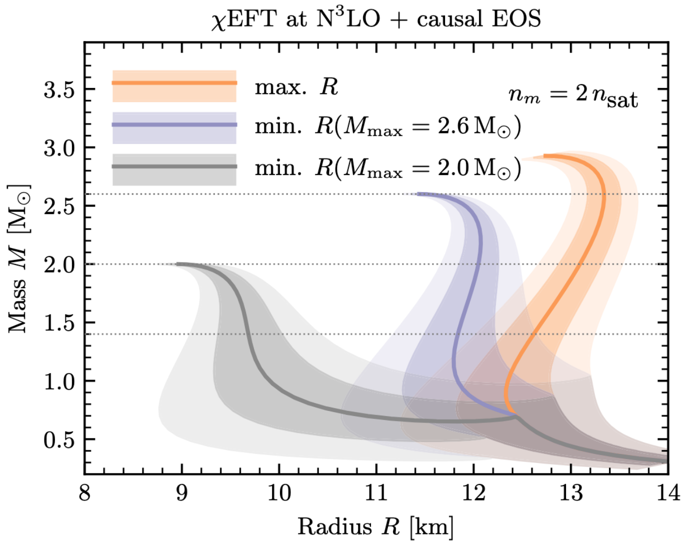

Figure 1.4: Maximally soft and stiff EOS allowed by Chiral EFT. Plot from Ref. [31]

Requiring that the low density equation of state match calculations from χEFT but also requiring that the equation of state be stable, causal, and permit $2\,M_\odot$ NSs places constraints on the possible mass-radius relationship (shown in Fig. 1.4) [31]. In particular, the fact that any putative model for high density matter must accommodate the $2\,M_\odot$ constraint significantly limits the theory space. A model with too many degrees of freedom and insufficiently repulsive forces between particles will be unable to reach this bound, putting strong constraints on scenarios in which hadrons with strangeness or quarks appear at high density. Requiring that perturbative QCD calculations be matched at high density while maintaining stability, causality, and thermodynamic consistency further constrains the range of possible EOSs [32–35] (shown in Fig. 1.5). There remain open questions about how best to implement these various constraints in a framework with rigorous error bars [36, 37]. Further constraints can in principle be gleaned by relating the EOS at finite isospin chemical potential (where lattice QCD is applicable) to large baryon chemical potential, though at present such calculations are less constraining than standard NS phenomenology [38].

Since the TOV equations give a one-to-one correspondence between the EOS and the mass-radius relationship of a single gravitationally bound fluid, understanding the EOS of dense matter is a central question in the study of NSs. The observation of a BNS merger in GW170817 [4] and recent results from NICER [39–41] provide some constraints on the mass-radius relationship of NSs, but uncertainties remain substantial. While the EOS on its own does not reveal the composition of a NS, it can contain clues about possible phase transitions or the appearance of exotic degrees of freedom.

1.4 Neutron star cooling

Although GW and x-ray observations can constrain the mass and radius of NSs (and therefore the EOS), this does not on its own give details about the composition of NSs. In order to probe the composition of NSs, we must rely on other observables. After its first few seconds of cooling a NS is transparent to neutrinos and any neutrino emission processes can be used to probe properties of the core. The cooling of young isolated NSs is dominated by emission of neutrinos from the core. Emission of photons in a nearly blackbody spectrum from its surface takes over at later times [15].

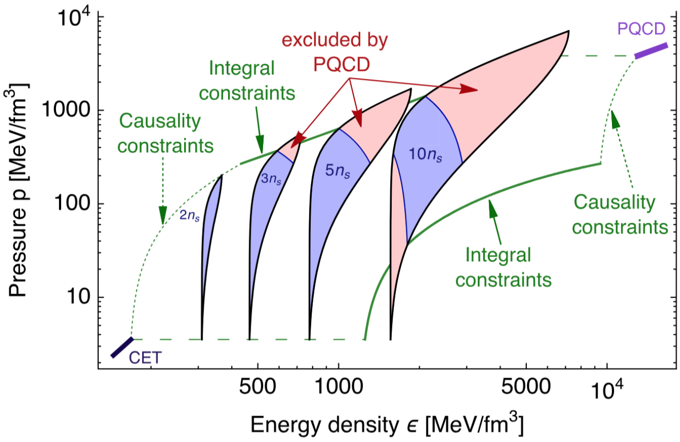

Figure 1.5: Causality, stability, and integrability constraints on the equation of state from Chiral EFT and perturbative QCD. Plot from Ref. [32]

Of particular relevance for this thesis is the direct Urca process. Direct Urca consists of the reactions $n \to p + e + \bar{\nu}$ and $e + p \to n + \nu$. Since neutrinos freely escape the star without interacting, their density is effectively zero and the neutrons, protons, and electrons are in equilibrium and this process occurs on the Fermi surfaces of all three particle species. Although direct Urca is by many orders of magnitude more efficient than other cooling processes available in typical NS conditions [42], it can only operate when the triangle inequality is satisfied, requiring $|k_{Fn}| \leq |k_{Fp}| + |k_{Fe}|$ in order to conserve momentum. In matter containing only neutrons, protons, and electrons, this corresponds to a proton fraction $Y_p \geq 1/9$. In practice, a slightly higher proton fraction is required as muons will appear in the star before this density is reached, somewhat reducing the population of electrons. As such, the rate of neutrino cooling is a sensitive function of the proton fraction in the vicinity of $Y_p \simeq 1/9$, allowing the thermal history of NSs to indirectly probe the symmetry energy of nuclear matter.

Some NSs, notably the transiently accreting binary SAX J1808.4-3658, seem to require the presence of direct Urca to explain their cooling. This system has an observed photon luminosity in quiescence of less than 10^{31} erg/ s and a time averaged accretion rate of $10^{-11} M_\odot$/ yr [43–45]. Under the assumption that this system has been transiently accreting long enough to be in time averaged thermal equilibrium, its neutrino luminosity can be constrained with the simple relation

$$C_V \langle \dot{T} \rangle = H - L_\gamma - L_\nu \tag{1.6}$$

where C_V is the heat capacity, $\langle \dot{T} \rangle$ is the time averaged rate of change in temperature, H is the heating rate, and L_γ and L_ν are the photon and neutrino luminosities, respectively. If $\langle \dot{T} \rangle = 0$ and H can be estimated by observing the accretion rate $\dot{M}$, the luminosity in neutrinos can be determined. With these simple relations, the neutrino luminosity of different nuclear models can be compared to x-ray observations of x-ray transients in outburst and quiesence. Figure 1.6 shows a sample output of such a calculation for a relativistic mean field model from Ref. [46] that accesses direct Urca in $1.7\, M_\odot$ neutron stars, compared to observational data of transiently accreting x-ray binaries from Ref. [47].

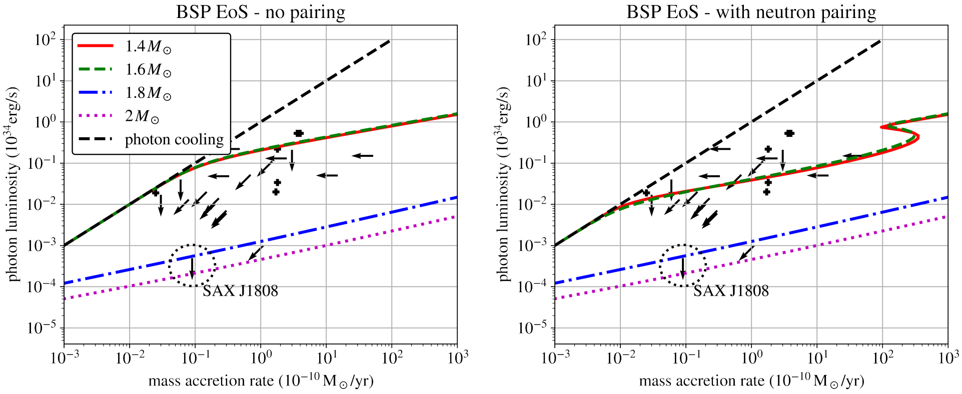

Figure 1.6: Photon luminosity vs. accretion rate for transiently accreting systems in quasi-thermal equilibrium in a relativistic mean field model (BSP [46]) compared with observational data from Ref. [47] with SAX J1808.4-3658 circled. Black crosses are data and black arrows are upper limits. In the left panel superfluidity is ignored while in the right panel the neutrons are paired using pairing gaps given in Ref. [48].

Using the estimate that approximately one MeV of heat is released per accreted baryon [47], SAX J1808 appears to require a neutrino luminosity of $L_\nu > 10^{32}$ erg/ s in spite of having a surface temperature $T \lesssim 3 \times 10^5$ K. This is impossible to achieve with only slow cooling methods and seems to suggest that direct Urca must be possible at some density that NSs can probe.

At the same time, the thermal evolution of most NSs is well-explained without invoking direct Urca [49]. At densities where $Y_p < 1/9$, modified Urca and neutral current bremsstrahlung dominate.

Modified Urca consists of the reactions $N+n\rightarrow N+p+e+\bar{\nu}$ and $N+p+e\rightarrow N+n+\nu$ while bremsstrahlung is achieved with the reaction $N+N\rightarrow N+N+\nu+\bar{\nu}$. The rates of these processes combined with uncertainties in envelope composition leading to uncertain inference of core temperature [22] allow the observed ages and temperatures of most NS to be explained. Either direct Urca is only accessible at the densities probed by the heaviest NSs, or there is some mechanism that suppresses it in low mass stars. Superfluidity of nucleons is one such explanation that will be discussed more in Sec. 1.6 though the high sensitivity of the pairing gap to density makes it questionable as a way to suppress neutrino cooling across such a broad range of densities. As such, any scenario that predicts a proton fraction of $Y_p\gtrsim 1/9$ at too low baryon density can be often be falsified by invoking observed ages and temperatures of isolated NSs.

Incorporating mean field nuclear interactions to calculations of cooling rates and other thermal processes is straightforward. In a mean field model, the dispersion of nucleons is given by

$$E_{n,p}=\sqrt{k^2+M^{*2}_{n,p}}+U_{n,p}\,. \tag{1.7}$$

As such, the Landau effective mass (which we will denote as M^*_L to avoid the unfortunate notation conflict with the effective mass in the relativistic mean field model) is given in a mean field model by

$$M^*_L\equiv\frac{k}{\partial E/\partial k}=\sqrt{k^2+M^{*2}} \tag{1.8}$$

which at the Fermi surface is just $\mu_{n,p}-U_{n,p}$. In a non-relativistic calculation (using the formulae in works like Ref. [42]), this expression for M^*_L and the modified dispersion are the only effects nuclear interactions have on the calculation. In a relativistic calculation, M^*_L takes the place of the energy in most parts of the formalism. The phase space factor used in any calculations with Fermi's golden rule takes the form

$$\int\frac{d^3k}{2E(2\pi)^3}\rightarrow\int\frac{d^3k}{2M^*_L(2\pi)^3} \tag{1.9}$$

and the relativistic spinors for nucleons are also modified.

$$\psi=\sqrt{E+M}\begin{bmatrix}\chi\\ \frac{\sigma\cdot\vec{k}}{E+M}\chi\end{bmatrix}\rightarrow\sqrt{M^*_L+M}\begin{bmatrix}\chi\\ \frac{\sigma\cdot\vec{k}}{M^*_L+M}\chi\end{bmatrix} \tag{1.10}$$

where χ is a two-component spinor for spin up or spin down.

1.5 Magnetic fields

NSs are known to possess strong magnetic fields, with typical NSs having a surface field of 10^{12-13} G or less with a subset of NSs known as magnetars possessing surface fields of up to 10^{15} G [25,50,51]. Recent observations of the radio pulsar GLEAM-X J1627 suggest it may have a surface field as strong as 10^{16} G, motivating the study of matter in the presence of such strong magnetic fields [52]. Although the protons in the cores of NSs are expected to be superconducting, it is expected that the field of a magnetar is stronger than the critical field strength and the Meissner effect does not expel the magnetic field in the core [53].

While the internal magnetic field configuration of magnetars is not fully known, (see Ref. [54] for a discussion) it is expected that magnetic fields inside magnetars may be several times larger than at their surface [55]. Although direct observation of radio pulsars only reveals the dipole component of the magnetic field, it is possible (and in fact likely) that near the surface of a neutron star the field configuration is more complicated. Simulations indicate that poloidal magnetic fields in rotating NSs will generically produce mixed poloidal-toroidal fields [56]. Figure 1.7 shows a sample output of such a simulation. Analysis of the x-ray pulse profile detected by NICER consistently suggests some of the observed sources have two hot spots in the same hemisphere [39–41], requiring a more complicated structure than a simple dipole.

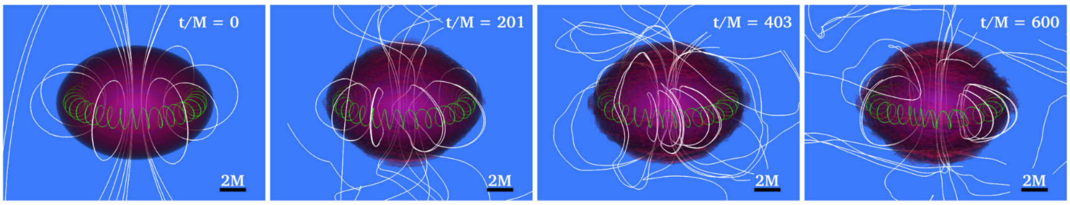

Figure 1.7: Magnetrohydrodynamical simulation of magnetic field evolution of a rotating NS in an initially poloidal field configuration. Plot from Ref. [56].

Magnetic fields seem to contribute to heating of NSs though a mechanism that is not fully understood (see Ref. [57] for a discussion), resulting in the hottest family of observed isolated neutron stars all being magnetars [51]. The presence of strong magnetic fields also modifies the dispersion of protons and electrons when $eB \gtrsim T\varepsilon_F$ for ε_F the Fermi energy and, as a result, modifies the cooling rates of NSs. In Chapter 4, we will discuss the effects that the modified dispersions of charged particles in a magnetic field has on the neutrino emissivity of such stars and on capture rates of neutrinos in the ejecta of BNS mergers.

1.6 Superfluidity

In the presence of any attractive interaction channel, a system of fermions will be unstable to the formation of Cooper pairs at sufficiently low temperature (the BCS instability). While the temperatures in NSs are hot by terrestrial standards, the interactions between nucleons are strong, allowing superfluid gaps of order $\mathcal{O}(\,\text{MeV})$ [58]. If the inner cores of NSs are composed of deconfined quark matter, the color degree of freedom opens up a wealth of possible paired phases [59]. For the sake of this thesis, the focus will be on superfluidity of nucleons though the possibility of color sextet (color symmetric) pairing of quarks will be discussed briefly in Chap. 5.

The most relevant partial waves for Cooper pairing of nucleons are ${}^1S_0$ and the three spin triplet p-wave channels. At low relative momentum, the ${}^1S_0$ channel is nearly bound and attractive so at lower densities, pairing in the ${}^1S_0$ channel is expected to dominate. This is the relevant scenario for dripped neutrons in the inner crust and protons in the outer part of the liquid core. At center of mass momentum $k \gtrsim 350\,\text{MeV}$ however, the ${}^1S_0$ interaction becomes repulsive in vacuum ($k_F = 350\,\text{MeV}$ corresponding to a density of $0.19\,\text{fm}^{-3}$). At somewhat lower momentum, the ${}^3P_0$ interaction becomes repulsive while the ${}^3P_1$ reaction is repulsive for all momenta. The ${}^3P_2$ interaction, however, becomes increasingly attractive at large momentum transfer in vacuum and so is expected to be the dominant pairing channel for neutrons in the core. All the preceding statements are based on scattering experiments with nucleons and as such do not include the effects of intermediate interactions with the medium. In Chapter 5, we will discuss the importance of medium corrections to the amplitude of NN scattering when calculating the superfluid gap.

Superfluidity primarily has two important effects on NS cooling. In the paired phase, the amount of energy necessary to produce a particle above the Fermi surface is increased by 2Δ, the energy gap of the spectrum. The presence of a gap in the spectrum depletes the number states immediately around the Fermi momentum, resulting in fewer particles above the Fermi surface and fewer holes below it, suppressing any scattering processes. If the temperature is far below the critical temperature ($T \ll \Delta$), equilibrium processes like Urca processes and bremsstrahlung are suppressed by roughly $e^{-\Delta/T}$. At the same time, if the critical temperature for pairing is of the same order as the temperature ($\Delta \sim T$), pair breaking and formation (PBF) becomes available as a new cooling channel, more efficient than modified Urca and bremsstrahlung but less efficient than direct Urca. In the paired phase, the U(1) symmetry associated with particle number conservation is broken to $\mathbb{Z}_2$, representing the fact that pairs of quasiparticles can enter and leave the condensate of Cooper pairs. Pairs of quasiparticles can annihilate while their energy produces two neutrinos.

While not as striking an enhancement as direct Urca, PBF is of particular interest because its emissivity is non-monotonic with temperature. Where all of the other neutrino processes scale as some power of the temperature, PBF is absent at temperatures far above and below the critical temperature for pairing and peaks when $T \simeq T_c$. This motivates the minimal cooling paradigm proposed in Ref. [49] to explain the diversity of NS temperatures and ages. Unfortunately, while superfluidity in neutron stars has many exciting possible signatures, the exact value of the pairing gap is not robustly known and likely relies on nuclear physics occurring at energy scales that presently available tools cannot access.

Chapter 2

Neutron Stars with Exceptionally Light QCD Axions[1]

2.1 Introduction

The quantum chromodynamics (QCD) axion is a well-motivated and minimal solution to the Strong Charge-Parity (CP) problem [60–63], the puzzle of the smallness of the neutron electric dipole moment (EDM). The neutron EDM is proportional to $\bar{\theta}$, a combination of Standard Model parameters,

$$\bar{\theta} = \theta + \arg\det Y_u Y_d, \tag{2.1}$$

where θ is the QCD θ angle, while Y_u and Y_d are the up- and down-type Yukawa matrices. The combination is experimentally bounded to be $\bar{\theta} \lesssim 10^{-10}$ based on the non-observation of the neutron electric dipole moment [64]. The smallness of $\bar{\theta}$ is particularly puzzling since the CP-violating angle in the Cabibbo-Kobayashi-Maskawa (CKM) matrix has been measured to be $\mathcal{O}(1)$, in agreement with theoretical expectation.

The axion is the pseudo-Nambu-Goldstone boson resulting from the spontaneously broken Peccei-Quinn symmetry and couples to gluons as

$$\mathcal{L} \supset \left(\frac{a}{f_a} - \bar{\theta}\right)\frac{\alpha_s}{8\pi} G^{\mu\nu}\tilde{G}_{\mu\nu}, \tag{2.2}$$

where a is the axion field, f_a the axion decay constant, α_s the strong coupling constant, $G^{\mu\nu}$ the color field strength tensor, and $\tilde{G}_{\mu\nu} \equiv \varepsilon_{\mu\nu\rho\sigma}G^{\rho\sigma}/2$ its dual. The entire dependence on $\bar{\theta}$ has been placed in the gluon term after a chiral rotation of the quarks. At low energies, the axion obtains a periodic potential

---

[1] This chapter summarizes work originally found in Ref. [10]

from the coupling to gluons, and the CP-violating angle $\bar{\theta}$ relaxes to zero during cosmic evolution of the axion field in its potential [65–67].

The QCD axion has inspired a diverse experimental campaign [68–71]. Searches for the QCD axion and axion-like particles (ALPs) through their electron and photon couplings (see Fig. 2.1 and 2.2 for the current best constraints) have seen tremendous progress in recent years. The axion-gluon coupling—the coupling that defines the QCD axion and distinguishes it from ALPs that do not solve the strong CP problem—is much more difficult to probe in the laboratory [72–76]. The sensitivity of current ground-based experiments is rapidly improving [77–87], but is as yet orders of magnitude away from the "QCD axion line" on which the axion decay constant f_a and the axion mass $m_a^{(\mathrm{QCD})}$ are related by the QCD prediction [60],

$$m_a^{(\mathrm{QCD})} = \sqrt{\frac{m_u m_d}{(m_u + m_d)^2}} \frac{m_\pi f_\pi}{f_a} \,. \tag{2.3}$$

Furthermore, these laboratory searches are at present far weaker than astrophysical constraints from Big Bang Nucleosynthesis [88], the evolution of supernova 1987A [89–94], stability of the Earth, the Sun and white dwarfs [95,96], LIGO-Virgo-Kagra (LVK) measurements of binary neutron star inspirals [95,97,98] and isolated neutron star cooling [99]. See e.g. [100,101], for recent reviews and Fig. 2.4 for the current best constraints from laboratory and astrophysical searches.

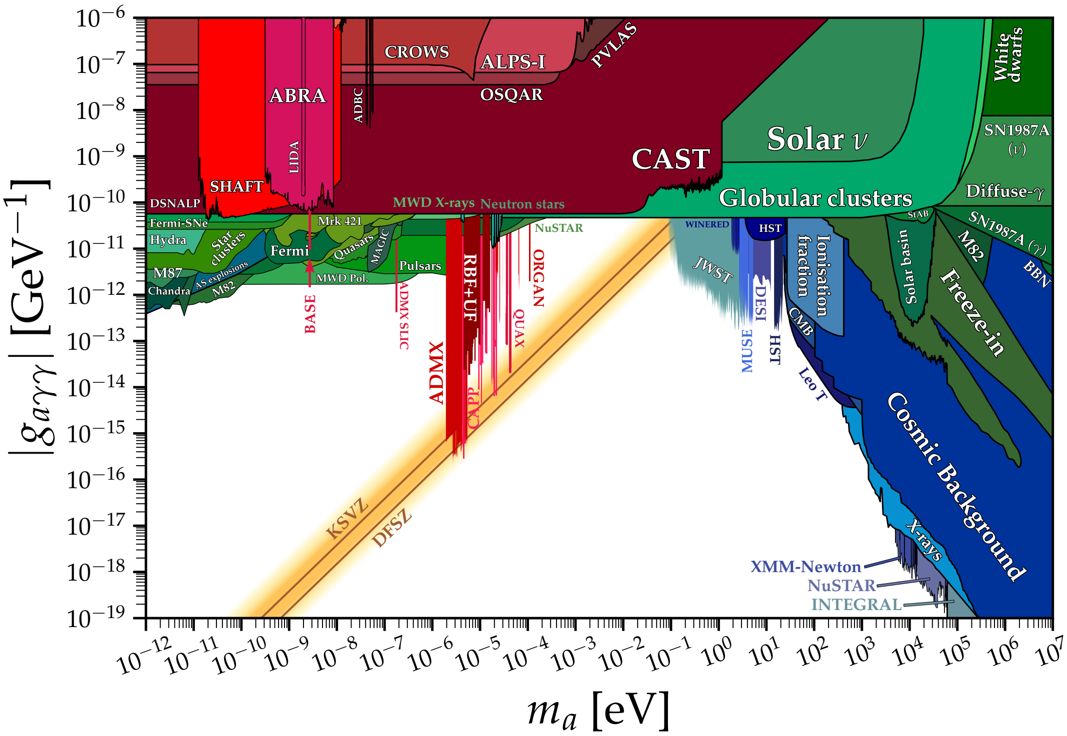

Figure 2.1: Existing constraints on the axion-photon coupling. The yellow band shows the QCD axion. Plot from Ref. [69]

Theoretically, there is renewed interest in the parameter space of axions which solve the strong CP problem but have an exceptionally light mass, $m_a < m_a^{(\mathrm{QCD})}$, in light of the discrete symmetry noted in

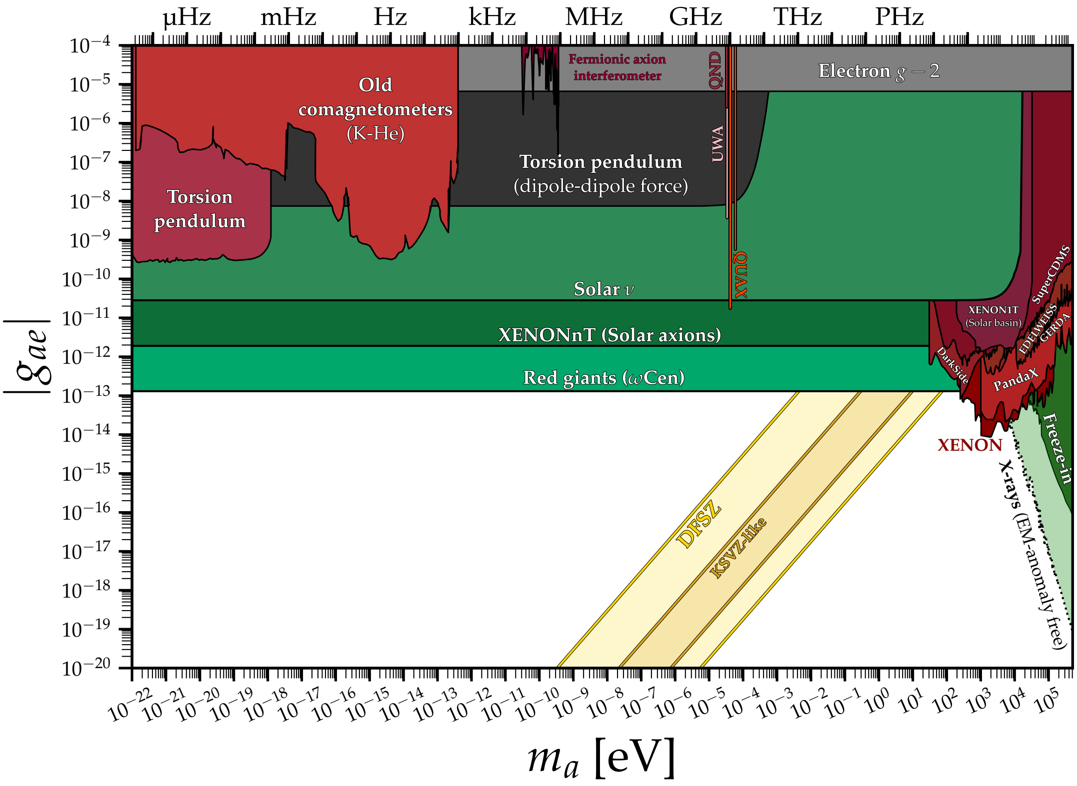

Figure 2.2: Existing constraints on the axion-electron coupling. The yellow band shows the QCD axion. Plot from Ref. [69]

Ref. [102]. A discrete $\mathbb{Z}_\mathcal{N}$ symmetry can suppress the axion mass below that predicted by Eq. (2.3) in a technically natural way by a factor of

$$\varepsilon^{1/2} \equiv \frac{m_a}{m_a^{(\mathrm{QCD})}} \approx \frac{1}{2^{\mathcal{N}/2-\log\mathcal{N}}} \tag{2.4}$$

in the large $\mathcal{N}$ limit [103]. This is accomplished by coupling θ to $\mathcal{N}$ mirror QCDs with a relative shift of $2n\pi/\mathcal{N}$ for n an integer between 0 and $\mathcal{N}-1$. As θ is the only specified portal between each mirror QCD, all properties of nuclear physics at finite θ are unchanged in each QCD except for the combined vacuum potential for θ, shown for $\mathcal{N}=3$ in Fig. 2.3.

A natural mechanism to tune down the strength of the axion potential motivates the study of lighter-than-expected QCD axions—hereafter referred to as exceptionally light QCD axions—that still solve the strong CP problem (for $\mathcal{N}$ odd). This chapter describes constraints that can be placed on the parameter space of exceptionally light QCD axions due to their effects on neutron star observables.

Even within the $\mathbb{Z}_\mathcal{N}$ model, we note that as a small θ angle is itself technically natural, the very small $\varepsilon \ll 1$ parameter space, in particular $\varepsilon \lesssim 10^{-10}$, cannot be well-motivated: it would introduce a tuning at the level of the original tuning of the Strong CP problem. As we discuss below, due to their high density, neutron stars provide a unique environment to test exceptional axions close to the QCD line: values of ε close to unity, and $\mathbb{Z}_\mathcal{N}$ models for modest values of $\mathcal{N}$. We note that the vacuum structure

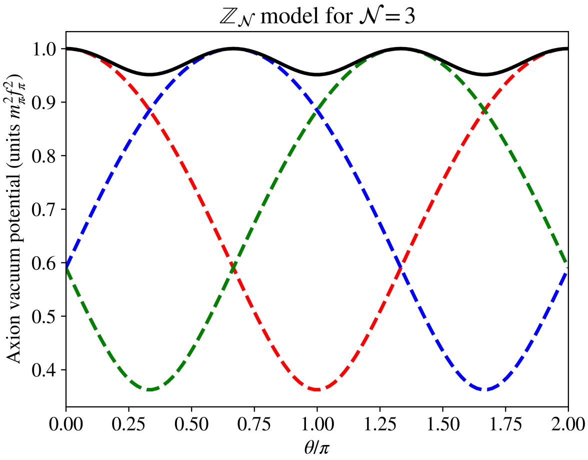

Figure 2.3: Vacuum potentials for $\mathcal{N} = 3$ mirror QCDs in the $\mathbb{Z}_{\mathcal{N}}$ model (dashed colored lines) and the combined potential experienced by an exceptionally light QCD axion in this model (solid black line).

of the $\mathbb{Z}_{\mathcal{N}}$ model is significantly different from the phenomenological ε model and can result in different dynamics and constraints.

Observationally, the above-mentioned studies of dense astrophysical objects place strong constraints on the axion-gluon coupling parameter space, and hence ε, especially at small axion masses. These constraints stem from the effect first noted in Ref. [95]. The axion potential is modified in the presence of matter, which suppresses the vacuum QCD contribution. For small ε, there is a critical density above which a large, dense object can contain a region with negative effective axion mass which, in turn, shifts the potential minimum from $\bar{\theta} = 0$ to $\bar{\theta} = \pi$ inside the object. For Earth and solar core densities, the $\bar{\theta} = \pi$ region emerges for $\varepsilon \lesssim 10^{-13}$, while in white dwarfs, $\bar{\theta} = \pi$ occurs at $\varepsilon \lesssim 10^{-7}$ [95]. Studies of the properties and stability of these objects have led to the most stringent constraint on the parameter space of $\varepsilon \lesssim 2 \times 10^{-7}$ for $f_a \lesssim 10^{16}\,\mathrm{GeV}$ [96].

In this study, we focus on axion condensation in neutron stars for $\varepsilon \gtrsim 5 \times 10^{-7}$. Earlier work has shown that for small axion masses ($m_a \lesssim 10^{-11}\,\mathrm{eV}$) the axion condensate extends far outside the radius of the star [95]. In this scenario, the extended axion field mediates a force between neutron stars and is constrained by LVK observations of neutron star mergers [95, 97, 98]. For a heavier axion with $m_a \gtrsim 10^{-8}\,\mathrm{eV}$, the axion field is largely confined inside the neutron star, and the effects of axion condensation on the neutron star interior need to be understood to predict the observational consequences. Prior work has considered neutron stars in the axion condensed phase in the non-interacting Fermi gas approximation [104] and in hybrid stars where axion interactions were included in the quark phase (but not the nuclear phase) via an effective 't Hooft determinant interaction in the NJL model [105].

In this work, we provide a dedicated study of the equation of state (EOS) for $5 \times 10^{-7} \lesssim \varepsilon < 1$ and its impact on neutron star structure. To calculate the EOS and phases present in the neutron star, we compare results from Chiral Effective Field Theory (ChiEFT) and relativistic mean field theory

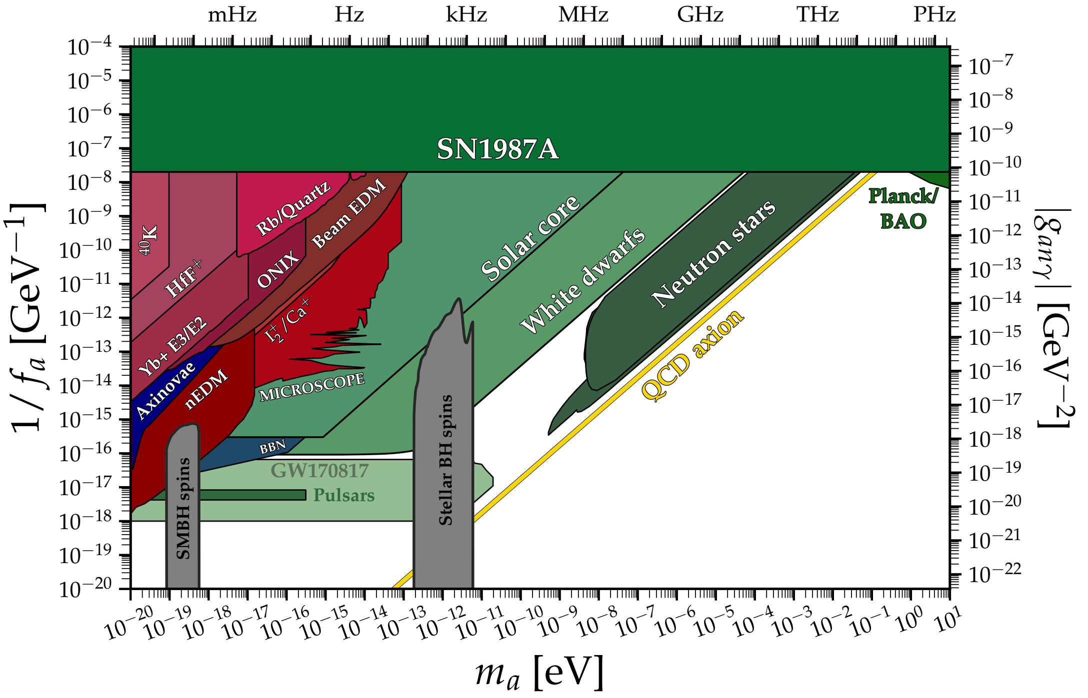

Figure 2.4: Existing constraints on the axion-gluon coupling. Plot from Ref. [69]

(RMFT). As noted in Ref. [95], the reduction in the effective mass of the axion in the presence of finite baryon density also leads to a reduction in the effective mass of nucleons. At fixed chemical potential, a smaller effective nucleon mass results in a larger baryon density. As a result, the transition from $\bar{\theta} = 0$ to $\bar{\theta} = \pi$ introduces a discontinuity in the EOS. For different ε, this transition occurs at different locations in the neutron star, leading to a variety of observational effects. For $\varepsilon \gtrsim 0.1$, the neutron star will have an inner region with $\bar{\theta} = \pi$, separated by an axion field profile from the outside region where $\bar{\theta} = 0$, while for smaller ε the entire star has $\bar{\theta} = \pi$ except for a thin region near the surface. When $\varepsilon \lesssim 0.1$, $\bar{\theta} = \pi$ becomes energetically favored at a baryon chemical potential lower than that of iron ($\mu_{\mathrm{Fe}}/A \simeq m_N - 8\,\mathrm{MeV}$) and the axion pressure itself becomes important at low density, producing a state with zero pressure at non-negligible energy density. This may result in a star that is almost entirely at a density above the neutron drip density or above the crust-core transition density. In this case, the remaining crust phases will only appear in a thin region where θ changes from π to 0.

Recent observations of neutron stars (NSs) have resulted in reliable measurements of NS masses and constraints on their size. Radio observations of pulsars have now provided compelling evidence for neutron stars with masses greater than 2 $\mathrm{M}_\odot$, while gravitational wave and x-ray observations suggest that typical NSs with mass $\simeq 1.4\,\mathrm{M}_\odot$ have radii in the range 11-13 km. Taken together, these observations and recent ChiEFT-based calculations of the EOS of neutron-rich matter indicate that the pressure of dense matter inside neutron stars is relatively small up to $2n_{sat}$, where $n_{sat} = 0.16$ nucleons per fm^3 is the nucleon density at nuclear saturation, and increases rapidly at higher densities encountered in the neutron star inner core to support massive neutron stars [106–108]. A relatively soft EOS in the outer core and inner crust of a neutron star has important implications for neutron star structure. As we discuss, axion condensation at $n_B \lesssim n_{sat}$ could have dramatic effects on the structure and dynamics of the outer regions of the neutron star with observable consequences.

The outline of this paper is as follows. In Sec. 2.2, we describe the most important features of axion condensation in a simple gas of non-interacting nucleons. In Sec. 2.3, we discuss the effects of axion condensation including the potential effects of nuclear interactions, with a focus on ChiEFT and RMFT models. Section 2.4 describes the impact that axion condensation has on the structure and properties of neutron stars within our nuclear model. In Sec. 2.5, we describe novel nuclear density objects stabilized by an axion potential rather than gravity, first proposed in Refs. [96,104] for a non-interacting Fermi gas. We present constraints in the f_a-m_a parameter space for the phenomenological ε model and comment on the $\mathbb{Z}_\mathcal{N}$ model based on neutron star observables in Sec. 2.6. Section 2.7 concludes this manuscript with a summary and outlook.

2.2 Axion condensation in a dilute gas of nucleons

In this section, we summarize the main properties of axions discussed in Refs. [95–98, 104, 109–112], which lead to the development of an axion profile around compact stellar objects with $\bar{\theta} = \pi$ inside these objects and $\bar{\theta} = 0$ outside. We focus here on the scenario of a dilute nucleon gas (see also [104]) and leave the impact of interactions to Sec. 2.3. We also review the main observational consequences for the Earth, the Sun, white dwarfs and neutron stars. Henceforth, we take the quark mass matrix to be real and $\bar{\theta} = \theta$. Throughout the paper, we work with an axion with the following potential in vacuum

$$V(\theta) = -\varepsilon m_\pi^2 f_\pi^2 \,\left[f(\theta) - 1\right] , \tag{2.5}$$

where [113]

$$f(\theta) = \sqrt{1 - \frac{4m_u m_d}{(m_u + m_d)^2} \sin^2\left(\frac{\theta}{2}\right)} , \tag{2.6}$$

and $\theta = a/f_a$. The minimum of this potential is at $\theta = 0$ and the mass of the axion is[2]

$$m_a = \varepsilon^{1/2} m_a^{(\mathrm{QCD})} = \varepsilon^{1/2} \sqrt{\frac{m_u m_d}{(m_u + m_d)^2}} \frac{m_\pi f_\pi}{f_a} . \tag{2.7}$$

2.2.1 Baryon and meson masses

The spectrum of baryons and mesons and the vacuum energy are altered when $\theta \neq 0$ [114, 115]. The θ dependence of the pion mass, which is most important for our study, can be calculated by noting that the θ term in the QCD Lagrangian can be eliminated by a unitary rotation of the quark fields. When

---

[2] The property of the potential in the $\mathbb{Z}_\mathcal{N}$ model is similar near $\theta = 0$ but can be quite different near $\theta = \pm\pi$. See sec. 2.4.2 and 2.6.4 for more details.

only up and down quarks are included, the transformation $u \to \exp\{(i\gamma_5\phi_u)\}u$ and $d \to \exp\{(i\gamma_5\phi_d)\}d$ where $\phi_u + \phi_d = \theta$ fully captures the effect of $\theta \neq 0$. From the relation $m_\pi^2 \propto m_q = m_u + m_d$, the θ dependence of the mass of the neutral pion is [115]

$$m_\pi^2(\theta) = f(\theta) m_\pi^2(\theta = 0). \tag{2.8}$$

At $\theta = \pi$, the net effect of this transformation is to change the sign of the up quark mass in the quark mass matrix and the neutral pion mass is $m_\pi(\theta = \pi) = (\sqrt{m_d - m_u}/\sqrt{m_d + m_u}) m_\pi^{\rm phys} \approx 80\,\mathrm{MeV}$ for $m_\pi^{\rm phys} = 138\,\mathrm{MeV}$, significantly lighter than at $\theta = 0$. The smaller pion mass implies a longer range of the force; implications for nuclear interactions will be discussed in Sec. 2.3.

We note that the θ-dependence of the masses of the σ and ρ mesons have been calculated from analysis of pion-pion amplitudes in Refs. [116–118]. The amplitudes are calculated using chiral perturbation theory (ChiPT) but depend on the unitarization scheme which is not unique and introduces a systematic error that cannot be easily quantified. When m_π is reduced to 80 MeV, Refs. [116,117] find a 6% reduction to the σ mass. In Ref. [118] it was found that the logarithmic derivative $K_\sigma = \mathrm{d}\ln m_\sigma/\mathrm{d}\ln m_q = 0.081 \pm 0.007$, which implies $\approx 7\%$ reduction to the σ mass at $\theta = \pi$. The ρ meson mass was also found to decrease with pion mass but to a lesser degree. In Sec. 2.3.3, we shall incorporate these observations to study the θ dependence of the nuclear EOS in a relativistic mean field model.

Apart from the mass of the mesons, the masses of baryons, especially protons and neutrons, also depend on the θ angle. Such a dependence can be parameterized as

$$\begin{aligned} m_n(\theta) &= m_n(\theta = 0) + \sigma_N \left(f(\theta) - 1\right) \left(1 - \frac{\Delta\sigma}{\sigma_N f(\theta)}\right), \\ m_p(\theta) &= m_p(\theta = 0) + \sigma_N \left(f(\theta) - 1\right) \left(1 + \frac{\Delta\sigma}{\sigma_N f(\theta)}\right), \end{aligned} \tag{2.9}$$

where σ_N is the isoscalar nucleon sigma term and $\Delta\sigma$ is the isovector sigma term. Despite much interest and effort the isoscalar nucleon sigma term is not precisely known and the best estimates from Lattice QCD and phenomenology indicate that $\sigma_N \simeq 50 \pm 10$ MeV [119]. The value of $\Delta\sigma$ can be inferred from the mass splitting of baryons. Determining $\Delta\sigma$ from the mass splitting of the neutron and proton gives $\Delta\sigma = (m_n - m_p)_{\rm non-em}/2 \simeq 1\,\mathrm{MeV}$ [120]. The mass splitting of the nucleons and Ξ baryon gives a somewhat larger value of 3.1 MeV [121]. In what follows, we shall adopt $\sigma_N = 50$ MeV and $\Delta\sigma = 1$ MeV. For this choice, at $\theta = \pi$, the proton and neutron masses decrease by about 32 MeV and the neutron-proton mass difference increases by about 3.5 MeV.

2.2.2 Effective axion potential at finite density

The dependence of the axion potential on the temperature and density of the medium is essential to understanding the behavior of the axion field in the hot, early universe and in dense astrophysical objects. The temperature dependence of the axion mass in the early universe is well-known to be key to obtaining a precise prediction of the range of QCD axion masses that can be the dark matter in the Universe [122]. The density dependence of the axion mass, on the other hand, is much less explored. In the limit where the medium can be treated as a dilute gas of nucleons with density n_B, the axion potential has been shown to become shallower as the nucleon density increases, following the equation [95]

$$m_{a,\text{eff}}^2(n_B, n_I) = m_a^2\left(1 - \frac{1}{\varepsilon}\frac{\sigma_N n_B}{f_\pi^2 m_\pi^2}\left(1 - \frac{n_I}{n_B}\frac{\Delta\sigma}{\sigma_N}\right) + \mathcal{O}\left[\left(\frac{\sigma_N n_B}{m_\pi^2 f_\pi^2}\right)^2\right]\right), \tag{2.10}$$

where baryon density $n_B = n_p + n_n$ and $n_I = n_p - n_n$ is the isospin density, with proton and neutron density n_p and n_n, respectively. The critical density for a phase transition to axion condensed matter is given by

$$n_B^c = \frac{\varepsilon m_\pi^2 f_\pi^2}{\sigma_N} \simeq 2.65 n_{sat}\varepsilon\left(\frac{50\text{ MeV}}{\sigma_N}\right). \tag{2.11}$$

For $\varepsilon = 1$, the critical density determined from Eq. (2.11) is sufficiently large that the expansion in $\sigma_N n_B/m_\pi^2 f_\pi^2$ breaks down near the critical density, and it is conceivable that axion condensation does not occur at any density. We will return to this question in Sec. 2.3.2. However, for $\varepsilon < 0.4$, Eq. (2.10) predicts axion condensation at $n_B \lesssim n_{\text{sat}}$. At these moderate densities where matter can be described reliably using nuclear physics, one can conclude that the axion potential is minimized at $\theta = \pi$. If the nuclear force is significantly modified by axion condensation, $\theta = \pi$ may be favored below the saturation density even for $\varepsilon \geq 0.4$, which we will discuss in more detail in Sec. 2.3 and Sec. 2.4.2.

An interesting consequence of Eq. (2.11) is that, for small enough ε, the ground state of nuclear matter is $\theta = \pi$ and ordinary nuclei are only stabilized by the fact that the axion field changes on a length scale of $1/m_a$, much larger than the size of a typical nucleus. At finite nucleon density, it is more convenient to analyze the transition to the axion condensed phase as a function of the baryon chemical potential μ_B. The phase transition will occur at a critical chemical potential μ_B^c where the free energy $\Omega(\mu_B^c, \theta = 0) = \Omega(\mu_B^c, \theta = \pi)$. Neglecting interactions between nuclei, the free energy of dilute non-relativistic matter at zero temperature and finite μ_B is given by, apart from gradient terms,

$$\Omega(\mu_B, \theta) = -P(\mu_B, \theta) = -\frac{k_F^5(\theta)}{10\pi^2 m_n(\theta)} + V(\theta), \tag{2.12}$$

where $P(\mu_B, \theta)$ is the pressure, $k_F(\theta) = \sqrt{\mu_B^2 - m_n^2(\theta)}$ and the neutron mass $m_n(\theta)$ is given in Eq. (2.9). From Eq. (2.12) we see that axion contribution to the pressure is negative, and for $\theta = \pi$, $P_{\text{axion}} = -V(\theta = \pi) = \varepsilon f_\pi^2[m_\pi^2(\theta = \pi) - m_\pi^2(\theta = 0)]$. The importance of this negative pressure was first pointed

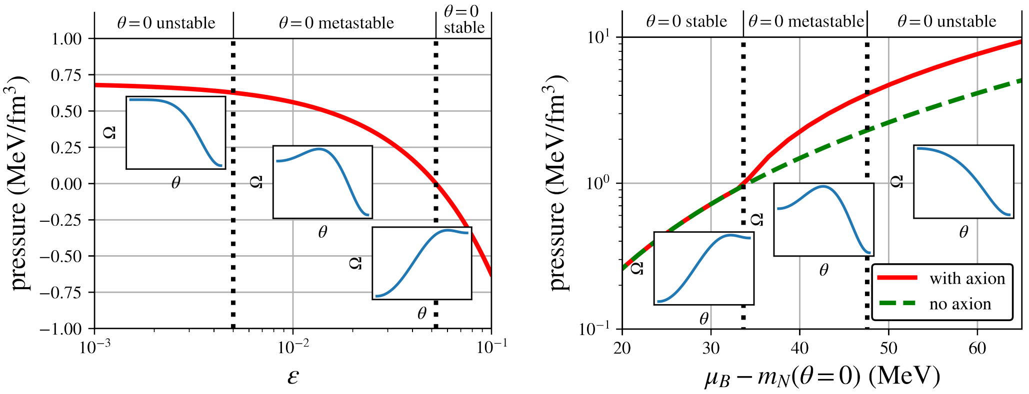

Figure 2.5: Left Panel: Pressure of axion condensed PNM at $\mu_B = m_n(\theta = 0)$ in the absence of nuclear interactions. Insets show free energy as a function of θ in each region. Right Panel: Phase diagram of a free neutron gas at $\varepsilon = 0.3$.

out in Ref. [96,123] where it was noted that for white dwarfs, which are stabilized by electron degeneracy pressure, this negative pressure would destabilize a large number of observed white dwarfs in the universe. This consideration leads to the strongest constraint on the axion parameter space for $\varepsilon < 2 \times 10^{-7}$ [96]. A neutron star, on the other hand, is much denser and balanced by the much larger neutron degeneracy pressure. It is unlikely that this negative pressure can lead to the collapse of a neutron star into a black hole, but it might significantly change the EOS of a neutron star [104].

We begin by analyzing the effects of axions on a dilute gas of neutrons. The left panel of Fig. 2.5 shows the pressure of a free Fermi gas of neutrons at $\theta = \pi$ and $\mu_B = m_n(\theta = 0)$. The insets show the θ-dependence of the free energy in each of the regions depicted. When the pressure is positive, axion condensation will be favored for dilute neutron matter. In the absence of nuclear interactions, dilute neutron matter with $\theta = 0$ is metastable for $0.005 \lesssim \varepsilon \lesssim 0.065$ and unstable when $\varepsilon \lesssim 0.005$. For $\varepsilon \gtrsim 0.065$, the first-order transition to the $\theta = \pi$ phase occurs at $\mu_B > m_n$ and low-density neutron matter with $\theta = 0$ is stable. In this case, the phase transition to axion condensed matter will occur at finite density. On the other hand, if $\varepsilon \lesssim 0.065$, the phase transition will occur at $\mu_B < m_n$, and bulk matter in its ground state will always have $\theta > \theta_c$, with $m_n(\theta_c) = \mu_B$. In the case where $2 \times 10^{-7} < \varepsilon \lesssim 0.005$, normal matter is unstable, and ordinary stars, planets, and white dwarfs are stabilized by Coulomb forces between atoms and nuclei. For $\varepsilon > 2 \times 10^{-7}$, a system of atoms or nuclei at fixed chemical potential must significantly increase its density to nucleate the $\theta = \pi$ phase, and an electrical barrier must be overcome to bring the nuclei closer together. For smaller ε, the required increase in density is more modest, and the constraint on axions from the stability of white dwarfs, stars, and planets applies.

For a given ε, if μ_B inside the star exceeds the critical chemical potential and it is possible to nucleate the $\theta = \pi$ phase, axions would condense in the inner region, separated by a domain wall with thickness $\Delta r_{\rm DW} \approx 1/m_a$ from the exterior $\theta = 0$ phase. In the Fermi gas model, for $\varepsilon \gtrsim 0.065$, the neutron star would consist of three regions: a normal outer region with $\theta = 0$, a metastable region which could, in principle, exist in the $\theta = 0$ phase if the nucleation timescale was long, and inner core characterized by $\theta = \pi$. In the right panel of Fig. 2.5, we plot pressure as a function of μ_B for $\varepsilon = 0.3$. It consists of the three regions just mentioned, and the insets show the θ dependence of the free energy, which delineates the stable, metastable, and unstable regions.

2.2.3 Axion field profile interpolating between $\theta = \pi$ and $\theta = 0$

The axion field profile across the domain wall, which minimizes the energy, is obtained by solving

$$f_a^2 \nabla^2 \theta = \frac{\mathrm{d}\Omega(\theta, \mu_B^{\mathrm{c}})}{\mathrm{d}\theta}\,, \tag{2.13}$$

where μ_B^{c} is the critical baryon chemical potential at which the transition occurs. This equation, though used here for a dilute gas of nucleons, remains exact when nuclear interaction is included in $\Omega(\theta, \mu_B^{\mathrm{c}})$. Such an axion profile will develop as long as the object that contains this dilute gas of nucleons is both dense enough (see Eq. (2.11)) and its radius, r_{NS}, large enough such that the bulk of the star can be subsumed within a domain wall of thickness

$$\Delta r_{\mathrm{DW}} \simeq \frac{1}{|m_{a,\mathrm{eff}}(n_B)|} \leq r_{\mathrm{NS}}. \tag{2.14}$$

We will focus on the condition on the density in Eq. (2.11) for now and return to the effects of the finite size of stellar objects in Sec. 2.5. For axions with $m_a < 10^{-11}\,\mathrm{eV}$, the axion profile can be treated as situated outside the neutron star. In binary systems, this field profile results in axion-mediated forces and axion radiation, which lead to the most stringent constraint from LVK observations of neutron star binaries [98]. On the other hand, when $m_a \gg 10^{-11}\,\mathrm{eV}$, the axion field profile can reside inside the neutron star, separating regions with different densities and pressure. Given the prior constraints on the exceptionally light QCD axion parameter space, we are mostly interested in the region of parameter space where $|m_a^2(n_B)| > m_a^2 > 1/r_{\mathrm{NS}}^2$.

For these larger axion masses, the thickness of the region in which θ changes from $\pm\pi$ to 0 is much smaller than the radius of a neutron star. On the other hand, constraints on QCD axions from SN cooling imply that the axion mass is below the tens of meV scale [93], i.e. the domain wall thickness is much larger than the relevant microphysical scales: the size of a nucleon, typical separation between nucleons, Debye screening length, and mean free path of neutrons and protons in a neutron star. As a result, we can treat the axion field profile in the parameter space of interest as smooth when considering interactions between the nucleons, while at the same time, studying the properties of the gas of nucleons in domains where $\theta = \pm\pi$ and $\theta = 0$ separately, and glue them together with a boundary condition at the location of a thin axion "domain wall."

Unlike a normal neutron star where density and pressure are continuous, with an axion field profile, both the density and pressure are no longer continuous when adopting the approximation that the domain wall is infinitely thin. In addition to the negative pressure from the condensation of the axion field itself, the domain wall also exerts a force inward due to domain wall tension of order $m_a f_a^2/r_{\rm NS}$. For $m_a \gg 1/r_{\rm NS}$, this additional pressure is parametrically smaller in the thin wall limit in the model in Eq. (2.5). We return to discuss the importance of domain wall pressure in the $\mathbb{Z}_\mathcal{N}$ model in Sec. 2.4.2.

2.3 Neutron and nuclear matter at $\theta = \pi$

In this section, we describe our efforts to model the properties of dense nuclear matter at $\theta = \pm\pi$, taking into account changes to the strength of nuclear interactions. Despite developments in Effective Field Theory (EFT) methods to describe nuclear interactions, the connection between fundamental parameters that appear in the QCD Lagrangian (the quark mass matrix $\mathcal{M}_q$ and θ) and the parameters needed to describe interactions between nucleons remains elusive. This is because the quark mass dependence of the low-energy constants (LECs) in the EFT that describe the strength of interactions at short distances is poorly known. Nevertheless, earlier studies have provided useful insights to address the question of the quark mass dependence of the nucleon-nucleon interaction.

We first briefly summarize earlier work in Refs. [118, 124, 125] which are based on nuclear potentials derived from ChiEFT as they are better suited to address how nuclear interactions are altered by changes to the quark mass matrix. To assess the quark mass dependence of the nuclear interactions at momentum scales of relevance to the large nuclei and neutron-rich matter encountered in neutron stars, we next compare results from ChiEFT and the three scenarios in RMFT which we will use to extract phenomenological results, summarized in Table 2.1.

In ChiEFT, nuclear forces are derived by explicitly including the contribution from pion-exchange as well as the short-distances components, which are included through a systematic expansion of operators of increasing dimension constructed from nucleon fields consistent with the symmetries of low-energy QCD. Such a low energy EFT description is expected to be applicable for $n_B \lesssim 2n_{\rm sat}$, and is described in Sec 2.3.2. We employ ChiEFT potentials at order N^{2}LO and perform calculations of the energy per particle in pure neutron matter (PNM) using many-body perturbation theory (MBPT). In this case, the quark mass dependence is taken into account through its modification of the pion mass, nucleon masses, the axial coupling constant g_A, and the pion decay constantf_π.

RMFT is based on the assumption that scalar and vector interactions provide the dominant contributions to the interaction energy of baryons in large systems. In this phenomenological model, the interaction between nucleons is mediated by the exchange of scalar and vector mesons. The model and the quark mass dependence of the model parameters are described in Sec. 2.3.3 (see table 2.1 for a sum-

Table 2.1: Summary of the three scenarios used in this work as benchmarks of nuclear force modification in the $\theta = \pi$ region. Parametrized by the logarithmic derivative evaluated at the physical quark mass $K_\sigma = \mathrm{d}\ln m_\sigma / \mathrm{d}\ln m_q$. See Section 2.3.3 for discussion.

Scenario	K_σ	Interpretation
A	0	Nuclear forces are not modified
B	0.08	Corresponds to an m_σ decrease of $\sim 6\%$ as found in Refs. [116–118]
C	0.16	Matches the largest binding of neutron matter found using ChiEFT. See Figs. 2.6 & 2.8.

mary). While ChiEFT is a microscopic theory in which potentials are constrained by nucleon-nucleon scattering data and properties of light nuclei, RMFT is a phenomenological model designed to provide a good description of large nuclei. RMFT also provides a convenient extrapolation to high density and permits efficient calculation of heterogeneous crust phases. In RMFT Scenario A, the only modification we make to nuclear physics is to modify the nucleon masses according to Eq. (2.9) since the pion does not explicitly appear in RMFT. In Scenario B, we modify the meson masses with θ dependence given by calculations in Refs. [116–118]. In Scenario C, we consider a more extreme modification to the RMFT based on the results around saturation density given by ChiEFT.

As noted earlier, in the low energy theory, finite θ manifests as a reduction of the pion mass as in Eq. (2.8). In what follows, we shall assume that the effect of $\theta = \pi$ can be adequately characterized by the reduction in the pion mass and calculate all other parameters of relevance to the two-nucleon interaction using ChiPT.

2.3.1 Pion mass dependence of two-nucleon observables

By explicitly accounting for the m_π dependence of the parameters that describe the nucleon-nucleon (NN) interaction in ChiEFT, one can calculate the quark mass dependence of low-energy NN observables such as the NN scattering phase shifts and the deuteron binding energy. In ChiEFT, at leading order (LO) in the momentum expansion, the NN potential is characterized by long-range one-pion exchange (OPE) and short-range NN contact interactions. While the m_π dependence of the parameters associated with the OPE potential is well understood, the m_π dependence of the NN contact interaction, which is typically called D_2, is not well determined and the resulting uncertainty in the scattering length and scattering phase shifts have been studied in earlier work [124, 125].

In Ref. [125], the authors find that when the quark mass is reduced, the binding energy of the deuteron increases, and the spin-singlet and spin-triplet scattering lengths decrease. To quantify the quark mass dependence of an observable $\mathcal{O}$, the authors define the logarithmic derivative at the physical point

$$K_{\mathcal{O}} = \frac{m_q}{\mathcal{O}} \left(\frac{\mathrm{d}\mathcal{O}}{\mathrm{d}m_q} \right)_{\mathrm{phys}} \simeq \left(\frac{m_\pi^2}{\mathcal{O}} \frac{\mathrm{d}\mathcal{O}}{\mathrm{d}m_\pi^2} \right)_{m_\pi = m_\pi^{\mathrm{phys}}} , \tag{2.15}$$

Table 2.2: Quark mass dependence of the scattering lengths and the deuteron binding energy $K_{\mathcal{O}}$, as defined in Eq. (2.15).

Reference	K_{a1S0}	K_{a3S1}	K_{deut}
Epelbaum et al. [125]	5 ± 5	1.1 ± 0.6	-2.8 ± 1.2
Beane et al. [124]	2.4 ± 3.0	3.0 ± 3.5	-7 ± 6
Berengut et al. [118]	$2.3^{+1.6}_{-1.5}$	$0.32^{+0.17}_{-0.18}$	$-0.86^{+0.45}_{-0.50}$

since at leading order in ChiPT, $m_\pi^2 \propto m_q$. The m_q dependence of the ${}^1S_0$ and ${}^3S_1$ scattering lengths and the deuteron binding energies are captured by the values of K_{a1S0}, K_{a3S1}, and K_{deut}, and their values obtained in earlier studies are shown in Table 2.2. Results shown in the first row were obtained using potentials derived from ChiEFT at next-to-leading order (NLO) in Weinberg power counting [125] and NLO results obtained in Ref. [124] using Kaplan-Savage-Wise power counting [126] are shown in the second row. In this case, the uncertainty is dominated by the poorly known LEC, D_2, which was mentioned earlier. Results obtained more recently in Ref. [118] are shown in the third row; here, the authors employ strategies to go beyond the NLO approach adopted in Refs. [124,125] and use information from resonance saturation models to constrain the quark mass dependence of the short-range contact operators and incorporate N^{2}LO corrections to g_A, f_π, and the nucleon mass.

With decreasing quark mass, these earlier studies found the ${}^1S_0$ phase shifts were reduced and the ${}^3S_1$ phase shifts were enhanced. Thus, in dilute neutron matter where spin singlet interactions dominate, the interaction energy will be less attractive when s-wave interactions dominate. In dilute nuclear matter with an equal number of protons and neutrons (symmetric nuclear matter), where spin triplet interactions dominate, the s-wave interaction energy is larger and more attractive when the quark mass is reduced. However, when the pion becomes lighter and of longer range, higher partial wave contributions are in general enhanced [127]. The attraction in the ${}^3P_0$ and ${}^3P_2$ channels is enhanced and the repulsion in the ${}^1P_1$ channel is reduced [125]. For these reasons, the analysis of the scattering lengths and the deuteron binding energy is insufficient to inform about the behavior of matter at densities of relevance to nuclei and neutron stars where contributions due to higher partial waves and higher-order quark mass-dependent short-distance operators can contribute.

2.3.2 Axion condensation in Chiral Effective Field Theory

To address how nuclear interactions influence axion condensation, we first make the simple observation that axion condensation is favored when the interaction energy per particle decreases with pion mass. From the discussion in Sec. 2.2, we infer that in this case, condensation would occur at $n_B \lesssim 2.6 n_{sat}$ for $\varepsilon = 1$. In ChiEFT, the m_π dependence of the long- and intermediate-range parts of the nucleon-nucleon and three-nucleon (3N) potentials is explicit because pion-exchanges are systematically included in Weinberg power counting. The m_π dependence of the nuclear interaction energy in PNM and symmet-

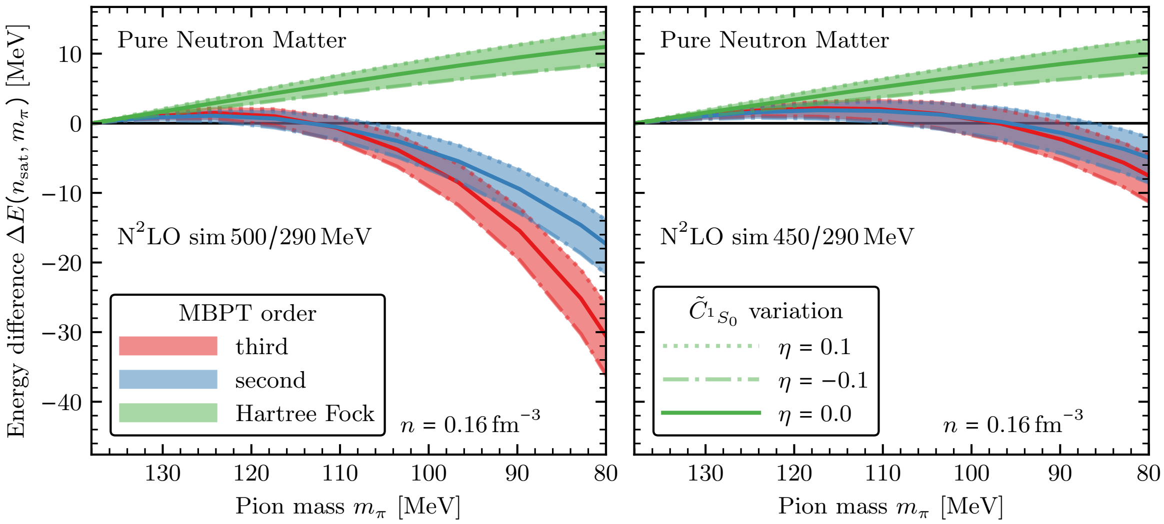

Figure 2.6: Difference in the energy per particle (2.17) for the N^{2}LO sim potentials [132] with two momentum cutoffs Λ at $n_B = n_{sat}$ as a function of m_π: $\Lambda = 500$ MeV (left panel) and $\Lambda = 450$ MeV (right panel), as annotated. In these potentials, we modify m_π, f_π, and the LO LEC $\tilde{C}_{^1S_0}$ (different line styles), whereas g_A is kept at its physical value. The bands depict the variation of the LO LEC $\tilde{C}_{^1S_0}$ according to Eq. (2.19). The results were obtained at the Hartree-Fock level (green bands) and using second-order (blue bands) and third-order MBPT (red bands). The energy per particle at the physical pion mass obtained from on our third-order calculations is $E(n_0) = 16.94\,\mathrm{MeV}$ and $E(n_0) = 17.21\,\mathrm{MeV}$ for $\Lambda = 450\,\mathrm{MeV}$ and $\Lambda = 500\,\mathrm{MeV}$, respectively. See the main text for details.

ric nuclear matter (SNM) has been studied in the context of addressing how $\langle\bar{q}q\rangle$, the chiral condensate, evolves at finite density [128–131]. In these studies, the Feynman-Hellmann theorem was exploited to relate the change in $\langle\bar{q}q\rangle$ to the derivative of the interaction energy with respect to m_π^2. Explicitly, one finds that

$$\frac{n_B}{f_\pi^2}\left(\frac{\mathrm{d}E_{\mathrm{int}}(n_B)}{\mathrm{d}m_\pi^2}\right)_{m_\pi=m_\pi^{\mathrm{phys}}} = R_0(n_B) - R(n_B)\,, \tag{2.16}$$

where $E_{\mathrm{int}}(n_B)$ is the interaction energy per nucleon in nuclear matter, $R(n_B) = \langle\bar{q}q\rangle_{n_B}/\langle\bar{q}q\rangle_0$ is the ratio of the chiral condensate at a finite density to that in vacuum, and $R_0(n_B)$ is the same ratio calculated by neglecting interactions.

ChiEFT-based calculations reported in Refs. [129–131] find that $R(n_B)/R_0(n_B) > 1$ over the entire range of densities where the ChiEFT is expected to be useful. Thus, the interaction energy increases with decreasing pion mass in the vicinity of $m_\pi = m_\pi^{\mathrm{phys}}$ in SNM and PNM. However, the study in Ref. [129], which was restricted to the case of SNM, found that the ratio $R(n_B)/R_0(n_B) < 1$ for smaller m_π. Their calculations indicate that $R_0(n_{sat}) - R(n_{sat}) \simeq 0.1$ at $m_\pi = 70$ MeV and $R_0(n_{sat}) - R(n_{sat}) \simeq 0.3$ in the chiral limit. Together, these results imply that the interaction energy increases with decreasing m_π for $m_\pi \simeq m_\pi^{\mathrm{phys}}$ and then decreases rapidly for smaller values of m_π. The microscopic calculations of the energy per particle of PNM as a function of m_π that we shall describe in the following show a similar trend.

Figure 2.6 shows the difference in the PNM energies per particle,

$$\Delta E(n_{\rm sat}, m_\pi) = E(n_{\rm sat}, m_\pi) - E(n_{\rm sat}, m_\pi^{\rm phys}), \tag{2.17}$$

for two chiral potentials at $n_B = n_{sat}$ as a function of m_π (see annotations). Here, we use the family of bare N^{2}LO potentials with chiral NN and 3N forces developed in Ref. [132]. These nonlocal potentials are called the sim potentials because they were simultaneously fit to scattering and bound-state observables in the pion-nucleon, NN, and few-nucleon sectors. Specifically, we use the two N^{2}LO potentials with the NN and 3N momentum cutoffs $\Lambda = 500$ (left panel) and 450 MeV (right panel); both constrained by NN scattering data at laboratory energies $T_{\rm lab} \leqslant 290$ MeV [132]. The analytic expressions that define these potentials and were used in this work are summarized in the Appendix of Ref. [133] and Section 5.1.2 in Ref. [134]. To obtain the PNM energy per particle, we apply the Monte Carlo framework for MBPT nuclear matter calculations developed in Ref. [135]. The green bands in Fig. 2.6 depict the Hartree-Fock reference energy and the blue and red bands the MBPT results at second and third order, respectively. All MBPT calculations are performed at the normal-ordered two-body level. More details on MBPT for nuclear matter can be found in Ref. [108]. This MBPT framework uses the operatorial definition of the chiral potentials, allowing us to straightforwardly vary the values of physical constants, such as the pion mass, low-energy couplings, and more. Not all chiral potentials are given in their operatorial form; e.g., when evolved to lower resolution scales using renormalization group (RG) methods, their operatorial definition is usually unknown. For the solid lines in Fig. 2.6, we keep the values of the low-energy couplings at their best-fit values determined in Ref. [132] and vary only the pion mass, nucleon mass, and the pion decay constant. The m_π dependence of the nucleon mass was discussed in Sec. 2.2.1, and the m_π dependence of the pion decay constant is given by

$$f_\pi = f\left[1 + \frac{m_\pi^2}{(16\pi^2 f^2)}\bar{l}_4\right], \tag{2.18}$$

with its value in the chiral limit $f = 86.2$ MeV and the LEC $\bar{l}_4 = 4.3$ [118]. The pion-mass dependence of the axial coupling constant g_A is relatively weak in the regime considered here, as can be seen in Figure 1 in Ref. [118], and thus we keep $g_A = 1.29$ at the physical value. We use these potentials to identify overall trends and emphasize the need to explore the pion-mass dependence of a wider range of chiral potentials in the future.

As noted earlier, the pion-mass dependence of the short-range components of the interaction that are incorporated through scale-dependent LECs is not well understood or constrained by data. To study the sensitivity of our results to variations in the short-range interaction, we have calculated the energy per particle by changing the LEC $\tilde{C}_{^1S_0}$ that governs the strength of the NN contact interaction at LO in the $^1S_0$ partial-wave channels. Specifically, we perform calculations for the energy per particle with a scaled value for this coupling constant,

$$\tilde{C}_{^1S_0}(\theta) = \tilde{C}^{\rm fit}_{^1S_0}\left(\frac{1+\eta f(\theta)}{1+\eta}\right) , \tag{2.19}$$

where $f(\theta) = \left(m_\pi(\theta)/m_\pi^{\rm phys}\right)^2$, $\eta = D_2(m_\pi^{\rm phys})^2/\tilde{C}^{\rm fit}_{^1S_0}$ and $\tilde{C}^{\rm fit}_{^1S_0}$ is the best-fit value in each isospin channel obtained in Ref. [132]. Here, D_2 is the LEC discussed in Ref. [124,126] that captures the pion-mass dependence at NLO. We choose the two values $\eta = \pm 0.1$ to set the limits of this variation and adopt $m_\pi^{\rm phys} = 138.04$ MeV for the physical pion mass. The dotted and dash-dotted lines in Fig. 2.6 depict the results for the PNM energy per particle with the modified LO coupling constant (2.19); the solid lines correspond to $\eta = 0$ and thus $\tilde{C}_{^1S_0}(\theta) \equiv \tilde{C}_{^1S_0}$. Increasing the strength of $\tilde{C}_{^1S_0}(\theta)$, corresponding to $\eta = -0.1$, reduces $\Delta E(n_{sat}, m_\pi)$, whereas decreasing the strength, corresponding to $\eta = +0.1$, increases $\Delta E(n_{sat}, m_\pi)$.

Several important insights can be drawn from the results in Fig. 2.6. MBPT appears to converge more slowly with decreasing pion mass, which could be further investigated using a Weinberg eigenvalue analysis [136]. Although the leading Hartree-Fock energies indicate a systematic increase in interaction energy with m_π across the range shown in Fig. 2.6, the second-order correction reverses this trend. The third-order correction is modest and of the same sign as the second-order correction. For relatively small reductions of the pion mass ($m_\pi \gtrsim 120$ MeV for $\Lambda = 500$ MeV and $m_\pi \gtrsim 110$ MeV for $\Lambda = 450$ MeV), the energy difference (2.17) is positive. The sensitivity of the results at the second and third order to the cutoff variation is larger than that of the LEC variation. These general trends are not altered by varying the momentum cutoff over the range shown in Fig. 2.6. However, the rather large dependence on the momentum cutoff is disconcerting and warrants a careful inclusion of the m_π dependence of the short-range components of the force. As discussed earlier, we have studied the effect of the m_π dependence of the leading LEC associated with scattering in the $^1S_0$ channel shows that the qualitative behavior is not changed. Based on these trends, we conclude that the interaction energy at $\theta = \pi$, where $m_\pi \approx 80$ MeV, can be smaller than that at $\theta = 0$, where $m_\pi \approx 138$ MeV. However, the energy difference ΔE remains quite sensitive to the regularization scheme.

Constructing a neutron star EOS with $\theta = \pi$ using ChiEFT poses challenges as more work is needed to include beta-equilibrium, charge neutrality, and heterogeneity in the crust. We defer this to future work and instead use the ChiEFT results in PNM to inform the simpler RMFT model, which we shall describe in the next section. In particular, we utilize the energy per particle of PNM at $\eta = 0$ and momentum cutoff $\Lambda = 500\,$MeV to fix a key parameter to account for changes to the nuclear interaction at $\theta = \pi$.

2.3.3 Axion condensation in Relativistic Mean Field Theory

To derive concrete results for neutron stars, we use a model within RMFT (see Ref. [137] for a review). The Lagrangian of this theory is given by the following, omitting terms that will be discarded after taking the meson fields to have their mean field values,

$$\begin{aligned}\mathcal{L}_{\mathrm{RMF}} = &\sum_{i=n,\,p} \overline{\psi}_i \left[i\partial\!\!\!/ - g_\omega \omega \gamma^0 - \frac{1}{2} g_\rho \rho \gamma^0 \tau_3 - (m_i - g_\sigma \sigma) \right] \psi_i \\ &+ \sum_{\ell=e,\,\mu} \overline{\psi}_\ell (i\partial\!\!\!/ - m_\ell)\psi_\ell + \frac{1}{2}(-m_\sigma^2 \sigma^2 + m_\omega^2 \omega^2 + m_\rho^2 \rho^2) + \mathcal{L}_{\sigma\omega\rho}\,,\end{aligned} \tag{2.20}$$

where the nucleon-meson couplings are denoted by g_σ, g_ω and g_ρ, the meson masses by m_σ, m_ω and m_ρ, and m_i are the nucleon masses. The term $\mathcal{L}_{\sigma\omega\rho}$ contains all meson-meson couplings that are fit, along with the nucleon-meson couplings to known properties of nuclear matter for the canonical choice of meson masses $m_\sigma = 550$ MeV and $m_\omega = m_\rho = 770$ MeV. τ_3 is the third Pauli matrix in isospin space. We use the IUFSU* parameter set from Ref. [138] because it is optimized for the calculation of finite nuclei and our study will focus on the crust. The mean field values of the mesons and Fermi momenta of the nucleons and leptons are calculated by solving the Euler-Lagrange equations for each field and enforcing charge neutrality and β equilibrium.

Since mean field models do not explicitly include pion fields, incorporating the effects of a reduced pion mass on nuclear interactions presents a challenge. To address this, we model the increased attraction predicted by ChiEFT at lower pion masses by reducing the mass of the σ meson. This approach is motivated by the fact that the two-pion exchange potential—which provides significant attraction in ChiEFT—can be effectively represented by scalar (σ) meson exchange in mean field models.

We consider three scenarios in our analysis. In Scenario A, we assume no change in the nuclear interaction, meaning the σ-meson mass is independent of θ. In Scenarios B and C, we introduce a modest reduction in the σ-meson mass to mimic the decrease in energy per particle predicted by ChiEFT at $m_\pi = 82$ MeV. The specific values of m_σ used in these scenarios are informed by studies of the θ dependence of meson masses reported in Refs. [116, 117].

As noted earlier, Scenario A is the simple case where interactions are unmodified and only the nucleon masses are modified by finite θ. For this case, Fig. 2.7 shows the energy per baryon, including axion energy and the reduction of the mass of the nucleons, of SNM, PNM, and beta equilibrated matter in this model. At fixed baryon density, the energy per baryon is minimized, leading to axion condensation due to the reduced nucleon mass. For small ε, the energy cost of having non-zero θ is small and axion condensation is favored at lower densities. Since the axions themselves contribute to the energy density, the energy per baryon of axion condensed matter will always diverge in the limit of zero density and a phase without axions will be favored. This has the effect of producing a minimum in the energy per

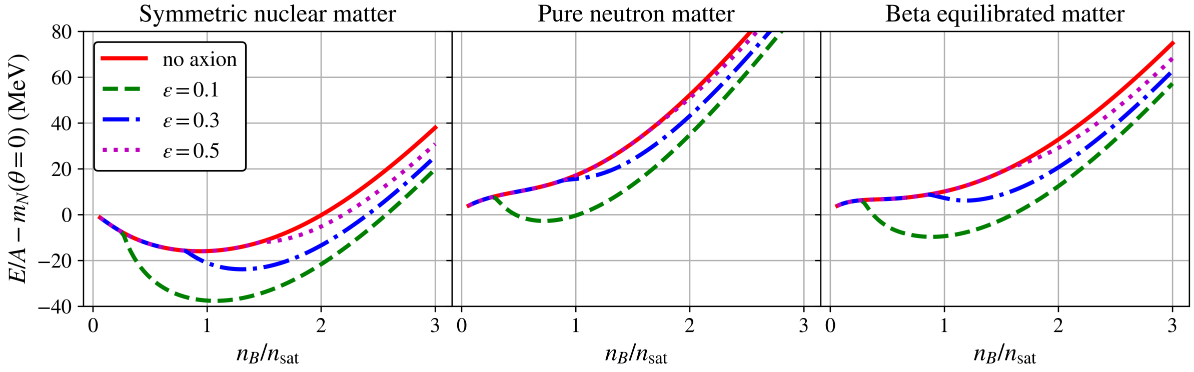

Figure 2.7: Energy per baryon for SNM, PNM, and β equilibrated matter with RMFT EOS with IUFSU* parameter set including axion energy in Scenario A.

baryon of axion condensed matter when ε is sufficiently small and allows a stable zero pressure phase of nuclear matter at lower energy than normal nuclei. We will return to discuss objects made out of such matter in Sec. 2.5.

The density where the energy per baryon of uniform nuclear matter has a minimum should be differentiated from a state with zero pressure *not* including the axion contribution to the energy per baryon that will be found in the crust. In the crust, the length scale over which the axion field profile changes is much longer than the length scale of the lattice of nuclei. When there are no dripped neutrons, these nuclei must be in a state with zero pressure after including the surface energy of nuclear matter since the lepton and axion fields take on the same value inside and outside the nuclei. If axion condensation causes the nuclear force to become more attractive, nuclear matter can be at zero pressure at a larger isospin asymmetry, resulting in more neutron-rich nuclei.

In a neutron star, the more natural parameter to fix is the baryon chemical potential μ_B. Due to the decreased nucleon mass, the value of μ_B corresponding to a system of nuclei in a lattice with $\theta = 0$ corresponds to bulk matter at $\theta = \pi$. As a result, the axion domain wall never separates two heterogeneous phases. While there can be a transition from homogeneous matter with $\theta = \pi$ to a normal crust, there will be no matter outside the domain wall in any star where an axion-condensed crust phase appears.

Of particular relevance to observations of neutron stars is the pressure at which neutron drip occurs. Neutron drip refers to the density at which it becomes energetically favorable for neutrons to come out of nuclei and form a background of free neutrons. As such, the neutron drip phase transition will occur when the baryon chemical potential is equal to the mass of the neutron (possibly modified by finite θ) in the case where PNM is not self-bound. If the axion-condensed phase persists to the surface of the neutron star, but the negative axion pressure is larger than the pressure of electrons at neutron drip density (nuclei make a small contribution to the pressure), the neutron drip phase transition will not be found in the neutron star and the surface of the star will have a thin domain wall covering either a phase of nuclei in a dripped neutron background or bulk nuclear matter.

Not included thus far is the pion mass dependence of the nuclear force itself. As noted earlier, we use a simple ansatz for modifications to the nuclear force, we modify the σ mass with a tunable parameter d_σ as follows:

$$m_\sigma^2(\theta) = m_\sigma^2(0)\frac{1+d_\sigma f(\theta)}{1+d_\sigma}\,. \tag{2.21}$$

The θ-dependence of the masses of the σ and ρ mesons have been calculated in Refs. [116,117]. They find that, comparing $\theta = 0$ and $\theta = \pi$, the σ mass decreases by about 6% and the ρ mass decreases by about 2%. At low density, the RMFT EOS is dominated by the σ meson and its modification is much larger than that of the vector mesons so we focus on the effect of modifying the scalar interaction. Note that the logarithmic derivative evaluated at the physical quark mass $K_\sigma = \mathrm{d}\ln m_\sigma/\mathrm{d}\ln m_q = d_\sigma/(2+2d_\sigma)$. Scenario A, in which the nuclear forces are not modified, corresponds to $K_\sigma = 0$. For positive K_σ, the σ mass is lower, leading to a larger mean field value of the σ field and a more attractive nuclear force. The limit $K_\sigma = 1/2$ corresponds to the σ mass having the same dependence as the π mass. The 6% reduction to the σ mass found in Refs. [116, 117] is reached for $K_\sigma = 0.08$. This is the value we adopt in Scenario B. We also note that Ref. [118] found that $K_\sigma = 0.081 \pm 0.007$. For Scenario C, we consider a more extreme modification to the nuclear force with $K_\sigma = 0.16$, which achieves the same binding for neutron matter found in our most attractive estimate from ChiEFT found for cutoff $\Lambda = 500\,\mathrm{MeV}$. These three scenarios together span the parameter space supported by our ChiEFT calculation. We will refer to our three scenarios based on the value of K_σ evaluated at the physical point, but the actual θ-dependence is given by Eq. (2.21) and K_σ is not a constant when θ is varied. Scenarios B and C are tuned to the properties of axion condensed matter at $\theta = \pi$; K_σ at the physical point is merely a convenient benchmark. The leading modification to the effective axion mass from this modification to the nuclear force is given by

$$m_{a,\mathrm{eff}}^2(n_B, n_I) = m_a^2\left[1 - \frac{1}{\varepsilon}\frac{\sigma_N n_B}{f_\pi^2 m_\pi^2}\left(1 + \frac{K_\sigma g_\sigma^2 n_B}{\sigma_N \chi m_\sigma^2} - \frac{n_I}{n_B}\frac{\Delta\sigma}{\sigma_N}\right)\right] \tag{2.22}$$

where g_σ is a parameter of the RMFT model and χ is the volume fraction of nuclei when in a heterogeneous phase and unity in a homogeneous phase. At saturation density, $g_\sigma^2 n_{\mathrm{sat}}/\sigma_N m_\sigma^2 \simeq 11$ for the RMFT model we use so for Scenario B, axion condensation should be expected below n_{sat} for $\varepsilon \lesssim 0.8$ and in Scenario C, axion condensation should be expected below n_{sat}, even for $\varepsilon = 1$! While this is a striking prediction, it should be noted that RMFT is a model for the nuclear interaction that does not have explicit pions and we are parameterizing the expected effects of a reduced pion mass via the meson masses and where Scenario C is chosen to recreate the most extreme prediction of ChiEFT. While the σ meson is typically understood as a two pion resonance, this comparison is certainly incomplete. More

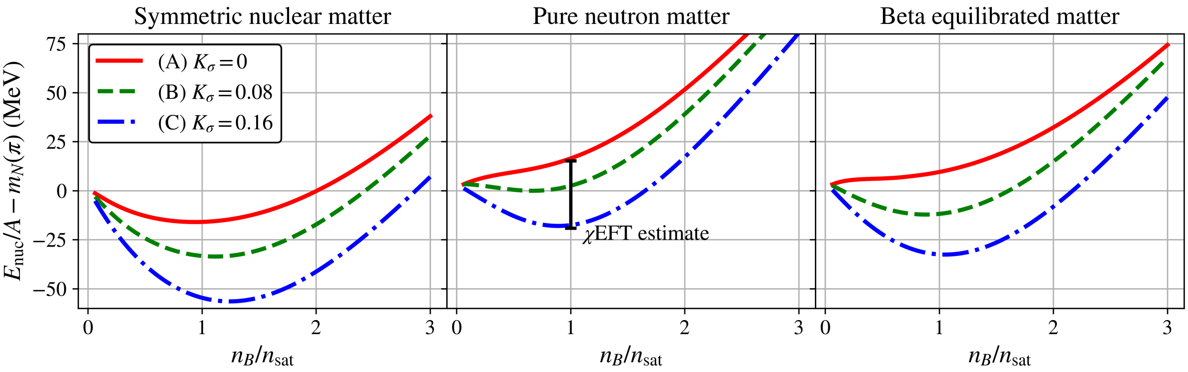

Figure 2.8: Kinetic and nuclear interaction energy per baryon for SNM, PNM, and β equilibrated matter at $\theta = \pi$ with RMFT EOS with IUFSU* parameter set and our three choices of K_σ. The estimate for the binding of PNM from ChiEFT is shown with the approximate error bar including cutoff- and η-dependence.

detailed study is required to determine the fate of neutron matter at saturation density. The predictive power of this model is additionally limited by the fact that we only consider isoscalar effects on the nuclear force. Axion condensation may also have an important impact on the symmetry energy of nuclear matter beyond the effect of $\Delta\sigma$. We expect this to have a more pronounced effect at high density where our model of the nucleon-axion interaction breaks down.

Figure 2.8 shows the kinetic and interaction energy per baryon for Scenarios A, B, and C at $\theta = \pi$. Since this only includes the energy from the kinetic energy of baryons and nuclear forces, this quantity is independent of ε. Note that this differs from Fig. 2.7 in that the reduction of the nucleon masses is not included in this value.

When ε is small enough that axion condensed matter is favored down to zero pressure, there can be striking effects on the crust of the star. We construct an axion-condensed inner crust of nuclei in a background of dripped neutrons, including Coulomb and surface energies. Since the constraints we derive on axion parameter space are tied to the properties of the crust, we choose a surface tension $\sigma = 0.75\,\mathrm{MeV/fm^2}$ tuned to recreate neutron drip pressure at $\theta = 0$ calculated with more detailed microphysics (see, e.g., Ref. [139]). To be self-consistent between the two phases, the phase transition will be calculated between the RMFT model in all crust phases for all values of θ rather than using a tabulated crust EOS. Where relevant, we compare quantitative results to the calculation of crust properties calculation in the BPS and NV EOSs [139, 140].

For sufficiently large K_σ, PNM saturates even for $\varepsilon = 1$, giving zero pressure solutions at finite density. For $0.035 \gtrsim K_\sigma \gtrsim 0.025$, there are two positive pressure branches to the PNM EOS, producing a jump in density in the inner crust. For $K_\sigma \gtrsim 0.035$, the neutron drip phase transition would become a first-order phase transition to a phase of saturated neutrons if it appeared in the neutron star, but as we will show later, within this model the neutron dripped phase is never favored for such large values of K_σ.

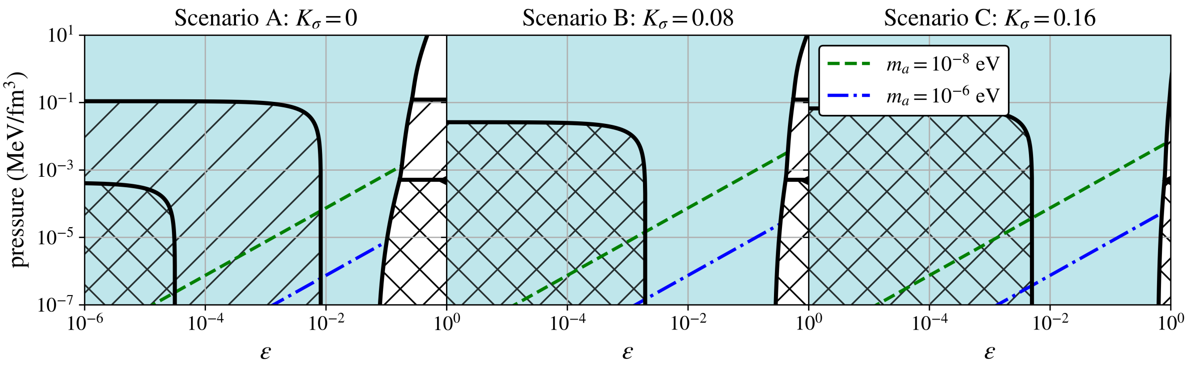

Figure 2.9: Phase diagram for RMFT model with IUFSU* parameter set and our three choices of K_σ. The colored diagonal lines show the domain wall pressure for a fiducial neutron star radius $R = 12$ km and two example axion masses. The blue shading (no shading) indicates the pressures for which $\theta = \pi$ ($\theta = 0$) is the favored phase. The hatching indicates the regions of increasing density within the neutron star: outer crust (cross-hatched), inner crust (diagonal hatched) and core (no hatch).

Figure 2.9 shows a phase diagram for the RMFT model as a function of pressure and ε. In the blue-shaded region, $\theta = \pi$ is favored while in the unshaded region, $\theta = 0$ is favored. The cross-hatched regions contain the outer crust of nuclei and electrons and the diagonal-hatched regions contain the inner crust of nuclei, dripped neutrons, and electrons. Regions without hatching are composed of homogeneous nuclear matter. The diagonal colored lines show the domain wall pressure for an axion of a given mass with the specified ε if the radius of the domain wall is 12 km. When the boundary region is treated as infinitely thin, this is the pressure difference across the domain wall. For small ε where the axion condensed phase is favored for all densities, this acts as a cutoff pressure at the surface of the star; lower pressures can only exist in the finite size of the domain wall itself. Effects of the domain wall will be discussed in more detail in Sec. 2.4.2.

Note that points in the axion condensed phase with the same pressure but different ε have different energy densities. Equal pressure but larger ε corresponds to larger energy density both from the energy of the axions themselves, but also because pressure equality results in a larger baryon density to compensate for the negative axion pressure. In the normal phase, this effect is not present and all points of a given pressure have the same density. For $\varepsilon \to 0$, if the nuclear force is not modified the phases present in the neutron star look very similar to what is found in a star without axions, but for intermediate values of ε, some phases may be missing because the negative axion pressure cuts off the edge of the neutron star before the density for that phase is reached. In this case, the missing phases will only be found in the domain wall region.

As K_σ is increased from 0, the pressure of the PNM surrounding the nuclei in the inner crust decreases significantly and, as a result, the chemical potential corresponding to the crust-core transition (the boundary between the diagonally hatched and unhatched regions) decreases. At the same time, a more attractive nuclear interaction causes nuclei to become more neutron-rich, increasing the electron chemical potential. An increased electron density corresponds to a larger pressure at neutron drip (the boundary between the diagonal hatched and cross-hatched regions). For sufficiently large K_σ, if ε is small enough for an axion condensed crust to be present, there will be a phase transition directly from bulk nuclear matter to a phase with nuclei and free electrons, with no dripped neutrons. This occurs because bulk matter is favored when the chemical potential is less than $m_n(\theta = \pi) + \Gamma_n(\theta = \pi)$ where $\Gamma_n(\theta)$ is the binding of PNM in the case where neutron matter is self-bound (Scenarios B and C) and 0 in the case where it is not.

2.3.4 EOS of axion condensed matter

Figure 2.10 shows the RMFT EOS for charge neutral, β-equilibrated matter for several choices of ε in the three scenarios discussed. We focus on the crust and outer regions of the core as those are the densities at which the effects of axion condensation are well understood. The solid red curve corresponds to the normal EOS without axions. For comparison, the black dotted curve shows the BPS+NV crust EOS [139, 140].

We first focus on the left panel of Fig. 2.10. For $\varepsilon = 10^{-6}$, the axion field itself contributes very little to the energy density and pressure at the densities pictured, and Scenario A looks very similar to the case with no axions. At pressures of order $\varepsilon m_\pi^2 f_\pi^2 \simeq 10 \times \varepsilon\,\mathrm{MeV/fm}^3$ the curve for Scenario A will diverge from the EOS without axions and go to zero pressure at finite energy density. For $\varepsilon = 10^{-6}$ this corresponds to $p \simeq 10^{-5}\mathrm{MeV/fm}^3$, outside the plot range shown. This occurs because zero pressure in the axion condensed phase occurs when the pressure of nuclear matter exactly cancels the negative axion pressure, corresponding to a much larger baryon density than normally found in nuclear matter at zero pressure. The point where the curves for Scenario B and C in the left panel diverge from Scenario A and the EOS without axions corresponds to the neutron drip phase transition for Scenario A and the EOS without axions. When K_σ is large enough that the inner crust is absent, the pressure is larger (the EOS is "stiffer") at energy densities where ordinarily dripped neutrons would be present because there are fewer degrees of freedom in the system, resulting in the lepton density being larger. At the crust-core transition, however, there is a large jump in energy density from the mixed phase to bulk nuclear matter, resulting in a lower pressure (the EOS is "softer") in the outermost part of the core.

The center and right panels of Fig. 2.10 can be understood in terms of the basic trends in the left panel. For $\varepsilon = 10^{-3}$, the outermost regions of the star are still axion condensed, and the only difference between the center and left panels is the much larger energy density and negative pressure from the axion field itself. This results in the equation of state going to zero pressure at large energy density because the nuclear matter at zero net pressure must contribute enough pressure to cancel the much larger axion pressure. In the right panel, Scenario B and C remain axion condensed down to zero pressure but the much larger value of ε means that this occurs before the crust-core phase transition and the jump in

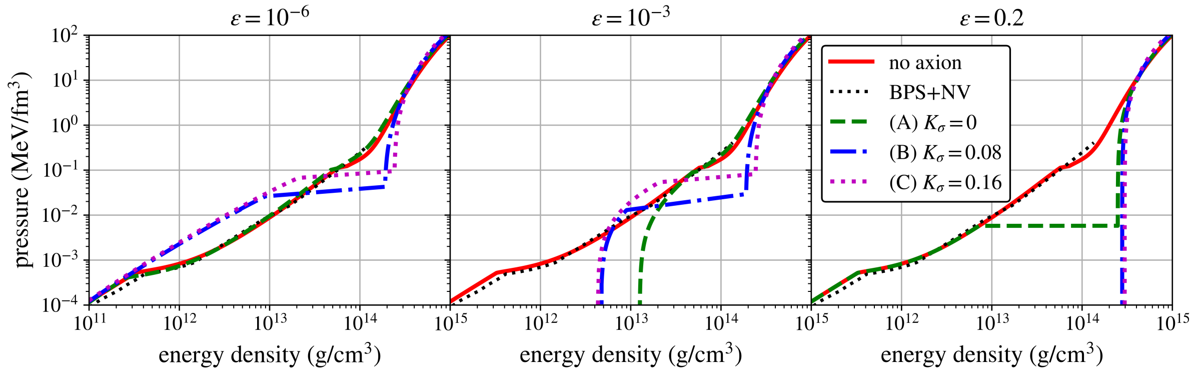

Figure 2.10: The RMFT EoS for three example values of ε and the three K_σ scenarios using the IUFSU* parameter set. The standard no axion RMFT EoS and the BPS+NV EoS for the crust are shown for comparison [139, 140]. See section 2.3.4 for details.

energy density seen at lower ε is not present. In Scenario A in the right panel, axion condensation is not favored at the lowest densities and there is a phase transition from axion condensed matter to normal matter, producing a discontinuity in the energy density due to the much lower baryon density in the normal phase.

2.4 Neutron stars with $\theta = \pi$ matter

In this section, we describe the modification to the neutron star EOS taking into account the effects we discussed in Secs. 2.2 and 2.3, including the negative pressure at $\theta = \pi$ and modifications to the nucleon masses and interactions, as well as the axion field profile and domain wall pressure. Neutron star structure can be derived by combining gravity and these new effects that depend on the axion coupling and masses, parameterized by ε and m_a. Qualitatively, for larger m_a ($m_a \gg 1/R_{\rm NS}$), the axion field profile can be treated as a thin wall over which the gravitational potential does not change, and the gravity and axion effects can be accounted for separately. We will first discuss neutron star structure in the simpler case where this approximation is valid, before commenting on the criteria for the validity of the approximation and working out the more general cases.

2.4.1 Neutron star structure in axion condensed stars

An ordinary neutron star has an outer crust composed of nuclei in a background of free electrons and an inner crust composed of nuclei in a background of free electrons and dripped neutrons, together having a thickness of around a kilometer (see the left panel of Fig. 2.11 for a sketch). The possibilities for the outer structure of a neutron star become more varied in the presence of axion condensation, depending on the value of ε and any modifications to the nuclear force. In the simplest case, for $\varepsilon \gtrsim 0.1$, the center of the star is axion condensed with a transition to normal matter at some intermediate radius. That

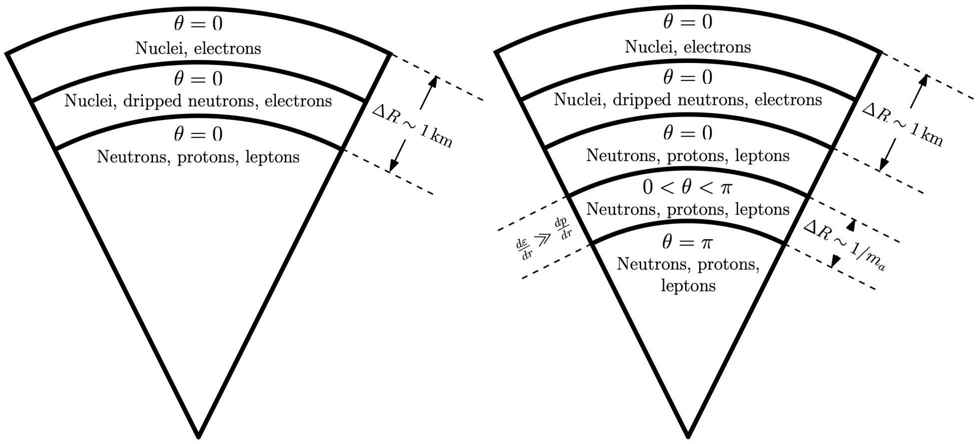

Figure 2.11: Layers of a normal neutron star (left) and a neutron star with an axion condensed inner core (right). The thickness of layers is not to scale. See section 2.4.1 for discussion.

radius may be large enough that portions of the normal crust are missing with, e.g., a transition directly from bulk matter at $\theta = \pi$ to an outer crust at $\theta = 0$ with possibly a thin inner crust in the domain wall region. For larger ε, the entire normal crust is present and only a portion of the bulk matter in the center of the star is axion condensed, with a domain wall region of thickness $\Delta r_{\mathrm{DW}} \sim 1/m_{a,\mathrm{eff}}$ in which the energy density changes rapidly but the pressure is nearly constant. This case is sketched in the right panel of Fig. 2.11.

For smaller ε, different structures for the outermost layers of the star are possible. For $0.01 \lesssim \varepsilon \lesssim 0.1$, there is no positive pressure where a heterogeneous phase is favored in all three scenarios and bulk matter at $\theta = \pi$ persists almost to the edge of the star. A crust in this case is only present in the thin domain wall region where the pressure of bulk matter is negative and hydrostatic equilibrium is maintained by the pressure produced by the axion gradient. In this case, $p_{\mathrm{bulk}} \approx -p_{\mathrm{grad}} = -f_a^2(\nabla\theta)^2/2$. This case is sketched in the left panel of Fig. 2.12 for Scenario A. Scenarios B and C look the same, but without a phase of dripped neutrons. If ε is smaller, it is possible to have an axion-condensed crust at positive pressure. In this case (sketched in the right panel of Fig. 2.12 for Scenario A), if the nuclear force is not significantly modified, some or all of the normal layers of the crust will be present in the $\theta = \pi$ region. The domain wall region still has a positive gradient pressure in this case and will support more crust at a negative bulk pressure.

Although our treatment of axion condensed matter does not apply at arbitrarily high density, we can still speculate about the effects of axion condensation on neutron star masses and radii. A similar calculation was performed in Ref. [104] for a non-interacting gas of neutrons, see also Ref. [141] for scalar effects on the crust thickness and EoS. As can be seen in Fig. 2.10, at low density, the EOS is typically softer for $\theta = \pi$ and ε not too small because of the contribution of the axion field. A naive extrapolation of nuclear matter to high density with only the axion-nucleon interaction we have considered thus far will eventually yield a stiffer EOS because of the lighter nucleon mass. This results in heavy neutron

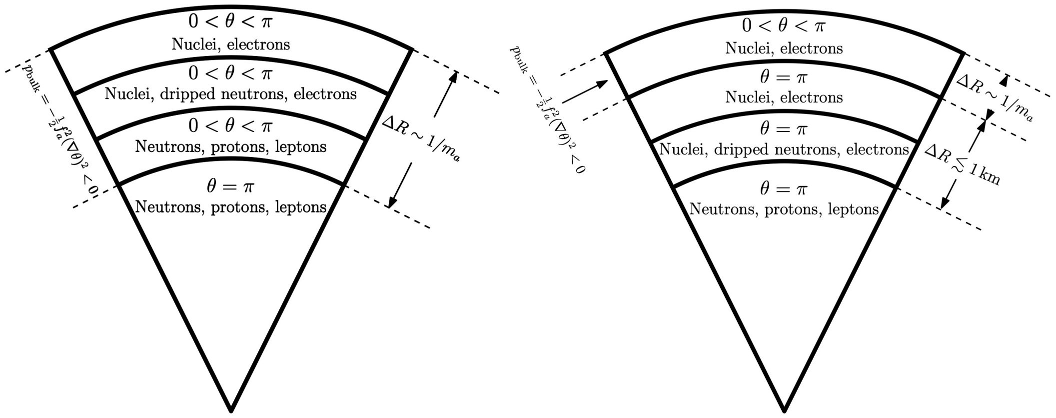

Figure 2.12: Layers of a neutron star with a crust only in the domain wall region (left) and one with an axion condensed crust (right) in Scenario A. Scenario B and C are the same, but with no dripped neutron phase. The thickness of layers is not to scale. See section 2.4.1 for discussion.

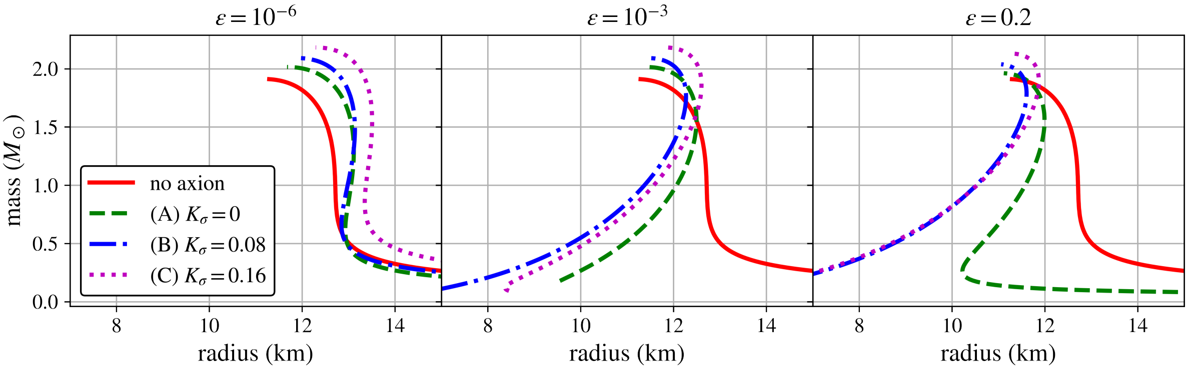

Figure 2.13: Mass-radius relationship for neutron stars with three fiducial ε values and K_σ in RMFT. We consider only the leading interaction between nucleons and axions (which leads to unknown uncertainties for $M \gtrsim 1.4\,M_\odot$) and neglect the thickness of the domain wall.

stars having larger radii and larger maximum mass. Figure 2.13 shows the relationship between mass and radius for neutron stars with various ε within this simplistic picture of the high density EOS and treating the domain wall as thin ($1/m_a \ll r_{\rm NS}$).

Counter-intuitively, larger K_σ yields larger NS radii for very small ε, pointing to a stiffer EOS. At high density, larger K_σ results in a stiffer EOS because of greater reduction to the effective nucleon mass. At low density, larger K_σ corresponds to nuclei with larger isospin asymmetry increasing the electron pressure once the neutron dripped phase is missing, again giving a stiffer EOS. Only in a range of energy densities just above the crust-core phase transition do Scenario B and C give a softer EOS than Scenario A with Scenario C having such a small region of softening that it has a minimal effect on the mass-radius curve and radii are larger for all masses.

For ε where the lowest density parts of the crust are missing, low mass stars may have very small radii, with a mass-radius relation akin to strange quark stars. Unlike a strange quark star, however, neutron stars with a condensed axion field lack a confining potential at their surface, and as a result have a thin

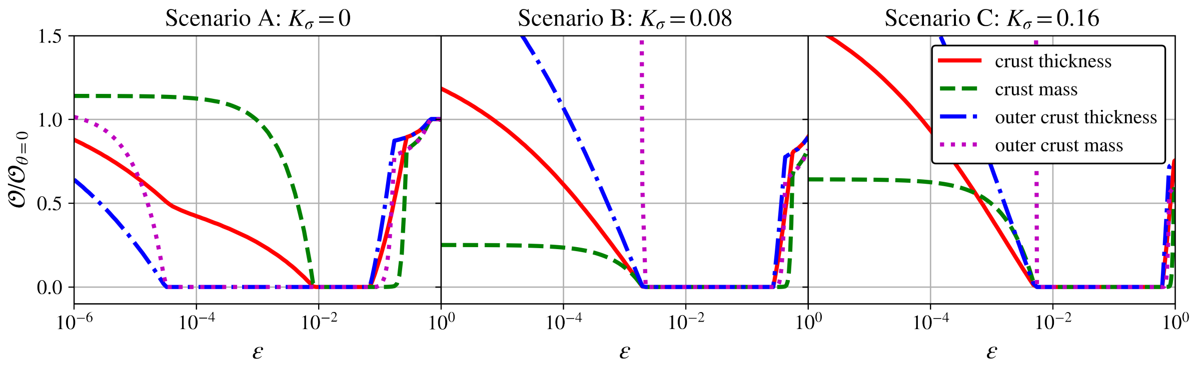

Figure 2.14: Crust and outer cruss mass and thickness of a $1.4\,M_\odot$ neutron star as a function of ε for RMFT EOS. The three panels correspond to the three interaction scenarios (Table 2.1). The curves are normalized to 1 for a star without axions.

crust of matter at intermediate θ in the domain wall region. Since the density and chemical potential smoothly go to zero on a length scale determined by the axion field profile, unusual surface properties of strange quark stars (see, e.g., Ref. [142] for a detailed discussion) are not present in axion condensed stars. For the same reason, the radius of an axion condensed star does not go to zero for vanishing mass for any ε but will always be limited by the finite size of the domain wall. The minimum stable mass and radius of a compact axion condensed object will be addressed in greater detail in Sec. 2.5.

Since our treatment of the interaction between axions and nucleons is only strictly accurate at densities around or below nuclear density, predictions from our calculation of the mass-radius relationship should be considered speculative for $M \gtrsim 1.4\,M_\odot$. As such, the constraints we draw will all be based on the structure of the crust in axion condensed stars. We will use masses and radii of $1.4\,M_\odot$ stars calculated with the uncertain high density equation of state as a starting point to calculate the crust and domain wall, but these will only have an effect by altering the gravitational potential and explicit dependence of gradients on the radius in spherical coordinates. Since the inclusion of axion condensation changes the radius of a $1.4\,M_\odot$ star by up to approximately a kilometer, and the uncertainties from nuclear physics are ±1-3 km (cf. Fig. 3 in Ref. [143]), this is a sub-leading source of uncertainty.

Focusing on the crust, Fig. 2.14 shows the total thickness and mass of the crust and thickness and mass of the outer crust alone of a $1.4\,M_\odot$ neutron star as a function of ε, normalized to the value for a star without axions. In Scenario A, the stars at very small ε have nearly the entire crust and look very similar to a star without axions, though the envelope (the region of the crust with $\rho < 10^{10}\,\mathrm{g/cm^3}$) is still diminished, providing a constraint from the cooling of isolated neutron stars, as will be discussed in Sec. 2.6.2. In Scenarios B and C, there is less overall mass in the crust because of the lack of dripped neutrons. This will reduce the moment of inertia in the crust and can be constrained with pulsar glitches, as will be discussed in Sec. 2.6.3. In all three scenarios, when $10^{-4} \lesssim \varepsilon \lesssim 0.1$ the overall thickness of the crust is diminished. Observations of the thermal relaxation timescale of neutron stars in x-ray binaries put a lower limit on the necessary thickness of the crust and will be discussed in Sec. 2.6.1.

2.4.2 Axion domain wall

An axion domain wall separates regions with densities that are larger and smaller than $n_B \sim \varepsilon m_\pi^2 f_\pi^2/\sigma_N$. This profile, in general, should be solved together with the density and pressure profile of the neutron star. In the limit where $m_a^{\rm QCD} > m_a > 1/r_{\rm NS}$, the axion profile is a thin domain wall, located at a radius r_a from the center of the neutron star. The tension σ_a of this field profile wrapping the nuclear matter inside the neutron star exerts a pressure of $\sigma_a/2r_a$, the minimal pressure of the matter inside the domain wall.

We solve the axion field profile in two regimes, extending the formalism described in section 2.2.3 to include nuclear interactions. First, consider the limit where an axion domain wall is in a smooth background of nuclear matter which is changing slowly over length scales much longer than $1/m_a$. In this case, we can solve the axion field profile in PNM as

$$\begin{aligned} \nabla^2 a &= \left(m_a^2 - \frac{\sigma_N (1+\delta^{(\rm loc)}) n_n(r)}{f_a^2} \right) f_a \, \sin[a/f_a] \\ &\simeq \frac{\sigma_N (1+\delta^{(\rm loc)})}{f_a} \left. \frac{{\rm d}n_n(r)}{{\rm d}r} \right|_{r=r_a} (r-r_a) \, \sin[a/f_a], \end{aligned} \tag{2.23}$$

where $\delta^{(\rm loc)} \propto K_\sigma n_B/\sigma_N m_\sigma^2$ is an order-one quantity that encodes the m_σ dependence of the effective axion mass. Details can be found in App. B.

For axion profiles with thickness much smaller than r_a, at linear order in a/f_a, the solution of this equation is an Airy function, where the field profile changes over a length scale of $(m_a^2/r_a)^{-1/3}$. The domain wall tension of this axion profile is $\sigma_a \leq m_a f_a^2$ and the resulting pressure difference due to this domain wall profile between inside and outside is smaller than that due to the vacuum energy difference of $m_a^2 f_a^2$.

The smooth density profile would be a good approximation only for the largest ε, where the axion domain wall is situated close to nuclear density. As we showed in Sec. 2.3, for most of the ε we consider, the domain wall is between regions with drastically different densities, and the density (and pressure) of the matter outside the domain wall is effectively zero. In this second case, inside the domain wall, the density $n_{\rm in}$ is such that the degeneracy pressure is

$$\frac{(3\pi^2)^{2/3}}{5m_n} n_{\rm in}^{5/3} \simeq m_a^2 f_a^2 \,, \tag{2.24}$$

and the axion mass in the region inside the domain wall is much larger than the axion mass in vacuum at small ε, by a factor of

$$\frac{m_a(n_{\rm in})}{m_a} = \left(\frac{\sigma_N n_{\rm in}}{m_a^2 f_a^2}\right)^{1/2} = \frac{\sigma_N^{1/2}(5m_n)^{3/10}}{(3\pi^2)^{1/5}(m_a^2 f_a^2)^{1/5}} \approx \frac{1.5}{\varepsilon^{1/5}}. \tag{2.25}$$

In this limit, the field profile is changing mainly inside the region of low density, and the field profile has an extent of $1/m_a$. This exerts a pressure of $\sim m_a f_a^2/r_{\rm NS}$ on the matter inside, again smaller than the pressure difference due to the changing vacuum energy[3].

For axion masses that are not too small, the chemical potential can be treated as approximately constant in the domain wall crust. Across a domain wall crust, the changing nucleon mass modulates the Fermi momenta in the same way that a changing baryon chemical potential does in a normal star, but on a much shorter distance scale. This approximation is good as long as the condition $\mathrm{d}\mu_B/\mathrm{d}r \ll \mathrm{d}m_N(\theta)/\mathrm{d}\theta \times \mathrm{d}\theta/\mathrm{d}r$. Since θ changes on a distance scale $1/m_a$ and the local chemical potential can be expressed in terms of the local spacetime metric $e^{\nu(r)} = g_{00}(r)$ and redshifted chemical potential $\tilde{\mu}_B$ according to $\mu_B(r) = \tilde{\mu}_B e^{-\nu(r)}$, this condition can be translated into a condition on the axion mass and the gravitational potential near the surface of the star,

$$m_a \gg \frac{GM_{\rm NS}}{r_{\rm NS}^2(1-2GM_{\rm NS}/r_{\rm NS})}\frac{m_N}{\sigma_N} \simeq 9\times 10^{-11}\,\mathrm{eV}\,, \tag{2.26}$$

with the final value given for a $1.4\,M_\odot$ star with a radius of 12 km. In what follows, we will consider axion masses $m_a > 10^{-10}\,\mathrm{eV}$ when calculating the domain wall crust and will treat the chemical potential as approximately constant in this regime.

The equivalent condition in the case where the domain wall is inside the star is

$$|m_{a,\rm eff}(n_B)| \gg \frac{GM_a}{r_a^2(1-2GM_a/r_a)}\frac{\mu_c}{\sigma_N}\left(1+\frac{4\pi r_a^3 p_c}{M_a}\right)\,, \tag{2.27}$$

where r_a is the radius of the domain wall, M_a is the mass contained within $r < r_a$, and p_c and μ_c are the critical pressure and chemical potential where the phase transition occurs. In practice, $p_c \lesssim 0.1\,\mathrm{MeV/fm^3}$ for ε where the crust is strongly affected and the GR correction is at most a few percent and we can instead use the approximate form

$$|m_{a,\rm eff}(n_B)| \gg \frac{GM_a}{r_a^2(1-2GM_a/r_a)}\frac{\mu_c}{\sigma_N}. \tag{2.28}$$

---

[3] In the $\mathbb{Z}_\mathcal{N}$ model, the vacuum energy difference is $m_a^2 f_a^2/\mathcal{N}^2$, while the domain wall pressure becomes comparable to this vacuum pressure when $r_{\rm NS} \simeq \mathcal{N}^2/m_a$, that is $m_a \simeq 10^{-8}\,\mathrm{eV}$ for $\varepsilon \simeq 2\times 10^{-7}$. The density $n_{\rm in}$ for which Eq. (2.24) is satisfied is still much larger than the critical density for which Eq. (2.11) saturates, since the equation Eq. (2.25) is only modified by logarithmic corrections.

This approximation fails in the case where the domain wall is very near the center of the star and M_a is small. In practice, this is a challenging constraint to implement since $m_{a,\mathrm{eff}}$ changes sign in the vicinity of the domain wall. In the core where the baryon density changes more slowly, this leads to a very extended domain wall even for axion masses that are larger than $1/R_{\mathrm{NS}}$, with the extent of the domain wall becoming comparable to the gravitational scale for $m_a \lesssim 10^{-9}\,\mathrm{eV}$. For the sake of calculating the contribution of the domain wall to the crust, we limit ourselves to axion masses $m_a \gtrsim 10^{-9}\,\mathrm{eV}$ when the domain wall is inside the star. This does not affect the final constraint we determine.

Apart from the two special cases, more generally, in order to numerically solve the axion field profile, we will work in the limit where the baryon chemical potential changes on a length scale that is long compared to the length scale for θ to change, set by Eq. (2.26) for the case where the domain wall is at the surface of the star and Eq. (2.28) for the case where the domain wall is in the interior of the star. In this case, we can solve the axion field profile at fixed chemical potential according to

$$\begin{aligned}\nabla^2\theta &= \frac{1}{f_a^2}\frac{d\Omega}{d\theta} \\ &= \frac{1}{f_a^2}\left\{\sigma_N(1+\delta^{(\mathrm{loc})})[n_p^{(s)}(\theta)+n_n^{(s)}(\theta)] + \frac{\Delta\sigma}{f^2(\theta)}[n_p^{(s)}(\theta)-n_n^{(s)}(\theta)] - \varepsilon m_\pi^2 f_\pi^2\right\} f'(\theta)\,,\end{aligned} \tag{2.29}$$

where $n_i^{(s)} = \partial E/\partial m_i$ is the scalar density of baryon species i which at leading order in bulk matter is given by $n_i^{(s)} = n_i - k_{Fi}^5/[10\pi^2 m_i^2(\theta)]$, the spatial gradients include corrections from gravity, and the scalar densities are found at fixed baryon chemical potential. The quantity $\delta^{(\mathrm{loc})}$ comes from the explicit m_σ-dependence of the RMFT Lagrangian and is approximately given by

$$\delta^{(\mathrm{loc})} \approx \frac{K_\sigma}{\chi\sigma_N}\left(\frac{g_\sigma}{m_\sigma}\right)^2\left(n_p^{(s)}+n_n^{(s)}\right)\,, \tag{2.30}$$

where g_σ is the coupling of the σ meson to nucleons in the RMFT model and χ is equal to the volume fraction of nuclei in the outer crust and unity in the core. Exact expressions including higher-order RMFT corrections and the more complicated expression for the inner crust can be found in App. B. This correction is order one for both Scenarios B and C in the outer crust and core and should not be neglected, but is suppressed in the inner crust. Note that this correction is due only to explicit m_σ dependence of the RMFT Lagrangian; implicit dependence via the effect of m_σ on the Fermi momenta of the nucleons and the mean-field value of the σ field vanishes since the mean-field approximation will always give Fermi momenta and a mean-field value for the σ field that minimize the free energy.

The fixed baryon chemical potential approximation leads to overestimating the amount of matter in the crust irrespective of the location of the crust. In the case where the domain wall is at the surface of the star, the small decrease to the baryon chemical potential in the domain wall will cause the baryon density to decrease more rapidly, resulting in a thinner crust. In the case where the domain wall is inside the star, a domain wall that is too broad would result in overestimating the size of the crust since, in reality, part of the domain wall would extend into the crust rather than being a separate layer that gets added to a normal crust. Since our constraint is derived from layers of the crust being missing or diminished, this approximation is conservative.

It is worth noting that the equations of hydrostatic equilibrium do not need to be solved separately in the domain wall because they are automatically satisfied by solving the Euler-Lagrange equation for the axion field given by Eq. (2.29). This can be seen by observing that

$$\frac{\mathrm{d}p_{\mathrm{bulk}}}{\mathrm{d}r} = -\frac{\mathrm{d}\Omega}{\mathrm{d}\theta}\frac{\mathrm{d}\theta}{dr} = -f_a^2\nabla^2\theta\frac{\mathrm{d}\theta}{\mathrm{d}r} = -\frac{1}{2}\frac{\mathrm{d}}{\mathrm{d}r}[f_a^2(\nabla\theta)^2] = -\frac{\mathrm{d}p_{\mathrm{grad}}}{\mathrm{d}r}. \tag{2.31}$$

The differential equation given by Eq. (2.29) can be solved by a shooting procedure, varying the initial conditions at the inner edge of the domain wall until a solution is found that smoothly goes from $\theta = \pi$ to zero. In practice, solving this equation is greatly simplified by making a change of variables to confine θ to be between zero and π, $\theta(y) \equiv \pi/(1+e^y)$ and solving the resulting equation for y. Numerical results from this calculation will be presented in Sec. 2.6.

Since we perform calculations in the domain wall region only in RMFT, the entire θ-dependence in the domain wall is contained in the nucleon and meson masses and the energy of the axion field itself. There are additional terms in the nuclear Lagrangian that contribute only when θ is at some intermediate value that violates parity and a detailed calculation of the domain wall from first principles should include these terms that we neglect. For further discussion, see App. A.

2.5 Finite size objects at zero pressure

As was first noted in Refs. [96, 104], an object comprised of nuclear matter at $\theta = \pi$ can be stabilized by the negative pressure $m_a^2 f_a^2$, rather than gravity. These objects, which we call π-balls, are held together by the attractive axion potential as long as the baryon chemical potential is too small to allow nucleons to escape (see also [141, 144, 145]). Given the constraint from white dwarf stability of $\varepsilon > 2 \times 10^{-7}$, a zero-pressure object balanced by electron degeneracy pressure cannot exist. If a neutron star has a central density large enough to be unstable against axion condensation, it is possible that when such a neutron star is disrupted in a binary neutron star merger, π-balls may be part of the ejecta. Having an axion field surrounding them, these objects may produce a unique electromagnetic signature. Such questions of production and observational signatures of π-balls will be explored in the future; in this work, we merely comment on their basic properties.

An object with size $R \gg 1/m_a$ made of PNM is stable at almost zero pressure when

$$p_{\mathrm{DW}} = \frac{m_a f_a^2}{2R} = -\varepsilon m_\pi^2 f_\pi^2[1 - f(\pi)] + \frac{(3\pi^2)^{2/3}}{5m_n} n_n^{5/3}\,, \tag{2.32}$$

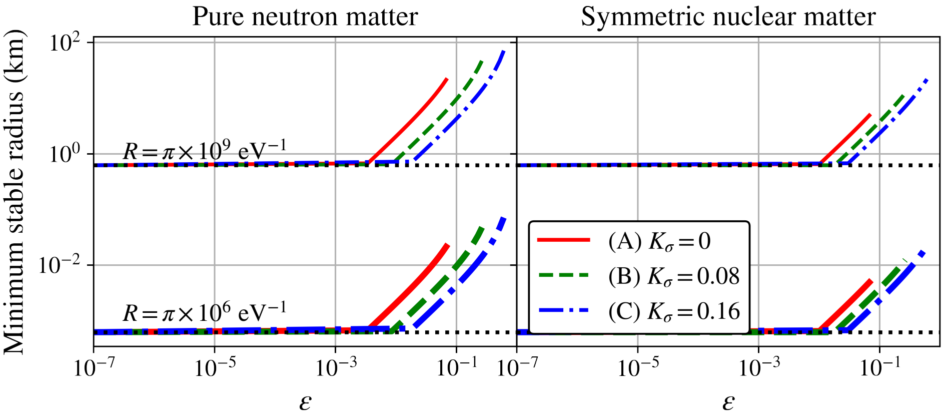

Figure 2.15: Minimum stable radius of a π-ball made of SNM and PNM as a function of ε. Thin lines: $m_a = 10^{-9}\,$eV, thick lines: $m_a = 10^{-6}\,$eV. The dotted black lines show lines of $R = \pi/m_a$ for the two axion masses.

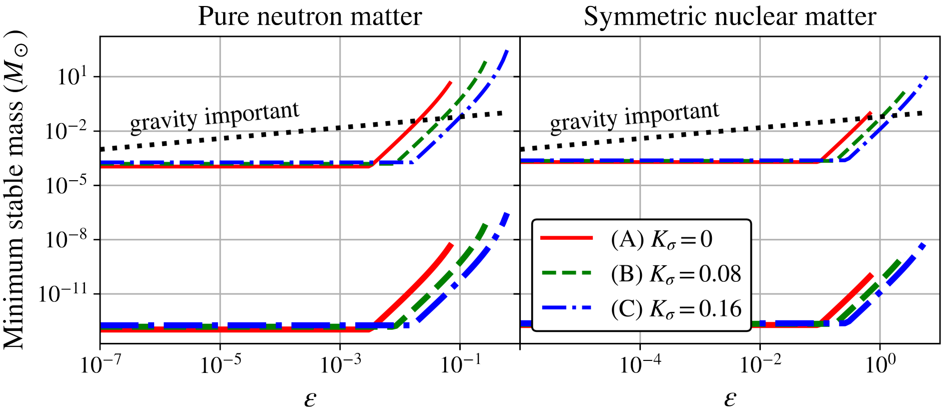

Figure 2.16: The corresponding minimum stable mass of a π-ball made of SNM and PNM. Thin lines: $m_a = 10^{-9}\,$eV, thick lines: $m_a = 10^{-6}\,$eV. The black dotted line is the maximum mass before gravity becomes important from Eq. (2.35).

and the Fermi energy of the neutrons is smaller than the kinetic energy required to escape the $\theta = \pi$ region

$$\frac{(3\pi^2)^{2/3}}{2m_n} n_n^{2/3} < \sigma_N[1 - f(\pi)], \tag{2.33}$$

which, when combined with Eq. (2.32), is identical to the condition for the appearance of the $\theta = \pi$ region ($\sigma_N n_n > \varepsilon f_\pi^2 m_\pi^2$) if the domain wall pressure is small. The mass-radius relation of this object can be found to be

$$\begin{aligned} M &\simeq \frac{4\pi R^3}{3} \frac{m_n(5m_n\varepsilon m_\pi^2 f_\pi^2)^{3/5}}{(3\pi^2)^{2/5}} \left[1 - f(\pi) + \frac{m_u m_d}{2Rm_a(m_u+m_d)^2}\right]^{3/5}, \\ &\simeq 2\times10^{18}\varepsilon^{3/5}\left(\frac{R}{1\,\mathrm{m}}\right)^3 \mathrm{kg}\,, \end{aligned} \tag{2.34}$$

where the last equality holds if $m_a R \gg 1$. The maximal radius of this object where gravity can be ignored can be found by equating the gravitational potential energy with the Fermi energy of the neutrons on the surface of this object, which yields $R \simeq 5\varepsilon^{-1/10}\,\mathrm{km}$ and the resulting maximal mass is

$$M_{\mathrm{max}} \simeq 0.12\,\varepsilon^{3/10} M_\odot\,, \tag{2.35}$$

beyond which the gravitational binding energy/pressure cannot be ignored. The minimal mass of a π-ball can either be found at $R = \pi/m_a$, when the thin wall approximation fails, or when the domain wall pressure becomes large enough that the baryon chemical potential exceeds the bare neutron mass. When the baryon chemical potential becomes larger than the bare neutron mass, it is energetically favorable for neutrons to leave the $\theta = \pi$ region. In the dilute approximation where nuclear interactions are ignored, the condition set by Eq. (2.33) is saturated when $R \simeq 1.2\varepsilon^{1/2}/m_a$, which is smaller than $1/m_a$ for any $\varepsilon < 0.7$. This leads to the final minimal mass of

$$M_{\mathrm{min}} \simeq 8\times 10^9 \varepsilon^{3/2}\,\mathrm{MeV}^4/m_a^3 = 2\times 10^{-7} M_\odot \left(\frac{\varepsilon}{10^{-1}}\right)^{21/10}\left(\frac{10^{-9}\,\mathrm{eV}}{m_a}\right)^3. \tag{2.36}$$

In practice, to calculate the minimum mass of a stable object, nuclear interactions must be included. In the case of PNM, the minimum stable size is determined by the requirement that the baryon chemical potential not exceed the bare neutron mass. In the case of SNM, the minimum stable size is determined by the requirement that the baryon chemical potential be less than the energy per baryon of the most bound symmetric nucleus, $\mu_{\mathrm{Fe}}/A = m_N - 8$ MeV.

Figure 2.15 shows the minimum stable radius for π-balls made of SNM and PNM and Fig. 2.16 shows the minimum stable mass, including nuclear interactions from the RMFT model and stabilized by axions. The horizontal dotted lines in Fig. 2.15 show when $m_a R = \pi$ and the domain wall approximation fails. The black dotted lines in Fig. 2.16 show the mass at which gravity cannot be neglected from Eq. (2.35). Note that when the constraints on axion parameter space from neutron star measurements we will derive in section 2.6 are taken into account, these π-balls should typically have masses larger than the Earth. They will have masses comparable to heavy planets or brown dwarfs, and sizes as large as a few kilometers. Observation of one of these objects would be quite remarkable.

2.6 Observable implications and constraints

In this section, we estimate constraints on the exceptionally light axion parameter space from neutron star observations. We focus on three observables based on modifications to the crust of an axion-condensed neutron star: thermal relaxation times of the crust in accreting systems (Sec. 2.6.1), cooling rates of isolated neutron stars based on a diminished envelope, first considered in Ref. [99], (Sec. 2.6.2), and

Table 2.3: Range of ε corresponding to different locations of the domain wall in the thin-wall approximation ($m_a \gtrsim 10^{-8}$ eV).

Region	(A) $K_\sigma = 0$	(B) $K_\sigma = 0.08$	(C) $K_\sigma = 0.16$
DW at surface	$\varepsilon < 0.068$	$\varepsilon < 0.27$	$\varepsilon < 0.61$
DW in crust	$0.068 < \varepsilon < 0.27$	$0.268 < \varepsilon < 0.56$	$0.61 < \varepsilon < 0.96$
DW in core at $n_B < n_{\text{sat}}$	$0.27 < \varepsilon < 0.38$	$0.56 < \varepsilon < 0.75$	$0.96 < \varepsilon < 1$

fractional moment inertia of the crust as inferred from pulsar glitches (Sec. 2.6.3). All of these rely only on the understanding of neutron star matter and dynamics below saturation density. In Sec. 2.6.4, we summarize the constraints in the context of the $\mathbb{Z}_\mathcal{N}$ model of exceptionally light axions.

We note also that the mass-radius relation of axion condensed stars has some unusual features (see Sec. 2.4.1) which could lead to constraints on axion models. Current measurements of the masses and radii of neutron stars are not yet precise enough to draw conclusions. Next-generation experiments may significantly reduce the error bars and yield a useful constraint if the EOS for a range of densities, and for both $\theta = 0$ and $\theta = \pi$, is better understood.

To understand the constraint from observation, we apply the methods discussed in Sec. 2.4 and specifically the understanding of the axion domain wall established in Sec. 2.4.2. There are three distinct regions for this calculation. First, when $\theta = \pi$ is the favored phase all the way to zero pressure, the domain wall sits at the surface and forms a thin shell surrounding the rest of the star at negative bulk pressure, resulting in a thinner crust if ε is not too small (cf. Fig. 2.14). Second, when the transition from $\theta = \pi$ to $\theta = 0$ occurs in the crust of the normal phase, the domain wall connects a homogeneous axion condensed phase to a heterogeneous normal phase and the size of the crust is diminished. Third, when the phase transition to $\theta = \pi$ occurs at a density above the crust-core phase transition, the entire normal crust is present and we draw no constraint.

If the domain wall is inside the star, the entire normal envelope is present and constraints can only be drawn from thermal relaxation and glitches, although the constraint from thermal relaxation is much weaker. When the domain wall is at the surface, all three constraints are relevant. Thus far we have focused on results for $\varepsilon \gtrsim 10^{-6}$; here, for the sake of calculating a constraint from the lack of an envelope, we consider ε as low as 5×10^{-7} as this is the ε at which the envelope appears for positive pressure at $\theta = \pi$ (i.e. not only in the domain wall). Table 2.3 shows the ranges of ε relevant for each region.

2.6.1 Constraint from crust thermal relaxation in x-ray binaries

Neutron stars in transiently accreting x-ray binaries go through periods of outburst and quiescence, reaching a quasi-steady state on astronomical timescales [146]. During outburst, matter is rapidly accreted onto the neutron star surface from a companion and pycnonuclear reactions deep in the crust heat the star. On timescales of tens to hundreds of days (see, e.g., Ref. [147]) the crust cools and comes back into thermal equilibrium with the core. Properties of the crust of neutron stars in these x-ray binaries can be inferred by observing the timescale for the crust to thermally relax following an outburst. The thermal timescale is roughly given by $\tau_{\rm th} \simeq C_V(\Delta r)^2/\kappa$ where C_V is the specific heat of the crust, κ is the thermal conductivity, and Δr is the thickness of the crust [148].

The specific heat capacity, C_V, in the crust of a neutron star is influenced by electrons, ions, and neutrons, depending on the ambient temperature. However, the thermal conductivity, κ, is primarily determined by electrons across all relevant temperatures [149]. For typical crustal temperatures in the range of 10^7-10^8 K, as found in accreting neutron stars, the electron contribution provides a lower bound for C_V, while the neutron contribution—typically suppressed due to superfluidity—sets an upper bound.

In Scenario A, since nuclear interactions remain unchanged, the crust's composition is also relatively unaltered for pressures much larger than the axion pressure. In Scenarios B and C we expect an increase in electron density above the neutron drip pressure of normal nuclear matter with a maximum increase by a factor of 3-4 near the crust-core boundary in Scenario C. In all scenarios, electron conduction is primarily limited by electron-phonon scattering. To estimate uncertainties in electron scattering rates due to electron-phonon interactions in Scenarios B and C, we modified the phonon spectrum for solids with varying nuclear charge Z, mass number A, and the corresponding plasma frequency, $\omega_p \sim (4\pi e^2 Z^2 n_I/A m_n)^{1/2}$ [150]. Axion condensation softens the spectrum of phonons, enhancing electron-phonon scattering and suppressing the contribution of phonons to C_V (for a review of thermal transport in neutron star crusts, see Ref. [20]).

At equal nuclear pressure (i.e. not including the negative axion pressure) the lack of dripped neutrons generically enhances κ in Scenarios B and C due to a significantly larger electron density when nuclei are treated in mean field theory. In order to outweigh the effects of increased electron density, Z/A would need to decrease by about an order of magnitude. At these densities, $A > 100$ and including shell effects is unlikely to produce such a massive change. Nonetheless, lacking an *ab initio* calculation of neutron-rich nuclei in the axion condensed phase, we place a generous uncertainty on this prediction. At low temperatures, the effect on C_V from axion condensation is dominated by a decreased contribution from phonons, which as with κ is susceptible to modifications from shell effects. For $T \gtrsim 5 \times 10^7$ K the increased electron density dominates the change to the heat capacity and shell effects are less important for C_V. When shell effects are neglected, the increase to C_V at high temperature is always smaller than the increase to κ, leading to a net decrease in C_V/κ.

We do not include any free neutrons in the heat capacity in our comparisons as the neutrons form a superfluid at most densities they appear; including them would only strengthen this claim by introducing an additional reservoir of heat. Furthermore, C_V/κ decreases as a function of nuclear pressure at these densities, so at equal pressure after including the axion pressure, C_V/κ would be expected to increase in the axion condensed phase at equal total pressure. At the lowest densities, shell effects in nuclei are

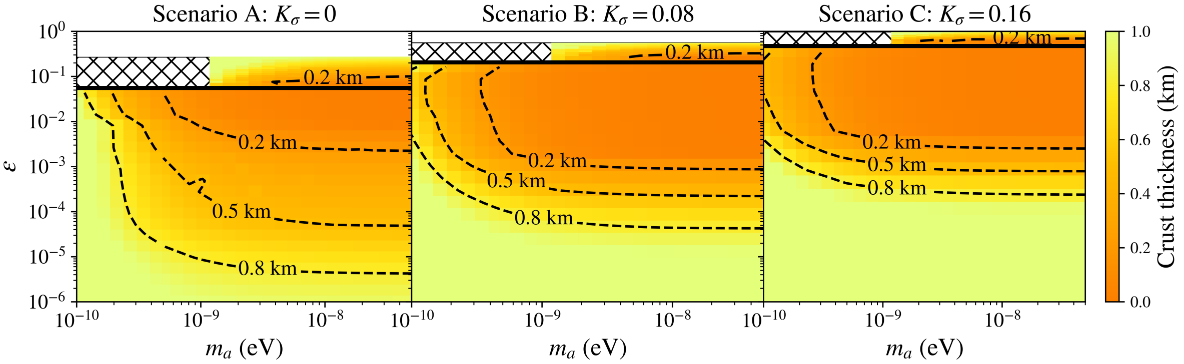

Figure 2.17: Total crust thickness of a $1.4\,M_\odot$ star as a function of m_a and ε in the RMFT model for three values of K_σ. In the hatched region, the domain wall approximation fails. In the white band, the entire normal crust is present.

expected to dominate and it is challenging to predict the exact properties of these nuclei. However, in the range of ε that we constrain with thermal relaxation, the part of the crust with positive pressure is all above the normal neutron drip pressure and these shell effects are only dominant in the thin domain wall.

To establish a bound on axion condensation from crust relaxation—without performing detailed self-consistent calculations of C_V and κ—we exploit the quadratic dependence of the thermal relaxation timescale on crust thickness. As a conservative constraint, we require that the total crust thickness be at least 0.2 km, which is approximately one-fifth of its value in a normal neutron star. This assumption effectively limits the increase of C_V/κ to no more than a factor of 25 when $\theta = \pi$, larger than the maximum increase in C_V/κ of a factor of 10 at $\theta = \pi$ suggested by the preceding arguments.

Figure 2.17 shows the total crust thickness as a function of m_a and ε for a $1.4\,M_\odot$ neutron star for our three scenarios in the RMFT model. The white band covers regions of the parameter space where the entire normal crust is present (i.e., the phase transition happens at a pressure greater than the crust-core boundary in a normal star) and the hatched region shows where the in-medium axion mass is low enough in the domain wall region that the constant chemical potential approximation fails. The solid black line divides the region where the domain wall is at the surface of the star and the region where it is inside the star. Based on the conservative estimate that the total crust thickness must be at least 0.2 km, our constraint is shown for our three scenarios in Fig. 2.18. Table 2.4 shows the constraint on ε in our three scenarios for $m_a \gtrsim 10^{-8}$ eV where the domain wall becomes insignificant and the constraint is dependent on ε only.

Scenario B gives the strongest constraint for small ε from crust thermal relaxation because the pressure at the crust-core phase transition that determines at what ε the crust appears is non-monotonic as a function of K_σ (cf. Fig. 2.9). As K_σ is increased from zero, the pressure for the crust-core phase transition decreases because the neutron matter surrounding nuclei in the inner crust becomes more

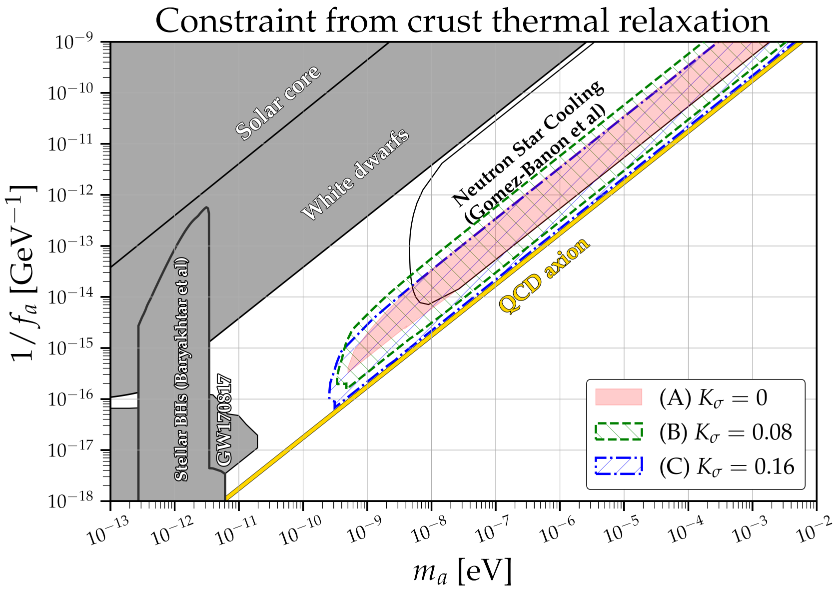

Figure 2.18: Constraint from crust thermal relaxation assuming a total crust thickness of $\Delta r < 0.2$ km is disfavored by observation of thermal relaxation timescales. Three scenarios are shown, assuming no change to nuclear interactions (A), which we take as the conservative bound, and moderate (B) or large (C) increases of attractive nuclear interactions in $\theta = \pi$ matter (see Sec. 2.3 for details). The grey shaded regions are excluded by prior studies of the Sun and white dwarf stability [95, 96], black hole superradiance [151, 152] and neutron star inspiral gravitational wave emission [98]. Recent constraints from isolated neutron star cooling [99] are shown as a contour. Plots of past constraints are generated with code from Ref. [69].

Table 2.4: Constraint on ε from crust thermal relaxation for $m_a \gtrsim 10^{-8}$ eV.

	(A) $K_\sigma = 0$	(B) $K_\sigma = 0.08$	(C) $K_\sigma = 0.16$
Min. excluded ε	2.2×10^{-3}	8.7×10^{-4}	2.5×10^{-3}
Max. excluded ε	0.10	0.32	0.69

attractive. At the same time, pressure in the outer crust that is dominated by electrons is increasing as nuclei become more neutron-rich. The pressure at the crust-core phase transition will decrease as K_σ is increased, giving a stronger bound on small ε, until the crust-core phase transition occurs at the same pressure as the transition from inner to outer crust (neutron drip pressure). The pressure at the crust-core phase transition will grow if K_σ is increased further, giving a weaker bound on ε, since there are no more dripped neutrons in the crust and the pressure due to electrons increases with K_σ.

2.6.2 Constraint from isolated neutron star cooling

The cooling of isolated neutron stars has been used to constrain light QCD axions in Ref. [99]. Their constraint hinges on the envelope being thinner in a star with an axion-condensed crust than in a normal neutron star, providing less thermal insulation between the core and exterior of the star and shortening the cooling timescale of the core. Taking the boundary of the envelope to be at an energy density of 10^{10}

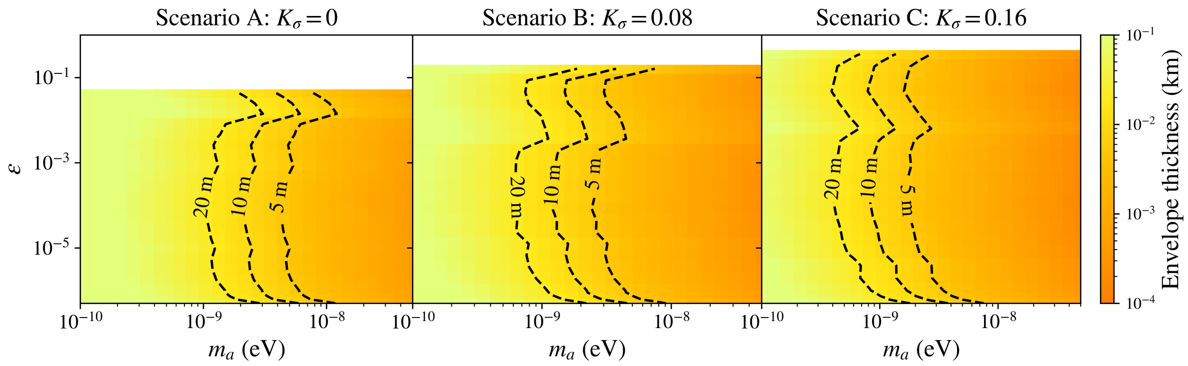

Figure 2.19: Envelope thickness of a $1.4\,M_\odot$ neutron star as a function of m_a and ε in the RMFT model for the three K_σ scenarios. In the white band, the entire normal envelope is present.

Table 2.5: Constraint on ε from isolated neutron star cooling for $m_a \gtrsim 10^{-8}$ eV.

	(A) $K_\sigma = 0$	(B) $K_\sigma = 0.08$	(C) $K_\sigma = 0.16$
Min. excluded ε	5.2×10^{-7}	5.8×10^{-7}	5.6×10^{-7}
Max. excluded ε	0.068	0.27	0.61

g/cm^3 when the energy density of the axion is not included, we find that for the range of ε we consider, the entire envelope is in the domain wall region.

Figure 2.19 shows the thickness of the envelope as a function of m_a and ε. In the white band, the phase transition to axion condensed matter occurs inside the star and the entire normal envelope is present. The feature around $\varepsilon \simeq 10^{-2}$ in all three panels is a result of a jump in the EOS just as the crust-core phase transition is at the bottom edge of the domain wall. Ref. [99] found that when the envelope is at least a few times thinner than its normal ~ 100 m, the star cools too quickly and this region of parameter space is excluded. Taking a conservative estimate that the envelope must be at least 5 m thick to explain neutron star cooling data, we show the constraint for our three scenarios in Fig. 2.20. Notably, this indicates that the constraint in Ref. [99] extends to lower axion masses and larger ε than previously considered when the modification to the nuclear force is taken into account. This occurs because the chemical potential in the crust is significantly lower for larger K_σ due to nuclei being more strongly bound. At a chemical potential much lower than that of normal nuclei, the baryon density goes to zero much more rapidly as θ decreases in the domain wall, resulting in a thinner envelope. The envelope constraint applies for all ε we consider where the domain wall is at the surface of the star (given by the first row of Table 2.3). At larger ε, the domain wall is inside the star and the entire normal envelope is present. Table 2.5 shows the constraint on ε in our three scenarios for $m_a \gtrsim 10^{-8}$ eV where the domain wall becomes insignificant and the constraint is dependent on ε only.

We mention in passing that a detailed calculation of constraints from neutron star cooling should include the modification to the Direct Urca threshold from axion condensation. When the central density of a neutron star exceeds the Direct Urca threshold (set by the density at which $k_{Fn} < k_{Fp} + k_{Fe}$,

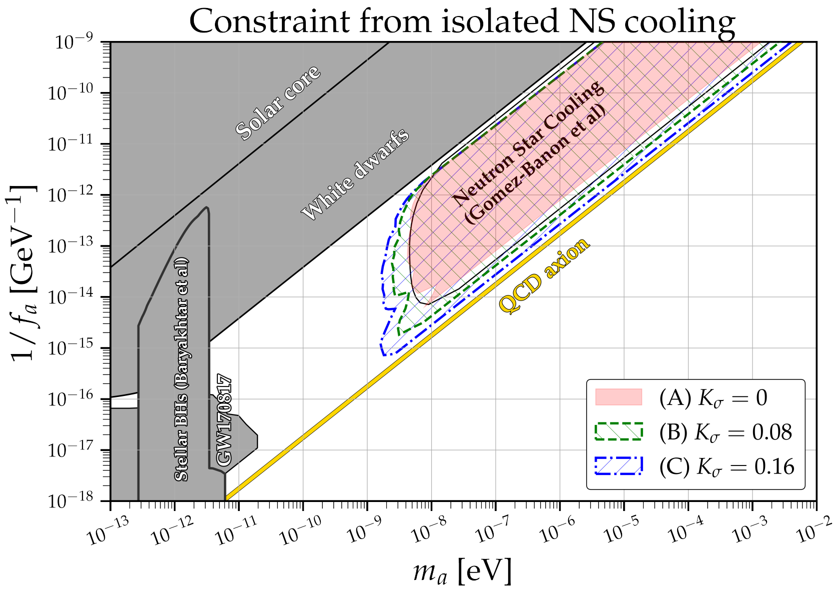

Figure 2.20: Constraint from isolated neutron star cooling based on the lack of an envelope in our three scenarios. We use the envelope thickness of 5 m as a conservative minimum consistent with neutron star cooling. Our scenario (A) is in good agreement with the neutron star cooling bound of Ref. [99]. Parameter space as in Fig. 2.18.

Table 2.6: Baryon density at the Direct Urca threshold ($k_{Fn} < k_{Fp} + k_{Fe}$) in the RMFT model.

	No axion	(A) $K_\sigma = 0$	(B) $K_\sigma = 0.08$	(C) $K_\sigma = 0.16$
n_{DU} (fm^{-3})	0.61	0.54	0.48	0.42

equivalently $Y_p \geq 0.11$ in matter containing neutrons, protons, and electrons), rapid cooling becomes possible. The isovector contribution to the nucleon masses from finite θ will result in a larger proton fraction at $\theta = \pi$, lowering the Direct Urca threshold. Additionally, a more attractive nuclear force with a lighter effective nucleon mass will result in a larger symmetry energy and a lower Direct Urca threshold. In the RMFT model, the symmetry energy is given by

$$a_{\text{sym}} = \frac{k_F^2}{6\sqrt{k_F^2 + m^{*2}}} + \frac{n_B}{8}\left(\frac{g_\rho}{m_\rho}\right)^2 , \tag{2.37}$$

where k_F is the Fermi momentum of SNM and m^* is the effective nucleon mass, decreased from its vacuum value by the effect of the σ meson. Finite K_σ results in a smaller effective nucleon mass m^*, increasing the symmetry energy and lowering the Direct Urca threshold. The exact value of the Direct Urca threshold in nuclear matter is not known and the effects of the axion at the relevant baryon densities is uncertain. Table 2.6 shows the baryon density at the Direct Urca threshold for the IUFSU* RMFT parameter set we have used throughout. These values should be considered illustrative of possible impacts of axion condensation on neutron star cooling and not a concrete prediction.

2.6.3 Constraint from pulsar glitches

Pulsars are spinning neutron stars that emit regular pulses of EM radiation at twice their spin frequency. Pulsar timing studies since the 1970s have cataloged about 3000 sources that exhibit remarkable stability. Precise measurements of the spin period and its steady rate of change have provided useful insights about neutron star populations and their magnetic fields. Some pulsars, however, have been observed to glitch, a phenomenon in which the rotation frequency rapidly increases on timescales of less than a minute. For a concise review of pulsar timing and glitches see [153].

In crust-based models of neutron star glitches, the phenomenon is thought to result from a sudden transfer of angular momentum from an interior superfluid that stores angular momentum in quantized vortices to the crust. As the star gradually spins down, the superfluid cannot adjust smoothly because its vortices are pinned—or otherwise hindered—by a lattice of neutron-rich nuclei [154–157]. Over time, this creates a buildup of angular momentum stress between the superfluid and the rest of the star. Eventually, this tension is released in a sudden, dramatic, and still poorly understood event that unpins many vortices at once, rapidly spinning up the star.

The spin-up is proportional to the ratio of the moment of inertia of the superfluid component, denoted by I_s, to the moment of inertia of the star, denoted by I. The Vela pulsar places the most stringent constraint on glitch models, requiring that the ratio of superfluid moment of inertia to the total moment of inertia lies between 1.6% and 7% [158]. While there remains ongoing debate about whether nuclear physics models can account for values at the upper end of this range [158–160]—and speculation about additional angular momentum reservoirs being necessary to fully explain Vela's glitches [161]—the conventional model, involving a neutron superfluid in the inner crust, remains both natural and viable.

The glitches of the Vela pulsar are challenging to describe in terms of other available models for glitch behavior. Starquakes are a possible alternate explanation for pulsar glitches [162, 163] and recent observations suggest that the Vela pulsar may experience starquakes [164]. However, to explain the high frequency of glitches in the Vela pulsar with starquakes requires either an extreme equation of state in tension with observations of NS masses and radii [165] or results in the Vela pulsar having an unrealistically small mass [166] with the connection between starquakes and glitches still typically requiring the presence of a neutron superfluid [167]. While the possibility of a phase transition deep in the neutron star is potentially relevant for glitches, without any concrete evidence for such a phase transition, this explanation remains speculative.

In the following, we constrain ε within the framework of the standard glitch model, which requires a substantial superfluid component in the inner crust with $I_s/I > 1.6\%$. In our Scenarios B and C, when axions condense in the crust, the crust-core phase transition occurs at a baryon density below the neutron drip, and there is no region of coexistence of solid and superfluid matter in the crust. Consequently, glitches cannot be explained in the presence of an axion condensate at the surface of the star when the nuclear force is more attractive. Thus, within the standard glitch models, $\varepsilon < 0.27$ is ruled out for Scenario B and $\varepsilon < 0.61$ is ruled out for Scenario C provided that f_a is not so large that the surface of star has small θ due to the large domain wall. Even in the domain wall, the increasing nucleon mass brings matter below neutron drip before the interactions become sufficiently repulsive to force neutrons out of nuclei. This result is in part a consequence of the fact that in the ansatz we use in the RMF model, the nuclear force becomes monotonically more attractive as θ increases. If nuclear matter with moderate isospin asymmetry were only more attractive near $\theta = \pi$ and rapidly became repulsive for intermediate θ, it is possible that enough neutrons could be present in the domain wall to explain glitches when $m_a \ll 10^{-8}\,\mathrm{eV}$. This is an issue that warrants further exploration in light of the prediction from our MBPT calculation that neutron matter will be more repulsive at intermediate θ and the work of past authors [128–131] that showed that reducing the pion mass made nuclear interactions in neutron matter more repulsive in the vicinity of the physical pion mass (but not at significantly reduced pion mass, as in the axion condensed phase).

We estimate this critical f_a by treating the neutron star as a uniform sphere of saturation density matter. The approximation of constant density is conservative since most of the star is at a higher density than the reference density used but is also not particularly impactful since within this approximation $f_a^2 \propto n_B^s$ and n_B^s changes by only a factor of at most $3-5$ within the core of a $1.4\,M_\odot$ star. Within this constant density approximation, the maximum f_a can be found by solving an inhomogeneous Poisson's equation.

$$\nabla^2\theta = -\frac{1}{r_0^2}\frac{\sin\theta}{f(\theta)} \tag{2.38}$$

where r_0 is given by

$$r_0^{-2} = \frac{\sigma_N n_{sat}(1+\delta^{(\mathrm{loc})})}{f_a^2} - m_a^2\,. \tag{2.39}$$

In practice, m_a has a very small effect on this constraint for ε that are not very close to the QCD axion line, which this part of the constraint does not touch. In the regime of $m_a \ll 1/R_{NS} \simeq 10^{-10}\,\mathrm{eV}$, this can be solved by matching the surface boundary condition to the lowest energy configuration of a massless field, $\theta(r) = \theta_0 R_{NS}/r$, where θ_0 is the critical θ at which dripped neutrons can appear at positive pressure. The bound on f_a we find is below the value necessary for the system to be stable against condensation due to the large extent of the axion field. At the ε relevant for this part of the constraint, β-equilibrated matter at or above saturation density is unstable to axion condensation and the system can adiabatically evolve to its ground state. If a more detailed calculation of the nuclear forces shows that β-equilibrated matter becomes significantly more repulsive for intermediate θ before becoming attractive at large θ, the exact limits of this bound will need to be revisited but the findings will be qualitatively unchanged.

Table 2.7: Constraint on ε from observation of crust-based pulsar glitches for $m_a \gtrsim 10^{-8}\,\mathrm{eV}$.

	(A) $K_\sigma = 0$	(B) $K_\sigma = 0.08$	(C) $K_\sigma = 0.16$
Min. excluded ε	8.3×10^{-3}	0	0
Max. excluded ε	0.17	0.42	0.79

In Scenario A where dripped neutrons can appear in an axion condensed crust or in any scenario when the critical pressure occurs in the outer crust of a normal star, if the domain wall is large a significant number of neutrons can be present in the domain wall region. For this case, we limit $m_a > 10^{-8}\,\mathrm{eV}$ so that the domain wall has a thickness of $\mathcal{O}(10\,\mathrm{m})$, more than an order of magnitude smaller than is normally seen. Since the neutron superfluid mechanism for glitches as currently understood requires nearly all of the superfluid neutrons to participate in a normal star, a reduction this severe excludes this possibility. This applies for Scenario A for $0.0083 < \varepsilon < 0.17$, for Scenario B for $0.27 < 0.42$, and for Scenario C for $0.61 < \varepsilon < 0.79$.

Lacking a complete and detailed picture of the crust glitch mechanism, we refrain from making a concrete numerical estimate of exactly how many neutrons are necessary to be in tension with observations and rely on the fact that near the boundaries of our constraint the quantity of neutrons changes by many orders of magnitude for relatively small changes in axion parameters. Scenario B and C are particularly notable for the fact that the neutron dripped phase is completely absent for much of the parameter space. The constraint that the quantity of neutrons is reduced by less than an order of magnitude is shown for our three scenarios in Fig. 2.21. Table 2.7 shows the constraint on ε in our three scenarios for $m_a \gtrsim 10^{-8}\,\mathrm{eV}$, where, as before, the domain wall does not play an important role and the constraint only depends on ε. Note that in Fig. 2.21, there is a small notch in the constraint curves for Scenarios B and C at $m_a = 10^{-8}\,\mathrm{eV}$. While this is a small effect on the typical log scale for constraint plots, it is a relevant difference when assessing how close constraints come to the QCD axion line at large and small axion masses. It should be noted that only this region of larger axion masses can be confidently constrained within this scheme when using the $\mathbb{Z}_\mathcal{N}$ model, which will be discussed in greater detail in the next section.

2.6.4 $\mathbb{Z}_\mathcal{N}$ model

The discrete $\mathbb{Z}_\mathcal{N}$ symmetry proposed in Ref. [102] provides a concrete realization of the exceptionally light QCD axion. This model predicts a suppression factor ε of the axion mass for odd integer $\mathcal{N}$, given by

$$\varepsilon^{1/2} \equiv \frac{m_a}{m_a^{(\mathrm{QCD})}} \approx \sqrt{\frac{1}{\sqrt{\pi}} \mathcal{N}^{3/2} z^{\mathcal{N}-1} (1+z) \sqrt{1-z^2}} \approx \frac{1}{2^{\mathcal{N}/2 - \log \mathcal{N}}}, \tag{2.40}$$

where $z \equiv m_u/m_d$ and the large $\mathcal{N}$ limit has been taken [103]. For small $\mathcal{N}$, the $\mathbb{Z}_\mathcal{N}$ model results in a modest change to the axion mass: for $\mathcal{N} = 3$, $m_a/m_a^{(\mathrm{QCD})} = 0.94$. The first significant decrease comes

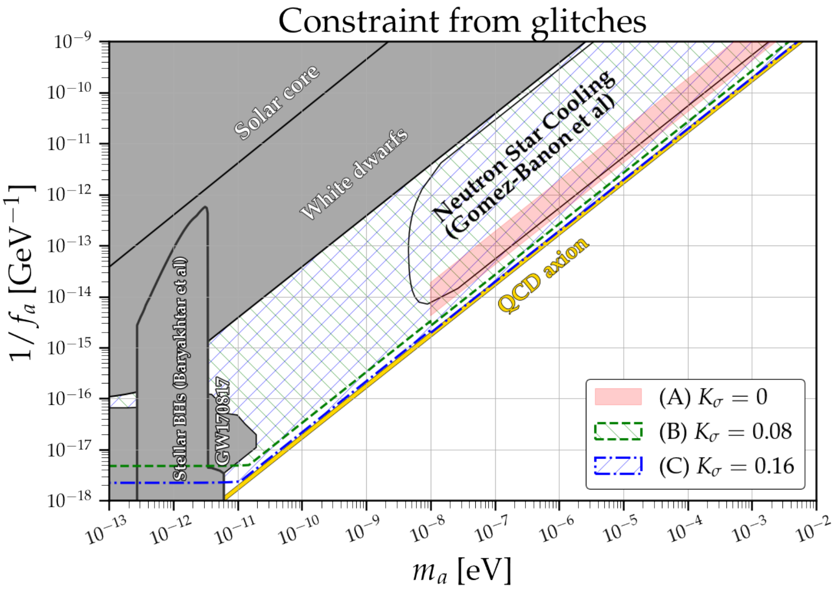

Figure 2.21: Constraint from observation of crust-based pulsar glitches in our three scenarios requiring the quantity of neutrons be reduced by less than an order of magnitude. Parameter space as in Fig. 2.18.

at $\mathcal{N} = 5$ giving $m_a/m_a^{(\mathrm{QCD})} = 0.65$ and $\mathcal{N} = 11$ corresponds to approximately an order of magnitude suppression.

In the $\mathbb{Z}_{\mathcal{N}}$ model for the exceptionally light QCD axion, the axion potential has a period of $2\pi/\mathcal{N}$ and the negative axion pressure is suppressed by an additional factor of $\mathcal{N}^2$ [102]. In the simple case where the domain wall connects $\theta = 0$ and $\theta = \pi$ smoothly and the axion mass is sufficiently large that the domain wall pressure is unimportant, the results are identical to our existing calculation but with a modified axion potential provided $\mathcal{N}$ is small enough that normal matter at saturation density is unstable to the nucleation of the $\theta = \pi$ phase. Thus, in the range $m_a \gtrsim 10^{-8}$ eV, the constraint on the $\mathbb{Z}_{\mathcal{N}}$ model parameter space can be inferred directly from the constraint on ε we have derived. The lower limit on $\mathcal{N}$ is determined from the difference in vacuum energy between the maximum at $\theta = \pi$ and minimum at $\theta = 0$ of the potential given in Ref. [103] since the dependence on the relationship between m_a and f_a and the change to the period of the axion potential is minimal in this region. This lower limit on $\mathcal{N}$ for the various effects and scenarios is given in Table 2.8. For $m_a \gtrsim 10^{-8}$ eV, the combined constraint is the same for all three scenarios, $\mathcal{N} \geq 19$. Combined with the upper limit from white dwarf of $\mathcal{N} \leq 31$ [96], this leaves a gap of $19 \leq \mathcal{N} \leq 31$. On the other hand, the upper limit on $\mathcal{N}$ is also determined by the conditions for the appearance of the domain wall in Tab. 2.3. Although $\mathcal{N} = 3$ and 5 appear to be constrained in Scenario A and $\mathcal{N} = 3$ appears to be constrained in Scenario B (see Table 2.8), for those choices of $\mathcal{N}$ and K_σ, the axion mass remains positive near $\theta = 0$ in the $\mathbb{Z}_{\mathcal{N}}$ model. Therefore, even though the ground state of matter is axion condensed, since matter at saturation is only metastable in these cases, it is conceivable that the axion mass squared is always positive near $\theta = 0$ anywhere in the neutron star, and these $\mathcal{N}$ cannot be conclusively excluded. However, it is possible that if axion condensation is favored at a sufficiently large density where the axion mass squared turns negative near $\theta = 0$, these $\mathcal{N}$ values could also be excluded in Scenarios A & B.

This might not be a complete story, if we were to only solve for the possible axion field profile inside a neutron star, while neglecting how neutron stars formed. For large $\mathcal{N}$, when only modifications to the nucleon masses are included, it was pointed out in Ref. [96] that the ground state of matter below the critical density is no longer $\theta = 0$ but $\theta = (\mathcal{N}-1)\pi/\mathcal{N}$, resulting in a vanishing axion potential but lighter nucleon masses . If this ground state is found, the full crust and envelope could be present at $\theta = (\mathcal{N}-1)\pi/\mathcal{N}$ and the constraint from neutron star cooling would not apply. In Scenario A, the constraints from crust thermal relaxation and glitches also likely do not apply in this case since a normal crust would be present. When nuclear interactions, and their dependence on θ are taken into account, the conclusion of Ref. [96] can be modified. In Scenarios B and C, the $\mathbb{Z}_{\mathcal{N}}$ model may still be excluded since the lack of a dripped neutron phase precludes crust-based glitches. Additionally, in Scenarios B and C, the dependence of the free energy as a function of θ is modified and the minimum $\mathcal{N}$ where the $\theta = \pi$ state is stable (instead of $\theta = (\mathcal{N}-1)\pi/\mathcal{N}$) at zero pressure decreases. In our Scenario C, for $\mathcal{N} = 17\,\&\,19$, the ground state remains at $\theta = \pi$ at zero pressure, and is disfavored as a result.

A better understanding of the nuclear physics at $\theta = \pi$ is necessary to provide a constraint on the $\mathbb{Z}_{\mathcal{N}}$ model that is independent of our knowledge about how neutron stars are created, and how the axion condensed phase could form following a supernova. On the other hand, it is unclear how a profile with $\theta = \pi$ in the core of a neutron star, and $\theta = (\mathcal{N}-1)\pi/\mathcal{N}$ in most of inner and outer crust could form in the event of neutron star formation in, for example, a core collapse supernova. In an event of a supernova, as the density of the core grows past the critical density in Eq. 2.11, a region of $\theta = \pi$ emerges in the core, with a domain wall interpolating between the original $\theta = 0$ region and the newly formed $\theta = \pi$ region. This domain wall, in particular the part that interpolates between $\theta = (\mathcal{N}-1)\pi/\mathcal{N}$ and $\theta = 0$, will need to expand significantly such that most of the inner and outer crust is at $\theta = (\mathcal{N}-1)\pi/\mathcal{N}$ (see Fig. 8 of [96]). During this process, as described in [109], the domain wall gains energy that is $\mathcal{O}(\sigma_N/m_n)$, roughly 5% of the total mass energy of the progenitor star, or at least the total mass energy of the inner and outer crust of the proto-neutron star. This energy, as outlined in [109], will be released slowly, heating up the medium surrounding the neutron star, leading to persistent bright X-ray/optical emissions from the supernova remnant that is not observed. Whereas it is possible that the axion field profile form nearly at rest and are not subsequently accelerated outward, it is hard to imagine how the field profile could gain this much energy through interactions with the baryons, while at the same time, experience exact the right amount of friction to land exactly at the boundary of the outer crust in every single supernova we observed [109, 112]. As a result, we do not consider this scenario further.

For axion masses below $10^{-8}\,\text{eV}$, the distribution and properties of nuclear matter in the axion domain wall region are significantly affected by the change of the period of the axion potential in the $\mathbb{Z}_{\mathcal{N}}$

Table 2.8: Minimum allowed $\mathcal{N}$ in the $\mathbb{Z}_\mathcal{N}$ model for $m_a \gtrsim 10^{-8}$ eV when the domain wall connects $\theta = 0$ and $\theta = \pi$. In Scenario A, the envelope constraint also permits $\mathcal{N} = 3$. $\mathcal{N}$ must be an odd integer for the axion to solve the strong-CP problem in these models. Note that these bounds assume the inner region is at $\theta = \pi$, as is preferred in a dynamical formation of the neutron star [109], rather than the critical density minimum at $\theta = (\mathcal{N} - 1)\pi/\mathcal{N}$. See text for further discussion.

Constraint	(A) $K_\sigma = 0$	(B) $K_\sigma = 0.08$	(C) $K_\sigma = 0.16$
Crust thickness	7	9	7
Envelope	19	19	19
Glitches	7	5	5

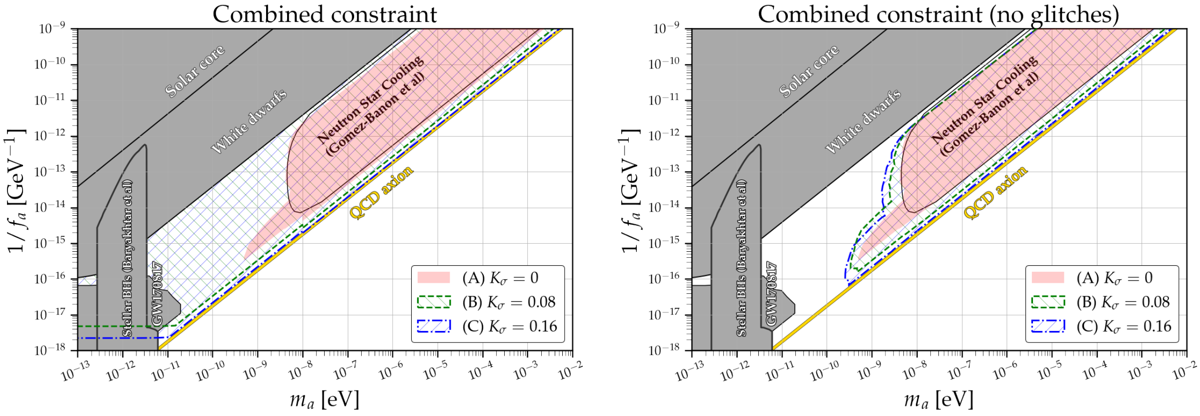

Figure 2.22: Combined constraint from crust thermal relaxation (Sec. 2.6.1), neutron star cooling (Sec. 2.6.2), and pulsar glitches (Sec. 2.6.3) (left) and without glitches (right) in our three scenarios accounting for modification of nuclear interactions in $\theta = \pi$ matter. In Scenario A, neutron star cooling is the dominant signature for $\varepsilon \ll 1$ while crust thermal relaxation and pulsar glitches set the strongest constraints for $\varepsilon \sim 1$. For Scenarios B and C, the glitch constraint covers the entire excluded parameter space. We consider the pink shaded region (Scenario A, no modification to nuclear interactions) to be the conservative benchmark constraint. Increasingly attractive nuclear interactions in axion condensed matter (Scenarios B and C) would cause the modification of crust structure to occur closer to the QCD axion line. Parameter space as in Fig. 2.18.

model, which requires further study. The parameter space in the gaps, as well as the lower axion mass region, might be probed by other considerations of the formation of neutron stars during a supernova explosion [109]. We leave a more detailed study of the $\mathbb{Z}_\mathcal{N}$ model to future work.

2.7 Conclusions

In this paper, we present a comprehensive study of the neutron star equation of state in the presence of exceptionally light QCD axions. In dense objects, the axion potential receives corrections proportional to the nucleon density due to axion couplings to QCD. For a wide range of ε (see Eq. (2.4)), a neutron star is both dense enough such that the minimum of the axion potential shifts to $\theta = \pi$, and large enough such that it is energetically favorable for a $\theta = \pi$ region to emerge at the center of the star and an axion domain wall profile between the $\theta = \pi$ inside and $\theta = 0$ outside to develop. In the $\theta = \pi$ region, there are three main effects, namely, a negative axionic pressure of order $-m_a^2 f_a^2$, lighter nucleon masses, and a decrease of the pion mass from 138 MeV to about 80 MeV. The latter can lead to the modification of nuclear interactions.

We study these changes with Chiral Effective Field Theory and Relativistic Mean Field Theory. The results of ChiEFT are somewhat inconclusive at $\theta = \pi$ and a pion mass of about 80 MeV, with the convergence of many-body perturbation theory becoming worse as the pion mass is decreased. Nevertheless, an initial assessment indicates that the nuclear force may become significantly more attractive at $\theta = \pi$ leading to self-bound neutron matter and axion condensation at $n_B \simeq n_{\rm sat}$ even for $\varepsilon \simeq 1$. We model this reduction of the pion mass in RMFT with a decrease of the σ mass ($K_\sigma > 0$, see definition given by Eq. (2.21), Table 2.1, and related discussion), resulting in an increase of the strength of the attractive part of the nuclear interaction. Using RMFT, we calculate modifications to the equation of state of nuclear matter at different densities at $\theta = \pi$. Combining these modifications to the nucleon masses and nuclear interaction strength, the negative axion pressure, axion domain wall profile, and gravity, we compute the neutron star equation of state and structure at different m_a and ε shown in Figs. 2.9, 2.11, and 2.12. Qualitatively, the negative axion pressure, the lighter nucleon masses, and the more attractive nuclear force at $\theta = \pi$ lead to neutron stars with a reduced or missing inner crust and a much reduced outer crust that is partially or entirely at a negative pressure in the axion domain wall for $\varepsilon \lesssim 0.1$. Our preliminary investigations of the $m_\pi-$dependence of the nuclear EOS in ChiEFT suggest the intriguing possibility of axion condensation for $\varepsilon \simeq 1$ at $n_B \lesssim 2n_{sat}$ and will be explored separately in future work. Our future work will also more closely examine the m_π-dependence of the underlying nuclear interactions, which is generally not well understood, especially those terms that are typically assumed to just renormalize the low energy constants.

This finding has observational consequences that are significantly constrained by isolated neutron star cooling (also recently considered in Ref. [99]), crust thermal relaxation, and pulsar glitches. The combination of these constraints is shown in Fig. 2.22 with and without pulsar glitches as the pulsar glitch mechanism is the least understood of these three observational constraints and most amenable to alternative explanations, difficult to fully justify as those may be. These all depend primarily on the equation of state at $n_B \lesssim n_{\rm sat}$ where our treatment of the interaction between axions and nucleons is robust. As the most conservative bound, Scenario A in the figure shall be considered as the benchmark constraint, while Scenarios B and C shall be considered as a generous estimate of the uncertainty and possibly stronger constraints to be drawn once the θ-dependence of QCD has been explored in greater detail. The possibility that much of the parameter space can be excluded by a lack of dripped neutrons in the crust invalidating the crust-based glitch mechanism for pulsars is an intriguing prediction which warrants further exploration. In particular, the pion mass dependence of the low energy constants in ChiEFT must be determined from Lattice QCD and the convergence of nuclear many-body perturbation theory at decreased pion mass must be addressed. Additionally, in the domain wall region, parity-violating nuclear interactions may become relevant and should be included in a detailed treatment in ChiEFT. More details are available in App. A.

We also suggest two intriguing observational consequences that require further observational and theoretical investigation, also previously noted in Ref. [104] (see also Ref. [141] for similar effects of scalar fields with Yukawa couplings to SM fermions). As shown in Fig. 2.13, the mass-radius relation of neutron stars with a $\theta = \pi$ core is indicative of rapid stiffening of the equation of state at intermediate density. Additionally, for some ε there are missing crust layers, resulting in very small radii for low-mass neutron stars, similar to strange quark stars. With data from the NICER x-ray observations as well as neutron star merger measurements with LVK and future gravitational wave observatories, a precisely known mass-radius relation would strongly constrain the presence or absence of a $\theta = \pi$ core. A second intriguing possibility is self-bound objects at $\theta = \pi$ which we call π-balls, with densities close to nuclear density and stabilized by the attractive axion potential rather than gravity. These objects can have different masses and sizes, ranging from planet to white dwarf masses. Further studies are required to understand their formation in violent events such as supernovae or neutron star mergers, their growth in the interstellar and intergalactic medium, as well as the resulting observational signatures.

Chapter 3

Does the QCD axion condense in neutron stars?

3.1 Introduction

In the previous chapter, we discussed constraints on exceptionally light QCD axions (axions with the same coupling as the QCD axion but a lighter mass) from neutron star observations. An axion condensate in dense matter is equivalent to varying the CP violating angle θ in the QCD Lagrangian, resulting in lighter pions and nucleons. Since exceptionally light axions condense at densities below saturation density, constraints can be qualitatively understood in terms of properties of the crust. An axion with a mass at the QCD prediction, however, would be expected to condense above twice saturation density when nuclear interactions are neglected. At these densities, interactions are crucial to understand whether such an axion will condense and the uncertainties in our previous calculation (see. Fig. 2.6) are unacceptably large in order to make any concrete predictions. The focus of this chapter will be on what steps we must take to reduce this uncertainty so that we can make robust predictions about the QCD axion. Final results will be deferred to future publications, but here we describe the steps that must be taken in order to address this problem.

Chiral EFT (χEFT) is an expansion for nuclear potentials with robust and systematically improvable error estimates. Since it is an expansion in momentum, there is a maximum density of $1.5 - 2n_{sat}$ below which the theory is applicable. While many aspects of χEFT carry over directly to finite θ with modified hadron masses, some new ingredients are necessary. Isospin breaking effects are amplified in the presence of an axion condensate, requiring the calculation of operators typically neglected in χEFT because isospin breaking is weak at the physical pion mass. To understanding the domain wall that connects the outside of the star at $\theta = 0$ to the inner core at $\theta = \pi$, it is also necessary to consider CP violating effects. CP violation results in a new operator for three nucleon forces (3NFs) which, along with D_2 (and the related F_2) discussed in the previous chapter and in greater detail in this chapter, contribute to chiral 3NFs at N2LO and should be included in our calculations.

In the many body calculation of the previous chapter, the energy of neutron matter was found to have significant cutoff dependence. Ideally any EFT calculation should depend on its regulator only within the error estimate of the EFT truncation, so this is concerning. In our prior treatment, short-range forces with pion mass dependence had unintended chaotic running with the cutoff because we used a standard chiral force tuned to work well only at the physical pion mass. This resulted in excessive cutoff dependence, at odds with standard theoretical predictions. Regulator artifacts when the pion mass is varied need to be better understood in order to diminish or eliminate this difficulty.

A careful treatment of the chiral forces in a fully consistent nuclear model reveals a crucial fact not relevant for the $\mathbb{Z}_{\mathcal{N}}$ model (described in detail in the introduction to Chap. 2): when the QCD axion condenses it is unavoidable that chiral symmetry be restored. The poses a challenge as χEFT is not a valid theory in the chirally symmetric phase but also an opportunity to find new constraints if the chirally symmetric phase is accessible below twice nuclear density.

First, we begin in Sec. 3.2 with a summary of the relevant features of χEFT needed to understand the problem of θ dependence in low energy nuclear physics. This is followed by Sec. 3.3 summarizing the results of prior work by ourselves and other authors discussing the qualitative features of the axion condensed phase and nuclear interactions near threshold. One deficiency of this past work is that it focused primarily on θ dependence arising from explicit dependence on the pion mass. To consider the full range of θ dependence, we must consider the full range of quark mass dependent operators and how they evolve with θ. The structure of these operators and which are relevant at N2LO is discussed in Sec. 3.4 while Sec. 3.5 specifically addresses operators that break isospin or violate CP. Section 3.7 addresses steps needed to reduce regulator dependence in our many body calculation. Sec. 3.6 discusses new 3NFs required by chiral symmetry and renormalizability that arise at N2LO. Finally, Sec. 3.8 discusses the relevance of chiral symmetry restoration for the study of the QCD axion in neutron stars.

3.2 Chiral EFT in brief

Chiral EFT is an effective theory of nucleons and pions with a heavy scale set by the QCD scale Λ_{QCD}, approximately 1 GeV. Equivalently, the heavy scale is approximately the nucleon mass, the mass of the heavy SU(2) mesons (the ω and the ρ), or the loop suppression in diagrammatic analysis of potentials involving pions (roughly $4\pi f_\pi$ for $f_\pi = 92.4\,\text{MeV}$). The light scale of the EFT is either the momentum (approximately 260 MeV in isospin symmetric nuclear matter at saturation density) or the pion mass (138 MeV when averaged between neutral and charged pions). The pions appear as light degrees of freedom because they are the pseudo-Goldstone bosons of broken chiral symmetry. This is based on the observation that the two flavor QCD Lagrangian is nearly invariant with respect to transformations of the quarks

$$q \to \exp\Big[i\alpha_0 + i\gamma^5\beta_0 + i\vec{\alpha}\cdot\vec{\tau} + i\gamma^5\vec{\beta}\cdot\vec{\tau}\Big]q \tag{3.1}$$

where $\vec{\alpha}$ and $\vec{\beta}$ are independent three-vectors, γ^5 differentiates between left- and right-handed quarks and τ is a vector of Pauli matrices in isospin space. The chiral symmetry associated with β is violated in the Lagrangian only by the small quark masses, $m_{u,d} \ll \Lambda_{\mathrm{QCD}}$. This appears to give the UV theory a SU(2) × SU(2) × $U(1)$ × $U(1)$ symmetry, but the low energy theory is organized into multiplets of SU(2) with a single conserved charged and no degeneracy between multiplets. Note for example that there is only one isospin doublet of nucleons and that the two isospin triplets (the pions and the ρ) have completely different mass scales. The symmetry of the system has been broken according to the following.

$$\mathrm{SU}(2)_L \times \mathrm{SU}(2)_R \times \mathrm{U}(1)_L \times \mathrm{U}(1)_R \to \mathrm{SU}(2)_V \times \mathrm{U}(1)_V \tag{3.2}$$

This corresponds to a spontaneously broken $\mathrm{SU}(2)_A$ and an anomalous $\mathrm{U}(1)_A$ where V (vector) corresponds to $\alpha_i = \beta_i$ and A (axial) corresponds to $\alpha_i = -\beta_i$. The remaining $\mathrm{U}(1)_V$ symmetry corresponds to conserved baryon number and $\mathrm{SU}(2)_V$ corresponds to isospin symmetry. Since there are three spontaneously broken generators, we expect the low energy theory to have three Goldstone bosons. These are precisely the three pions which have a small non-zero mass because the original symmetry is weakly broken by the non-zero quark masses. The broken $\mathrm{U}(1)_A$ does not have an associated Goldstone boson because it is anomalous and is not a good symmetry in the UV or the IR.

The prescription of Weinberg for power counting the nuclear potential, also known as naive dimensional analysis (NDA), is to associate to any Feynman diagram a power $(p/\Lambda)^n$ where p represents either powers of the momentum or powers of the pion mass and Λ is the heavy scale. A careful analysis of the structure of operators that respect the chiral symmetry and the topology of Feynman diagrams gives the following method for counting the order of any diagram: [168]

$$\nu = -4 + 2N + 2L + \sum_i V_i \Delta_i \tag{3.3}$$

where N is the number of nucleons participating in the diagram, L is the number of loops, Δ_i is the power of the i-th vertex in the diagram and V_i is the multiplicity of vertices with power Δ_i. This simple formula demonstrates the origin of the empirical observation that two nucleon forces dominate the energy of nuclear systems while 3NFs and higher body forces are suppressed. When considering the structure of a given vertex, the following rule is used to calculate the value of Δ_i,

$$\Delta_i = d_i + \frac{1}{2}n_i - 2 \tag{3.4}$$

where d_i is the number of derivatives in the operator (quark mass insertions count as two derivatives) and n_i is the number of nucleon legs in the vertex (count both incoming and outgoing). For example, the axial vector coupling

$$\mathcal{L}_{\text{AV}} = -\frac{g_A}{2f_\pi}\bar{N}\tau \cdot (\sigma \cdot \nabla)\pi N \tag{3.5}$$

is $\Delta = 0$ ($d_i = 1$ and $n_i = 2$) but the leading contribution to the pion mass dependence of the nucleon masses

$$\mathcal{L} \supset c_1 \bar{N} N m_\pi^2 \left(1 - \frac{\pi^2}{2\pi^2} + ...\right) \tag{3.6}$$

is $\Delta = 1$ ($d_i = 2$ and $n_i = 2$).

The relatively simple prescription of NDA has been used to great effect for a wide range of applications of nuclear forces. Scattering phase shifts in peripheral partial waves where no LECs contribute (i.e. there are no free parameters to improve the fit to data) are successfully reproduced by chiral forces [133, 169]. Weinberg eigenvalues have been calculated for chiral potentials to verify that they are perturbative (see Ref. [170] for a detailed discussion), but practical computational issues presently limit the range of cutoffs over which calculations can be performed and the possibility of lingering regulator artifacts remains an issue of concern. Chiral forces based on NDA have been used to reproduce the binding energy of nuclei [171–173] and to predict properties of dense matter [170, 174, 175]. See Fig. 3.1 for an example of such a calculation for neutron matter. However, NDA experiences some difficulties when θ dependence becomes involved. As will be discussed in greater detail in Secs. 3.4, 3.5, and 3.6, sometimes this power counting needs to be modified for certain applications.

It should be noted that in calculations of forces between nucleons, this is an expansion for nuclear potentials, not amplitudes. Nucleon propagators should in principle be summed to all orders in vacuum (in the two nucleon system in momentum space, equivalent to solving the Lippmann-Schwinger equation). Calculations of individual diagrams should only have off-shell nucleons and should never include summing over nucleon poles as those will be included when nucleons are summed to all orders. For an extensive discussion of the convergence of χEFT in matter, see Ref. [170]. For contrast with a theory where the EFT is applied to amplitudes rather than potentials, see Ref. [126].

3.3 Nuclear observables near threshold

In dilute matter ($k_F \to 0$), the energy associated with a system of nucleons is contained in the masses of the nucleons, the s-wave scattering lengths of the NN interaction, and the energy of any bound states.

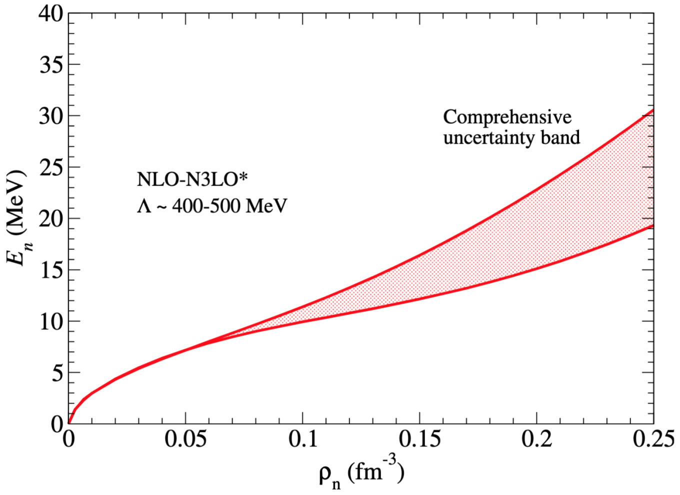

Figure 3.1: Energy per baryon in pure neutron matter with N3LO chiral forces. The error band includes theory uncertainties from the convergence of the many body expansion, truncation at finite chiral order, and resolution scale. Figure from Ref. [175]

The masses of baryons and mesons is typically decreased for finite θ [114, 115]. The θ dependence of nuclear physics can be calculated by noting that the θ term in the QCD Lagrangian can be eliminated by a chiral rotation of the quark fields. In the limit $m_{u,d} \ll m_s$, the transformation $u \to \exp\{(i\gamma_5\phi_u)\}u$ and $d \to \exp\{(i\gamma_5\phi_d)\}d$ where $\phi_u + \phi_d = \theta$ fully captures the effect of $\theta \neq 0$. When considering only $\theta = 0$ and $\theta = \pi$, the effect of finite θ is to flip the sign of the lightest quark. At intermediate θ, more complicated dependencies that violate CP appear which will be discussed in Sec. 3.5. From the relation $m_\pi^2 \propto m_u + m_d$, the θ dependence of the mass of the neutral pion is [115]

$$m_\pi^2(\theta) = f(\theta) m_\pi^2(\theta = 0) \tag{3.7}$$

where

$$f(\theta) = \sqrt{1 - \frac{4m_u m_d}{(m_u + m_d)^2}\sin^2\frac{\theta}{2}}\,. \tag{3.8}$$

Since long range nuclear forces are carried by pions which produce attraction at intermediate range, it is generally expected that finite θ will produce longer range forces which are possibly more attractive. The only other hadrons to explicitly appear in standard χEFT are the nucleons. Their dependence can be parameterized as

$$\begin{aligned} m_n(\theta) &= m_n(\theta = 0) + \sigma_{\pi N}\left(f(\theta) - 1\right)\left(1 - \frac{\Delta\sigma}{\sigma_N f(\theta)}\right), \\ m_p(\theta) &= m_p(\theta = 0) + \sigma_{\pi N}\left(f(\theta) - 1\right)\left(1 + \frac{\Delta\sigma}{\sigma_N f(\theta)}\right), \end{aligned} \tag{3.9}$$

where $\sigma_{\pi N}$ is the isoscalar nucleon sigma term and $\Delta\sigma$ is the isovector sigma term. Despite much interest and effort the isoscalar nucleon sigma term is not precisely known and the best estimates from Lattice

Table 3.1: Quark mass dependence of the scattering lengths and the deuteron binding energy $K_{\mathcal{O}}$, as defined in Eq. (3.10).

Reference	K_{a1S0}	K_{a3S1}	K_{deut}
Epelbaum et al. [125]	5 ± 5	1.1 ± 0.6	-2.8 ± 1.2
Beane et al. [124]	2.4 ± 3.0	3.0 ± 3.5	-7 ± 6
Berengut et al. [118]	$2.3^{+1.6}_{-1.5}$	$0.32^{+0.17}_{-0.18}$	$-0.86^{+0.45}_{-0.50}$

QCD and phenomenology indicate that $\sigma_N \simeq 50 \pm 10$ MeV [119]. The value of $\Delta\sigma$ can be inferred from the mass splitting of baryons. Determining $\Delta\sigma$ from the mass splitting of the neutron and proton gives $\Delta\sigma = (m_n - m_p)_{\text{non-em}}/2 \simeq 1\,\text{MeV}$ [120]. As we will see, the leading contributions to $\sigma_{\pi N}$ and $\Delta\sigma$ appear in the $\Delta = 1$ chiral Lagrangian from the operators proportional to c_1 and c_5 respectively.

In leading order (LO) χEFT, the NN potential is composed of a long-range one-pion exchange (OPE) and short-range NN contact interaction. While the dependence of all parameters in the OPE is known, the leading contact (often called C_0) gets a contribution from the operator D_2 (to be discussed throughout this chapter), whose value is not well-constrained. This gives an effective coupling of $C_0 + D_2 m_\pi^2$ whose separate contributions cannot be disentangled by NN scattering data. The effects of D_2 on the scattering length and phase shifts have been studied in earlier work [124, 125].

In Ref. [125], the authors find that with reduced pion mass, the deuteron is more bound and the s-wave scattering lengths decrease in magnitude. While uncertainties in the size of D_2 are sufficient that a bound $^1S_0$ state in the axion condensed phase is not out of the question, this is a more exotic scenario that we will not consider. If the $^1S_0$ state is bound, this likely has little relevance for matter above saturation density.[1] To quantify the quark mass dependence of an observable $\mathcal{O}$, the authors define the logarithmic derivative at the physical point

$$K_{\mathcal{O}} = \frac{m_q}{\mathcal{O}} \left(\frac{\mathrm{d}\mathcal{O}}{\mathrm{d}m_q} \right)_{\text{phys}} \simeq \left(\frac{m_\pi^2}{\mathcal{O}} \frac{\mathrm{d}\mathcal{O}}{\mathrm{d}m_\pi^2} \right)_{m_\pi = m_\pi^{\text{phys}}} , \tag{3.10}$$

since at leading order in χEFT $m_\pi^2 \propto m_q$. The pion mass dependence of the $^1S_0$ and $^3S_1$ scattering lengths and the deuteron binding energy are captured by the values of K_{a1S0}, K_{a3S1}, and K_{deut}, and their values obtained in earlier studies are shown in Table 3.1. For more details on the assumptions of these studies, see Sec. 2.3 of the previous chapter.

The results of these studies imply that the $^3S_1$ channel that has a positive scattering length becomes more attractive at finite θ (negative K_{deut} and positive K_{a3S1}). Since the $^1S_0$ channel has a negative scattering length, positive K_{a1S0} corresponds to a less attractive $^1S_0$ interaction. Thus, in dilute neutron matter where spin singlet interactions at low momentum dominate, matter will be less bound at finite θ. In contrast, symmetric nuclear matter with an equal number of protons and neutrons at low density is

---

[1] It would, however, place strong constraints on the presence of an axion condensate at the time of Big Bang nucleosynthesis. At the densities expected when $T \simeq B_d$ for B_d the deuteron binding energy, there is no hope of the QCD axion condensing so this remains relevant only for exceptionally light axions.

dominated by spin triplet interactions, and greater nuclear binding would be predicted at finite θ. While this is true in the limit of very dilute matter where s-wave interactions give the leading contribution to the nuclear force, when the pion mass is reduced higher partial waves are generically enhanced [127]. The attraction in the ${}^3P_0$ and ${}^3P_2$ channels is enhanced and the repulsion in the ${}^1P_1$ channel is reduced [125]. Since the QCD axion is expected to condense above saturation density if it condenses at all, these higher partial wave interactions surely cannot be neglected and nuclear observables at threshold will not contain the full dependence of nuclear interaction energy on θ necessary to study the QCD axion in neutron stars.

3.4 Quark mass dependence in Chiral EFT

Quark mass dependence appears in χEFT via insertions of the following operator.

$$\frac{\chi_\pm}{B} = u\mathcal{M}_q^\dagger u \pm u^\dagger \mathcal{M}_q u^\dagger \tag{3.11}$$

where $\mathcal{M}_q = \mathrm{diag}(m_u, m_d)$ is the quark mass matrix, B is an order Λ_{QCD} constant that sets the size of the pion mass, $u^2 = U$, and $U = \exp[i\tau \cdot \pi / f_\pi]$ contains the pion fields. To determine the full quark mass dependence of nuclear forces, we need to consider the full range of dependencies these operators can generate, not just $\langle \chi_+ \rangle \propto m_\pi^2$ (where $\langle \cdot \rangle$ means a trace in isospin space). This simple dependency contributes to almost all of the terms considered in Chap. 2 ($\sigma_{\pi N}$, D_2, the pion mass, ℓ_4, and the axion vacuum potential itself). Useful expansions of $\chi_\pm$ to two pion fields are given by

$$\chi_+ = \frac{2(m_\pi^{\mathrm{phys}})^2}{\bar{m}^{\mathrm{phys}}}\left[\mathrm{Re}[\bar{m}]\left(1 - \frac{\pi^2}{2f_\pi^2}\right) + \mathrm{Re}[\delta m]\left(\tau_3 - \frac{1}{2}\frac{\pi_0(\tau\cdot\pi)}{f_\pi^2}\right) + \mathrm{Im}[\bar{m}]\tau \cdot \frac{\pi}{f_\pi}\right] \tag{3.12}$$

and

$$\chi_- = \frac{2i(m_\pi^{\mathrm{phys}})^2}{\bar{m}^{\mathrm{phys}}}\left[\mathrm{Re}[\bar{m}]\left(-\tau \cdot \frac{\pi}{f_\pi}\right) + \mathrm{Re}[\delta m]\left(-\frac{\pi_0}{f_\pi}\right) + \mathrm{Im}[\bar{m}]\left(1 - \frac{\pi^2}{4f_\pi^2}\right)\right] \tag{3.13}$$

where $\bar{m} = m_u + m_d$, $\delta m = m_u - m_d$, and terms without Pauli matrices have an implied identity matrix in isospin space. $\mathrm{Im}[\delta m]$ contributions are omitted because they cancel in the two flavor case and are $\mathcal{O}(m_{u,d}/m_s)$ when strange quarks are included. The various quark mass combinations are modified in the axion condensed phase as follows [115].

$$\mathrm{Re}[\bar{m}] = \bar{m} f(\theta) \tag{3.14}$$

$$\mathrm{Re}[\delta m] = \frac{\delta m}{f(\theta)} \tag{3.15}$$

$$\mathrm{Im}[\bar{m}] = \frac{2m_u m_d}{m_u + m_d}\frac{\sin\theta}{f(\theta)} \tag{3.16}$$

$$\mathrm{Im}[\delta m] = 0\,. \tag{3.17}$$

Recalling that $f(\pi) \simeq 1/3$, these dependencies reveal a necessary modification to NDA when analyzing θ dependence of nuclear forces. When comparing the shift from $\theta = 0$ to $\theta = \pi$, a term that scales as $(\mathrm{Re}[\bar{m}])^n$ will introduce a *correction* that scales as roughly $(1/3^n - 1)$. As n becomes large, the size of this correction is bounded. In contrast, a term that scales as $(\mathrm{Re}[\delta m])^n$ will cause a correction scaling as $(3^n - 1)$, which is not bounded as n becomes large. As a result, isospin breaking terms that are normally neglected in chiral forces must be included because their relative importance is magnified when considering *corrections* from finite θ, even if their absolute size remains small. Indeed, terms with quark mass dependence should be systematically analyzed to determine which operators, if any, must be promoted to a lower order in the chiral expansion in order to accurately capture their relevance. The issue of isospin breaking in the pion masses will be addressed later in this section while new isospin breaking forces that need to be promoted will be addressed in Sec. 3.5.

The full set of quark mass dependent operators we need to consider at N2LO are given by the following terms.

$$\begin{aligned}\mathcal{L} \supset \frac{f_\pi^2}{4}\langle\chi_+\rangle + c_1\langle\chi_+\rangle\bar{N}N + c_5\bar{N}(\chi_+ - \langle\chi_+\rangle/2)N + \frac{\ell_4}{4}\langle\chi_+\rangle\langle D_\mu U^\dagger D^\mu U\rangle - \frac{\ell_7}{16}\langle\chi_-\rangle^2 \\ - \frac{ic_F}{8}\langle\chi_-\rangle\left[\bar{N}\sigma N\cdot\nabla(\bar{N}N) + \frac{1}{3}\bar{N}\sigma\tau N\cdot\nabla(\bar{N}\tau N)\right] - \frac{D_2}{8}\langle\chi_+\rangle(\bar{N}N)^2\end{aligned} \tag{3.18}$$

The first two terms of Eq. (3.18) when expanded give the familiar contribution to the Hamiltonian

$$\mathcal{H} \supset -f_\pi^2 m_\pi^2 f(\theta) + \frac{1}{2}m_\pi^2 f(\theta)\vec{\pi}\cdot\vec{\pi} - c_1 m_\pi^2 f(\theta)N^\dagger N\,. \tag{3.19}$$

The term proportional to c_5 in Eq. (3.18) is a standard term in the $\Delta = 1$ chiral Lagrangian though it is typically neglected because it is small. The term with ℓ_4 is responsible for the pion mass dependence of f_π, ℓ_7 provides the leading strong correction to the pion mass splitting, and c_F is a new operator first proposed in Ref. [176] that will be discussed in greater detail in Secs. 3.5 and 3.6. While there are additional terms in the $\Delta = 2$ Lagrangian for pions with quark mass dependence other than ℓ_4 and ℓ_7, these are the only two that we need consider at this order because ℓ_4 introduces a wavefunction renormalization on the pions and ℓ_7 is isospin breaking. The wavefunction renormalization from ℓ_4 manifests as pion mass dependence for f_π.

$$f_\pi(m_\pi) = f_0 + \frac{\ell_4 m_\pi^2}{16\pi^2 f_0} \tag{3.20}$$

where $f_0 \simeq 86.2\,\mathrm{MeV}$ is the value of f_π in the chiral limit. Other terms with pion mass dependence involving nucleons do not arise until the $\Delta = 2$ Lagrangian (d_5, d_{16}, d_{17}, d_{18}, and d_{19}). A subset of these terms were addressed in Ref. [115] and they are all enumerated in App. A. The only terms potentially relevant at N2LO are generated by the following vertices (apart from the regular Golberger-Treiman discrepancy, accounted for in our choice of g_A[2])

$$V_{\pi N} \supset (d_{18}+2d_{19})q\cdot\sigma m_\pi^2\left(\frac{m_d-m_u}{m_d+m_u}\frac{1}{f(\theta)}\frac{\pi_0}{f_\pi}+\frac{1}{4}\frac{2m_um_d}{(m_u+m_d)^2}\frac{\sin(\theta)}{f(\theta)}\frac{\pi^2}{f_\pi^2}\right). \tag{3.21}$$

The first term is an isospin breaking contribution to the Golberger-Treiman discrepancy and is in principle N2LO while the second enters at $\mathcal{O}(p^5)$ in NN and 3N forces, possibly of marginal relevance after isospin breaking enhancement. The current laboratory data gives a value for the combination $d_{18}+2d_{19}$ that is consistent with zero, so we shall neglect this term [177].

Implementing the leading corrections to the pion mass splitting is straightforward since, for the modifications we consider, corrections to the ρ mass are negligible (approximately 2% in the axion condensed phase [116,117]). At this order, the electromagnetic contribution to the mass squared splitting of the charged pions from the isospin symmetric pion mass is constant. Note that since the overall pion mass is reduced, a constant mass squared splitting leads to a larger absolute splitting in the axion condensed phase. The leading strong correction comes from the term proportional to ℓ_7 [178,179] which gives rise to a shift to the neutral pion mass of

$$\delta m_{\pi_0}^2 = -2\frac{\ell_7}{f(\theta)^2}\left(\frac{(m_\pi^{\text{phys}})^2\delta m}{\bar{m}f_\pi}\right)^2 \tag{3.22}$$

Using these scaling relations along with modern lattice results [180] for the size of the strong and electromagnetic contributions to the pion mass splitting gives

$$m_{\chi PT} = \sqrt{f(\theta)}\times 135.18\,\text{MeV} \tag{3.23}$$

$$\sqrt{m_{\pi\pm}^2-m_{\chi\text{PT}}^2} = 34.73\,\text{MeV} \tag{3.24}$$

$$\sqrt{m_{\chi\text{PT}}^2-m_{\pi_0}^2} = \frac{7.35\,\text{MeV}}{f(\theta)} \tag{3.25}$$

where $m_{\chi PT}$ is the unsplit pion mass that appears explicitly in the Lagrangian in terms like $\sigma_{\pi N}$, c_1, D_2, and corrections to f_π. In the axion condensed phase, this gives a neutral pion mass of 78.76 MeV, a charged pion mass of 88.46 MeV, and a Lagrangian pion mass of 81.36 MeV. The average pion mass to use in propagators is 85.23 MeV. The correction to a term proportional to m_π^2 in the $I=1$ np channel scales as follows.

$$\frac{2m_{\pi\pm}^2-m_{\pi_0}^2-m_{\chi PT}^2}{m_{\chi PT}^2} \simeq \frac{0.132}{f(\theta)}+\frac{0.003}{f(\theta)^3} \tag{3.26}$$

When $f(\theta)=1$, this error is approximately $\mathcal{O}(p^2/\Lambda_\chi^2)$ and can be neglected beyond the LO pion exchange when working at N2LO. This is consistent with ℓ_7 being a $\Delta=2$ operator. However at $\theta=\pi$, this

---

[2] In practical calculations it is usually preferable to leave g_A constant and neglect diagrams that renormalize g_A as well as the pion mass dependence of the Golberger-Treiman discrepancy (i.e. fix $g_A=1.29$). As was shown in Ref. [118], g_A is a nearly constant but very slowly converging function of m_π and expanding it to what appears to be a consistent order in NDA leads to spurious shifts in g_A.

becomes an error of 43% and terms that are at least quadratic in the pion mass should have this splitting promoted two orders and be accounted for in all pion exchanges.

In RG corrections to the running of the contact interactions, logarithmic corrections to the pion mass splitting return to $\mathcal{O}(p^2/\Lambda_\chi^2)$ or less and the average pion mass can be used, leaving nearly all of the isospin breaking in short range forces due to pion mass splitting in C_S. In the standard treatment, C_S already differentiates between isospin projections so this introduces no difficulties. At N2LO, the only potentially problematic part of the pion mass splitting to implement is the short range correction proportional to $c_4 m_\pi \tau_1 \cdot \tau_2$. However with just a single power of the pion mass, this is an order 10% correction that is at most promoted one order and only becomes important at N3LO. All other appearances of the pion mass are either isoscalar or come in the long range part of the force and can be implemented identically to the long range part of the pion exchanges at LO as follows.

$$V(m_\pi)\tau_1 \cdot \tau_2 \rightarrow \begin{cases} V(m_{\pi_0}) & I = \pm I_z = 1 \\ -V(m_{\pi_0}) + 2V(m_{\pi_\pm}) & I = 1,\, I_z = 0 \\ -V(m_{\pi_0} - 2V(m_{\pi_\pm}) & I = I_z = 0 \end{cases} \tag{3.27}$$

3.5 CP violating and isospin breaking NN and 3N forces

At N2LO, there are several isospin breaking and CP violating terms that appear in the $\Delta = 1$ Lagrangian, generated by the operator proportional to c_5 in Eq. (3.18). Although c_5 is normally ignored because it is small, it is amplified relative to other N2LO corrections in the axion condensed phase because it is isospin breaking and should be included. As a point of reference, c_1 enters at the same order as c_5 and where c_1 contributes to $\sigma_{\pi N}$, c_5 contributes to $\Delta\sigma$. The ratio of the importance of these operators scales roughly as $\Delta\sigma/[f(\theta)^2\sigma_{\pi N}]$ which is about 2% when $\theta = 0$ but grows to about 20% when $\theta = \pi$.

Using c_5 is challenging because it is not fitted as part of the normal procedure of generating a chiral potential because its effect at $\theta = 0$ is small. Since c_5 gives the leading strong correction to the nucleon mass splitting, we parameterize it with $\Delta\sigma$. The two- and three-body forces generated by c_5 are given by the following.

$$V_{\rm IB}^{\rm 2NF} = \frac{g_A^2 \Delta\sigma}{16\pi f_\pi^4} \frac{(m_\pi^{\rm phys})^2}{m_\pi^2} (\tau_1^z + \tau_2^z)\tilde{w}^2 A(q) \tag{3.28}$$

Note that although this is an isospin breaking operator, because it has $I_z = 0$, it does not violate isospin in the NN sector.

$$V_{\rm IB}^{\rm 3NF} = \frac{g_A^2 \Delta\sigma}{16 f_\pi^4} \frac{(m_\pi^{\rm phys})^2}{m_\pi^2} \sum_{i \neq j \neq k} \frac{(\sigma_i \cdot q_i)(\sigma_j \cdot q_j)}{(q_i^2 + m_\pi^2)(q_j^2 + m_\pi^2)} (\tau_i^z \tau_j \cdot \tau_k + \tau_j^z \tau_i \cdot \tau_k) \tag{3.29}$$

When adding forces of this form to a typical chiral potential that does not normally include c_5 the contribution at $\theta = 0$ should always be subtracted so that the normal phase is not modified. The only CP violating contribution we need consider at N2LO is given by

$$\begin{aligned} V_{\mathrm{CP}}^{2\mathrm{NF}} = \tau_1 \cdot \tau_2 \Bigg[&\frac{2m_u m_d}{m_d^2 - m_u^2} \Delta\sigma \sin\theta \frac{(m_\pi^{\mathrm{phys}})^2}{m_\pi^2} \frac{g_A}{2f_\pi^2} \frac{q \cdot (\sigma_1 - \sigma_2)}{q^2 + m_\pi^2} \\ &+ \left(\frac{2m_u m_d}{m_d^2 - m_u^2} \Delta\sigma \sin\theta \right)^2 \frac{(m_\pi^{\mathrm{phys}})^4}{m_\pi^4} \frac{1}{f_\pi^2} \frac{1}{q^2 + m_\pi^2} \Bigg] \end{aligned} \tag{3.30}$$

where for the sake of the first term, q is defined as the momentum transfer from 1 to 2. Note that since this term is CP violating, it is only relevant in the domain wall and does not affect $\theta = 0$ or $\theta = \pi$.

It was pointed out in Ref. [176] that regulating the ${}^1S_0 - {}^3P_0$ transition generated by c_5 in the presence of finite θ requires a new operator. Looking at the expansions of $\chi_\pm$ in Eqs. (3.12) and (3.13), the only option for a CP-violating short range force between nucleons is generated by $\langle \chi_- \rangle$ giving the term proportional to c_F in Eq. (3.18). Note that Ref. [176] refers to the LEC we call c_F as C_0. Since this operator lacks a standard notation and C_0 is commonly used to refer to the leading order contact interaction while c_D and c_E are LECs generating 3NFs, we prefer the name c_F. Regulating the nuclear force in the presence of non-zero θ requires promoting this operator from $\Delta = 3$ to $\Delta = 1$. The CP violating short range force generated by c_F that regulates the potential in Eq. (3.30) is given by

$$V_F = c_F \frac{2m_u m_d}{(m_u + m_d)^2} (m_\pi^{\mathrm{phys}})^2 \frac{\sin\theta}{f(\theta)} q \cdot (\sigma_1 - \sigma_2) \,. \tag{3.31}$$

This LEC is also responsible for a three nucleon force that will be discussed in Sec. 3.6. At the present time, there are limited avenues to constrain the size of c_F. A renormalization group (RG) calculation of the same style as that for D_2 and F_2 gives an approximate size for this operator.

$$\frac{\mathrm{d}}{\mathrm{d}\log\mu} c_F \simeq \frac{g_A \Delta\sigma M_N^2 C_0 C_2}{16\pi^2 f_\pi^2} \tag{3.32}$$

where C_0 is projected onto the ${}^1S_0$ channel and C_2 is projected onto the ${}^3P_0$ channel.[3] Note that for c_F to regulate the ${}^1S_0 - {}^3P_0$ transition, it should be $\Delta = 1$ though this estimate gives a size that is closer to $\Delta = 2$. However, since this is an isospin breaking correction, its size is amplified in the axion condensed phase and it should be included in 3NF at N2LO for the sake of calculating θ dependence.

3.6 New three nucleon forces

Three nucleon forces (3NFs) are an important component of high density nuclear matter as they provide additional repulsion at increasing density, an ingredient necessary to produce high mass NSs. At N2LO

---

[3] We prefer not to use notation like C^{1S0} as the spectroscopic LECs have a standard normalization in the literature that does not match the standard expressions for the RG running of D_2 and F_2.

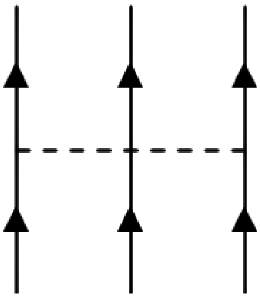

Figure 3.2: Leading 3NF in PNM arising at N2LO in the chiral expansion due to the LECs c_1 and c_3.

in neutron matter, the 3NFs historically included are particularly simple because only one topology of diagram is present, shown in Fig. 3.2. This 3NF, known as the Fujita-Miyazawa term, is increasingly repulsive at reduced pion mass, leading to competition between more attractive forces in the two body sector and more repulsive 3NFs. Other 3NFs associated with the operators c_D and c_E (sometimes called D and E in older literature) do not have an effect on PNM in the limit of large cutoff due to the requirement that interactions between fermions be antisymmetric.

This, however, is not the whole story. It was recently noted in Ref. [181] that promoting D_2 to LO also requires promoting the leading 3NF generated by D_2 (shown in the first two panels of Fig. 3.3) to N2LO. That work also introduces operators E_2 and F_2 that couple to the time-like and space-like derivatives of the interacting nucleon pair that must also be promoted. Since E_2 couples to the frequency of the nucleon pair, it is effectively a higher order in nucleon interactions and we need only consider D_2 and F_2. This makes it possible to estimate the size of D_2 for use in $^1S_0$ scattering by analyzing properties of dense matter and light nuclei.

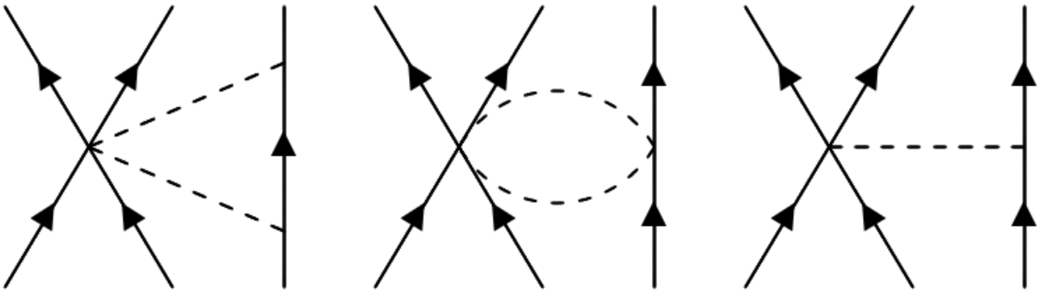

Figure 3.3: Feynman diagrams for new 3NF. The left and center panel use operators D_2 and F_2 and the right panel uses c_F

An additional 3NF must be introduced proportional to c_F. Although this operator was introduced to regulate a part of the nuclear force that scales with $\sin\theta$, chiral symmetry dictates that it contributes to the nuclear force even when $\theta = 0$ or π and CP is a good symmetry. This operator produces a 3NF of the same topology as that generated by c_D (shown in the right panel of Fig. 3.3) but that, unlike c_D, does contribute to pure neutron matter (PNM) given by

$$V_F^{3\mathrm{NF}} = \frac{c_F \delta m g_A}{2\bar{m} f_\pi^2} \frac{(m_\pi^{\mathrm{phys}})^2}{f(\theta)} \sum_{i \neq j \neq k} \frac{(\sigma_k \cdot q_k)(\sigma_i \cdot q_j)}{q_k^2 + m_\pi^2} \left(1 + \frac{\tau_i \cdot \tau_j}{3}\right) \tau_k^z \,. \tag{3.33}$$

The Hartree-Fock energy associated with this operator in PNM is given by

$$\frac{E}{A} = \frac{c_F g_A f(\theta)^2}{1728 f_\pi^2} (m_\pi^{\mathrm{phys}})^8 \frac{m_d - m_u}{m_u + m_d} [12u^2 - 72u^4 + 32u^6 + 96u^3 \tan^{-1}(2u) - (3 + 36u^2) \log(1 + 4u^2)] \tag{3.34}$$

for $u = k_F / m_\pi(\theta)$. As with the new 3NFs generated by D_2, F_2, and c_5 the correction from this diagram is effectively N2LO in the axion condensed phase and introduces another unknown LEC that must be accounted for in our error budget. It is possible that the values of D_2, F_2, and c_F could be determined by fitting to properties of few nucleon systems or nuclear matter although the contribution of c_F is expected to be so small in the normal phase, the uncertainty from such an extraction is likely to be substantial. Future study will determine whether these avenues will bear fruit.

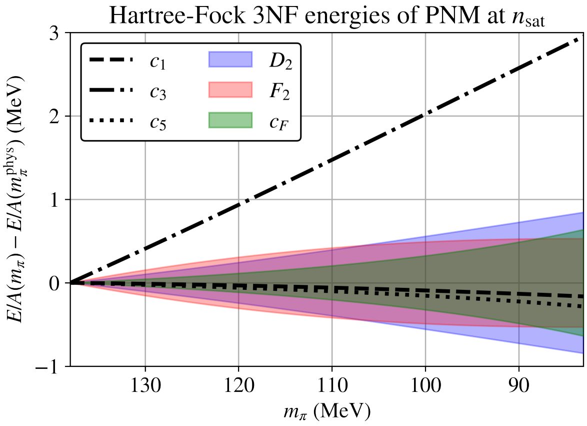

Figure 3.4: Shift to the Hartree-Fock energies of each 3NF in PNM at n_{sat} compared to the physical point as a function of pion mass. The values of c_1 and c_3 are from the Roy-Steiner analysis of Ref. [182]. Together c_1 and c_3 make up the Fujita-Miyazawa force. c_5 is fitted to $\Delta\sigma$. D_2 and F_2 are varied within the range predicted by Ref. [126] and c_F is varied within the range predicted by Eq. (3.32).

To compare the relevance of these terms, Fig. 3.4 shows the Hartree-Fock energies associated with the Fujita-Miyazawa force (separated into contributions from the LECs c_1 and c_3), D_2 and F_2 (using expressions from Ref. [181]), and the operators c_5 and c_F. Note that c_5 and c_F have unimportant contributions at the physical point because their expected size scales with $\Delta\sigma$, but because they are isospin breaking they produce corrections of the same scale as the correction from the 3NF generated by D_2 and F_2.

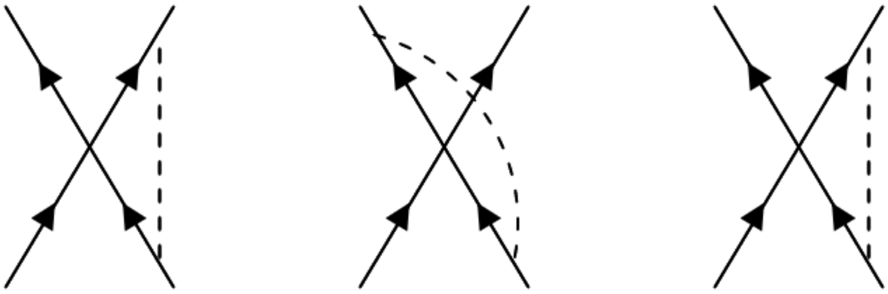

Figure 3.5: Additional diagrams contributing to renormalization of C_S and C_T at NLO. There are three more diagrams that are mirror images of these three.

3.7 Regulator dependence

In the previous sections, we have enumerated multiple important corrections not included in our prior analysis needed to confidently predict the properties of neutron star matter at finite θ. However, these do not address the most significant deficiency of our prior calculation: the large cutoff dependence. Since, in the standard treatment of chiral forces, short range components of pion exchanges are absorbed in LECs and diagrams that only renormalize LECs are neglected since LECs are fitted to data, not explicitly accounting for these changes in the axion condensed phase is equivalent to employing a regulator scheme in which all of these corrections are absorbed into D_2 and equivalent operators in other partial waves. However, the calculation of Ref. [126] that determined the expected size of D_2 and established that its RG behavior was not pathological assumed that pion exchanges that can be predicted from theory and LECs that must be fitted to data have not been mixed. The procedure we previously employed had the effect of generating artificially large and chaotic running of D_2 and the equivalent operators in higher partial waves. As a result, our prior calculation which varied D_2 within a constant modest range had significant regulator artifacts.

To cancel out these effects, the LECs should be modified from their best-fit value which implicitly include parts of the pion exchanges and several diagrams that are neglected in the standard scheme. These corrections have a part that is independent of regularization scheme (the standard β function) and a part that is scheme-dependent. While calculable in any given scheme, the scheme-dependent contributions are only meaningful when we have a prediction for the value of D_2 from experiment, so they should instead be included in our final error budget. Although including all these effects does not fix the value of D_2 and related operators, it restores the validity of the RG prediction for the expected size of D_2 and the smoothness of its running so that uncertainty can be meaningfully quantified.

3.7.1 New diagrams

There are a group of diagrams at NLO which are normally neglected as they only renormalize C_S and C_T. This covers the six diagrams where a LO contact has a pion loop added. Three representative diagrams are shown in Fig. 3.5 while the other three are mirror images. No new diagrams of this kind arise at N2LO. Throughout the calculation of these diagrams, we use LECs at their normal physical point. Technically speaking, this introduces errors as the physical LECs include the very contributions from pion exchanges and new diagrams that we are quantifying in this section. However, these errors would appear at N3LO as possible double counting of diagrams. Since we work at N2LO, this is not an issue, but a future calculation at N3LO would require careful analysis in order to include all LEC renormalization self-consistently.

We will need the angular integral

$$\frac{1}{4\pi}\int d\Omega \hat{\ell}\cdot\sigma_1\hat{\ell}\cdot\sigma_2 = \frac{1}{3}\sigma_1\cdot\sigma_2\,. \tag{3.35}$$

When the pion leg connects the same leg incoming and outgoing and C_S is at the contact, this just multiplies by ℓ^2 for ℓ the loop three momentum. For C_T, a spin structure appears of the form

$$\begin{aligned}\sigma_2^i(\sigma_1\cdot\ell)\sigma_1^i\sigma_1\cdot\ell &= \sigma_2^i\sigma_1\cdot\ell(\ell^i + i\varepsilon^{ijk}\ell^j\sigma_1^k)\\ &= \sigma_1\cdot\ell\sigma_2\cdot\ell + i\varepsilon^{ijk}\sigma_2^i\ell^j(\ell^k + i\varepsilon^{mkn}\ell^m\sigma^n)\\ &= 2\sigma_1\cdot\ell\sigma_2\cdot\ell - \sigma_1\cdot\sigma_2\ell^2\\ &\to -\frac{1}{3}\sigma_1\cdot\sigma_2\ell^2\end{aligned} \tag{3.36}$$

where the final line is the result after doing the angular part of the loop integral. When the pion connects two incoming or two outgoing legs, a spin structure appears of the form

$$\begin{aligned}(\sigma_1\cdot\ell\sigma_1^i)(\sigma_2\cdot\ell\sigma_2^i) &= (\ell^i + i\varepsilon^{jik}\ell^j\sigma_1^k)(\ell^i + i\varepsilon^{min}\ell^m\sigma_2^n)\\ &= \ell^2 - (\ell^2\sigma_1\cdot\sigma_2 - \sigma_1\cdot\ell\sigma_2\cdot\ell)\\ &\to (1 - \frac{2}{3}\sigma_1\cdot\sigma_2)\ell^2\,.\end{aligned} \tag{3.37}$$

When the pion connect incoming and outgoing legs from different nucleon currents, the same spin structure is the same but with one i replaced by $-i$ in the first line, giving

$$\ell^2 + (\ell^2\sigma_1\cdot\sigma_2 - \sigma_1\cdot\ell\sigma_2\cdot\ell \to (1 + \frac{2}{3}\sigma_1\cdot\sigma_2)\ell^2\,. \tag{3.38}$$

The contribution of all six diagrams is, therefore:

$$\begin{aligned} V &= [(3C_S - C_T\sigma_1\cdot\sigma_2) - \tau_1\cdot\tau_2(\frac{1}{3}C_S\sigma_1\cdot\sigma_2 + C_T(1-\frac{2}{3}\sigma_1\cdot\sigma_2)) \\ &\quad + \tau_1\cdot\tau_2(\frac{1}{3}C_S\sigma_1\cdot\sigma_2 + C_T(1+\frac{2}{3}\sigma_1\cdot\sigma_2))]\left(\frac{g_A}{2f_\pi}\right)^2 I \\ &= (12\pi^2 C_S - 4\pi^2 C_T\sigma_1\cdot\sigma_2 + \frac{8\pi^2}{3}\sigma_1\cdot\sigma_2\tau_1\cdot\tau_2)\left(\frac{g_A}{4\pi f_\pi}\right)^2 I \end{aligned} \tag{3.39}$$

where I is given by the divergent integral

$$\begin{aligned} &-2\int\frac{d^4\ell}{(2\pi)^4}\frac{i}{\ell_0+i\varepsilon}\frac{i}{\ell_0\pm i\varepsilon}\frac{i\ell^2}{\ell_0^2-\ell^2-m_\pi^2+i\varepsilon} \\ &\qquad = \int\frac{d^3\ell}{(2\pi)^3}\frac{\ell^2}{(\ell^2+m_\pi^2)^{3/2}} \end{aligned} \tag{3.40}$$

where as per the usual Weinberg prescription, the nucleon poles have been ignored. In dim reg, this is given by

$$I = \frac{m_\pi^2}{4\pi^2}\frac{3}{2}\left(-\frac{2}{\varepsilon}+\gamma-\frac{1}{3}-\log 4\pi + 2\log\frac{m_\pi}{\mu}\right). \tag{3.41}$$

With cutoff regularization, this is given by

$$\begin{aligned} I &= -\frac{m_\pi^2}{4\pi^2}\left[3\tanh^{-1}\left(\frac{\Lambda}{\sqrt{\Lambda^2+m_\pi^2}}\right) - \left(3+\frac{\Lambda^2}{m_\pi^2}\right)\frac{\Lambda}{\sqrt{\Lambda^2+m_\pi^2}}\right] \\ &\to \frac{m_\pi^2}{4\pi^2}\frac{3}{2}\left(\frac{2\Lambda^2}{3m_\pi^2}+\frac{5}{3}-2\log 2+2\log\frac{m_\pi}{\Lambda}\right) \end{aligned} \tag{3.42}$$

After doing a Fierz transformation to return to the standard operator basis, this gives a final result of

$$(\frac{9}{2}C_S - 3C_T - \frac{3}{2}C_T\sigma_1\cdot\sigma_2)\left(\frac{g_A}{4\pi f_\pi}\right)^2 m_\pi^2(\infty + X + 2\log\frac{m_\pi}{Y}) \tag{3.43}$$

for these six diagrams where $X = \gamma - 1/3 - \log 4\pi$ for dim reg and $5/3 - 2\log 2$ for cutoff and Y is μ or Λ respectively.

One might initially be concerned by the fact that unphysical combinations of C_S, C_T, and spin operators appear in this expression. This is easily resolved by noting that this calculation has assumed isospin symmetry but at this order there are three different ${}^1S_0$ phase shifts. In terms of these components, the terms in Eq. (3.43) should be modified as follows:

$$C_S^{(\mathrm{np})} \supset \frac{9}{2}C_S - 3C_T \to \frac{3}{8}(14C_S^{(\mathrm{np})} - C_S^{(\mathrm{nn})} - C_S^{(\mathrm{pp})}) - 3C_T \tag{3.44}$$

$$C_S^{(\mathrm{nn})} \supset \frac{9}{2}C_S - 3C_T \to \frac{3}{8}(9C_S^{(\mathrm{nn})} + 5C_S^{(\mathrm{pp})} - 2C_S^{(\mathrm{np})}) - 3C_T \tag{3.45}$$

$$C_S^{(\mathrm{pp})} \supset \frac{9}{2}C_S - 3C_T \to \frac{3}{8}(9C_S^{(\mathrm{pp})} + 5C_S^{(\mathrm{nn})} - 2C_S^{(\mathrm{np})}) - 3C_T \tag{3.46}$$

$$C_T \supset -\frac{3}{2}C_T \to -\frac{3}{2}C_T + \frac{5}{8}(C_S^{(\mathrm{nn})} + C_S^{(\mathrm{pp})} - 2C_S^{(\mathrm{np})}) \tag{3.47}$$

where all LECs are evaluated at the physical pion mass (arguments and overall factors dropped for brevity). In the next section, we will show expressions including pion mass splitting corrections.

3.7.2 Renormalized contact operators

With only scheme-independent contributions, the following corrections to the LECs are needed at N2LO. The pion mass dependent LECs in the $^1S_0$ and $^3S_1$ channels are D_2 and D_2' respectively. The normalization is chosen for D_2 such that the prediction of Ref. [126] is approximately $1/5f_\pi^4$ and the expectation from naive dimensional analysis would be $1/f_\pi^2\Lambda_\chi^2$. The shorthand $\Delta f(m_\pi) = f(m_\pi) - f(m_\pi^{\rm phys})$ is used throughout. μ is the characteristic scale of the regulator scheme employed (whether a cutoff or dimensional regularization). If the charge of the pion is ever not specified, the average pion mass should be used. Expressions for the short range part of the normal NLO and N2LO two pion exchanges are adapted from Ref. [169].

The corrections to C_S common to all isospin projections is given by

$$\begin{aligned}
\bar{C}_S &= \bar{C}_S(m_\pi^{\rm phys}) + \frac{D_2+3D_2'}{4}\Delta m_\pi^2 + \frac{1}{64\pi^2}(15g_A^4-6g_A^2-1)\Delta\left(\frac{m_{\pi_\pm}^2+m_{\pi_0}^2}{f_\pi^4}\log\frac{m_\pi}{\mu}\right) \\
&+ \frac{g_A^2}{16\pi^2}\left[(3C_S^{(\rm nn)}+3C_S^{(\rm pp)}+3C_S^{(\rm np)})\Delta\left(\frac{m_\pi^2}{f_\pi^2}\log\frac{m_\pi}{\mu}\right) - 6C_T\Delta\left(\frac{m_{\pi_0}^2}{f_\pi^2}\log\frac{m_\pi}{\mu}\right)\right] \\
&- \frac{3g_A^2}{4\pi}\left[c_1\Delta\left(\frac{m_{\chi PT}^2 m_\pi}{f_\pi^4}\right) - c_3\Delta\left(\frac{m_\pi^3}{f_\pi^4}\right)\right].
\end{aligned} \tag{3.48}$$

The isospin breaking corrections are given by

$$\begin{aligned}
C_S^{(\rm nn)} - \bar{C}_S &= C_S^{(\rm nn)}(m_\pi^{\rm phys}) - \bar{C}_S(m_\pi^{\rm phys}) + \frac{1}{64\pi^2}(15g_A^4-6g_A^2-1)\Delta\left(\frac{m_{\pi_\pm}^2-m_{\pi_0}^2}{f_\pi^4}\log\frac{m_\pi}{\mu}\right) \\
&+ \frac{g_A^2}{16\pi^2}\left[(3C_S^{(\rm np)}-3C_S^{(\rm pp)})\Delta\left(\frac{m_\pi^2}{f_\pi^2}\log\frac{m_\pi}{\mu}\right)\right. \\
&\left.+ \frac{5}{4}(C_S^{(\rm nn)}+C_S^{(\rm pp)}-2C_S^{(\rm np)})\Delta\left(\frac{8m_{\pi_0}^2-5m_{\pi_\pm}^2}{f_\pi^2}\log\frac{m_\pi}{\mu}\right)\right] \\
&- \frac{g_A^2\Delta\sigma}{8\pi}(m_\pi^{\rm phys})^2\Delta\left(\frac{1}{m_\pi f_\pi^4}\right),
\end{aligned} \tag{3.49}$$

$$\begin{aligned}
C_S^{(\rm pp)} - \bar{C}_S &= C_S^{(\rm pp)}(m_\pi^{\rm phys}) - \bar{C}_S(m_\pi^{\rm phys}) + \frac{1}{64\pi^2}(15g_A^4-6g_A^2-1)\Delta\left(\frac{m_{\pi_\pm}^2-m_{\pi_0}^2}{f_\pi^4}\log\frac{m_\pi}{\mu}\right) \\
&+ \frac{g_A^2}{16\pi^2}\left[(3C_S^{(\rm np)}-3C_S^{(\rm nn)})\Delta\left(\frac{m_\pi^2}{f_\pi^2}\log\frac{m_\pi}{\mu}\right)\right. \\
&\left.+ \frac{5}{4}(C_S^{(\rm nn)}+C_S^{(\rm pp)}-2C_S^{(\rm np)})\Delta\left(\frac{8m_{\pi_0}^2-5m_{\pi_\pm}^2}{f_\pi^2}\log\frac{m_\pi}{\mu}\right)\right] \\
&+ \frac{g_A^2\Delta\sigma}{8\pi}(m_\pi^{\rm phys})^2\Delta\left(\frac{1}{m_\pi f_\pi^4}\right),
\end{aligned} \tag{3.50}$$

and

$$\begin{aligned} C_S^{(\mathrm{np})} - \bar{C}_S = C_S^{(\mathrm{np})}(m_\pi^{\mathrm{phys}}) - \bar{C}_S(m_\pi^{\mathrm{phys}}) + \frac{g_A^2}{16\pi^2}\bigg[&- 12 C_T \Delta\bigg(\frac{m_{\pi_\pm}^2 - m_{\pi_0}^2}{f_\pi^2}\log\frac{m_\pi}{\mu}\bigg) \\ &+ \frac{5}{4}(C_S^{(\mathrm{nn})} + C_S^{(\mathrm{pp})} - 2C_S^{(\mathrm{np})})\Delta\bigg(\frac{2m_{\pi_0}^2 - 5m_{\pi_\pm}^2}{f_\pi^2}\log\frac{m_\pi}{\mu}\bigg)\bigg]. \end{aligned} \tag{3.51}$$

We use the convention that C_T is common to all isospin channels, giving the following.

$$\begin{aligned} C_T = C_T(m_\pi^{\mathrm{phys}}) &+ \frac{D_2' - D_2}{4}\Delta m_\pi^2 + \frac{1}{64\pi^2}(15g_A^4 - 6g_A^2 - 1)\Delta\bigg(\frac{m_{\pi_\pm}^2}{f_\pi^4}\log\frac{m_\pi}{\mu}\bigg) \\ &- \frac{g_A^2}{16\pi^2}\bigg[3C_T\Delta\bigg(\frac{m_\pi^2}{f_\pi^2}\log\frac{m_\pi}{\mu}\bigg) + \frac{5}{12}(C_S^{(\mathrm{nn})} + C_S^{(\mathrm{pp})} - 2C_S^{(\mathrm{np})})\Delta\bigg(\frac{2m_{\pi_0}^2 - 5m_{\pi_\pm}^2}{f_\pi^2}\log\frac{m_\pi}{\mu}\bigg)\bigg] \end{aligned} \tag{3.52}$$

The NLO contacts are renormalized as follows.

$$C_1 = C_1(m_\pi^{\mathrm{phys}}) + \frac{1}{384\pi^2}(23g_A^4 - 10g_A^2 - 1)\Delta\bigg(\frac{1}{f_\pi^4}\log\frac{m_\pi}{\mu}\bigg) + \frac{3g_A^2}{16\pi}c_3\Delta\bigg(\frac{m_\pi}{f_\pi^4}\bigg) \tag{3.53}$$

$$C_2 = C_2(m_\pi^{\mathrm{phys}}) + \frac{1}{96\pi^2}(23g_A^4 - 10g_A^2 - 1)\Delta\bigg(\frac{1}{f_\pi^4}\log\frac{m_\pi}{\mu}\bigg) - \frac{g_A^2}{4\pi}c_4\Delta\bigg(\frac{m_\pi}{f_\pi^4}\bigg) \tag{3.54}$$

$$C_3 = C_3(m_\pi^{\mathrm{phys}}) + \frac{3g_A^4}{64\pi^2}\Delta\bigg(\frac{1}{f_\pi^4}\log\frac{m_\pi}{\mu}\bigg) - \frac{g_A^2}{32\pi}c_4\Delta\bigg(\frac{m_\pi}{f_\pi^4}\bigg) \tag{3.55}$$

$$C_4 = C_4(m_\pi^{\mathrm{phys}}) + \frac{1}{96\pi^2}(23g_A^4 - 10g_A^2 - 1)\Delta\bigg(\frac{1}{f_\pi^4}\log\frac{m_\pi}{\mu}\bigg) \tag{3.56}$$

$$C_6 = C_6(m_\pi^{\mathrm{phys}}) - \frac{3g_A^4}{64\pi^2}\Delta\bigg(\frac{1}{f_\pi^4}\log\frac{m_\pi}{\mu}\bigg) + \frac{g_A^2}{32\pi}c_4\Delta\bigg(\frac{m_\pi}{f_\pi^4}\bigg) \tag{3.57}$$

$$C_7 = C_7(m_\pi^{\mathrm{phys}}) + \frac{g_A^2}{4\pi}c_4\Delta\bigg(\frac{m_\pi}{f_\pi^4}\bigg) \tag{3.58}$$

3.8 Chiral symmetry restoration in the axion condensed phase

One crucial way in that the the QCD axion differs from the $\mathbb{Z}_\mathcal{N}$ model (described in detail in the introduction to Chap. 2) is that the $\mathbb{Z}_\mathcal{N}$ model explicitly differentiates between axion and pion couplings resulting from operators containing $\chi_\pm$. Since the axion is coupled to multiple mirror QCDs while any pions in a neutron star only couple to our QCD, the behavior of the self energy of the pion and axion can be quite different. In terms of 1PI diagrams contributing to the axion self energy in the $\mathbb{Z}_\mathcal{N}$ model, the diagrams with only axions are suppressed compared to diagrams where axions couple to pions. Contributions to the axion mass from modifications to the pion masses can be thought of as summing up all possible even numbers of external axion lines connecting to pion propagators in normal MBPT diagrams, or equivalently 1PI insertions of $\langle\chi_+\rangle$ in a massless pion propagator. For examples of the interactions contributing to the axion mass seen in diagrammatic language, see Fig. 3.6. Note that all of these diagrams could equally well have external pion legs instead of axions. Comparing the strengths of the couplings for axions and pions, in the $\mathbb{Z}_\mathcal{N}$ model the vacuum mass of the axion is relatively suppressed while for the QCD axion theory, the relative sizes of these operators are the same between the pion and the axion.

The result is that if there is a density at which the effective axion mass goes to zero for the QCD axion, then $\omega = k = 0$ will be a solution to the pion equation of motion up to errors of order $\Delta\sigma/\sigma_{\pi N}$. Such a solution does not appear in the $\mathbb{Z}_\mathcal{N}$ model at the density where the axion becomes massless because in the $\mathbb{Z}_\mathcal{N}$ model the axion receives contributions from $\mathcal{N}$ copies of QCD while the pions only see effects from their own QCD.

The presence of an $\omega = k = 0$ solution to the pion equation of motion is not equivalent to the effective pion mass going to zero. The pion has important frequency dependence in medium that the axion does not share ($\partial_0 a$ operators are suppressed by $1/f_a$ in the EFT) and it seems likely that this zero frequency solution to the pion should be understood as a sound mode if it is a well-defined mode at all (which we will shortly see it is not).

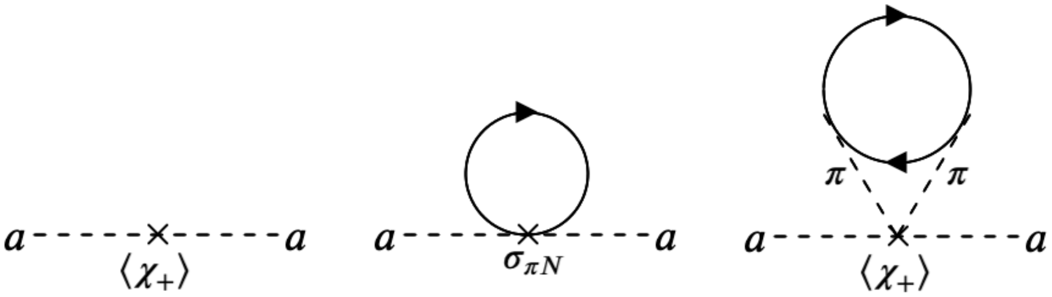

Figure 3.6: Example diagrams contributing to axion effective mass. The left panel is the 1PI diagram giving the axion its vacuum mass. The center panel is the leading linear density contribution coming from the isoscalar σ. The right panel is an example of a diagram contributing to the axion mass via the effect of the axion on the pion mass in a pion exchange Fock diagram.

More importantly, a density at which the effective axion mass is zero is one at which $\mathrm{d}(E/A)/\mathrm{d}\theta = 0$. The Hellman-Feynman theorem allows us to write the chiral condensate as a function of this quantity.

$$\langle \bar{q}q \rangle = \frac{n_B}{\mathcal{M}_q f'(\theta)} \frac{\mathrm{d}E/A}{\mathrm{d}\theta} \tag{3.59}$$

In the isospin limit, the density at which the axion becomes massless is the exact density at which chiral symmetry is restored. Since χEFT is an expansion around the ground state of the chirally broken phase, it is no longer a good expansion when chiral symmetry is restored. In this phase, the pion is no longer a good degree of freedom, its coupling diverges, and the predictions of χEFT can no longer be trusted.

More generally, if χEFT predicts some function $E/A(m_\pi)$ at a given density with a finite allowed domain for m_π, the ground state of the system must be at a value of m_π such that $\mathrm{d}(E/A)/\mathrm{d}m_\pi = 0$

unless it is at one of the boundaries of the domain. If it as the minimal allowed m_π then it is also possible that the ground state has $\mathrm{d}(E/A)\,/\mathrm{d}m_\pi < 0$ while if it is at the maximal allowed m_π then the ground state may have $\mathrm{d}(E/A)\,/\mathrm{d}m_\pi > 0$. However, chiral symmetry remains broken only so long as $\mathrm{d}(E/A)\,/\mathrm{d}m_\pi > 0$. Since finite θ necessarily decreases the pion mass, if the ground state of QCD is at finite θ, it is impossible that chiral symmetry remain broken in the conventional way in such a phase. In retrospect, it becomes clear that the behavior found in our prior MBPT calculation where the interaction energy per baryon increased at small θ before decreasing at large θ was the only possible behavior favoring axion condensation that would not have indicated the breakdown of χEFT . Future analysis of axion constraints should include this non-monotonic behavior with θ. Note that this argument relies on the fact that $\sigma_{\pi N} \gg \Delta\sigma$. If it were not the case that $\langle \bar{u}u \rangle \simeq \langle \bar{d}d \rangle$ then it is possible that isospin breaking effects may modify this prediction.

This places us in a difficult position. While a calculation in χEFT might rule out axion condensation below the breakdown scale of the EFT, it can never definitely show such a phase must exist nor can it describe such a phase. Calculating trends at densities below the critical density for condensation can give us clues about whether one should expect the onset of a chirally restored phase if the axion exists, but this does not on its own indicate the value of θ in such a phase and does not indicate any properties of such a phase. Constraints on the QCD axion in neutron stars will likely require some amount of speculation about the properties of the chirally restored phase. These issues will be explored in future publications.

3.9 Conclusion

We have identified the necessary modifications to the parameters of a χEFT calculation at reduced pion mass in order to mitigate significant regulator dependence and have enumerated the additional operators that must be included up to N2LO in a MBPT calculation. Isospin breaking effects are amplified in the axion condensed phase, requiring a modification of the power counting. The most relevant impact of this modification is the inclusion of the pion mass splitting in the NLO and N2LO pion exchanges and renormalization of the LECs. Although several CP violating and isospin breaking operators potentially contribute to pion-nucleon interactions at N2LO, the only ones with concrete empirical justification for their inclusion are the operator associated with c_5 and the neutral pion mass correction. The isospin breaking and CP violating forces generated by c_F also ought to contribute at this order by requiring the renormalizability of the theory at arbitrary θ.

Although the picture for nuclear forces at reduced pion mass in the axion condensed phase seems relatively under control in the two nucleon sector, three nucleon forces continue to pose challenges as the associated LECs can be troublesome to fit. A full error budget for an N2LO calculation should include at minimum, the inclusion of three nucleon forces generated by D_2, F_2, and c_F.

One final wrinkle that must be addressed before neutron stars might be used to constrain the QCD axion is the issue of chiral symmetry restoration. If the pion mass is allowed to vary and the minimum of the energy of the system is not at the maximum allowed pion mass, it is guaranteed that chiral symmetry restoration must precede the appearance of such a phase. As such, χEFT will not be able to describe the axion condensed phase and can merely point to the likelihood (or not) of its presence. If the existence of the QCD axion would hasten the restoration of chiral symmetry at high density, that would in itself be an intriguing prediction that warrants further study.

Chapter 4

Effects of Landau quantization on neutrino emission and absorption[1]

4.1 Introduction

Observing the thermal evolution of neutron stars is one means by which to probe their interiors. Young neutron stars cool primarily via emission of neutrinos produced by weak reactions in nuclear matter (see Refs. [15, 42, 49] for reviews). Since these neutrinos originate deep in the NS, they provide useful information about the composition of the core. In Chap. 2 the cooling history of NSs was one means by which we could constrain the presence of an axion condensate in neutron star cores. In this chapter we will focus on the particular features of neutrino cooling in strong magnetized NSs, known as magnetars. The tools we develop will also have applicability to calculating neutrino opacities in the presence of strong magnetic fields, an important ingredient for understanding the dynamics of BNS mergers and supernovae. At the end of this chapter, we present an initial development of these ideas. Appendix C contains more details about how to perform such a calculation in a computationally efficient manner.

One of the fastest cooling channels available is the Direct Urca (DU) process, consisting of the reactions $n \rightarrow p + e + \overline{\nu}$ and $p + e \rightarrow n + \nu$. This mechanism is very efficient but can only operate at high density because the Fermi momenta of the particles must obey the so-called triangle inequality ($|k_{Fn}| < |k_{Fp}| + |k_{Fe}|$) in order to conserve momentum. Due to constraints of β equilibrium and charge neutrality in NS matter, this is only possible for large proton fraction ($Y_p > 1/9$ for matter containing neutrons, protons, and electrons). At sufficiently high density (the "DU threshold"), DU becomes available causing more massive NSs to cool rapidly. Below this threshold, slower neutrino emission processes dominate. Modified Urca (MU), in which a spectator nucleon conserves momentum, and neutral current Bremsstrahlung are the primary sources of neutrino cooling at these densities [49].

---

[1] This chapter summarizes work originally found in Ref. [11]

In the presence of strong magnetic fields, electrons and protons have their momentum perpendicular to the field quantized into Landau levels (LL) [183]. The momentum-space wavefunction associated with each LL has a long tail allowing momentum to be conserved in DU reactions even at low densities [184, 185]. For higher energy states, denoted by quantum number n, there is a larger contribution from high momentum components. Higher values of n correspond to larger amounts of energy stored in motion perpendicular to the field, in analogy with larger momenta perpendicular to the field for a free particle.

Understanding which NSs can access Direct Urca is important information in order to match theory onto observation since the cooling histories of stars above and below the Direct Urca threshold are so different. As mentioned in the introduction, most NSs have magnetic fields of around 10^{12-13} G [25, 50], too small to see this effect. Magnetars, however, have surface magnetic fields of 10^{15} G [51] (or possibly more [52]) at which point $eB \simeq \mathrm{MeV}^2$ and quantization effects occur at the nuclear scale. The thermal evolution of magnetars in particular is also a subject worth exploring as magnetars make up the hottest observed NSs and have rich phenomenology for the purposes of x-ray astronomy that will be affected by how they age and cool [186].

When many LL are available, one can make the quasiclassical (QC) approximation and treat the levels as nearly continuous. The DU rate in the presence of a strong magnetic field has been calculated in Refs. [42,184,185] in the QC approximation, giving useful formulae at NS densities for magnetic fields $B \lesssim 10^{15}$ G, and in the limit of super-strong fields $B \gtrsim 10^{18}$ G where all of the charged particles are confined to the lowest LL. In this work, we address the region in between the quasiclassical and strong field limits where a finite number of LL are occupied and quantization effects cannot be neglected. Recent work in Ref. [187] extended the quasiclassical result to high temperatures relevant for NS mergers, incorporating a finite isospin chemical potential necessary at high temperatures first discussed in Refs. [24, 188]. Our calculation differs from theirs in that our matrix element is fully relativistic and we consider lower temperatures where the isospin chemical potential is insignificant, but where quantization effects are important and the proton anomalous magnetic moment cannot be neglected. A similar calculation was also performed in Ref. [189] where mean field and relativistic effects were included, taking the low temperature limit and setting the momenta of the particles to their Fermi momenta. We find that even at temperatures as low as a few keV, this is a troublesome approximation due to quantization effects and also perform our calculation higher temperatures than they considered.

The case of a finite number of populated LL has been studied in the context of supernovae [16, 190] where neutrino processes in hot, low density matter were considered, including terms up to $\mathcal{O}(k/M_N)$ for M_N the nucleon mass. Those works found modest modifications to the neutrino cross section at field strengths of 10^{16} G and temperatures of a few MeV. This work is complementary, first considering high density matter at keV to MeV temperatures and later considering low density matter at temperatures exceeding an MeV and stronger fields. Our high density calculation is fully relativistic for the V-A weak

Lagrangian going beyond $\mathcal{O}(k/M_N)$ used by previous authors, but does not include additional terms in the weak nucleon current as is done in Ref. [16]. We defer this improvement to future work. At low density, we apply the same tools for stronger fields and at similar and higher temperatures than considered by Refs. [16, 190] which may have applications to simulations of binary NS mergers. It is expected that magnetic fields in some regions of the merger remnant may be as strong as 10^{17} G, strongly modifying particle dispersions and opacities [191, 192]. If the opacity for neutrinos is strongly amplified in regions of the merger remnant, this may have implications for the viability of the r-process nucleosynthesis which sensitively depends on the proton fraction. Detailed thermal simulations of supernovae and neutron star mergers may also need to include these effects as the densities at which neutrinos decouple can be significantly modified, especially for low energy neutrinos.

In Sec. 4.2 we describe our nuclear Lagrangian and the modifications the magnetic field and nuclear mean field potentials make to the nucleon and lepton wavefunctions. In Sec. 4.3 we calculate the full DU emissivity, including the effects of interactions, relativity, and Landau quantization (LQ). The calculation of Fermi-Dirac factors and integration over phase space is complicated by singularities in the density of states and must be treated carefully. We present a semi-analytic (SA) approximation to this calculation and discuss computational approaches to performing the full integration in each Landau level. We then give results for the DU rate in NSs. Turning to neutrino absorption, Sec. 4.4 gives expressions for neutrino opacities at low density and discusses appropriate approximations for this energy regime. We then present results for the neutrino opacity, comparing to prior results that were calculated at more modest magnetic field. Sec. 4.5 summarizes our results and concludes.

4.2 Nuclear model and wavefunctions

To include the effects of nuclear interactions, we use a relativistic mean field model (RMF) (for a review, see Ref. [193]). The charged particle species also couple to the electromagnetic field.

$$\begin{aligned}\mathcal{L} = &\sum_{i=n,p} \overline{\psi}_i \left[i\partial\!\!\!/ - g_\omega \omega \gamma^0 - \frac{1}{2} g_\rho \rho \gamma^0 \tau_3 + e\frac{1+\tau_3}{2} A\!\!\!/ - (M_N - g_\sigma \sigma) \right] \psi_i + \mathcal{L}_{\sigma\omega\rho} \\ &+ \frac{G_F \cos\theta_c}{\sqrt{2}} (L^\dagger_\mu N^\mu + N^\dagger_\mu L^\mu) + \sum_{\ell=e,\mu} \overline{\psi}_\ell (i\partial\!\!\!/ - eA\!\!\!/ - m_\ell)\psi_\ell + \overline{\psi}_\nu i\partial\!\!\!/ P_L \psi_\nu - \frac{1}{4} F_{\mu\nu}F^{\mu\nu}\end{aligned} \tag{4.1}$$

where τ_3 is the third Pauli matrix in isospin space, P_L projects onto the left-handed neutrino, G_F is the Fermi constant, and the Cabibbo angle $\theta_c \approx 13°$. We use the standard notation $v\!\!\!/ = v^\mu \gamma_\mu$. The charged weak currents L^μ and N^μ are given by

$$L^\mu = \overline{\psi}_\nu \gamma^\mu (1 - \gamma^5) \psi_e \tag{4.2}$$

$$N^\mu = \overline{\psi}_p \gamma^\mu (g_V - g_A \gamma^5) \psi_n \tag{4.3}$$

where $g_V = 1$ and $g_A = 1.27$ are the vector and axial vector form factors of the nucleon. Since the contribution of muons to any weak processes is suppressed by their large mass and low density, we do not consider muonic charged current interactions. The σ, ω, and ρ meson fields take on their mean field value given by their equations of motion, enforcing charge neutrality and beta equilibrium. These modify the in-medium effective mass and dispersion of the nucleons given by $E(k) = \sqrt{k^2 + M^{*2}} + U$ where $M^* = M_N - g_\sigma \langle \sigma \rangle$ and $U = g_\omega \langle \omega \rangle \pm g_\rho \langle \rho \rangle / 2$ where the plus sign is for protons and the minus for neutrons. $\mathcal{L}_{\sigma\omega\rho}$ contains the free Lagrangian for the meson fields as well as meson-meson interactions which are tuned to reproduce known properties of nuclear matter and finite nuclei (see Refs. [46, 193] for details). We use the IUFSU* choice of RMF parameters from Ref. [46] because it produces NSs with maximum mass $M_{\text{TOV}} \simeq 2M_\odot$ and $R_{1.4} \simeq 12\,\text{km}$, in line with observational constraints [27, 28, 39, 40, 194–197]. Additionally, the Direct Urca threshold for IUFSU* is approximately $4n_{\text{sat}}$, well above the central density of the canonical $1.4M_\odot$ NS we shall focus on. For fields less than 10^{18} G, the calculated equation of state, particle densities, and Fermi momenta are nearly identical whether or not one includes the effects of LQ. We do not implement anomalous magnetic moments at the Lagrangian level and instead modify the dispersion following Ref. [198]. This has the advantage of making shifts to available LL intuitive, but produces discrepancies with a more detailed microphysical approach at order eB/M^2 (cf. Refs. [189,199]) which are negligible for field strengths we consider. This gives a dispersion for the proton:

$$E_p(k_{zp}, n_p, s) = \sqrt{k_{zp}^2 + M^{*2} + 2n_p eB - (g-2)eBs} + U_p \tag{4.4}$$

where s is the spin of the proton ($\pm 1/2$) and g is the gyromagnetic ratio of the proton. For the proton, $g \simeq 5.6$, making this an important contribution when determining when new LLs become available for each choice of spin. The electron and muon have $g \simeq 2.002$ and the anomalous magnetic moment can be ignored. The neutron also has an anomalous magnetic moment of a similar scale to the proton, but since the density of states for the neutron is smooth, the effect of the anomalous magnetic moment is unimportant at high density, contributing about an MeV to the energy of the neutron at the strongest field strengths we consider. At low density, the magnetic energy of the neutron is a sizable fraction of the neutron energy and of the same order as the mass splitting of the proton and neutron and must be included.

Following Ref. [183] we consider a magnetic field in the $\hat{z}$ direction and a vector potential in a symmetric gauge.

$$\vec{A} = \frac{B}{2}(-y, x, 0) \tag{4.5}$$

Solving the Dirac equation with such a potential gives quantized wavefunctions for the electron and proton.

$$I_{n,r}(x) \equiv \sqrt{\frac{r!}{n!}} e^{-x/2} x^{(n-r)/2} L_r^{n-r}(x) \tag{4.6}$$

L_r^{n-r} is a generalized Laguerre polynomial, n indexes the LL of the wavefunction, and $r \leq n$ indexes the degeneracy of each level. If n or r is negative, this is set to zero. The dimensionless argument x takes the form $eBx_\perp^2/2$ in the wavefunction where $x_\perp$ is the radial coordinate perpendicular to the direction of the magentic field.

We add modifications to the spinors to clarify the normalization and include mean field effects. Note that we retain the dimension of the space L to make clear how the unusual dimensional scaling of the emissivity is resolved. From here on, we use M to refer to the in-medium effective mass of the nucleon $M = M_N - g_\sigma \langle \sigma \rangle$ and M_L^* to refer to the Landau effective mass $M_L^* = k/(\partial E/\partial k)$. For leptons, there are no modifications to the dispersion from interactions and the Landau effective mass is just the energy of the lepton. For nucleons in a mean field model, $M_L^* = E - U$. The electron wavefunction is given by the following [183].

$$\psi_e = \sqrt{E_e} \frac{e^{-i(E_e t - k_{ze} z)} e^{i(n_e - r_e)\phi}}{\sqrt{2\pi L/eB}} u_e^{(s)} \tag{4.7}$$

$$u_e^{(\uparrow)} = \begin{bmatrix} e^{-i\phi} I_{n_e-1,r_e}(eB\xi^2/2) \\ 0 \\ \frac{k_{ze}}{E_e} e^{-i\phi} I_{n_e-1,r_e}(eB\xi^2/2) \\ \frac{i\sqrt{2n_e eB}}{E_e} I_{n_e,r_e} \end{bmatrix}, \; u_e^{(\downarrow)} = \begin{bmatrix} 0 \\ I_{n_e,r_e}(eB\xi^2/2) \\ -\frac{i\sqrt{2n_e eB}}{E_e} e^{-i\phi} I_{n_e-1,r_e} \\ -\frac{k_{ze}}{E_e} I_{n_e,r_e}(eB\xi^2/2) \end{bmatrix} \tag{4.8}$$

Note that the electron spin up spinor is zero if $n = 0$ since there is no spin up state in the lowest LL. The proton wavefunctions are the same as for the electron, but with a non-zero mass, nuclear interactions, and flipped charge.

$$\psi_p = \sqrt{M_{Lp}^* + M} \frac{e^{-i(E_p t - k_{zp} z)} e^{-i(n_p - r_p)\phi}}{\sqrt{2\pi L/eB}} u_p^{(s)} \tag{4.9}$$

$$u_p^{(\uparrow)} = \begin{bmatrix} I_{n_p,r_p}(eB\xi^2/2) \\ 0 \\ \frac{k_{zp}}{M_{Lp}^*+M} I_{n_p,r_p}(eB\xi^2/2) \\ -\frac{i\sqrt{2n_p eB}}{M_{Lp}^*+M} e^{i\phi} I_{n_p-1,r_p} \end{bmatrix}, \; u_p^{(\downarrow)} = \begin{bmatrix} 0 \\ e^{i\phi} I_{n_p-1,r_p}(eB\xi^2/2) \\ \frac{i\sqrt{2n_p eB}}{M_{Lp}^*+M} I_{n_p,r_p} \\ -\frac{k_{zp}}{M_{Lp}^*+M} e^{i\phi} I_{n_p-1,r_p}(eB\xi^2/2) \end{bmatrix} \tag{4.10}$$

The neutron and neutrino spinors are standard.

$$\psi_n = \sqrt{M_{Ln}^* + M} \frac{e^{-ik_n \cdot x}}{L^{3/2}} u_n^{(s)} \tag{4.11}$$

$$u_n^{(s)} = \begin{bmatrix} \chi^{(s)} \\ \frac{\sigma\cdot k}{M^*_{Ln}+M}\chi^{(s)} \end{bmatrix} \tag{4.12}$$

where $\chi^{(s)}$ is a two component vector in spin space. The antineutrino wavefunction is similar.

$$\psi_{\overline{\nu}} = \sqrt{E_\nu}\frac{e^{ik_\nu\cdot x}}{L^{3/2}}v_\nu^{(s)} \tag{4.13}$$

$$v_\nu^{(s)} = \begin{bmatrix} -\frac{\sigma\cdot k_\nu}{E_\nu}\chi^{(s)} \\ \chi^{(s)} \end{bmatrix} \tag{4.14}$$

The positron and neutrino wavefunctions are analogous. We will use the following identities along with standard trace techniques to calculate the matrix element:

$$\sum_s u_n^{(s)}\overline{u}_n^{(s)} = \frac{\tilde{\not{k}}_n + M}{M^*_{Ln}+M} \tag{4.15}$$

$$\sum_x v_\nu^{(s)}\overline{v}_n^{(s)} = \frac{\not{k}_\nu}{E_\nu} \tag{4.16}$$

The tilde indicates additional mean field effects on the normal spin sum.

$$\tilde{k}_n = \begin{bmatrix} M^*_{Ln} & k_{xn} & k_{yn} & k_{zn} \end{bmatrix} \tag{4.17}$$

4.3 Direct Urca Emissivity

4.3.1 Reduced matrix element

To summarize the contributions of the wavefunctions and spatial integrations, we calculate a reduced matrix element for β decay defined as

$$\begin{aligned} \mathcal{M}_{\text{red}} = (M^*_{Ln}+M)\frac{eB}{2\pi L^2}\sum_{spins}\sum_{r_e,r_p}\Big|\int d^2x_\perp e^{i(k_{\perp n}-k_{\perp\nu})\cdot x_\perp}e^{-i(n_e-r_e-n_p+r_p)\phi} \\ \times(\bar{u}_p\gamma^\mu(g_V-g_A\gamma^5)u_n)(\bar{u}_e\gamma_\mu(1-\gamma^5)v_\nu)\Big|^2. \end{aligned} \tag{4.18}$$

Since the neutrino momentum is order T and the neutron momentum is order $\sqrt{2M\varepsilon_F}$ at high density and $\sqrt{2MT}$ at low density where ε_F is the Fermi energy of the neutron, make the approximation $k_{\perp n} - k_{\perp\nu} \approx k_{\perp n}$. Using the following formula from Refs. [16, 200], the spatial integration can be carried out.

$$\begin{aligned} &\int_0^\infty x_\perp dx_\perp \int_0^{2\pi} d\phi\, e^{ik_{\perp n}\cdot x_\perp - i(n_e-r_e-n_p+r_p)\phi} I_{n_p,r_p}(eBx_\perp^2/2) I_{n_e,r_e}(eBx_\perp^2/2) \\ &= \frac{2\pi}{eB} i^{n_e-r_e-n_p+r_p} e^{-i(n_e-r_e-n_p+r_p)\phi_n} I_{n_e,n_p}(k_{\perp n}^2/2eB) I_{r_e,r_p}(k_{\perp n}^2/2eB) \end{aligned} \tag{4.19}$$

This allows us to make many simplifications. Note that while some elements in the spinor may have index n or $n-1$, all of them have the same r, so every term in $\mathcal{M}_{\text{red}}$ has a common factor $I^2_{r_e,r_p}$. Using the following two identities, this term can be simplified:

$$\sum_r I_{n,r}(x) I_{n',r}(x) = \delta_{n,n'} \tag{4.20}$$

$$\sum_r 1 = \frac{eBL^2}{2\pi} \tag{4.21}$$

The normalization $eB/2\pi L^2$ exactly cancels with this term and the prefactor from the spatial integration. Additionally, notice that all final terms in the sum will have the same factors of i and $e^{i\phi_n}$ except for the terms with explicit $e^{\pm i\phi} I_{n-1,r}$. After cancelling out the global phase, the matrix element can be calculated simply by taking the spin sum of the product of the currents in the second line of Eq. (4.18) squared, with the following substitutions.

$$e^{\pm i\phi} \to \mp i e^{\pm i\phi_n},\ I_{n,r} I_{n',r'} \to I_{n,n'} \tag{4.22}$$

To analytically continue to cases where $n - n' < 0$, use the following identity.

$$I_{n,n'}(x) = (-1)^{n-n'} I_{n',n} \tag{4.23}$$

We use a trick to calculate the contribution of the spinors for the charged particles. Define a set of four-vectors a, b, c, and d:

$$\sum_s u_e^{(s)} \overline{u}_e^{(s)} = \not{a}_e + \gamma^0 \not{b}_e + \not{c}_e \gamma^5 + \gamma^0 \not{d}_e \gamma^5 \tag{4.24}$$

$$u_p^{(s)} \overline{u}_p^{(s)} = \not{a}_p^{(s)} + \gamma^0 \not{b}_p^{(s)} + \not{c}_p^{(s)} \gamma^5 + \gamma^0 \not{d}_p^{(s)} \gamma^5 \tag{4.25}$$

While it is convenient to sum over spins for the electron, for the proton the matrix element for each spin must be calculated separately since the large anomalous magnetic moment of the proton means different LL are available for each spin. This decomposition of the matrix is equivalent to a decomposition into scalar, vector, tensor, axial vector, and pseudoscalar terms, but is written in such a way to easily utilize trace identities. The spin sums for charged particles in a magnetic field has been calculated in Ref. [201] (see also the calculation in Ref. [189]), but we prefer this approach as it makes the traces more straightforward and the intermediate expressions more compact. The coefficients of $a-d$ are easily found with the help of Mathematica or equivalent.

In terms of these vectors, the square of the currents can be found simply. The nucleon current gives the following.

$$\begin{aligned}(\overline{u}_p^{(s)}\gamma^\alpha(g_V - g_A\gamma^5)u_n)(\overline{u}_p^{(s)}\gamma^\beta(g_V - g_A\gamma^5)u_n)^\dagger &= (g_V^2 + g_A^2)\mathrm{Tr}[\gamma^\alpha \tilde{\not{k}}_n \gamma^\beta(\not{a}_p^{(s)} + \not{c}_p^{(s)}\gamma^5)] \\ &+ 2g_V g_A \mathrm{Tr}[\gamma^\alpha \tilde{\not{k}}_n \gamma^\beta(\not{c}_p^{(s)} + \not{a}_p^{(s)}\gamma^5)] + M(g_V^2 - g_A^2)\mathrm{Tr}[\gamma^\alpha\gamma^\beta\gamma^0(\not{b}_p^{(s)} + \not{d}_p^{(s)}\gamma^5)]\end{aligned} \tag{4.26}$$

The leptonic current is given by

$$(\overline{u}_e\gamma_\alpha(1-\gamma^5)v_\nu)(\overline{u}_e\gamma_\beta(1-\gamma^5)v_\nu)^\dagger = 2\mathrm{Tr}[\gamma_\alpha \hat{\not{k}}_\nu \gamma_\beta(\not{a}_e + \not{c}_e)(1+\gamma^5)]\,. \tag{4.27}$$

Taking the traces and dropping terms that vanish after doing the neutrino angular integration, this takes a compact form.

$$\begin{aligned}\mathcal{M}_{\mathrm{red}} = 64[&(g_V + g_A)^2 M_{Ln}^*(a_e + c_e)\cdot(a_p + c_p) + (g_V - g_A)^2(a_p^0 - c_p^0)\tilde{k}_n \cdot (a_e + c_e) \\ &+ M(g_V^2 - g_A^2)(\vec{d}_p \cdot (\vec{a}_e + \vec{c}_e) - b_p^0(a_e^0 + c_e^0)]\end{aligned} \tag{4.28}$$

For the final matrix element, use the following shorthand.

$$[e^\pm] = 1 \pm \frac{k_{ze}}{E_e},\ [p_z^\pm] = \left(1 \pm \frac{k_{zp}}{M_{Lp}^* + M}\right)^2,\ [p_B] = \left(\frac{\sqrt{2n_p eB}}{M_{Lp}^* + M}\right)^2 \tag{4.29}$$

Filling in the final values for *a*–*d* and dropping terms that go to zero after integrating over ϕ_n, gives the final matrix element with the argument of all the I_{n_1,n_2} functions being $k_{\perp n}^2/2eB$. For spin up protons:

$$\begin{aligned}\mathcal{M}_{\mathrm{red}}^\uparrow = {}& 16(g_V + g_A)^2 M_{Ln}^*\Bigg[I_{n_e,n_p}^2[p_z^-][e^+] + I_{n_e-1,n_p-1}^2[p_B][e^-] \\ &+ 2I_{n_e,n_p}I_{n_e-1,n_p-1}\left(1 - \frac{k_{zp}}{M_{Lp}^* + M}\right)\frac{2eB\sqrt{n_e n_p}}{(M_{Lp}^* + M)E_e}\Bigg] \\ &+ 8(g_V - g_A)^2\Bigg[(M_{Ln}^* - k_{zn})(I_{n_e,n_p}^2[p_z^+][e^+] + I_{n_e,n_p-1}^2[p_B][e^+] \\ &+ (M_{Ln}^* + k_{zn})(I_{n_e-1,n_p}^2[p_z^+][e^-] + I_{n_e-1,n_p-1}^2[p_B][e^-])\Bigg] \\ &+ 16(g_V^2 - g_A^2)M\Bigg[I_{n_e,n_p}^2\left(-1 + \frac{k_{zp}^2}{(M_{Lp}^* + M)^2}\right)[e^+] + I_{n_e-1,n_p-1}^2[p_B][e^-] \\ &- 2I_{n_e,n_p}I_{n_e-1,n_p-1}k_{zp}\frac{2eB\sqrt{n_e n_p}}{(M_{Lp}^* + M)^2 E_e}\Bigg]\end{aligned} \tag{4.30}$$

For spin down protons:

$$\begin{aligned}
\mathcal{M}^{\downarrow}_{\text{red}} = 16(g_V+g_A)^2 M^*_{Ln}\Big[& I^2_{n_e,n_p}[p_B][e^+] + I^2_{n_e-1,n_p-1}[p_z^+][e^-] \\
& + 2I_{n_e,n_p}I_{n_e-1,n_p-1}\left(1+\frac{k_{zp}}{M^*_{Lp}+M}\right)\frac{2eB\sqrt{n_e n_p}}{(M^*_{Lp}+M)E_e}\Big] \\
& + 8(g_V-g_A)^2\Big[(M^*_{Ln}-k_{zn})(I^2_{n_e,n_p}[p_B][e^+] + I^2_{n_e,n_p-1}[p_z^-][e^+] \\
& + (M^*_{Ln}+k_{zn})(I^2_{n_e-1,n_p}[p_B][e^-] + I^2_{n_e-1,n_p-1}[p_z^-][e^-])\Big] \\
& + 16(g_V^2-g_A^2)M\Big[I^2_{n_e,n_p}[p_B][e^+] + I^2_{n_e-1,n_p-1}\left(-1+\frac{k^2_{zp}}{(M^*_{Lp}+M)^2}\right)[e^-] \\
& + 2I_{n_e,n_p}I_{n_e-1,n_p-1}k_{zp}\frac{2eB\sqrt{n_e n_p}}{(M^*_{Lp}+M)^2E_e}\Big]
\end{aligned} \tag{4.31}$$

Integrating over momenta and adding normalizations gives the total neutrino emissivity, doubled to account for the reverse process.

$$\begin{aligned}
Q = 2\,\frac{eBG_F^2\cos^2\theta_c}{4\pi} & \sum_{s_p=\{\uparrow,\downarrow\}}\sum_{n_e,n_p}\int \frac{d^3k_\nu}{2E_\nu(2\pi)^3}\frac{d^3k_n}{2M^*_{Ln}(2\pi)^3}\frac{dk_{zp}}{2M^*_{Lp}(2\pi)}\frac{dk_{ze}}{2E_e(2\pi)} \\
& \times (M^*_{Lp}+M)E_eE_\nu\, n_{FD}(E_n-\mu_n)\, n_{FD}(\mu_p-E_p)\, n_{FD}(\mu_e-E_e)\mathcal{M}^{(s_p)}_{\text{red}} \\
& \times (2\pi)^2\delta(E_n-E_p-E_e-E_\nu)\delta(k_{zn}-k_{zp}-k_{ze}-k_{z\nu})
\end{aligned} \tag{4.32}$$

where $n_{FD}(E-\mu) = (\exp[(E-\mu)/T]+1)^{-1}$ is the Fermi-Dirac distribution. The angular integration is done in a straightforward way by noticing that k_ν is much smaller than all the other momenta and removing it from the momentum δ-function. We add an explicit sum over the sign of k_{zp} and k_{ze} and set the limits of integration to $[0,\infty)$. $\Theta(x)$ is a step function that is one if $x \geq 0$ and zero otherwise.

$$\sum_{k_z\text{signs}}\int d\Omega_n\, d\Omega_\nu\, \delta(k_{zn}-k_{zp}-k_{ze}) = \frac{8\pi^2}{k_n}\sum_{k_z\text{signs}}\Theta(k_n-|k_{zp}+k_{ze}|) \tag{4.33}$$

The δ-function is used to set the value of k_{zn} which along with $k_{\perp n}$ in the matrix element should be set based on the values of k_{zp} and k_{ze}. Note that in the process of this integration, we did free integrals $d\Omega_\nu$ and $d\phi_n$. These cause many terms in the matrix element to cancel, which we have already accounted for.

4.3.2 Levels of approximation

Calculating the phase space integral has the first major deviation from the standard DU calculation. We must calculate

$$Q = \frac{eBG_F^2\cos^2\theta_c}{256\pi^5}\sum_{n_e,n_p}\sum_{s_p=\pm}\frac{M^*_{Lp}+M}{M^*_{Lp}}\Phi\,, \tag{4.34}$$

where Φ is given by

$$\begin{aligned}\Phi(n_e, n_p, s_p) = \int \frac{k_n d|k_n|}{M^*_{Ln}}\, E_\nu^3\, dE_\nu\, d|k_{zp}|\, d|k_{ze}|\, n_{FD}(E_n - \mu_n)\, n_{FD}(\mu_p - E_p) \\ \times\, n_{FD}(\mu_e - E_e)\delta(E_n - E_p - E_e - E_\nu)\, \mathcal{M}^{(s_p)}_{\text{red}}\,. \end{aligned} \tag{4.35}$$

For $B \lesssim 10^{16}$ G, LL are spaced closely together and a quasiclassical (QC) approximation can be made, disregarding effects of LQ [185]. The emissivity is given by $Q = R_B Q^0_\nu$ where Q^ν_0 is the emissivity for zero magnetic field given by [42]

$$Q^0_\nu = \frac{457\pi G_F^2 \cos^2\theta_c(1+3g_A^2)}{10080} M^*_{Ln} M^*_{Lp} \mu_e T^6 \tag{4.36}$$

and R_B quantifies the amount of suppression from being in the "forbidden region" where DU is not normally allowed. In the forbidden region, the QC suppression R^{qc}_B is given by [185]

$$\begin{aligned} R^{\text{qc}}_B &= 2\int d\cos\theta_p\, d\cos\theta_e \frac{k_{Fp}k_{Fe}}{4eB} I^2_{n_p,n_e} \Theta(k_{Fn} - |k_{Fp}\cos\theta_p + k_{Fe}\cos\theta_e|) && (4.37)\\ &\approx 2^{-2/3}\int_{-\infty}^{\infty} ds \int_0^\pi d\theta\, \sin^{2/3}\theta\, \text{Ai}^2\left(\frac{x+s^2}{2^{4/3}\sin^{2/3}\theta}\right)\,, && (4.38)\end{aligned}$$

where $x = [k^2_{Fn} - (k_{Fp} + k_{Fe})^2]/(k^2_{Fp} N^{-2/3}_{Fp})$ quantifies how far the density is from the DU threshold. Equation (22) of Ref. [185] gives useful approximate expressions for this integral that we will use when comparing to our results.

To do better, the integral can be performed for each LL separately. Following the spirit of the standard calculation of the DU rate without a magnetic field (see, for example, the appendix of Ref. [202]), the Fermi surface approximation can be made by setting explicit factors of the energy and momenta as being on the Fermi surface in the second expression.

$$\int d|k_{zp}|\, d|k_{ze}|\, n_{FD}(-E_p) n_{FD}(-E_e) \to T^2 \frac{M^*_{Lp}\mu_e}{|k_{Fze}k_{Fzp}|} \int dx_p\, dx_e \frac{1}{e^{-x_e}+1}\frac{1}{e^{-x_p}+1} \tag{4.39}$$

where $x_i = (E_i - \mu_i)/T$. This presents an obvious problem: this expression is infinite at the exact energy where a new LL becomes available, since at that energy $k_z = 0$ in the highest LL on the Fermi surface. This occurs because the density of states has a resonance at these energies. Near the resonance, k_z is small and a large range of k_z corresponds to energies within T of the Fermi surface. Doing the full integral gives an enhancement from the resonance in the density of states. In the highest LLs, finite temperature effects are important, even if $T \ll \varepsilon_F$, since T may be of the same order as k_z^2/E. Additionally, the functions I_{n_e,n_p} oscillate rapidly as a function of $k^2_{\perp n}/2eB$ for large n_e and n_p, and applying a Fermi surface approximation to the argument of I_{n_e,n_p} in order to avoid the computationally costly repeated evaluation of the modified Laguerre polynomial introduces errors.

These resonances were observed in Refs. [187, 189] when calculating the DU rate at low temperature and in Refs. [16, 190] when calculating the neutrino cross section in low density matter and neglecting the nucleon momentum. Including the nucleon momentum is equivalent in our case to doing the full finite temperature momentum integral, smearing out the resonance due to thermal effects.

An analytical approximation to Φ can be used based on the substitution in Eq. (4.39) when the ratios $k_{Fze}^2/\mu_e T$ and k_{Fzp}^2/MT are both not too small for a given pair of LLs. Continuing with the Fermi surface approximation and performing the integrals, the emissivity for a specific LL is given by

$$Q^{\mathrm{FSA}}(n_e, n_p) = eBG_F^2 \cos^2\theta_c T^6 \frac{457\pi}{1290240} \sum_{s_p=\{\uparrow,\downarrow\}} \frac{(M_{Lp}^* + M)\mu_e}{|k_{Fzp}k_{Fze}|} \sum_{k_z \text{signs}} \mathcal{M}_{\mathrm{red}}\,. \tag{4.40}$$

So long as the following conditions are met, this approximation is robust.

$$\cos\theta_p \gg \frac{\sqrt{2M_N T}}{n_p^{1/3}},\ \cos\theta_e \gg \sqrt{\frac{T}{n_e^{1/3}}} \tag{4.41}$$

In what follows, we will use this result for LL with the simple prescription that both $\cos\theta_e$ and $\cos\theta_p$ are greater than 0.2 and neither the electron nor the proton are in their highest two LLs, giving a speed boost of a factor of 5–10. We use these values because the maximum value that the quantity $\sqrt{2M_N T}/n_p^{1/3}$ takes for $T = 100\,\mathrm{keV}$ is about 0.16. The condition that the highest two LL be calculated numerically catches edge cases of poor accuracy at low density. These choices ensure that the dominant contributions to the emissivity (which come from LLs with small k_{Fz}) are computed in full, while speeding up the computation in parameter space that affects the final result less. If a greater speed boost is desired, a more precise implementation of these conditions can be used. We call this the semi-analytic (SA) approximation. The error introduced by the SA approximation is generally low, particularly for low temperatures, and can be made arbitrarily small by adjusting the tolerance lower. The choice of how stringently to use the SA approximation depends on the desire for accuracy versus computational speed.

For the highest few LL, the full integral must be calculated. The integral over the neutron energy can be done analytically.

$$\int_{x_e+x_p}^{\infty} dx_n \frac{(x_n - x_e - x_p)^3}{e^{x_n}+1} = -6\ \mathrm{Li}_4(-e^{-x_e-x_p}) \tag{4.42}$$

$\mathrm{Li}_4(z)$ is the polylogarithm of order 4, defined by $\sum_{k=1}^{\infty} z^k/k^4$ where it converges and its analytic continuation elsewhere. Making the substitution $k_{zi} \to \bar{k}_{zi} \equiv k_{zi}/T$ gives

$$\Phi = -6T^6 \int d\bar{k}_{ze} d\bar{k}_{zp} n_{FD}(-x_e) n_{FD}(-x_p) \mathrm{Li}_4(-e^{-x_e-x_p}) \Theta(k_{Fn} - |k_{zp} + k_{zn}|) \mathcal{M}_{\mathrm{red}}^{(s)}\,. \tag{4.43}$$

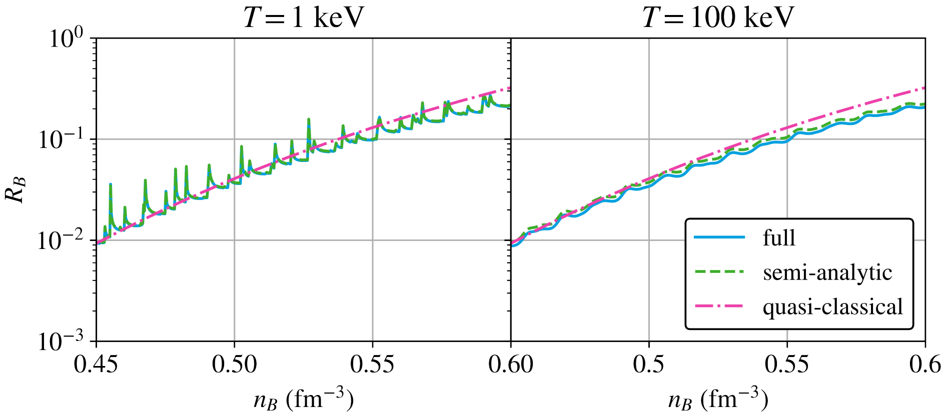

Figure 4.1: R_B comparing the semi-analytic and quasi-classical approximations with the full calculation just below the DU threshold at $B = 5 \times 10^{16}$ G. In the left panel the semi-analytic approximation and full calculation are indistinguishable.

This integral can be found numerically. Figure 4.1 compares R_B in the full calculation with the SA and QC approximations for $B = 5 \times 10^{16}$ G at $T = 1$ keV and 100 keV. Clearly visible at low temperature are the densities at which new LLs become available and there is an enhancement to the emissivity. Since the proton has a large anomalous magnetic moment, there are separate peaks when new LLs become available for electrons and for spin up and spin down protons. The deviation from the QC calculation at high density is due to relativistic corrections that we include that the QC approximation neglects.

Different LL for the proton are spaced much more closely together in energy than for the electron because of the large mass of the proton. When the temperature is of the same order as the energy splitting $T \simeq eB/M$, peaks in the emissivity due to new proton LL become are thermally smeared. For a magnetic field of 10^{16} G this becomes an important effect at $T \gtrsim 100$ keV and LL above the Fermi surface should be included. In contrast, the energy splitting of the electron LL is $\sqrt{eB/4n_e}$ for $n_e \gg 1$. Thermal smearing of electrons becomes important for $n_e \leq 100$ and $B = 10^{16}$ G only when $T \gtrsim 1$ MeV. Once the star is more than a few seconds old, thermal smearing of electron LL can be neglected for such strong fields.

4.3.3 Solutions to computational challenges

Computing $I_{n,r}(x)$ is the main bottleneck for the calculation of the full emissivity (and later the opacity). A significant improvement can be gained by using the identity

$$L_r^{n-r}(x) \to \binom{n}{r} M(-r, n-r+1, x) \tag{4.44}$$

to remove the need for recursive computation of Laguerre polynomials. To get a more significant improvement for modest densities, we pre-compute $I_{n_e,n_p}(x)$ for $n_e, n_p \leq 250$. For a given pair of indices

n_e and n_p, $I_{n_e,n_p}(k_{\perp n}^2/2eB)$ is mostly confined to the region

$$2eB(\sqrt{n_e} - \sqrt{n_p})^2 < k_{\perp n}^2 < 2eB(\sqrt{n_e} + \sqrt{n_p})^2 \,. \tag{4.45}$$

Far above and below this range, the function $I_{n_e,n_p}(k_{\perp n}^2/2eB)$ is suppressed. This condition is equivalent to the requirement that the electron and proton wavefunctions contain transverse momentum components of the same order as the transverse momentum of the neutron. When in the forbidden region, the integral solely samples values of $k_{\perp n}$ near the boundaries of this region and values should be precomputed somewhat beyond these limits. Additionally, I_{n_e,n_p} has $n_e + 1$ extrema if $n_e \leq n_p$ and $n_p + 1$ extrema if $n_p < n_e$. If one of n_e or n_p is small, relatively few points need to be pre-computed to capture the full functional dependence on $k_{\perp n}$.

Based on these observations, the final computation of I_{n_e,n_p} uses a lookup table, with values of $k_{\perp n}$ in the relevant region and precision scaling with the number of extrema. Between the precomputed points, quadratic Lagrange interpolation approximates the value of the function. This reduces the runtime of the function from tens of microseconds to 200-300 nanoseconds, with relative error less than 0.1% for almost all values of $k_{\perp n}$.

4.3.4 Emissivity results

To understand the relevance of our results to the thermal evolution of NSs, we compare the Direct Urca emissivity calculated in the QC approximation, in our SA approximation, and by calculating the full integral. Where relevant, we compare these emissivities to the cooling rates calculated for Modified Urca and bremsstrahlung processes calculated with zero magnetic field.

Figures 4.2 and 4.3 show the emissivity as a function of radius for a $1.4\,M_\odot$ NS with a redshifted temperature $\tilde{T} = 1\,\text{keV}$ and $100\,\text{keV}$ respectively with various choices of magnetic field. We consider a $1.4M_\odot$ NS as a representative example where effects below the Direct Urca threshold are important as, in our equation of state, the entire star is below the Direct Urca threshold. Integrated total emissivity is given in Table 4.1. For a field strength of $2 \times 10^{16}\,\text{G}$, slow cooling is many orders of magnitude more efficient than Direct Urca while for larger fields DU dominates. At $B = 2 \times 10^{16}\,\text{G}$, our results are parametrically lower than the QC approximation because we include relativistic corrections while the QC approximation is non-relativistic. At larger magnetic fields, we find that the QC approximation somewhat underestimates the emissivity but is unexpectedly robust even when only tens of LL are occupied. Since relativistic corrections in general decrease the emissivity we find, a non-relativistic calculation of the full emissivity would find a somewhat larger deviation from the QC approximation, but the results would still be within the same order of magnitude.

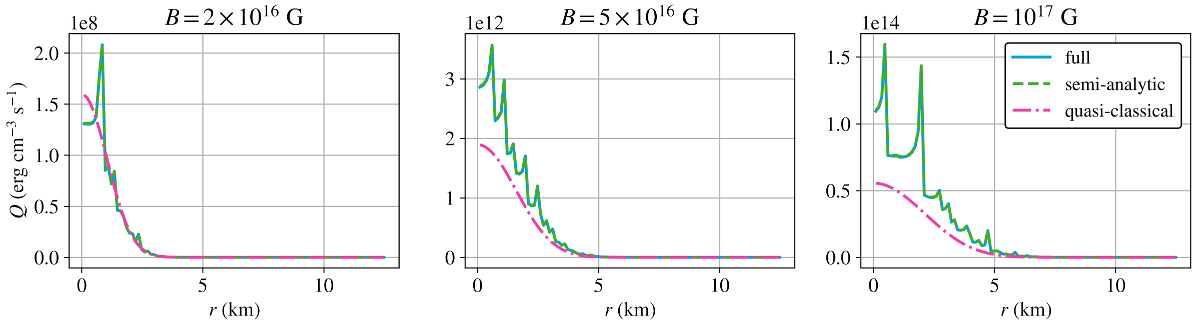

Figure 4.2: Radial profiles of the DU emissivity for various magnetic field strengths in a NS with $M = 1.4M_\odot$ and redshifted temperature $\tilde{T} = 1$ keV. At this temperature, the semi-analytic approximation and full calculation are indistinguishable.

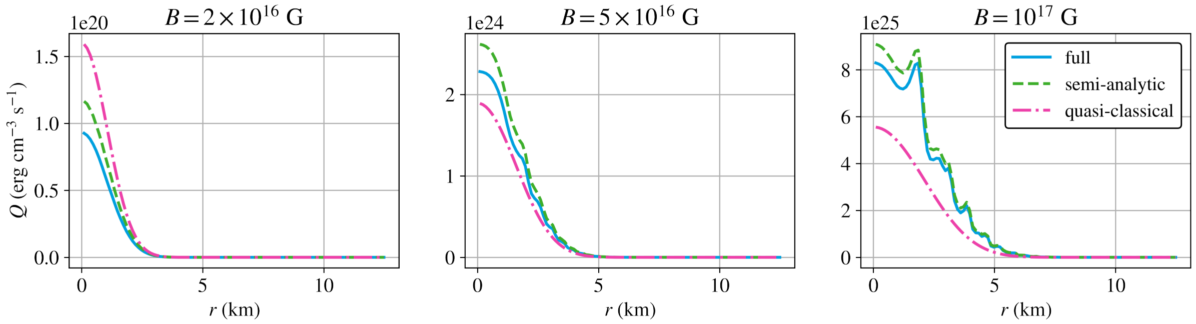

Figure 4.3: Radial profiles of the DU emissivity for various magnetic field strengths in a NS with $M = 1.4M_\odot$ and redshifted temperature $\tilde{T} = 100$ keV.

Table 4.1 gives the total emissivity of a $1.4\,M_\odot$ NS for a variety of temperatures and magnetic fields. Since the peaks due to resonances are averaged over, the enhancement from the full calculation is modest. For the purposes of a simulation of an entire NS to predict its observed surface temperature, this is probably not an important correction. Only if some phenomenon hinges on the thermal behavior of the star at specific densities does this effect become important. It is possible that transport coefficients are one such parameter, with Urca processes being a source of viscosity in neutron star matter [203]. The possibility of a non-monotonic viscosity sourced by resonant Urca processes may have implications for understanding the oscillations of magnetars and should be further studied.

Table 4.1: Total emissivity (erg/s) of a $1.4\,M_\odot$ NS for Direct Urca calculated in full, in the SA approximation, and in the QC approximation in the presence of a strong magnetic field. Slow cooling (Modified Urca and bremsstrahlung) with zero magnetic field shown for comparison.

B (10^{16} G)	$\tilde{T}$ (keV)	Full DU	SA DU	QC DU	Slow ($B = 0$)
2	1	2.83×10^{24}	2.84×10^{24}	2.74×10^{24}	5.40×10^{24}
2	100	1.65×10^{36}	2.05×10^{36}	2.74×10^{36}	5.40×10^{40}
5	1	1.67×10^{29}	1.68×10^{29}	1.05×10^{29}	5.40×10^{24}
5	100	1.35×10^{41}	1.56×10^{41}	1.05×10^{41}	5.40×10^{40}
10	1	1.48×10^{31}	1.49×10^{31}	6.89×10^{30}	5.40×10^{24}
10	100	1.33×10^{43}	1.45×10^{43}	6.89×10^{42}	5.40×10^{40}

4.4 Neutrino Opacities

4.4.1 Low density conditions

The same tools we use to calculate the DU emissivity can be applied to calculate the opacity for neutrinos to capture on neutrons ($\nu + n \to e + p$) and for antineutrinos to capture on protons ($\bar{\nu} + p \to e^+ + n$). In the ejecta from a NS merger, the neutrino decoupling region ranges from $T \simeq 10\,\text{MeV}$ and $n \simeq 0.1\, n_{\text{sat}}$ for soft neutrinos ($E_\nu \sim 3\,\text{MeV}$) to $T \simeq 2\,\text{MeV}$ and $n \simeq 10^{-5}\, n_{\text{sat}}$ for harder neutrinos ($E_\nu \sim 50\,\text{MeV}$) [204]. Magnetohydrodynamic instabilities in the merger remnant can amplify the magnetic field of the merging NSs by many orders of magnitude, possibly larger than 10^{16} G [191, 192]. We calculate modifications to the neutrino opacity in the merger environment due to magnetic fields. This is similar to previous calculations performed in Refs. [16, 190] where minimal deviation from the zero field result was found, but we will consider stronger magnetic fields and higher densities where Maxwell-Boltzmann statistics they utilize are no longer appropriate and final state blocking becomes relevant.

The opacity for neutrinos capturing on neutrons not including the effects of stimulated absorption is given by

$$\begin{aligned}\kappa_{\nu n} = \frac{G_F^2 \cos^2\theta_c eB}{64\pi^3} \sum_{\substack{s_n,s_p\\ n_e,n_p}} \int dk_{ze}\, dk_{zp}\, E_n \Theta(k_n - |k_{zp} + k_{ze} - k_{z\nu}|) \mathcal{M}_{\text{red}}^{(s_n,s_p)} \\ \times\, n_{FD}(E_n - \mu_n) n_{FD}(\mu_p - E_p) n_{FD}(\mu_e - E_e)\,.\end{aligned} \tag{4.46}$$

To include stimulated absorption, this quantity should be multiplied by $1/(1-\mathcal{F}'_\nu)$ for $\mathcal{F}_\nu$ the invariant distribution function for neutrinos that need not be in chemical equilibrium. Note that we are using a different normalization for the reduced matrix element at low density so that it is dimensionless and does not have an internal sum over the neutron spin since at low density the neutron anomalous magnetic moment is important. The opacity for antineutrinos capturing on protons is given by

$$\begin{aligned}\kappa_{\bar{\nu} p} = \frac{G_F^2 \cos^2\theta_c eB}{64\pi^3} \sum_{\substack{s_n,s_p\\ n_e,n_p}} \int dk_{ze}\, dk_{zp}\, E_n \Theta(k_n - |k_{zp} + k_{z\nu} - k_{ze}|) \mathcal{M}_{\text{red}}^{(s_n,s_p)} \\ \times\, n_{FD}(\mu_n - E_n) n_{FD}(E_p - \mu_p) n_{FD}(-\mu_e - E_e)\,.\end{aligned} \tag{4.47}$$

For simplicity, we expand the matrix element to zeroth order in the momentum of the nucleons since we are considering matter well below saturation density. As noted in Ref. [16], one cannot neglect the nucleon momentum when calculating chemical equilibrium and energy conservation without producing spurious infinities, even at low density. However, the matrix element can safely be expanded to low order in the momentum at low density since the dependence is linear in k/M. At this order, and within the approximation $E_\nu \ll \sqrt{2MT} \simeq k_n$, the matrix elements for both processes are the same and are given

Table 4.2: Conditions in which we calculate the opacity

Label	B (G)	T (MeV)
I	5×10^{16}	1
II	5×10^{16}	3
III	10^{17}	1
IV	10^{17}	8

by the following [16].

$$\begin{aligned}
\mathcal{M}_{\text{red}}^{(s_n=+,s_p=+)} &= 2(g_V+g_A)^2\left(1+\frac{k_{ze}}{E_e}\right)(1+\cos\theta_\nu)I^2_{n_e,n_p} \\
&\quad + 2(g_V-g_A)^2\left(1-\frac{k_{ze}}{E_e}\right)(1-\cos\theta_\nu)I^2_{n_e-1,n_p} \\
\mathcal{M}_{\text{red}}^{(s_n=+,s_p=-)} &= 8g_A^2\left(1-\frac{k_{ze}}{E_e}\right)(1+\cos\theta_\nu)I^2_{n_e-1,n_p-1} \\
\mathcal{M}_{\text{red}}^{(s_n=-,s_p=+)} &= 8g_A^2\left(1+\frac{k_{ze}}{E_e}\right)(1-\cos\theta_\nu)I^2_{n_e,n_p} \\
\mathcal{M}_{\text{red}}^{(s_n=-,s_p=-)} &= 2(g_V+g_A)^2\left(1-\frac{k_{ze}}{E_e}\right)(1-\cos\theta_\nu)I^2_{n_e-1,n_p-1} \\
&\quad + 2(g_V-g_A)^2\left(1+\frac{k_{ze}}{E_e}\right)(1+\cos\theta_\nu)I^2_{n_e,n_p-1}
\end{aligned} \tag{4.48}$$

To compare with the literature, we also calculate the cross sections for these processes using Maxwell-Boltzmann statistics for the target nucleon. Figure 4.4 shows the cross section for these two processes (given by the same integration as Eqs. (4.46) and (4.47), without final state blocking and dividing by the target nucleon density) for neutrinos propagating perpendicular to the magnetic field. The orientation of the neutrino momentum was found in Refs. [16,190] to have a very small effect on the neutron branch and almost no effect on the proton branch. As a benchmark, we compare with the cross sections calculated in Ref. [16] at $B = 10^{16}$ G and $T = 2$ MeV and the cross section with no magnetic field. Table 4.2 lists the choices of magnetic field and temperatures we use. At low neutrino energy, the cross section is strongly enhanced by the magnetic field because of the contribution of the anomalous magnetic moment of the neutron shifting the effective mass splitting of the nucleons. For sufficiently large fields, the cross section for capture on protons does not go to zero even for zero neutrino energy because the contribution of the anomalous magnetic moment is of the same order as $m_n + m_e - m_p \simeq 1.8$ MeV.

As expected, the first resonance occurs at higher neutrino energy and enhances the cross section by a much larger factor than at smaller magnetic field. This warrants further inquiry, particularly at a larger range of densities, temperatures, and with the necessary additional angular integrations to safely consider higher neutrino energies. The results of Refs. [16,190] indicate that at large neutrino energy, the opacities should approach the value with zero field with small corrections. Whether the highest energy neutrinos from a neutron star merger are in this regime for such strong fields is unclear.

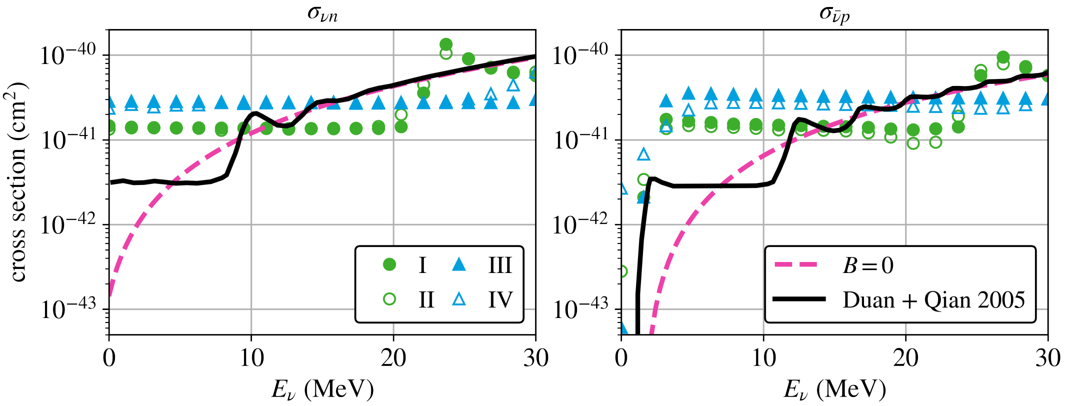

Figure 4.4: Cross sections for neutrinos to capture on nucleons. Green circles correspond to $B = 5\times10^{16}$ G while blue triangles are for $B = 10^{17}$ G. Filled marks are at $T = 1$ MeV while unfilled are at $T = 3$ MeV and 8 MeV, respectively. (See Table 4.2) The black curve for comparison was calculated in Ref. [16] at $B = 10^{16}$ G and $T = 2$ MeV.

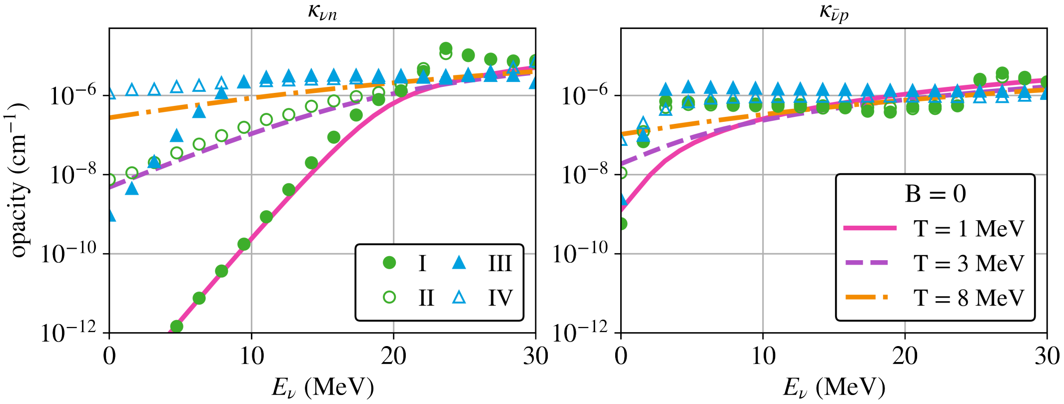

Figure 4.5: Neutrino opacities at $n_B = 0.001\, n_{\text{sat}}$ and $Y_p = 0.25$. Green circles correspond to $B = 5 \times 10^{16}$ G while blue triangles are for $B = 10^{17}$ G. Filled marks are at $T = 1$ MeV while unfilled are at $T = 3$ MeV and 8 MeV, respectively. (See Table 4.2) Curves show results calculated at zero magnetic field.

4.4.2 Opacity results

We calculate $\kappa_{\nu n}$ and $\kappa_{\bar{\nu} p}$ at two densities in the ejecta, $0.1\, n_{\text{sat}}$ and $0.001\, n_{\text{sat}}$ with proton fraction $Y_p = 0.1$ and $Y_p = 0.25$ respectively. Figures 4.5 and 4.6 show our results for $\kappa_{\nu n}$ and $\kappa_{\bar{\nu} p}$ at our low and high density respectively and show the results for the opacity at the same densities and temperatures with no magnetic field.

The most important effects the magnetic field has on the opacity for capturing on neutrons is due to suppression of Pauli blocking of electrons at very low density. At $0.001\, n_{\text{sat}}$ and $Y_p = 0.25$ (Fig. 4.5), a strong magnetic field suppresses the electron chemical potential by a factor of a few because the density is linearly dependent on μ_e when the number of LL is small, bringing the system much closer to beta equilibrium and suppressing Pauli blocking of electrons. This enhances the opacity by many orders of magnitude (compare Conditions I and III in the left panel of Fig. 4.5, both at $T = 1$ MeV but

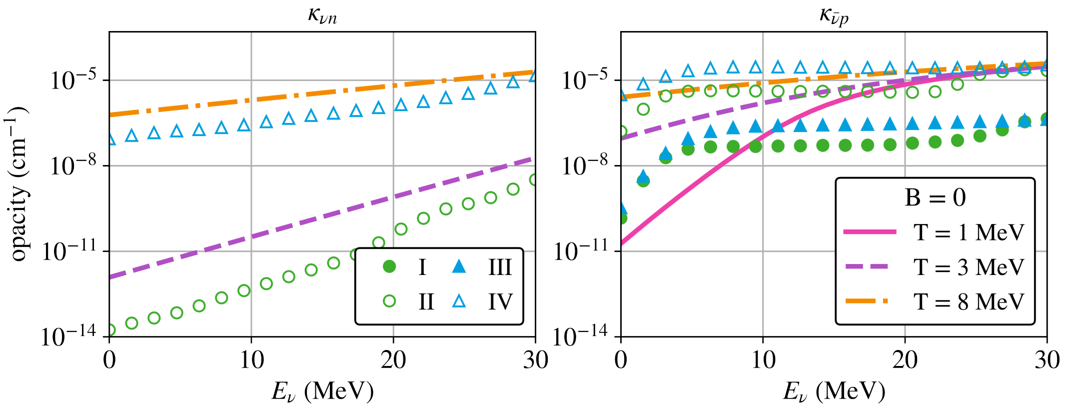

Figure 4.6: Neutrino opacities at $n_B = 0.1\, n_{\rm sat}$ and $Y_p = 0.1$. Green circles correspond to $B = 5 \times 10^{16}$ G while blue triangles are for $B = 10^{17}$ G. Filled marks are at $T = 1$ MeV while unfilled are at $T = 3$ MeV and 8 MeV, respectively. (See Table 4.2) Curves show results calculated at zero magnetic field. At $T = 1$ MeV, the opacity for capture on neutrons is strongly suppressed with or without a magnetic field due to being far out of beta equilibrium.

with different magnetic field strength). At $0.1\, n_{\rm sat}$ and $Y_p = 0.1$ (Fig. 4.6), the electrons are strongly degenerate and the system is far from beta equilibrium, suppressing capture on neutrons even in the presence of a strong magnetic field. The opacity with a magnetic field is suppressed relative to the zero field calculation since the energy available for an electron (approximately $\mu_n - \mu_p + E_\nu$) is only sufficient to populate the lowest few LL. As the neutrino energy is increased, the opacity approaches the zero field value.

For capture on protons, the most important effect for low energy neutrinos is from the magnetic moments of the nucleons. Since this process produces positrons, the leptons are not Pauli blocked. Normally, the opacity for neutrinos with energy $E_\nu < m_e + m_n - m_p$ to capture on protons is suppressed. For the strongest magnetic fields we consider $B \simeq 10^{17}$ G, the energy contribution of the anomalous magnetic moments of the nucleons are of the same order as the positron mass and the mass splitting of the nucleons and this suppression is lifted. In the presence of a strong magnetic field, neutrinos with energies $E_\nu \lesssim 10$ MeV have their opacity to capture on protons enhanced by orders of magnitude due to this effect. For higher energy neutrinos, the opacity is suppressed just like the capture rate on neutrons is suppressed at $0.1\, n_{\rm sat}$ due to only being able to access the lowest few LLs. At higher neutrino energies once many LL can be populated, the opacity will approach the zero field value.

4.5 Conclusion

In this work, we calculate the Direct Urca emissivity in the presence of magnetic fields $B \geq 2 \times 10^{16}$ G including the effects of Landau quantization and full relativity for the V-A weak Lagrangian. We find that relativistic corrections tend to suppress the emissivity, but that the often utilized quasiclassical approximation of Ref. [185] underestimates the emissivity for fields $B \geq 5 \times 10^{16}$ G. We present a semi-analytic approximation, in which analytic results within the Fermi surface approximation given by Eq. (4.40) are used for Landau levels far from resonance and the full phase space integral given by Eq. (4.35) is calculated for the highest few Landau levels. The semi-analytic approximation captures resonances at specific densities that the quasiclassical approximation misses, especially at low temperatures. When calculating the emissivity of an entire neutron star, we find that the quasiclassical approximation is correct to within less than an order of magnitude even for these very large fields and the high thermal conductivity of the core likely washes out these resonances when considering global thermal evolution. Whether these resonances might have implications for transport warrants further study.

Applying the same techniques, we calculate neutrino opacities in conditions relevant for binary neutron star merger ejecta at magnetic fields $B \geq 5 \times 10^{16}$ G. We find significant enhancement to the rates of absorption at these strong fields for low energies neutrinos relative to the zero field result. This is due to the large anomalous magnetic moments of the nucleons and suppression of the electron chemical potential by the magnetic field at low density. If small regions of strong magnetic fields develop in the ejecta of a neutron star merger, neutrino capture would be locally enhanced, the neutrinosphere could become distorted, and the proton fraction in these regions would be changed. These results motivate a more exhaustive study of neutrino opacities at superstrong magnetic fields which may have important implications for neutrino transport and nucleosynthesis in binary neutron star merger simulations. Initial progress on this topic is summarized in App. C where analytic expressions in different regimes of neutrino energy and magnetic field are given applicable at low density.

Chapter 5

The Kohn-Luttinger effect in dense matter and its implications for neutron stars[1]

5.1 Introduction

The discovery of massive neutron stars by radio observations of pulsars [27, 28, 194] confirmed that the maximum mass of neutron stars $M_{\max} > 2\ M_{\odot}$, and gravitational wave and x-ray observations constrain the radius of a neutron star with mass $\simeq 1.4\ M_{\odot}$ to the range $11 - 13$ km [39, 40, 195–197]. These constraints and theoretical calculations of the EOS of neutron-rich matter at $n_B \lesssim 2n_{sat}$ [30,172,205–207], taken together strongly suggest a rapid increase in the pressure and the speed of sound in the NS core [208]. This, in turn, implies strong repulsive interactions are necessary for any putative phase of high-density matter in the core. This chapter addresses whether such repulsion can have other observable consequences. In particular, we investigate if such repulsion can lead to Cooper pairing between fermions with non-zero angular momentum due to the Kohn-Luttinger(KL) effect [209] in the cores of neutron stars.

Cooper pairing in neutron stars is expected across a range of densities and in a variety of channels. In the crust, neutrons are expected to form a $^1S_0$ superfluid while protons form a $^1S_0$ superconductor in the core due to their lower density. The $^1S_0$ gap for neutrons in the crust is shown in Fig. 5.1 where the uncertainties are relatively small. At higher densities, the $^1S_0$ interaction between nucleons becomes repulsive and attraction in the $^3P_2$ channel is expected to dominate for neutrons. The exact size of the $^3P_2$ gap and what densities it appears over remains highly uncertain. Figure 5.2 shows a recent

---

[1] This chapter summarizes work originally found in Ref. [12]

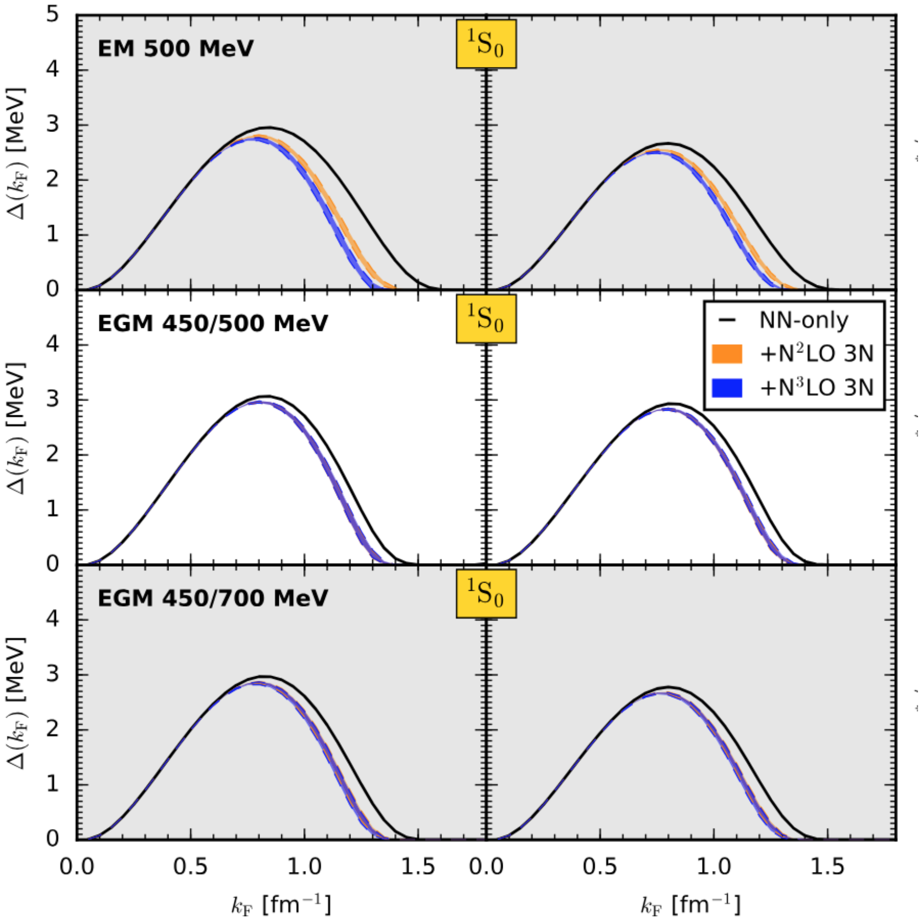

Figure 5.1: Recent calculation of the $^1S_0$ gap for neutrons in χEFT. The left column uses a free spectrum for neutrons and the right column uses Hartree-Fock. Figure from Ref. [210].

calculation of the $^3P_2$ gap in χEFT. At the highest densities, a variety of pairing channels are available for quarks if they deconfine in neutron stars. Figure 1.1 sketches the approximate regions of the NS over which each type of superfluidity is expected to dominate.

The KL effect, which arises because the interaction at the Fermi surface is modified due to screening in the medium, implies that the Cooper pairing instability in high angular momentum states is inevitable and occurs even when the bare interaction is repulsive [209]. The effect has been discussed extensively in condensed matter physics (For a recent pedagogic review, see Ref. [211]). In the context of dense nuclear matter, early work in [212–214] recognized that the interaction between nucleons induced by polarization effects in the medium would significantly alter the pairing gaps (for recent reviews, see [58, 215]). The induced interaction, typically calculated in second-order perturbation theory or Fermi liquid theory, naturally incorporates the KL effect. In dilute Fermi systems with attractive s-wave short-range interactions, it has been known since the work of Gor'kov and Melik-Barkhudarov that the induced interaction suppresses the s-wave pairing gap relative to the BCS prediction [216]. In neutron matter, when the s-wave interaction is repulsive, the induced interaction was initially expected to increase the

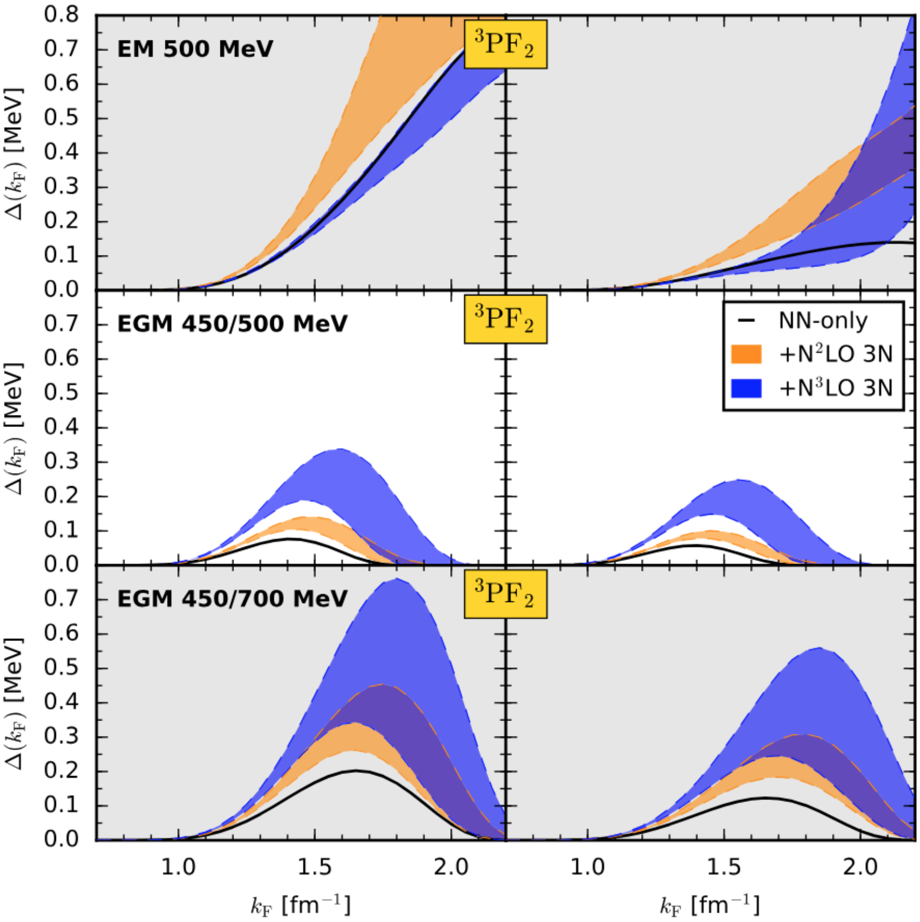

Figure 5.2: Recent calculation of the $^3P_2$ gap for neutrons in χEFT. The left column uses a free spectrum for neutrons and the right column uses Hartree-Fock. Figure from Ref. [210].

p-wave attraction between neutrons [212]. However, more recent work in Ref. [217] finds that the induced spin-orbit interaction can dominate and result in a net suppression instead at modest density. Here, we revisit calculating the induced interaction in high-density matter characterized by a large sound speed to study its implications for $^3P_2$ pairing. We consider short-range interactions that contain central and non-central components and study the competition between the attractive and repulsive components of the induced p-wave interaction and its density dependence.

In quark matter, when the Fermi surfaces of up, down, and strange quarks are split due to charge neutrality and a larger strange quark mass, the KL effect provides a mechanism to pair quarks of the same flavor and color. However, in this case, we find that p-wave interaction induced by short-range repulsion introduced to increase the pressure of quark matter is too small to be of phenomenological relevance.

Our study, which relies on extrapolating results derived from perturbation theory to strong coupling, provides order-of-magnitude estimates for the pairing gaps. Although the method we employ is inade-

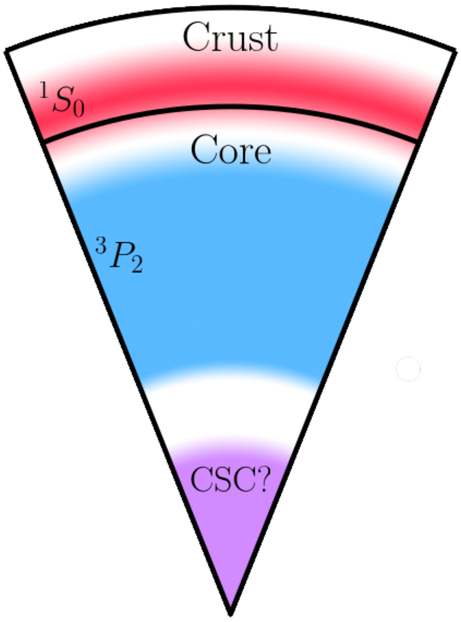

Figure 5.3: Schematic showing different regions for neutron superfluidity and a possible region of quark color superconductivity in the inner core.

quate to make quantitative predictions, it identifies a mechanism for $^3P_2$ pairing in dense Fermi systems with large repulsive interactions mediated by short-range interactions mediated by heavy vector bosons.

In section 5.2, we review the KL mechanism for non-relativistic fermions. In section 5.3, we derive the induced interaction between neutrons at high density by assuming that the bare interaction is due to the exchange of heavy vector mesons. In section 5.4, we consider the possible effects of the KL mechanism in quark matter. We discuss the implications for neutron star cooling in section 5.5, summarize our main findings, and discuss open questions in section 5.6.

5.2 Kohn-Luttinger Mechanism

Kohn and Luttinger showed that a short-range repulsive potential can induce attraction in large odd partial waves due to medium effects that can overscreen the effective interaction between fermions at finite density [209]. There has been renewed interest in studying the KL effect in condensed matter systems because calculations suggest that the induced pairing gaps in p-waves and low-order partial waves could be large enough to be realized in experiments (see, for example, [218–221]). KL's original calculation included terms at second order in the potential; more recent analysis [222] calculates the potential up to fourth order in a constant potential characterized by a large scattering length as well as including retardation effects where pairing occurs away from the Fermi surface, also contributing at fourth order.

In weak coupling, the KL effect arises naturally at second order in the potential by evaluating the diagrams in Fig. 5.4. We refer to these diagrams from left to right as the screening, vertex, and exchange diagrams, respectively. The vertex diagram also has a mirror image, which must be included. We consider interactions that occur at the Fermi surface, so $|k| = |k'| = k_F$. The momentum transfer is labeled $q = k' - k$.

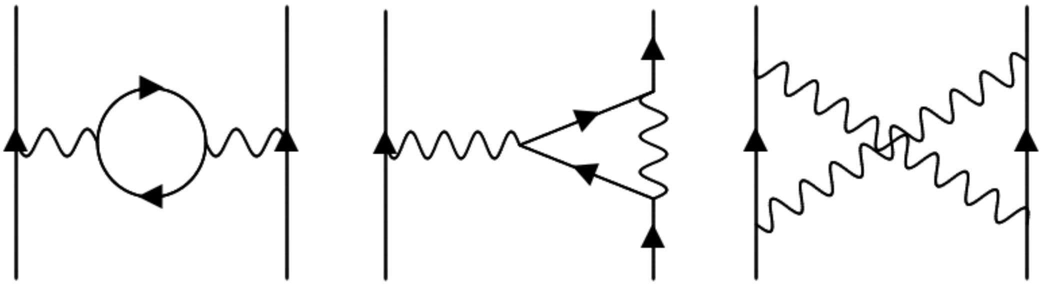

Figure 5.4: Irreducible second order diagrams for Kohn-Luttinger mechanism

For a short-range potential with zero range and strength denoted by U_0, the non-relativistic calculation of these diagrams is straightforward. In this case, the screening diagram cancels the contribution from the two vertex diagrams, and only the exchange diagram contributes. The exchange diagram also gets an overall sign since it is crossed and is given by

$$V_{KL}(q) = U_0^2 \frac{1}{\beta} \sum_{\ell_0} \int \frac{d^3\ell}{(2\pi)^3} \frac{1}{\ell_0 - \ell^2/2m} \frac{1}{\ell_0 - (\ell + q)^2/2m} \tag{5.1}$$

Notice that since $|k| = |k'|$, the frequency transfer q_0 is just zero. Taking the Matsubara sum and simplifying it gives a singular contribution to the potential. Since we are considering the effects of interactions with the medium, the loop integral has a factor $n_F(\ell^2/2m) = 1/(e^{\beta(\ell^2/2m - \mu)} + 1)$ and does not need to be regulated. At the low temperatures we consider ($T \ll \epsilon_F = k_F^2/2m$) this simplifies $n_F(\ell^2/2m) \approx \Theta(k_F - \ell)$. The momentum integral in Eq. (5.1) yields the Lindhard function defined by

$$U(q) = -\frac{m}{4\pi^3 q} \int \ell \, d\ell \, d\Omega_\ell \frac{\Theta(k_F - \ell)}{\cos\theta_{q\ell} - q/2\ell} = \frac{mk_F}{4\pi^2} \left[1 - \frac{1}{\bar{q}} \left(1 - \frac{\bar{q}^2}{4} \right) \log \left| \frac{1 - \bar{q}/2}{1 + \bar{q}/2} \right| \right] \tag{5.2}$$

where $\bar{q} = q/k_{\mathrm{F}}$. Thus, Eq. (5.1) can be written as

$$V_{KL}(q) = -U_0^2 \, U(q) \tag{5.3}$$

For any potential, the contribution to the induced potential from the singularity at $q = 2k_F$ of the Lindhard function scales as $(-1)^L L^{-4}$ for large L [209, 223] where L is the angular momentum quantum number. Since the regular contributions to the total potential falls off exponentially with L, attraction is guaranteed for large odd partial waves.

Although these results are only generically true for large L, they persist for relatively low partial waves for some potentials. It was shown by [218, 222] that the constant potential calculated above would result in p-wave attraction. The p-wave contribution from the potential in Eq. (5.3) can be found easily by making a change of integration variable from $\int_{-1}^{1} d\cos\theta$ to $\int_{0}^{2} \bar{q}d\bar{q}$. The matrix element in the Born approximation should be doubled due to a diagram with outgoing momenta switched, but we will absorb this normalization into the gap equation to match the literature. The p-wave potential from the exchange diagram and its crossed counterpart is then given by

$$V_{\ell=1} = -U_0^2 \frac{mk_F}{4\pi} \frac{4}{5\pi}(2\log 2 - 1) \tag{5.4}$$

The superfluid gap due to the induced attraction in p-waves was calculated several decades earlier in Ref. [212, 224]. In the BCS approximation, the p-wave gap

$$\Delta_p \simeq \epsilon_F \ \exp\left\{\left(\frac{2}{N(0)V_{\ell=1}}\right)\right\} = \epsilon_F \ \exp\left\{\left(\frac{-5\pi^2}{4(2\ln 2 - 1)(ak_{\mathrm{F}})^2}\right)\right\}, \tag{5.5}$$

where $\epsilon_F = k_{\mathrm{F}}^2/2m$ is the Fermi energy, $N(0) = mk_{\mathrm{F}}/2\pi^2$ is the density of states at the Fermi surface for each spin, and the scattering length $a = mU_0/4\pi$ in weak coupling.

In strong coupling, we cannot calculate the effective interaction at the Fermi surface reliably, and in the following, we shall assume that Eq. (5.5) provides a useful estimate. Further, we shall also assume that the s-wave scattering amplitude between quasi-particles at the Fermi surface, denoted by f_0, is directly related to the strength of the bare interaction U_0. In Fermi liquid theory (FLT), the sound speed

$$c_s = \frac{k_F}{\sqrt{3mm^*}}\sqrt{(1+F_0)}\,, \tag{5.6}$$

where $F_0 = N(0)f_0$ is dimensionless measure of the quasi-particle interaction and m^* is the fermion effective mass at the Fermi surface. Using this relation, we can estimate the interaction strength $U_0 \approx f_0$ at a given density if c_s and m^* are known. If $m^* \approx m$ and $U_0 = f_0$, then the induced p-wave gap in Eq. (5.5) can be rewritten as

$$\Delta_p \approx \epsilon_F \ \exp\left\{\left(-\frac{5}{(2\ln(2) - 1)F_0^2}\right)\right\}, \tag{5.7}$$

to illustrate its extreme sensitivity to F_0 and the sound speed through Eq. (5.6). For example, models of high-density neutron matter typically predict $F_0 \gtrsim 2$ for $n_B \gtrsim 3\ n_{sat}$ [225]. Under these conditions, Eq. (5.7) predicts robust p-wave pairing with gaps $\Delta_p \gtrsim 1$ MeV due to the induced interaction.

In the next section, we will calculate the induced interaction between neutrons in more realistic scenarios where the bare potential is momentum-dependent and contains central and non-central components.

5.3 Induced p-wave pairing in dense neutron matter

The s-wave potential at the Fermi surface becomes repulsive in the neutron star core when $n_B \gtrsim n_{\rm sat}/2$. At these higher densities, $^3P_2$ pairing is favored because the bare potential in this channel remains attractive, and non-central components of the interaction, especially the spin-orbit interaction, favor the alignment of spin and orbital angular momentum. Calculations of the $^3P_2$ pairing gap in the BCS approximation reported in Refs. [48, 215] show that the pairing gaps are model dependent, especially for $n_B > 2n_{\rm sat}$ because the nucleon-nucleon potentials at the relevant momenta are not well constrained by scattering data. In these calculations, the maximum value of the gap $\Delta_{^3P_2} \simeq 1-2$ MeV occurs between $2-3\ n_{sat}$ and decreases rapidly with increasing density. At lower density, when the nucleon momenta $p \ll \Lambda_\chi$ where $\Lambda_\chi \simeq 500$ MeV is the breakdown scale of chiral EFT, a recent study used chiral EFT potentials and found that the maximum value $\Delta_{^3P_2} \simeq 0.4$ MeV was reached at $n_B \simeq 1.3\ n_{sat}$ and its decrease at higher density was found to be sensitive to the details of the short-distance physics [210]. Together, these findings suggest that if neutron matter persists at the highest densities encountered in neutron stars, the bare $^3P_2$ potential could be small, and $\Delta_{^3P_2}$ depends on model assumptions about the nuclear interaction at short distances.

When the bare $^3P_2$ potential weakens, the gap is especially sensitive to corrections due to induced interactions in the medium (see, for example, the discussion in section 3.4 of Ref. [215]). In early work, the interaction induced by the central components of the nuclear force was found to increase the $^3P_2$ gap [212, 226], as would be expected from the discussion of the KL mechanism in section 5.2. However, as mentioned earlier, calculations that employed realistic low-energy nuclear potentials with significant non-central components found that the interference between the central and spin-orbit component of the nuclear force led to significant suppression of the $^3P_2$ gap for $n_B < 2n_{\rm sat}$ [217].

At $n_B \gtrsim 2n_{\rm sat}$, the description of nuclear interactions relies on model assumptions since the typical nucleon momenta $p \gtrsim \Lambda_\chi$. To investigate the competition between a strong and repulsive central force and the spin-orbit component of the nuclear force at high density, we revisit the calculation of the induced interaction in simple models. In what follows, we shall assume that the dominant contribution to the nucleon-nucleon interaction at short distances is due to the exchange of heavy vector mesons such as the ω and ρ mesons with masses $m_\omega \approx m_\rho \simeq 800$ MeV. For $n_B \lesssim 4n_{\rm sat}$, $k_{\rm F}/\Lambda$ where $\Lambda \simeq m_\omega$ remains a useful expansion parameter. In this case, including terms up to $\mathcal{O}[(k_{\rm F}/\Lambda)^2]$, the interaction can be described by the potential

$$\begin{aligned} V(q,q') = {} & C_0 + \tilde{C}_0 \sigma_1 \cdot \sigma_2 + C_2(q^2+q'^2) + C_2'(q'^2-q^2) \\ & + \left[\tilde{C}_2(q^2+q'^2) + \tilde{C}_2'(q'^2-q^2)\right] \sigma_1\cdot\sigma_2 + iV_{SO}\ q\times q'\cdot(\sigma_1+\sigma_2) \\ & + V_T q\cdot\sigma_1 q\cdot\sigma_2\,. \end{aligned} \tag{5.8}$$

In neutron matter, due to the Pauli principle, only the combinations $\bar{C}_0 = C_0 - 3\tilde{C}_0$, $\bar{C}_2 = C_2 - 3\tilde{C}_2$, and $\bar{C}'_2 = C'_2 + \tilde{C}'_2$ are relevant. In the full expansion of the vector meson potential, there is also a term proportional to $(q \times q' \cdot \sigma_1)(q \times q' \cdot \sigma_2)$ and higher powers of momentum in the central and spin-orbit interactions. An exchange tensor term proportional to $q' \cdot \sigma_1 q' \cdot \sigma_2$ is also allowed by the symmetries of the interaction but is not present in the vector exchange. In this exploratory study, we shall neglect the spin-orbit squared and tensor exchange components and truncate the potential at order k_F^2. In this case, 5 LECs denoted by $\bar{C}_0$, $\bar{C}_2$, $\bar{C}'_2$, V_{SO}, and V_T are adequate. The large and attractive spin-orbit interaction, whose strength is set by V_{SO} plays an important role, as discussed below. Since we consider incoming and outgoing momenta at the Fermi surface with zero center-of-mass momentum, $q = k_1 - k_3$ and $q' = k_1 - k_4$ with the momenta of neutrons in the initial state are given by k_1 and k_2, and the final state momenta are k_3 and k_4.

It is straightforward to repeat the calculation of the diagrams described in the preceding section with the potential in Eq. (5.8). However, it is simpler to define the anti-symmetrized potential

$$\begin{aligned}V(q,q') = {} & C_0(\delta_{13}\delta_{24} - \delta_{14}\delta_{23}) + C_2(q^2 + q'^2)(\delta_{13}\delta_{24} - \delta_{14}\delta_{23}) \\ & + C'_2(q'^2 - q^2)(\delta_{13}\delta_{24} + \delta_{14}\delta_{23}) + \tilde{C}_0(\sigma_{13} \cdot \sigma_{24} - \sigma_{14} \cdot \sigma_{23}) \\ & + \tilde{C}_2(q^2 + q'^2)(\sigma_{13} \cdot \sigma_{24} - \sigma_{14} \cdot \sigma_{23}) + \tilde{C}'_2(q'^2 - q^2)(\sigma_{13} \cdot \sigma_{24} + \sigma_{14} \cdot \sigma_{23}) \\ & + 2iV_{SO} q \times q' \cdot (\sigma_{13}\delta_{24} + \sigma_{24}\delta_{13}) + V_T(q \cdot \sigma_{13} q \cdot \sigma_{24} - q' \cdot \sigma_{14} q' \cdot \sigma_{23})\end{aligned} \tag{5.9}$$

that includes the effect of the exchange processes. We use the notation $\delta_{ij} = \chi_j^\dagger \chi_i$ and $\sigma_{ij} = \chi_j^\dagger \sigma \chi_i$ for incoming and outgoing two-component spinors χ_i and $\chi_j^\dagger$. In this case, the induced interaction at second-order is calculated by evaluating the diagrams depicted in Fig. 5.5. The diagram on the left is called the zero-sound diagram and denoted as ZS, and the diagram on the right is called the exchange zero-sound diagram and is denoted by the symbol ZS'. A detailed derivation of the total induced interaction $V_{ind} = V_{ind}^{ZS} - V_{ind}^{ZS'}$ is presented in Appendix D.

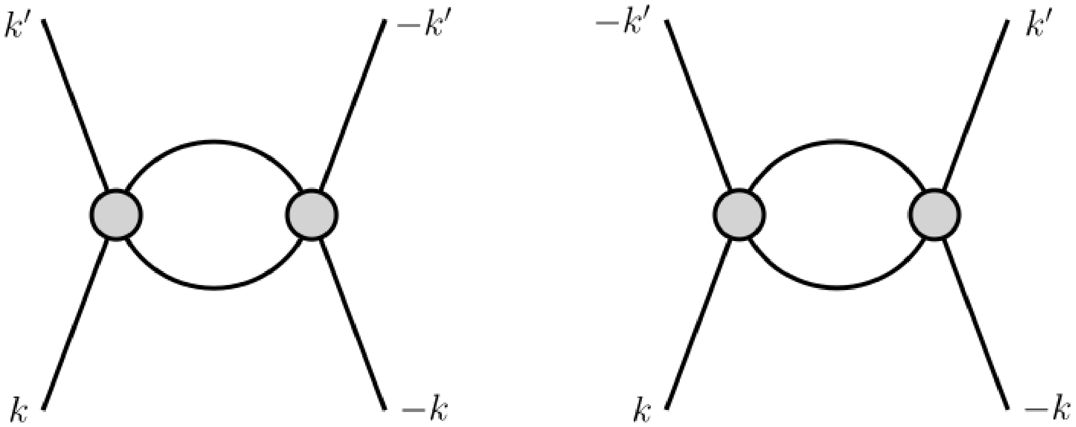

Figure 5.5: ZS (left) and ZS' (right) diagrams. The shaded gray blobs represent the anti-symmetrized interaction defined in Eq. (5.9).

First, we present the result obtained by neglecting the momentum-dependent components of the bare central interaction. In this case, the induced potential

$$\begin{aligned} V^{\text{ind}} &= -(C_0^2 + 3\tilde{C}_0^2)(U(q)\delta_{14}\delta_{23} - U(q')\delta_{13}\delta_{24}) + 6C_0\tilde{C}_0(U(q)\delta_{13}\delta_{24} - U(q')\delta_{14}\delta_{23}) \\ &\quad + (-\tilde{C}_0^2 + 2C_0\tilde{C}_0)(\sigma_{13}\cdot\sigma_{24} - \sigma_{14}\cdot\sigma_{23})(U(q) + U(q')) \\ &\quad - 3\tilde{C}_0^2(\sigma_{13}\cdot\sigma_{24} + \sigma_{14}\cdot\sigma_{23})(U(q) - U(q')) \end{aligned} \tag{5.10}$$

The s- and p-wave potentials given by this interaction are

$$\begin{aligned} V^{\text{ind}}_{{}^1S_0}(0) &= \bar{C}_0^2 \frac{mk_F}{3\pi^2}(2\log 2 + 1) \\ V^{\text{ind}}_{{}^3P_J}(0) &= -\bar{C}_0^2 \frac{mk_F}{5\pi^2}(2\log 2 - 1)\,. \end{aligned} \tag{5.11}$$

where again $\bar{C}_0 = C_0 - 3\tilde{C}_0$ is the momentum-independent bare ${}^1S_0$ potential.

The calculation of the induced potential, including the momentum-dependent central interactions, is tedious, and the analytic results contain a large number of terms. Details of the intermediate expressions can be found in Appendix D.

We find analytic results for the second-order induced potentials in the s and p induced potentials. The induced ${}^1S_0$ and ${}^3P_J$ potentials calculated to $\mathcal{O}(mk_F^3)$ are given by

$$\begin{aligned} V^{\text{ind}}_{{}^1S_0} &= mk_F\bar{C}_0^2\frac{1}{3\pi^2}(1 + 2\log 2) + mk_F^3[\bar{C}_0\bar{C}_2\frac{2}{3\pi^2}(5 + 4\log 2) \\ &\quad + \bar{C}_0\bar{C}_2'\frac{2}{5\pi^2}(7 - 4\log 2) - \bar{C}_0V_T\frac{16}{15\pi^2}(2 + \log 2)]\,, \end{aligned} \tag{5.12}$$

and

$$\begin{aligned} V^{\text{ind}}_{{}^3P_J} &= mk_F\bar{C}_0^2\frac{1}{5\pi^2}(1 - 2\log 2) + mk_F^3[\bar{C}_0\bar{C}_2\frac{2}{105\pi^2}(59 - 68\log 2) \\ &\quad - \bar{C}_0\bar{C}_2'\frac{2}{105\pi^2}(29 + 52\log 2) \\ &\quad + \bar{C}_0V_T\frac{1}{105\pi^2}(91J^2 - 221J + 50 + (224J^2 - 544J + 220)\log 2)]\,, \end{aligned} \tag{5.13}$$

respectively.

When momentum dependence of the central interaction is neglected, the bare spin-orbit force does not contribute to the induced interaction, and the leading order dependence of the induced potential on J is determined by the tensor interaction. See Appendix D for a detailed discussion.

These contributions have the same behavior as the leading order KL result. The contribution to the induced interaction in a particular partial wave arising from terms in the bare interaction that do not contribute to that partial wave is strongly influenced by the KL singularity at $q = 2k_{\text{F}}$. For this reason, their contribution is suppressed relative to other terms in the interaction at the same order in the expansion. Notice, for example, that in the p-wave induced potential, the term proportional to $\bar{C}_0\bar{C}_2'$

has a numerical factor five times larger than $\bar{C}_0\bar{C}_2$ and fifteen times larger than $\bar{C}_0 V_T$ for ${}^3P_2$. This implies that the singularity at $q = 2k_\mathrm{F}$ does not play an essential role when $\bar{C}_2'$ is of modest size. By comparing the relevant terms in Eq. (5.13), we find that the KL singularity plays an essential role only when $\bar{C}_2' \ll \bar{C}_0/(16k_\mathrm{F}^2)$. In what follows, we shall continue to use the term Kohn-Luttinger effect to refer to the induced interaction, but it should be borne in mind that the singularity at $q = 2k_\mathrm{F}$ does not play a dominant role for typical values of $\bar{C}_2'$ we explore in this study.

Since the spin-orbit force is strong and important in the ${}^3P_2$ channel, we expect that it may contribute to the induced interaction even though it enters at a higher order in the momentum expansion. To investigate the impact of the spin-orbit coupling, we calculate a subset of the terms that contain the central and spin-orbit interactions at $\mathcal{O}(mk_F^5)$. These corrections to the induced potentials are given by:

$$\begin{aligned} V^{(5)}_{{}^1S_0} = mk_F^5 [&\bar{C}_2^2 \frac{8}{315\pi^2}(277 + 96\log 2) - \bar{C}_2'^2 \frac{8}{105\pi^2}(43 + 24\log 2) \\ &+ \bar{C}_2\bar{C}_2' \frac{32}{105\pi^2}(37 + 6\log 2) + V_{SO}^2 \frac{8}{35\pi^2}(17 + 16\log 2)] \,, \end{aligned} \tag{5.14}$$

and

$$\begin{aligned} V^{(5)}_{{}^3P_J} = mk_F^5 [&\bar{C}_2^2 \frac{16}{567\pi^2}(83 - 24\log 2) + \bar{C}_2'^2 \frac{64}{567\pi^2}(34 - 3\log 2) \\ &- \bar{C}_2\bar{C}_2' \frac{16}{2835\pi^2}(523 + 204\log 2) + \bar{C}_2' V_{SO}[J(J+1) - 4]\frac{32}{945\pi^2}(43 + 24\log 2) \\ &+ V_T V_{SO}[J(J+1) - 4]\frac{16}{945\pi^2}(43 + 24\log 2) \\ &+ V_{SO}^2 (7J^2 - 17J + 10)\frac{32}{4725\pi^2}(43 + 24\log 2)] \,. \end{aligned} \tag{5.15}$$

These are not all of the terms that contribute at $\mathcal{O}(mk_F^5)$. Not included are terms proportional to $\bar{C}_2 V_T$, $\bar{C}_2' V_T$, and V_T^2.

From Eq. (5.15), we deduce that when the bare spin-orbit interaction is attractive, it could enhance ${}^3P_2$ pairing if

$$2\bar{C}_2' + V_T + \frac{4}{5}V_{SO} > 0 \,. \tag{5.16}$$

The relation of this result to the suppression of ${}^3P_2$ pairing at low density due to spin-orbit interactions found in Ref. [217], which employed a realistic low-momentum nucleon-nucleon potential fit to scattering data warrants further study.

We consider three scenarios to study the implications of these results for dense neutron matter. Each scenario is defined by a specification of the LECs that appear in the bare potential defined in Eq. (5.8). In scenario A, we shall assume that the exchange of heavy vector mesons mediates the interactions between neutrons. When the mass of the vector meson is large compared to the neutron Fermi momentum, and interaction is described by a current-current four-fermion Lagrangian

$$\mathcal{L}_{\text{int}} = -\frac{G_V}{2}(\overline{n}\gamma_\mu n)(\overline{n}\gamma^\mu n)\,. \tag{5.17}$$

Retaining only the leading terms in the k/m_n expansion, the LECs appearing in Eqs. (5.12) and (5.13) are given by

$$\bar{C}_0 = G_V\,, \quad \bar{C}_2 = \frac{5G_V}{8m_n^2}, \quad \bar{C}_2' = \frac{3G_V}{8m_n^2}, \quad V_{SO} = -\frac{3G_V}{8m_n^2}, \quad V_T = \frac{G_V}{4m_n^2} \tag{5.18}$$

Although the simple vector interaction cannot capture the complex nature of interactions between neutrons, which could involve a richer operator structure due to pion exchange and many nucleon forces, it is able to describe the qualitative aspects of the nucleon-nucleon interaction at high momentum; it predicts negative phase shifts in the ${}^1S_0$, ${}^3P_0$, and ${}^3P_1$ channels. The phase shift in the ${}^3P_2$ channel vanishes because $V_{SO} = -\bar{C}_2'$, and the spin-orbit interaction exactly cancels the contribution from the central force. This aspect of short-range vector interactions that leads to a vanishing bare potential in the ${}^3P_2$ channel is a generic feature of any four-fermion interaction without derivative couplings since initial and final states constructed only from spin and helicity operators cannot be combined to form a tensor of rank greater than 1. As a result, such an interaction cannot generate potentials in channels with $J \geq 2$ at the tree level. Including momentum dependence in the meson propagator, explicit derivative couplings (i.e., momentum dependence beyond that found in the Dirac spinors), or momentum dependence from loops lifts this restriction.

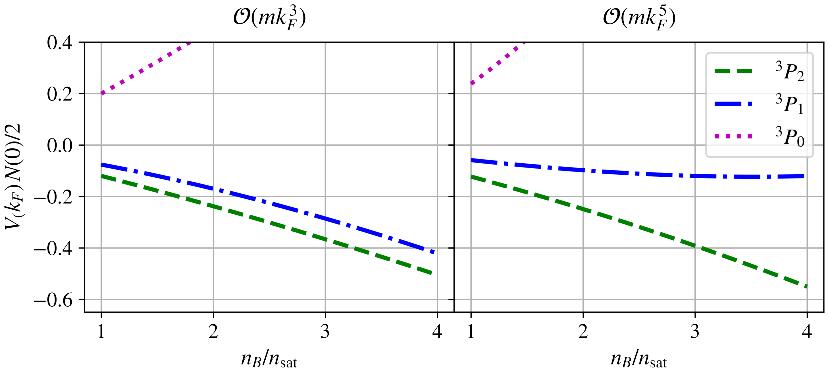

Figure 5.6: Total potential for heavy vector boson exchange at $\mathcal{O}(mk_F^3)$ (left) and at $\mathcal{O}(mk_F^5)$ (right). The coupling constant is tuned to $F_0 = 3$ at $3n_{sat}$.

The couplings are related to the Fermi liquid parameters F_0 and G_0. In the mean-field theory, F_0 and G_0 depend only on the central components of the interaction and are given by

$$F_0 = N(0)\left(\bar{C}_0 + 2k_{\text{F}}^2(\bar{C}_2 + 3\bar{C}_2{}')\right)\,, \tag{5.19}$$

$$G_0 = -N(0)\left(\bar{C}_0 + 2k_{\text{F}}^2(\bar{C}_2 - \bar{C}_2{}')\right)\,, \tag{5.20}$$

where $N(0) = \sqrt{k_\mathrm{F}^2 + m_n^2}\, k_\mathrm{F}/2\pi^2$ is the density of states for each spin at the Fermi surface. Thus, if F_0 and G_0 are specified, the strength of the s-wave components of the interaction are constrained by the equation $(2\bar{C}_0 + 4k_F^2\bar{C}_2) = (F_0 - 3G_0)/2N(0)$ and the p-wave component is obtained using the relation $\bar{C}_2' = (F_0 + G_0)/(8N(0)k_F^2)$. In scenario A, the interaction contains just one parameter, G_V. In this case, F_0 and G_0 are not independent and G_V is determined by specifying F_0, which we take to be in the range $2 - 4$ at $n_B = 3\ n_{sat}$.

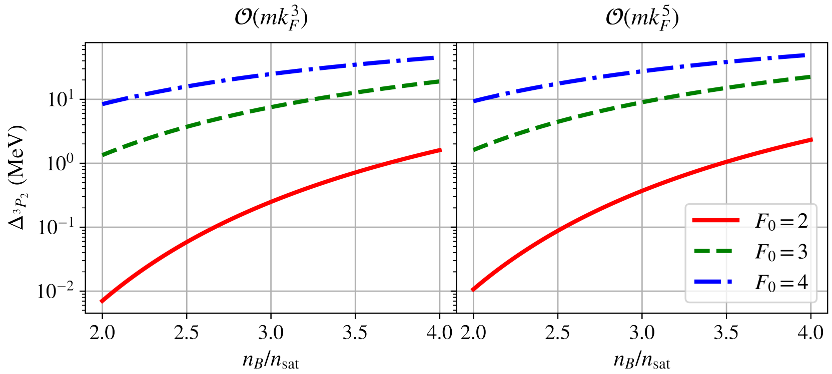

Figure 5.7: The $^3P_2$ gap corresponding to the short-range vector interaction in Eq. (5.17). Results at $\mathcal{O}(mk_F^3)$ are shown in the left panel and at $\mathcal{O}(mk_F^5)$ in the right panel. The coupling constant is tuned to the given value of F_0 at $3n_{sat}$.

The induced and total p-wave interactions at the Fermi surface are shown in Fig. 5.6 for $F_0 = 3$ at $n_B = 3n_{sat}$. The actual value shown $VN(0)/2$ is the quantity in the exponent of the BCS equation. The model naturally prefers $^3P_2$ pairing because although the induced interaction at the Fermi surface is attractive for all values of the total angular momentum $J = 0, 1, 2$, the sum $V^\mathrm{bare} + V^\mathrm{ind}$ is only attractive for $J = 1, 2$ and the net attraction is larger for $J = 2$. In Fig. 5.7, we show the $^3P_2$ pairing gaps calculated using the BCS formula in Eq. (5.5). Results are shown for three choices of the coupling G_V obtained by setting $F_0 = 2, 3$ and 4 at $n_B = 3\ n_{sat}$.

To study the interplay between the central p-wave and the spin-orbit interactions, we consider scenario B, in which we introduce parameters ξ_p and ξ_SO to control the strength of the central p-wave interaction and the spin-orbit interaction, respectively. In this case, we neglect the tensor coupling, and the LEC constants are given by:

$$\bar{C}_0 = G_V, \quad \bar{C}_2 = \frac{G_V}{\Lambda^2}, \quad \bar{C}_2' = \xi_\mathrm{p}\frac{G_V}{\Lambda^2}, \quad V_{SO} = -\xi_{SO}\frac{G_V}{\Lambda^2}, \quad V_T = 0 \tag{5.21}$$

As a generic choice at the same order as the nucleon and meson masses, we take $\Lambda = 1\,\mathrm{GeV}$. Fig.5.8 shows curves of constant $VN(0)/2$ in the space of ξ_p and ξ_{SO} for $G_V = 20\,\mathrm{GeV}^{-2}$ and $G_V = 40\,\mathrm{GeV}^{-2}$. Corresponding values of F_0 for each value of ξ_p are shown on the right axis. The black line shows where the bare interaction is zero. Above this line, the bare interaction is repulsive, and below it is attractive.

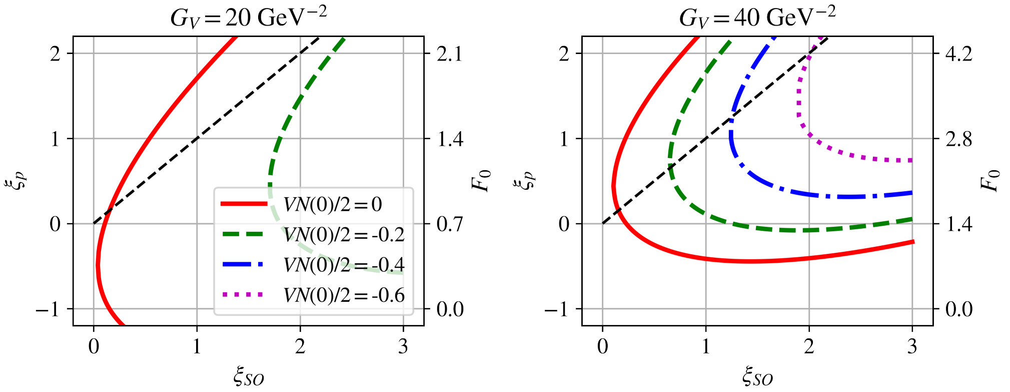

Figure 5.8: Contours of constant $^3P_2$ potential in model B in the $\xi_p - \xi_{SO}$ plane for two choices of G_V at $3n_{sat}$. F_0, calculated using Eq. (5.19) is also shown. The black dashed line shows where the bare interaction vanishes.

The general behavior of the induced interaction is set by terms proportional to $\bar{C}_2'^2$, $\bar{C}_2' V_{SO}$, and V_{SO}^2 with some secondary effects from terms proportional to $\bar{C}_0\bar{C}_2'$ and $\bar{C}_2\bar{C}_2'$. Even though some of these terms enter at higher order in the gradient expansion, they are generally more important than lower-order terms in the induced interaction because they do not rely on the KL singularity to contribute to the $^3P_2$ potential. Of these five terms, the only ones that can be attractive are $\bar{C}_0\bar{C}_2'$ and $\bar{C}_2\bar{C}_2'$ when ξ_p is positive, and $\bar{C}_2' V_{SO}$ when ξ_{SO} and ξ_p are of the same sign. As a result, for stronger couplings, the overall interaction is repulsive when ξ_p is negative and of reasonable size, even though that corresponds to a more attractive bare interaction. There is significant net attraction only when ξ_p and ξ_{SO} are both positive and ξ_p is not much larger than ξ_{SO} as this leads to a more repulsive bare interaction without producing enough induced attraction to match.

Fig.5.9 shows the $^3P_2$ gap as a function of ξ_{SO} for a few choices of ξ_p and the same choices of G_V. This interplay between the relative size of ξ_p and ξ_{SO} sensitively determines the size of the gap. This model is not detailed enough to make quantitative predictions, but the general trend remains that high-order terms in the expansion play an important role in determining the size of the gap. An attractive spin-orbit appears to be necessary to have gaps of a reasonable size. An attractive bare p-wave potential precludes pairing even though the bare interaction is stronger because of the repulsion due to the induced interaction.

To incorporate trends observed in the nucleon-nucleon phase shifts that have been measured up to $E_{\rm lab} \simeq 300$ MeV which correspond $p_{\rm CM} = \sqrt{m_n E_{\rm lab}/2} \simeq 375$ MeV, we consider scenario C in which we incorporate a non-zero V_T by introducing a parameter ξ_T that sets the strength of the tensor interaction, and $V_T = -G_V \xi_T/\Lambda^2$. This allows us to obtain any desired ordering of the p-wave phase shifts for $J = 0, 1, 2$ and match scattering data that require a weakly attractive bare $^3P_2$ interaction and repulsive interactions in the $^3P_0$ and $^3P_1$ channels. Since the induced interaction at $\mathcal{O}(mk_{\rm F}^5)$ in Eq. (5.15) neglected the part of the potential proportional to $\bar{C}_2' V_T$, the results we present here are strictly only

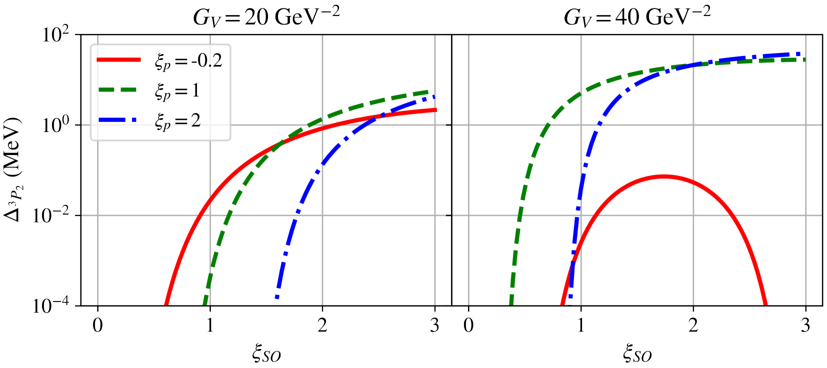

Figure 5.9: $^3P_2$ gap as a function of ξ_{SO} in model B for a few choices of ξ_p and G_V at $3n_{sat}$.

valid for $\xi_T \ll \xi_{SO}$. Thus, scenario C must be viewed as an initial exploration into the effects of V_T to be continued in future work.

To obtain the correct ordering of the p-wave interactions, the parameters must satisfy the following conditions. To have an attractive bare $^3P_2$ potential, $\xi_{SO} > \xi_p$ and to have a repulsive bare $^3P_0$, $\xi_p + 2\xi_{SO} - 3\xi_T/2 > 0$. The condition $2\xi_{SO}/5 < \xi_T < 2\xi_{SO}$ ensures that the $^3P_1$ potential is most repulsive and $^3P_2$ is most attractive. We define α and β to be the ratio between the bare potentials given by

$$\begin{aligned} \alpha &\equiv \frac{V_{^3P_2}}{V_{^3P_0}} = \frac{\xi_p - \xi_{SO}}{\xi_p + 2\xi_{SO} - 3\xi_T/2} \\ \beta &\equiv \frac{V_{^3P_1}}{V_{^3P_0}} = \frac{\xi_p + \xi_{SO} + \xi_T}{\xi_p + 2\xi_{SO} - 3\xi_T/2} \end{aligned} \tag{5.22}$$

Phase shifts for lab energies between 250 MeV and 350 MeV favor α between -1 and -3 and β between 2 and 4. The blue horizontal hatched and orange vertical hatched bands in Fig. 5.10 and Fig. 5.11 identify regions $-3 < \alpha < -1$ and $2 < \beta < 4$, respectively with the correct sign for each bare potential. We only show regions with $\xi_{SO} > 0$ and $\xi_T > 0$ since this is required to obtain the correct ordering of p-waves phase shifts. These are also the signs favored by a tensor interaction arising from pion exchange and a spin-orbit force from heavy meson exchange.

To illustrate the relevance of the induced interaction, Fig. 5.10 shows the interaction for scenario C broken down into bare potential, $\mathcal{O}(mk_F^3)$ induced potential, and $\mathcal{O}(mk_F^5)$ corrections to the induced potential for a few choices of ξ_{SO} and ξ_T and the same two values of G_V used for scenario B. In the right panel, ξ_{SO} is fixed to match the value of ξ_p so that the bare interaction is always zero, as is found in the meson exchange model. The range of ξ_p chosen is motivated by the observation that meson exchange models predict $0.5 \lesssim \xi_p \lesssim 1.5$ and matching to phase shifts between 250 and 350 MeV predicts $-0.5 \lesssim \xi_p \lesssim 0$. As seen before, the $\mathcal{O}(mk_F^3)$ induced interaction is dominated by the term proportional to $\bar{C}_0\bar{C}_2'$ and gives more attraction for positive ξ_p and repulsion for negative ξ_p. The induced interaction

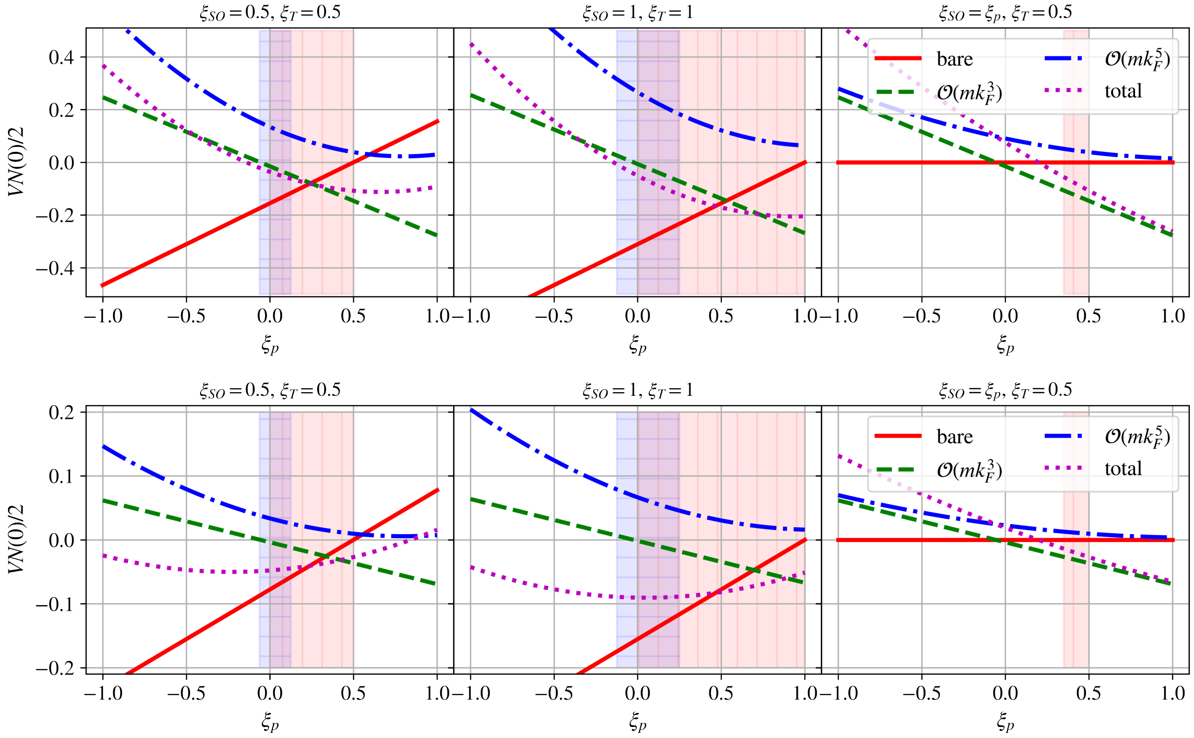

Figure 5.10: The bare ${}^3P_2$ potential, the induced potential at $\mathcal{O}(mk_F^3)$, and the induced V_{SO} at $n_B = 3n_{sat}$. $G_V = 40\,\mathrm{GeV}^{-2}$ in the upper panel and $G_V = 20\,\mathrm{GeV}^{-2}$ in the lower panel. Blue horizontal hatched and orange vertical hatched bands indicate where $-3 < \alpha < -1$ and $2 < \beta < 4$ respectively with the correct sign for all phase shifts for α and β defined in Eq. (5.22).

does not exactly go through the origin for $\xi_p = 0$, but the KL suppression of the terms that do not include $\bar{C}_2'$ or V_{SO} is sufficient that it is not visible on this scale. Negative values of ξ_p lead to more repulsive $\mathcal{O}(mk_F^5)$ corrections, with this effect being stronger for larger values of ξ_{SO}.

Fig. 5.11 shows the contours of constant potential for scenario C. As in scenario B, negative or zero ξ_p corresponds to repulsion for most of the parameter space. However, unlike scenario B, when ξ_T is of reasonable size, increasing ξ_{SO} results in repulsion much more quickly. This is a result of the term proportional to $V_T V_{SO}$. The contribution of the spin-orbit terms can be easily summarized in terms of the constants of this model:

$$V_{{}^3P_2}^{(5SO)} = \xi_{SO}\left(\xi_T + \frac{4\xi_{SO}}{5} - 2\xi_p\right)\frac{G_V^2}{\Lambda^4}\frac{32mk_F^5}{945\pi^2}(43 + 24\log 2) \tag{5.23}$$

In scenario A, ξ_T is negative and $\xi_{SO} = \xi_p$, so the term in parentheses is always negative, and the spin-orbit corrections give additional attraction. However, when we allow the constants to vary and take ξ_T positive as is favored by pion exchange and phase shift data, much of the favored region of the phase diagram shows suppression due to these corrections. The black dashed line in Fig. 5.11 shows where $\xi_T + 4\xi_{SO}/5 - 2\xi_p = 0$. The spin-orbit corrections suppress the potential above and to the right of this line, while the potential is enhanced below and to the left.

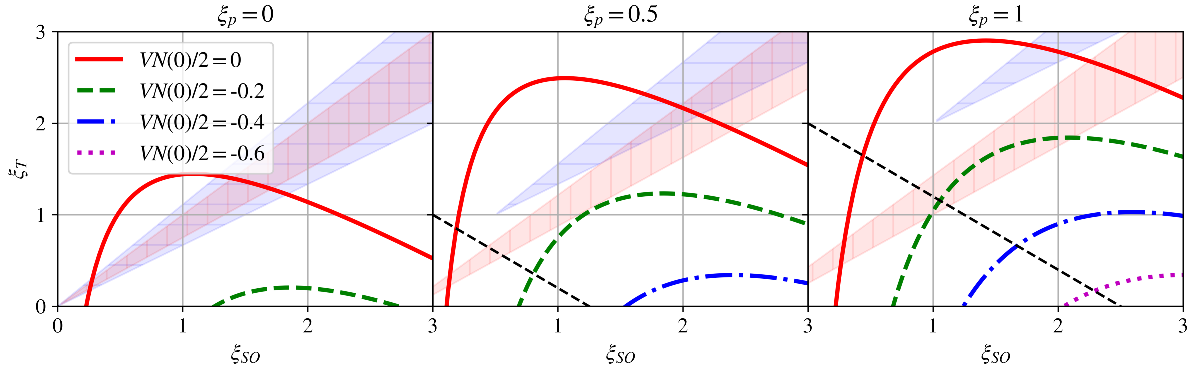

Figure 5.11: Curves of constant total potential for different choices of ξ_p at $3n_{sat}$. The black dashed line shows where the spin-orbit correction vanishes. The coupling constant is $G_V = 40\,\mathrm{GeV}^{-2}$. Blue horizontal hatched and orange vertical hatched bands indicate where $-3 < \alpha < -1$ and $2 < \beta < 4$ respectively with the correct sign for all phase shifts for α and β defined in Eq. (5.22).

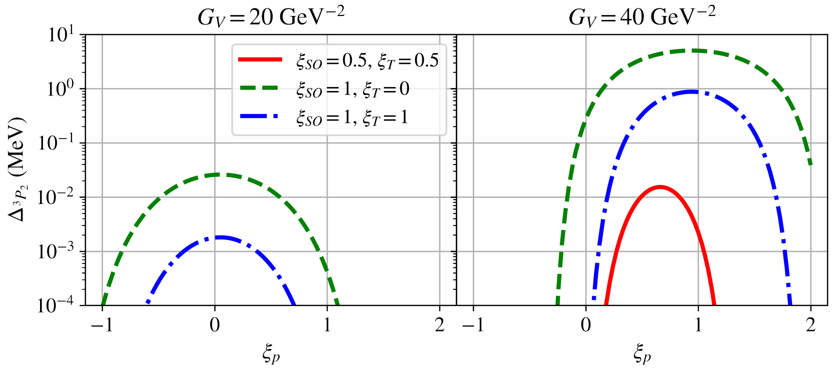

Figure 5.12: $^3P_2$ gap as a function of ξ_p for a few choices of G_V, ξ_{SO}, and ξ_T at $n_B = 3n_{sat}$.

Fig. 5.12 shows the $^3P_2$ gap at $3n_{sat}$ as a function of ξ_p for a few choices of ξ_{SO} and ξ_T. For negative ξ_p, even though the bare interaction is more attractive, the induced interaction strongly suppresses the gap. The contribution of positive ξ_T suppresses the gap. For positive ξ_p, MeV-scale gaps are possible. These results are sensitive to the value of F_0, as can be inferred by comparing the upper and lower panels of Fig.5.10. For smaller F_0, the relative importance of the induced interaction is diminished, and for most of the parameter space, the induced interaction suppresses an attractive bare interaction. This still has a significant effect as the gap is exponentially sensitive to the potential. In this case, for almost all the explored parameter space, the induced interaction suppresses the gap by an order of magnitude or more.

5.4 Induced p-wave pairing in quark matter

The inner cores of neutron stars may be made up of deconfined quark matter. Quarks are expected to form a color superconductor at asymptotic densities, with the dominant pairing being in the color antitriplet channel (antisymmetric). See [59] for a review. Color symmetric pairing is generally not considered since gluon exchange in the color sextet (symmetric) is repulsive, while the antitriplet channel is attractive. At asymptotic densities, pairing all three colors and flavors (up, down, and strange) in color and flavor antisymmetric pairs is expected (the CFL phase). At lower densities where the strange quark mass cannot be neglected, up and down quarks can pair in the color antisymmetric channel. This pairing involves two colors, typically denoted as red and green, and is called the 2SC phase. In this phase, the strange quarks and blue-up and blue-down quarks are unpaired.

Pairing of quarks of the same flavor and color was considered in Ref. [227] in which possible pairing channels were found for strange quarks in color symmetric and antisymmetric channels for a bare interaction with the quantum numbers of gluon exchange. The attractive color symmetric channel they find is model-dependent and, in the case of massive quarks with all contributions from gluon exchange, receives competition from repulsive terms with the same spin and angular momentum quantum numbers but different chirality. Since they consider contact interactions without explicit derivative couplings, they explore $J = 0$ and 1. Pairing of quarks of the same flavor was also studied in Ref. [228] in which attractive color antisymmetric channels with $J = 1$ were considered, finding the transverse color-spin locked phase to be favored.

The possibility that quarks left over in the 2SC phase could pair due to the KL mechanism in QCD was first studied in Ref. [229]. This study investigated the KL effect in gauge theories where fermions interact via long-range forces that are dynamically screened due to Landau damping of the magnetic gauge bosons. Here, the energy dependence of the interaction plays a critical role, and the results of Ref. [229] indicate that a gap arises via a mechanism analogous to the Kohn-Luttinger effect but conclude that it is too small to be phenomenologically relevant.

To assess if the KL mechanism could be relevant in quark matter with short-range interactions that are independent of energy, we shall calculate the induced interaction in the $^3P_2$ channel between quarks of the same flavor and color due to the short-range, flavor and color-independent, repulsive vector interaction. Such pairing would include the strange and the up and down blue quarks. In what follows, we shall focus on the induced interaction between strange quarks of the same color at moderate density when $m_s \gg k_{Fs}$ The specific question we address here is if repulsive short-range interactions introduced to stabilize quark matter inside neutron stars [230] can lead to pairing gaps of phenomenological relevance.

For concreteness, we consider a description of quark matter within the purview of the Nambu-Jona-Lasino(NJL) models (see [231] for a comprehensive review). In these models, defined by the interaction Lagrangian [230–232]

$$\mathcal{L}_V = G(\bar{q}q)^2 + H(\bar{q}\bar{q})(qq) - g_V\ (\bar{q}\gamma_\mu q)^2\,, \tag{5.24}$$

where G and H are the four-fermion scalar quark-antiquark and diquark coupling strengths, and vector coupling g_V is introduced to generate higher pressures as noted earlier. The scalar interaction between quarks and antiquarks leads to a non-trivial vacuum with $\langle \bar{q}q \rangle \neq 0$ that spontaneously breaks chiral symmetry and the coefficient G is determined by hadron masses and the pion decay constant in the vacuum. For typical momentum cut-off $\Lambda_{\rm NJL} \approx 600$ MeV, $G\Lambda^2_{\rm NJL} \simeq 2$ [231]. At densities of interest to neutron stars, chiral symmetry remains broken. The constituent strange quark mass is expected to be $300 - 500$ MeV, while the up and down quark masses can be significantly smaller. The diquark coupling H and the vector coupling g_V are expected to be of similar size because they can be thought of as arising from the same underlying high-energy color current-current interactions in QCD [232]. Their values at the densities of interest to neutron stars are determined phenomenologically. The diquark coupling H, which encodes the attraction in the color antisymmetric channel, leads to s-wave pairing between quarks. For $H \simeq G$, the s-wave pairing gap between up and down quarks is about 50 MeV and is typically inadequate to induce pairing between strange quarks and light quarks [233], as mentioned above. The analysis of the quark matter EOS in [230, 234] concluded that vector coupling needed to be of moderate size with $g_V \simeq G$ to support the large sound speed needed to support a two solar mass neutron star.

First, we note that the contribution to the induced interaction from the closed fermion loop (the first diagram in Fig. 5.4) is enhanced by a factor $N_f N_c$. This is because the bare vector interaction introduced to stiffen the quark matter EOS is independent of color and flavor. Thus, in contrast to the one-component Fermi system, where the contribution from the closed fermion loop was canceled by the diagram that encoded the vertex corrections, in quark matter with $N_f = N_c = 3$, the first diagram in Fig. 5.4 makes the dominant contribution to the induced potential. In computing this diagram, the up and down quarks must be treated as relativistic particles, leading to a somewhat more complicated expression. After doing the Matsubara sum and noting that $\bar{u}_3 \not{q} u_1 = \bar{u}_4 \not{q} u_2$ for u_1 and u_2 incoming and $\bar{u}_3$ and $\bar{u}_4$ outgoing spinors, the induced potential from the first diagram is given by:

$$V^{\rm ind} = g_V^2 (\bar{u}_3 \gamma_\mu u_1)(\bar{u}_4 \gamma_\nu u_2) \left(\frac{E_k + m_s}{2m_s} \right)^2 \sum_{f,c} \int \frac{\ell d\ell d\Omega_\ell}{4\pi^3 q E_\ell} \frac{\Theta(k_{fc} - \ell)}{c_{q\ell} - q/2\ell} (2\ell^\mu \ell^\nu - g^{\mu\nu} \vec{\ell} \cdot \vec{q}) \tag{5.25}$$

The calculation of the induced interaction, including both the electric ($\bar{u}\gamma^i u$ for $i = 0$) and magnetic ($\bar{u}\gamma^i u$ for $i = (1, 2, 3)$) components is unwieldy. In what follows, we shall focus on the electric component as the magnetic component is suppressed by the strange quark mass. In this case, setting $\mu = \nu = 0$ in Eq. (5.25) we find that

$$V^{\rm ind} = \frac{g_V^2 \delta_{13} \delta_{24}}{2\pi^2 q} \sum_c \int \frac{d\ell dc_{q\ell}}{c_{q\ell} - q/2\ell} \left[\sum_{f=u,d} (2\ell^2 - \ell q c_{q\ell}) \Theta(k_{fc} - \ell) + 2\ell m_s \Theta(k_{sc} - \ell) \right] . \tag{5.26}$$

After performing the momentum integrals, we find that

$$V^{\rm ind} = g_V^2 \delta_{13} \delta_{24} \sum_c \left[\sum_{f=u,d} \left(-\frac{k_{fc}^2}{2\pi^2} + \frac{q^2}{2} U_0^{\rm rel} \left(\frac{q}{k_{fc}} \right) - 2k_{fc}^2 U_2^{\rm rel} \left(\frac{q}{k_{fc}} \right) \right) - 2U(q) \right] \tag{5.27}$$

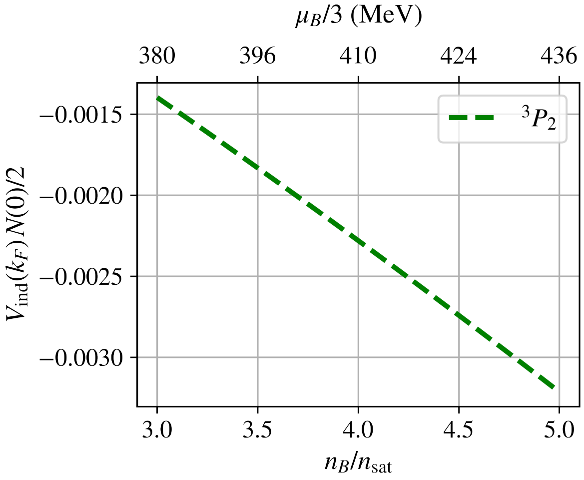

Figure 5.13: Induced p-wave potential between strange quarks for $g_V = 2/\Lambda^2_{NJL}$, $\Lambda_{NJL} = 600\,\text{MeV}$, and $m_s = 350\,\text{MeV}$.

where the relativistic Lindhard functions $U_0^{\rm rel}$ and $U_2^{\rm rel}$ defined in Appendix F.

Note that by not including the magnetic part of the vector integration ($\bar{u}\gamma^i u$ for $i = (1,2,3)$), explicit dependence on J has been removed, and all the p-waves have the same potential. Nonetheless, the $^3P_2$ gap remains of primary interest because the bare interaction vanishes for $J = 2$, while it is repulsive for $J = 0,1$. Fig. 5.13 shows the induced p-wave potential for strange quarks of mass 350 MeV, for $g_V = 2/\Lambda^2_{NJL}$ and $\Lambda_{NJL} = 600\,\text{MeV}$. Densities of each color and flavor are determined assuming 2SC pairing of up and down quarks, charge neutrality, and beta equilibrium. Since the pairing gap $\Delta \simeq \mu\ \exp\{(2/V_{\rm ind}(k_F)N(0))\}$, from Fig. 5.13 we can deduce that the induced potential is too small to be relevant for neutron star phenomenology. This is mostly due to the fact that the value of g_V needed in NJL models to support massive neutron stars is significantly smaller than the coupling we considered for nucleons.

5.5 Implications for Neutron Stars

The thermal evolution of neutron stars, especially those that are reheated by accretion from a companion at late times, is sensitive to heat capacity and neutrino emissivity in their cores [19,235,236]. The neutrino emissivity and the specific heat of dense matter are both strongly modified by Cooper pairing. When the pairing gap is large compared to the temperature, the neutrino emissivity and the specific heat are exponentially suppressed by the factor $\exp\{(-\Delta/k_BT)\}$. Additionally, in the vicinity of the critical temperature, Cooper pair breaking and formation (PBF) processes enhance the neutrino emissivity. This enhancement is especially important for neutron Cooper pairing in the $^3P_2$ channel in the core of the neutron star [19, 236]. Studies of isolated neutron star cooling reported in Ref. [236] that include the modified URCA ($nn \to npe^-\bar{\nu}_e$ and $e^-pn \to nn\nu_e$) reactions and the PBF process but discount the possibility of other more rapid neutrino emission processes such as direct URCA [237] find that a critical temperature for ${}^3P_2$ pairing, $T_c \approx \Delta_{{}^3P_2}/1.7$, that is larger than 5×10^8 K ($\approx$ 50 keV) throughout the inner core would be disfavored by observations. This favors a scenario in which the $\Delta_{{}^3P_2}$ is suppressed at the modest density encountered in the outer core due to the competition between the interactions induced by the central and spin-orbit components of the nuclear forces [217] but is insensitive to the behavior of the gap at higher density.

Accreting neutron stars exhibit a diversity of cooling behaviors, and a few neutron stars show behavior that requires rapid neutrino cooling [235, 238]. Such rapid neutrino cooling can be realized in the dense nuclear matter when the proton fraction in the core exceeds about 11% to lift kinematic restrictions on the direct URCA reactions $e^- + p \to n + \nu_e$ and $n \to e^- + p + \bar{\nu}_e$ [237]. In addition, rapid cooling would also require ${}^3P_2$ pairing to be absent at high density. Our finding that the induced interaction disfavors ${}^3P_2$ when the spin-orbit and tensor forces are strong and attractive provides some insight into the conditions necessary to realize unpaired neutron matter at high density characterized by a high sound speed. On the other hand, if the central component of the p-wave interaction is strongly repulsive and the non-central components are weak, the induced interaction favors ${}^3P_2$ pairing between neutrons, and rapid neutrino cooling cannot be realized in nuclear matter at high density. In this scenario, rapid cooling in neutron stars would require new ungapped fermionic excitations, such as hyperons or quarks, to enable the direct URCA reaction.

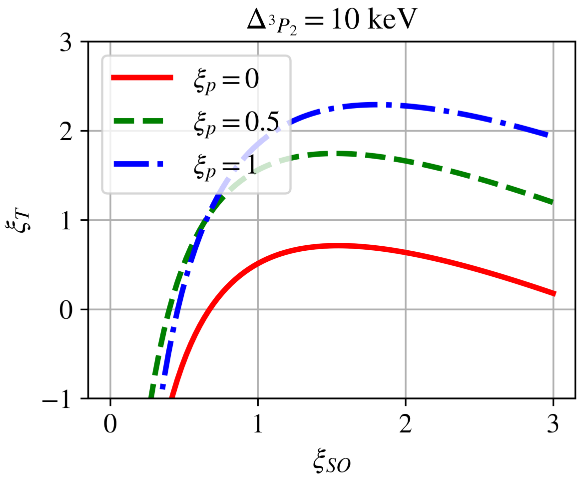

Figure 5.14: Contours for $\Delta_{{}^3P_2} = 10\,\mathrm{keV}$ for $G_V = 40\,\mathrm{GeV}^{-2}$ at $3n_{sat}$ for a few choices of ξ_p. Below and to the right of the contour, the gap is larger than 10 keV.

In transiently accreting neutron stars, inference of the heat deposition due to deep crustal heating from observations of accretion outbursts and the inference of the core temperature from subsequent observation in quiescence have been used to derive a lower limit to the neutron star core heat capacity [238, 239]. Further, if the neutron stars cooling can be observed during quiescence, an upper limit on the core heat capacity can also be deduced from observations [238, 239]. For neutron stars in the low mass x-ray binaries KS 1731-260, MXB 1659-29, and XTE J1701-462, with core temperatures in the range $10^7 - 10^8$ K, the lower limit was found to be a factor of a few below the core heat capacity expected if neutrons and protons in the core are paired. However, upper limits from future cooling observations in these systems could constrain the extent of neutron pairing in the neutron star core. For example, the analysis in Ref. [238] suggests that if the neutron star in MXB 1659-29 cools by about 4% during a 10-year period, a very large fraction of the neutrons in the neutron star core must be superfluid with a gap that is much larger than a few keV. If observed, it would disfavor a large attractive tensor interaction and would require an attractive spin-orbit interaction as shown in Fig.5.14. Repulsive bare p-wave interactions permit larger regions of parameter space, while attractive bare p-wave interactions are more restrictive.

5.6 Conclusion

We have calculated the induced potential between fermions at the Fermi surface to study the role of polarization effects in the dense medium. We find that short-range repulsive interactions due to the exchange of heavy vector mesons between neutrons, whose strength is related to the Fermi liquid parameter F_0 and the sound speed at high density, induce an attractive p-wave potential. Using a model that allows us to independently vary the strength of central and non-central p-wave interactions, we have investigated the competition between the bare and induced interactions to determine the conditions necessary to realize $^3P_2$ pairing in neutron matter at high density. When neutron matter is characterized by a large speed of sound $c_s^2 > 1/3$ and $F_0 \gtrsim 2$, the induced interaction plays an important role. We find that

- The contribution to the induced interaction in a particular partial wave arising from terms in the bare interaction that do not contribute to that partial wave are suppressed because their contribution is strongly influenced by the KL singularity at $q = 2k_{\mathrm{F}}$. For this reason, the bare p-wave and the spin-orbit interactions are generally more important than lower-order terms for the induced $^3P_2$ potential.

- The induced interaction favors $^3P_2$ pairing if the central component of the s-wave and p-wave interaction are strongly repulsive and the non-central components are small. The resulting gap, $\Delta_{^3P_2}$, can be in the range $0.1 - 10$ MeV in the neutron star core and is exponentially sensitive to the induced potential.

- When the central p-wave and the spin-orbit interaction are both strong and attractive, the induced interaction is repulsive. Although the bare interaction is strongly attractive, the induced repulsion can preclude pairing or suppress $\Delta_{^3P_2}$ by orders of magnitude.

- In the presence of a strongly attractive spin-orbit interaction, the induced interaction favors ${}^3P_2$ pairing when the central p-wave is repulsive. Pairing persists even when the strength of the central p-wave repulsion is greater than the attractive spin-orbit interaction.

An important caveat to these findings is our assumption that the bare interaction at the Fermi surface is well represented by Eq. (5.8). Further, at the high momenta of relevance when $n_B > 2n_{sat}$, the nucleon-nucleon potential, and thereby the parameters of our model, are not well constrained by scattering data. Nonetheless, results obtained within the purview of the model allowed us to explore the connection between pairing and the strong repulsive central interactions needed to generate a high sound speed and large F_0 at densities expected in the cores of massive neutron stars. Our calculation, which includes the effect due to strong spin-orbit forces, provides useful formulae to gauge the interplay between repulsive central interaction and attractive spin-orbit interactions. However, further study of the role of strong tensor interactions warrants further study.

Another aspect that warrants mention is the role of many-body forces. Although we have not explicitly accounted for them in our study here, earlier work has demonstrated that three-body forces can be incorporated through a density-dependent two-body potential that can then be constructed by normal ordering the three-body force with respect to a convenient reference state, such as the ground state of the non-interacting many-body system [205, 240]. Including the three-body force would thereby introduce a density dependence to the parameters of our model that set the strength of the two-body s-wave and p-wave interactions in dense matter. We believe the large range of parameter values we explored should be sufficient to account for corrections due to many-body forces partially. The density-dependence of the two-nucleon partial-wave matrix elements at the Fermi surface and the correlation between the parameters induced by the 3-body forces will be explored in future work. Finally, as cautioned earlier, the magnitude of the ${}^3P_2$ gap was calculated using the BCS approximation, which restricted the interaction to the Fermi surface. More work is needed to assess the reliability of this approximation.

Chapter 6

Summary and outlook

In this thesis we have studied the properties of matter in neutron stars in order to constrain theories of axions and to understand the properties of interactions in dense matter. Such calculations are crucial in order to accurately interpret astrophysical observations.

Exceptionally light QCD axions are at present strongly constrained though substantial theoretical uncertainties remain regarding the nature of nuclear forces at reduced pion mass. We have identified the modifications to existing nuclear forces and new operators necessary to address this question within a cohesive framework and possibly probe the QCD axion itself ($\varepsilon = 1$). Future publications will show these results.

We extended prior results calculating the Direct Urca rate below the threshold $Y_p = 1/9$ in the presence of a strong magnetic field. Past approximations neglected the effect of resonances in the density of states that lead to local enhancements of the neutrino emissivity. Although these effects are washed out in the high thermal conductivity core of the neutron star, it is possible that this may be relevant for transport. Of greater note was the observation that in the presence of strong magnetic fields, the opacity of low energy neutrinos to capture on nucleons was strongly enhanced. We will address this question in more detail in a future study in order to understand its relevance for nucleosynthesis and simulations of supernovae and binary neutron star mergers.

We calculated the effect of the induced interaction on superfluidity in high density matter. At large sound speed and F_0, the induced interaction was an important contribution to the overall interaction strength, breaking the expectations of the gradient expansion in cases where the Kohn anomaly was a necessary ingredient to produce an interaction. The contribution from the induced interaction was sufficient to produce keV to MeV gaps, potentially observable in the cooling of isolated neutron stars.

Acknowledgments

The U.S. DOE supported my work under Grant No. DE-FG02- 00ER41132. This work would not have been possible without collaborators Masha Baryakhtar, Maria Dawid, Wouter Dekens, Christian Drischler, Maya Ednie, Yuki Fujimoto, Junwu Huang, Peter Rau, Sanjay Reddy, John Stroud, and Catherine Welch. I would additionally like to thank Silas Beane, David Cyncynates, Roland Farrell, Bengt Friman, Susan Gardner, Wick Haxton, Anson Hook, David Kaplan, Ken McElvain, Dany Page, Daniel Phillips, Jose Pons, Yong-Zhong Qian, David Radice, Achim Schwenk, Steve Sharpe, Stefan Stelzl, Richard Mikaël Slevinsky, and Neill Warrington for helpful conversations and correspondence with myself or my collaborators in the course of this research.

Data availability statement

The data that support the findings of this thesis are openly available [241, 242].

Appendix A

Additional nuclear interactions in the axion domain wall

The energy density and pressure of the axion domain wall has a somewhat weak effect on the EoS of typical neutron stars. However, inside the axion domain wall, the properties of nuclear matter can be affected by the following additional terms [115],

$$\begin{aligned}\mathcal{L}_{\mathrm{DW}} \supset\, & i(c_- + 4c_4)\frac{m_u m_d \sin\theta}{\left[m_u^2 + m_d^2 + 2m_u m_d \cos\theta\right]^{1/2}}\bar{\mathcal{N}}\gamma_5\mathcal{N} \\ & + c_+\frac{m_u m_d \sin\theta}{\left[m_u^2 + m_d^2 + 2m_u m_d \cos\theta\right]^{1/2}}\bar{\mathcal{N}}\frac{\pi^a\tau^a}{f_\pi}\mathcal{N},\end{aligned} \tag{A.1}$$

where $\mathcal{N}$ contains both nucleon fields and τ are the Pauli matrices in isospin space.

The LEC c_+ is equivalent (up to overall normalization) to c_5 in the normal chiral power counting. The term with c_+ in Eq. (A.1) is exactly equivalent to the first term in our Eq. (3.30). Similarly, c_- and c_4 refer to the same operators as d_{18} and d_{19} in the normal chiral language, which gives a contribution consistent with zero up to the uncertainty of modern nuclear data [177]. The total set of θ dependent operators in the $\Delta = 2$ pion-nucleon Lagrangian is given in Table A.1 [243]. We do not need to include any of these terms at N2LO.

Table A.1: Table showing all θ dependent operators at $\Delta = 2$ coupling nucleons and pions. v is the nucleon 4-velocity, S is the spin operator, and D is the chiral covariant derivative.

LEC	Operator	Description
d_5	$\bar{N}[\chi_-, v \cdot u]N$	Pion mass correction to Weinberg-Tomozawa vertex
d_{16}	$\bar{N}S \cdot uN\langle\chi_+\rangle$	Renormalization of g_A
d_{17}	$\bar{N}N\langle S \cdot u\chi_+\rangle$	Isospin breaking renormalization of g_A
d_{18}	$i\bar{N}[S \cdot D, \chi_-]N$	Golberger-Treiman discrepancy
d_{19}	$i\bar{N}[S \cdot D, \langle\chi_-\rangle]N$	Isospin breaking Golberger-Treiman discrepancy

Appendix B

RMFT corrections to the domain wall calculation

In general, $\delta^{(\mathrm{loc})}$ is given by:

$$\delta^{(\mathrm{loc})} = \frac{1}{\sigma_N n_B^{(s)}} \frac{\partial \Omega}{\partial m_\sigma} \frac{\mathrm{d} m_\sigma}{\mathrm{d}\theta} \tag{B.1}$$

where $n_B^{(s)}$ is the total scalar density of baryons. In the outer crust and core, the expression in terms of the mean-field value of the σ field is simple.

$$\begin{aligned} \delta^{(\mathrm{loc})} &= \frac{d_\sigma}{\sigma_N [2 + 2 d_\sigma f(\theta)]} \frac{\chi}{n_B^{(s)}} \left(\frac{m_\sigma}{g_\sigma}\right)^2 \\ &\times \left[(g_\sigma \langle\sigma\rangle)^2 + \frac{\kappa_3}{3 m_N^{\mathrm{phys}}} (g_\sigma \langle\sigma\rangle)^3 + \frac{\kappa_4}{12 (m_N^{\mathrm{phys}})^2} (g_\sigma \langle\sigma\rangle)^4 \right] \end{aligned} \tag{B.2}$$

where g_σ, κ_3, and κ_4 are parameters of the RMFT model, χ is the volume fraction of nuclei (or one in the core), and $g_\sigma\langle\sigma\rangle = m_N(\theta) - m_N^*(\theta)$ for $m_N^*(\theta)$ the effective mass of the nucleon with mean field effects included. In the inner crust, this expression becomes more complicated.

$$\begin{aligned} \delta^{(\mathrm{loc})} &= \frac{d_\sigma}{\sigma_N [2 + 2 d_\sigma f(\theta)]} \frac{1}{n_B^{(s)}} \left(\frac{m_\sigma}{g_\sigma}\right)^2 \\ &\times \Bigg\{ \chi \left[(g_\sigma \langle\sigma\rangle_{\mathrm{nuc}})^2 + \frac{\kappa_3}{3 m_N^{\mathrm{phys}}} (g_\sigma \langle\sigma\rangle_{\mathrm{nuc}})^3 + \frac{\kappa_4}{12 (m_N^{\mathrm{phys}})^2} (g_\sigma \langle\sigma\rangle_{\mathrm{nuc}})^4 \right] \\ &+ (1-\chi) \left[(g_\sigma \langle\sigma\rangle_{\mathrm{neut}})^2 + \frac{\kappa_3}{3 m_N^{\mathrm{phys}}} (g_\sigma \langle\sigma\rangle_{\mathrm{neut}})^3 + \frac{\kappa_4}{12 (m_N^{\mathrm{phys}})^2} (g_\sigma \langle\sigma\rangle_{\mathrm{neut}})^4 \right] \Bigg\} \end{aligned} \tag{B.3}$$

where $\langle\sigma\rangle_{\mathrm{nuc}}$ is the mean field value of the sigma field in nuclei and $\langle\sigma\rangle_{\mathrm{neut}}$ is the mean field value of the sigma field in the dripped neutron phase. Since $n_B^{(s)}$ is dominated by the dripped neutron phase except in the vicinity of the neutron drip phase transition, but the σ field has a small mean field value in the dripped neutron phase, this suppresses $\delta^{(\mathrm{loc})}$ in the inner crust.

Appendix C

Neutrino opacity in magnetic fields for neutron star merger simulations

In this appendix we lay out the necessary steps to simplify the calculation of neutrino opacities in magnetic fields for use in simulations.

C.1 Regimes of interest

There are four distinct regimes in supernovae and neutron star merger ejecta with magnetic fields that we need to consider that have different features that need to be included (though the last two are very similar in terms of computations) and a fifth regime where the zero field result holds.

Table C.1: Table showing relevant conditions of magnetic field strength and temperature where each approximation is appropriate and what features must be included in that regime

Name	Conditions	e^- quantized?	p^+ quantized?	AMM important?
Strong field	$eB \gtrsim MT$	yes	yes	yes
Medium field	$MT \gg eB \gtrsim T^2$	yes	no	low E_ν only
Weak field	T^2 or $E_\nu^2 \gg eB \gtrsim M\Delta M/g$	no	no	low E_ν only
Low T	$E_\nu^2 \gg eB \gtrsim MT$	no	no	yes
Zero field	$M\Delta M/g \gg eB$	no	no	no

For the first three rows, we assume $E_\nu \sim T$ and $\Delta M \simeq 1.3\,\mathrm{MeV}$ is the mass splitting of the nucleons. The strong field regime is only applicable for $T \lesssim 2\,\mathrm{MeV}$ when $B \lesssim 10^{17}\,\mathrm{G}$ and the weak field regime is only applicable for $T \gtrsim 40\,\mathrm{MeV}$ or $E_\nu \gtrsim 40\,\mathrm{MeV}$.

The use of Maxwell-Boltzmann statistics is justified for nucleons so long as the following condition is met.

$$\left(\frac{T}{10\,\mathrm{MeV}}\right)^{3/2}\frac{n_{sat}}{n} > 30 \tag{C.1}$$

where n is the number density of the particle species in question. For electrons, one can use Maxwell-Boltzmann statistics only when

$$\left(\frac{T}{10\,\mathrm{MeV}}\right)^3 \frac{n_{sat}}{n_e} > 2 \times 10^4\,. \tag{C.2}$$

While the former condition is true in all but the densest part of the merger ejecta, the latter is only true in the most dilute regions. As such, for computational expediency we will use Maxwell-Boltzmann statistics for nucleons throughout while using Fermi-Dirac statistics for electrons.

The most computationally intensive part of the Direct Urca calculation was dealing with the functions $I_{n,r}$. However, the low density regime permits several helpful approximations because the relative quantization of the electron and proton levels consistently scales with T/M. In the regime where the proton is quantized ($eB \gtrsim MT$), the electron can only access its lowest Landau level. Since the generalized Laguerre polynomial $L_0^n(x) = 1$, we can use the following simplification.

$$I_{n_p,0}(x) = \frac{1}{\sqrt{n_p!}} e^{-x/2} x^{n_p/2} \tag{C.3}$$

In the regime where the electron is quantized and the proton is not, the following limit can be used.

$$\lim_{\substack{eB\to 0\\ n_p eB \text{ fixed}}} I_{n_p,n_e}(x) = \delta_{n_p,x} \tag{C.4}$$

where the right-hand side is a Kronecker delta. Note that this is a natural consequence of Eq. (4.45) when $n_p \gg n_e$ and the expectation that in the zero field limit one should recover the normal Dirac spinors. As such, in the large temperature and low density regime of neutron star mergers and supernovae, one need not calculate $I_{n,r}$ and more importantly one need not calculate any generalized Laguerre polynomials, one of the most severe computational bottlenecks of the high density calculation. It is easy to verify that after doing azimuthal integrations, the matrix element without a magnetic field reduces to precisely the one given in Eq. (4.48) with all special functions set to 1.

The next simplification comes from the observation that due to the electron being ultra-relativistic and the nucleons being non-relativistic, energy conservation is dominated by the electron while momentum conservation is dominated by the nucleons.

$$\delta\left[\frac{k_{zp}^2}{2M} + \frac{n_p eB}{M} - \frac{k_{zn}^2}{2M} - \frac{k_{\perp n}^2}{2M} \pm (E_e - E_0)\right] \to \delta(E_e - E_0) \tag{C.5}$$

$$\delta[k_{zp} - k_{zn} \pm (k_{ze} - k_{z\nu})] \to \delta(k_{zp} - k_{zn} \pm k_{z\nu}) \tag{C.6}$$

where $E_0 = E_\nu \pm (\Delta M + g_n s_n \mu B - g_p s_p \mu B)$ contains the neutrino energy, nucleon mass splitting, and nucleon magnetic moments and the sign is chosen based on whether the reaction has an electron or a positron.

Using Maxwell-Boltzmann statistics for nucleons is a necessity for expedient calculations since it permits the separation of transverse and longitudinal momenta so that most integrals are Gaussian with simple solutions. Note that the normalization for the proton distribution has an unusual normalization when the anomalous magnetic moment is neglected

$$n_{MB}(k_{zp}, n_p) = \tanh\left[\frac{eB}{2MT}\right]\sqrt{\frac{(2\pi)^3}{MT}}\frac{1}{eB}\exp\left(-\frac{k_{zp}^2 + 2n_p eB}{2MT}\right), \tag{C.7}$$

and the following normalization when it is included

$$n_{MB}(k_{zp}, n_p) = \sinh\left[\frac{eB}{2MT}\right]\operatorname{sech}\left[\frac{g_p eB}{4MT}\right]\sqrt{\frac{(2\pi)^3}{MT}}\frac{1}{eB}\exp\left(-\frac{k_{zp}^2 + 2n_p eB - (g_p - 2)s_p eB}{2MT}\right). \tag{C.8}$$

The following are the more non-trivial integrals.

$$\int \mathrm{d}^2 k_{\perp n} e^{-w_\perp^2/2eB} e^{-k_{\perp n}^2/2MT} = \frac{2\pi eBMT}{eB + MT} e^{-k_{\perp\nu}^2/(2eB+2MT)} \tag{C.9}$$

$$\int \mathrm{d}^2 k_{\perp n} e^{-w_\perp^2/2eB}\left(\frac{w_\perp^2}{2eB}\right)^{n_p} = 2\pi eB(n_p!) \tag{C.10}$$

$$\int \mathrm{d}k_{zn}\mathrm{d}k_{zp} e^{-k_{zn}^2/2MT} e^{-k_{zp}^2/2MT}\delta(k_{zp} - k_{zn} \pm k_{z\nu}) = e^{-k_{z\nu}^2/4MT}\sqrt{\pi MT} \tag{C.11}$$

$$\begin{aligned}\int \mathrm{d}^2 k_{\perp n} e^{-w_\perp^2/2eB} e^{-k_{\perp n}^2/2MT}\left(\frac{w_\perp^2}{2eB}\right)^{n_p} &= e^{-k_{\perp\nu}^2/2MT}\frac{2eBMT}{eB+MT}\left(\frac{MT}{eB+MT}\right)^{n_p} \\ \times\sum_{j=0}^{n_p}\binom{n_p}{j}\Gamma\left(n - j + \frac{1}{2}\right)\Gamma\left(j + \frac{1}{2}\right)\,{}_1F_1&\left(j + \frac{1}{2}, \frac{1}{2}, \frac{k_{\perp\nu}^2 eB}{2MT(eB+MT)}\right) \\ = e^{-k_{\perp\nu}^2/(2eB+2MT)}\frac{2\pi eBMT}{eB+MT}&\left(\frac{MT}{eB+MT}\right)^{n_p} n_p!\, L_{n_p}\left[-\frac{k_{\perp\nu}^2 eB}{2MT(eB+MT)}\right]\end{aligned} \tag{C.12}$$

Also useful to deal with the last integral is the relation

$$\sum_{n=0}^{\infty} t^n L_n(z) = \frac{1}{1-t}e^{-tx/(1-t)} \tag{C.13}$$

for $0 < t < 1$. Note that in these limits, all terms at $\mathcal{O}[(T/M)^0]$ in the matrix element with explicit $\cos\phi_w$ integrate to zero. Also since the electron momentum has been entirely decoupled from the neutrino momentum, terms with explicit k_{ze} dependence in the $\mathcal{O}[(T/M)^0]$ matrix element will integrate to zero.

The recipe to find the results in each regime are the following.

- Use either Eq. (C.3) or (C.4) to get rid of the special functions.
- Use the energy delta function to set $E_e = E_\nu \pm (\Delta M + g_n s_n \mu B - g_p s_p \mu B)$. When the electron is strongly quantized, the highest LL should be averaged over an energy range of $E_0 \pm T$ to avoid the singularity in the density of states.

- Use the momentum delta function to give the proton momentum in terms of neutron momentum and external neutrino momentum.
- Do Gaussian integrals over nucleon momenta exploiting separability of Maxwell-Boltzmann statistics. Note that this is often easier in Cartesian coordinates than cylindrical when the azimuthal momentum of the neutrino needs to be included (either in a delta function or $w_\perp^2$).

C.2 Summary of opacities

Below the formulae for matrix elements and opacities in the different regimes are summarized. Number densities of protons and neutrons are denotes as ρ_p and ρ_n to avoid confusion with the proton Landau level. The relevant matrix elements are given by the following. Note that factors of $(1-\delta_{n_p,0})$ are removed since when doing the final integrals we will shift the sums anyway so this has no effect. In the strong field regime, $n_e = 0$ always and terms with $(1-\delta_{n_e,0})$ should be removed. In the medium field regime, the $n_e = 0$ case will need to be handled within whatever ansatz is used for the resonances.

$$\begin{aligned}
\mathcal{M}_{\text{red}}^{(s_n=+,s_p=+)} &= 2(g_V+g_A)^2(1+\cos\theta_\nu) + 2(g_V-g_A)^2(1-\cos\theta_\nu)(1-\delta_{n_e,0}) \\
\mathcal{M}_{\text{red}}^{(s_n=+,s_p=-)} &= 8g_A^2(1+\cos\theta_\nu)(1-\delta_{n_e,0}) \\
\mathcal{M}_{\text{red}}^{(s_n=-,s_p=+)} &= 8g_A^2(1-\cos\theta_\nu) \\
\mathcal{M}_{\text{red}}^{(s_n=-,s_p=-)} &= 2(g_V+g_A)^2(1-\cos\theta_\nu)(1-\delta_{n_e,0}) + 2(g_V-g_A)^2(1+\cos\theta_\nu)
\end{aligned} \tag{C.14}$$

For convenience, define the quantities

$$E_0^\pm = E_\nu \pm (\Delta M - g_n s_n \mu B + g_p s_p \mu B) \tag{C.15}$$

$$E_0'^\pm = E_\nu \pm [\Delta M - g_n s_n \mu B + (g_p - 2) s_p \mu B] \tag{C.16}$$

where μ is the nuclear magneton $(e/2M)$ and also define the following.

$$z = -\frac{k_{\perp\nu}^2 eB}{2MT(eB+MT)} \tag{C.17}$$

$$\tilde{G}_n = \frac{G_F^2 \cos^2\theta_c eB}{4\pi\cosh[g_p eB/4MT]} \tag{C.18}$$

$$\tilde{G}_p = \frac{G_F^2 \cos^2\theta_c eB}{4\pi\cosh[g_n eB/4MT]} \tag{C.19}$$

Note that the following only apply when $E_0^\pm > 0$ (upper sign for neutrons, lower sign for protons). To handle the case of negative $E_0^\pm$ (relevant for particularly strong fields or $\bar{\nu}+p+e \to n$), the delta function must be treated differently.

C.2.1 Strong field ($MT \lesssim eB$)

Remember that in this case $n_e = 0$ so several terms in the matrix element are removed. Since this case has several intermediate steps, first we show one intermediate expression.

$$\begin{aligned}
\kappa_{\nu n} &= \frac{\tilde{G}_n \rho_n}{2} \sum_{s_n,s_p} \mathcal{M}_{\text{red}}^{s_n,s_p} e^{g_n s_n eB/2MT} e^{-k_{\perp\nu}^2/(2eB+2MT)} n_{FD}[\mu_e - E_0^{\prime +}] \\
&\times \sum_{n_p} \left[\frac{eB}{MT} - \frac{\rho_p e^{(g_p-2)s_p eB/2MT}}{\cosh[g_p eB/4MT]} \left(\frac{2\pi}{MT} \right)^{3/2} \sinh\left(\frac{eB}{2MT} \right) e^{-n_p eB/MT} e^{-k_{z\nu}^2/4MT} \right] \\
&\times \left(\frac{MT}{eB+MT} \right)^{n_p} \left(\frac{MT}{eB+MT} \delta_{s_p,+} L_{n_p}(z) + \delta_{s_p,-} L_{n_p-1}(z) \right)
\end{aligned} \tag{C.20}$$

$$\begin{aligned}
\kappa_{\bar{\nu} p} &= \tilde{G}_p \rho_p \tanh\left[\frac{eB}{2MT} \right] \sum_{s_n,s_p} \mathcal{M}_{\text{red}}^{s_n,s_p} e^{(g_p-2)s_p eB/2MT} \left[\frac{1}{1-e^{-eB/MT}} \right. \\
&- \frac{\rho_n e^{g_n s_n eB/2MT}}{\cosh[g_n eB/4MT]} \exp\left(-\frac{k_{\perp\nu}^2}{2eB+2MT} - \frac{k_{z\nu}^2}{4MT} \right) \left(\frac{\pi}{MT} \right)^{3/2} \\
&\left. \times \sum_{n_p} \left(\frac{MT}{eB+MT} \right)^{n_p} e^{-n_p eB/MT} \left(\frac{MT}{eB+MT} \delta_{s_p,+} L_{n_p}(z) + \delta_{s_p,-} L_{n_p-1}(z) \right) \right]
\end{aligned} \tag{C.21}$$

After doing the sum over n_p, the final opacities in the strong field regime are given by the following.

$$\begin{aligned}
\kappa_{\nu n} = \frac{\tilde{G}_n \rho_n}{2} \sum_{s_n,s_p} \mathcal{M}_{\text{red}}^{s_n,s_p} n_{FD}[\mu_e - E_0^{\prime +}] e^{g_n s_n eB/2MT} &\left[1 - \frac{\rho_p e^{(g_p s_p - 1)eB/2MT}}{\cosh[g_p eB/4MT]} \left(\frac{\pi}{MT} \right)^{3/2} \sinh\left(\frac{eB}{2MT} \right) \right. \\
\times \frac{2MT}{eB + MT(1-e^{-eB/MT})} \exp&\left. \left(-\frac{k_{\perp\nu}^2}{2eB+2MT} \frac{eBe^{-eB/MT}}{eB+MT(1-e^{-eB/MT})} - \frac{k_{z\nu}^2}{4MT} \right) \right]
\end{aligned} \tag{C.22}$$

$$\begin{aligned}
\kappa_{\bar{\nu} p} = \tilde{G}_p \rho_p \sinh\left[\frac{eB}{2MT} \right] \sum_{s_n,s_p} \mathcal{M}_{\text{red}}^{s_n,s_p} e^{(g_p s_p - 1)eB/2MT} &\left[\frac{1}{1-e^{-eB/MT}} - \frac{\rho_n e^{g_n s_n eB/2MT}}{\cosh[g_n eB/4MT]} \left(\frac{\pi}{MT} \right)^{3/2} \right. \\
\times \frac{MT}{eB + MT(1-e^{-eB/MT})} \exp&\left. \left(-\frac{k_{\perp\nu}^2}{2} \frac{1-e^{-eB/MT}}{eB+MT(1-e^{-eB/MT})} - \frac{k_{z\nu}^2}{4MT} \right) \right]
\end{aligned} \tag{C.23}$$

C.2.2 Medium field ($T^2 \lesssim eB \ll MT$)

$$\begin{aligned}
\kappa_{\nu n} &= \frac{\tilde{G}_n \rho_n}{2} \sum_{s_n,s_p} \tilde{V} \left[\frac{(E_0^+)^2}{2eB} \right] n_{FD}[\mu_e - E_0^+] \mathcal{M}_{\text{red}}^{s_n,s_p} e^{g_n s_n eB/2MT} \\
&\times \left[1 - \frac{\rho_p e^{g_p s_p eB/2MT}}{\cosh[g_p eB/4MT]} \left(\frac{\pi}{MT} \right)^{3/2} \sinh\left(\frac{eB}{2MT} \right) \frac{MT}{eB} e^{-k_\nu^2/4MT} \right]
\end{aligned} \tag{C.24}$$

$$\begin{aligned}
\kappa_{\bar{\nu} p} &= \tilde{G}_p \rho_p \sinh\left[\frac{eB}{2MT} \right] \frac{MT}{eB} \sum_{s_n,s_p} \tilde{V} \left[\frac{(E_0^-)^2}{2eB} \right] \mathcal{M}_{\text{red}}^{s_n,s_p} e^{g_p s_p eB/2MT} \\
&\times \left[1 - \frac{\rho_n e^{g_n s_n eB/2MT}}{2\cosh[g_n eB/4MT]} \left(\frac{\pi}{MT} \right)^{3/2} e^{-k_\nu^2/4MT} \right]
\end{aligned} \tag{C.25}$$

where the function $\tilde{V}$ contains all the resonance information. When $\tilde{V} = 1$, as is the case in the strong field limit, it is straightforward to show that this result is the weak field limit of Eqs. (C.22) and (C.23). In the low temperature limit, $\tilde{V}$ is given by

$$\lim_{T \to 0} \tilde{V}(x^2) = \sum_{n=0}^{\lfloor x \rfloor} \left(1 - \frac{n}{x^2}\right)^{-1} \tag{C.26}$$

while in the continuum limit, it is given by

$$\lim_{x \to \infty} \tilde{V}(x^2) = 2x^2 \, . \tag{C.27}$$

The latter choice would be equivalent to the quasiclassical approximation from Ref. [185] in this context. A useful finite temperature ansatz is given by the following.

$$\tilde{V}(x^2) \simeq \sum_{n=0}^{\lfloor x \rfloor} \int_{\sqrt{n}}^{\infty} \mathrm{d}u \, e^{-(u-x)^2 eB/T^2} \sqrt{\frac{eB}{\pi T^2 (1 - n/u^2)}} \frac{2}{\mathrm{erfc}[\sqrt{eB}(\sqrt{n} - x)/T]} \tag{C.28}$$

This function becomes computationally intensive for large x quite rapidly. For $x \gtrsim 10$ (or maybe even lower) it is advisable to use the large x approximation. A computationally inexpensive approximation that captures the most important functional dependence but does not capture resonances is the following.

$$\tilde{V}(x^2) = \begin{cases} 1 & x^2 \leq \frac{1}{2} \\ 2x^2 & x^2 > \frac{1}{2} \end{cases} \tag{C.29}$$

C.2.3 Weak field ($M\Delta M/g \lesssim eB \ll T^2$) or low T ($M\Delta M/g \lesssim eB \ll E_\nu^2$)

$$\begin{aligned} \kappa_{\nu n} = \frac{\tilde{G}_n \rho_n}{2} \sum_{s_n, s_p} \frac{(E_0^+)^2}{eB} n_{FD}[\mu_e - E_0] \mathcal{M}_{\text{red}}^{s_n, s_p} e^{g_n s_n eB/2MT} \\ \times \left[1 - \frac{\rho_p e^{g_p s_p eB/2MT}}{2\cosh[g_p eB/4MT]} \left(\frac{\pi}{MT}\right)^{3/2} e^{-k_\nu^2/4MT}\right] \end{aligned} \tag{C.30}$$

$$\begin{aligned} \kappa_{\nu p} = \frac{\tilde{G}_n \rho_p}{2} \sum_{s_n, s_p} \frac{(E_0^-)^2}{eB} \mathcal{M}_{\text{red}}^{s_n, s_p} e^{g_p s_p eB/2MT} \\ \times \left[1 - \frac{\rho_n e^{g_n s_n eB/2MT}}{2\cosh[g_n eB/4MT]} \left(\frac{\pi}{MT}\right)^{3/2} e^{-k_\nu^2/4MT}\right] \end{aligned} \tag{C.31}$$

It is straightforward to show that using the continuum limit of $\tilde{V}$ given in Eq. (C.27), these are the weak field limit of Eqs. (C.24) and (C.25). When the magnetic field goes to zero and Pauli blocking is neglected, this gives precisely the cross sections found in Ref. [17].

Appendix D

Induced interactions

In this appendix, we derive analytic results for the induced interaction in two steps. First, for the sake of simplicity and clarity, we assume that the bare potential only contains a momentum-independent s-wave interaction characterized by the C_0 and $\tilde{C}_0$, and spin-orbit force with strength V_{SO}. In this case, the ZS diagram involves the product $V_L \times V_R$, where

$$\begin{aligned} V_L &= C_0(\delta_{13}\delta_{ab} - \delta_{1b}\delta_{a3}) + \tilde{C}_0(\sigma_{13}\cdot\sigma_{ab} - \sigma_{1b}\cdot\sigma_{a3}) - V_{SO}2iq\times(\ell+k')\cdot(\sigma_{13}\delta_{ab} + \sigma_{ab}\delta_{13}) \\ V_R &= C_0(\delta_{24}\delta_{ba} - \delta_{2a}\delta_{b4}) + \tilde{C}_0(\sigma_{24}\cdot\sigma_{ba} - \sigma_{2a}\cdot\sigma_{b4}) + V_{SO}2iq\times(\ell-k)\cdot(\sigma_{24}\delta_{ba} + \sigma_{ba}\delta_{24})\,. \end{aligned} \tag{D.1}$$

Evaluating term-by-term, we find that the C_0^2 contribution is given by

$$C_0^2 \sum_{ab=\{\uparrow,\downarrow\}} (\delta_{13}\delta_{ab} - \delta_{1b}\delta_{a3})(\delta_{24}\delta_{ba} - \delta_{2a}\delta_{b4}) = C_0^2\delta_{14}\delta_{23} \tag{D.2}$$

To calculate the $\tilde{C}_0^2$ contribution, we use the following identities:

$$\begin{aligned} \sum_{ab=\{\uparrow,\downarrow\}} \sigma^i_{ab}\sigma^j_{ba} &= 2\delta^{ij} \\ \sum_{b=\{\uparrow,\downarrow\}} \sigma^j_{bc}\sigma^i_{ab} &= \chi_b^\dagger\sigma^j\sigma^i\chi_a = \delta_{ab}\delta^{ij} - i\varepsilon^{ijk}\sigma^k_{ab} \\ \sum_{bc=\{\uparrow,\downarrow\}}\sum_{i=1}^{3}\sigma^i_{cd}\sigma^j_{bc}\sigma^i_{ab} &= \sum_{i=1}^{3}\chi_d^\dagger\sigma^i(2\delta^{ij} - \sigma^i\sigma^j)\chi_a = -\sigma^j_{ad} \end{aligned} \tag{D.3}$$

to find that

$$\tilde{C}_0^2 \sum_{ab=\{\uparrow,\downarrow\}} (\sigma_{13}\cdot\sigma_{ab} - \sigma_{1b}\cdot\sigma_{a3})(\sigma_{24}\cdot\sigma_{ba} - \sigma_{2a}\cdot\sigma_{b4}) = \tilde{C}_0^2(4\sigma_{13}\cdot\sigma_{24} + 3\delta_{14}\delta_{23} + 2\sigma_{14}\cdot\sigma_{23}) \tag{D.4}$$

The $C_0\tilde{C}_0$ contribution is calculated by noting that $\sum_{ab}\delta_{ab}\sigma_{ba} = \mathrm{Tr}[\sigma] = 0$ and $\sum_b \sigma_{bc}\cdot\sigma_{ab} = 3\delta_{ac}$. Explicitly,

$$\begin{aligned}
&C_0\tilde{C}_0 \sum_{ab=\{\uparrow,\downarrow\}} [(\delta_{13}\delta_{ab} - \delta_{1b}\delta_{a3})(\sigma_{24}\cdot\sigma_{ba} - \sigma_{2a}\cdot\sigma_{b4}) + (\sigma_{13}\cdot\sigma_{ab} - \sigma_{1b}\cdot\sigma_{a3})(\delta_{24}\delta_{ba} - \delta_{2a}\delta_{b4})] \\
&\quad = C_0\tilde{C}_0[-2(3\delta_{13}\delta_{24} + \sigma_{13}\cdot\sigma_{24}) + 2\sigma_{14}\cdot\sigma_{23}]
\end{aligned} \tag{D.5}$$

We have calculated the leading order contributions from the spin-orbit interaction, proportional to $C_0\ V_{SO}$ and $\tilde{C}_0\ V_{SO}$ and find that their contributions vanish. First, consider the $C_0\ V_{SO}$ term

$$\begin{aligned}
C_0 V_{SO} \sum_{ab=\{\uparrow,\downarrow\}} &[(\delta_{13}\delta_{ab} - \delta_{1b}\delta_{a3}) 2iq\times(\ell - k)\cdot(\sigma_{24}\delta_{ba} + \sigma_{ba}\delta_{24}) \\
&+ (\delta_{24}\delta_{ba} - \delta_{2a}\delta_{b4}) 2iq\times(-\ell - k')\cdot(\sigma_{13}\delta_{ab} + \sigma_{ab}\delta_{13})] \\
&= 2iC_0V_{SO}[q\times(\ell - k)\cdot(2\delta_{13}\sigma_{24} - \sigma_{24}\delta_{13} - \sigma_{13}\delta_{24}) \\
&+ q\times(-\ell - k')\cdot(2\delta_{24}\sigma_{13} - \sigma_{13}\delta_{24} - \sigma_{24}\delta_{13})]\,.
\end{aligned} \tag{D.6}$$

Eq. D.6 can be simplified further by noting that terms proportional to $q\times\ell$ vanish upon integrating over the angle $\theta_{q\ell}$ and using the fact that $q\times k = q\times k' = -q\times q'/2$. We find the induced interaction proportional to $C_0\ V_{SO}$

$$iC_0V_{SO}[q\times q'\cdot(2\delta_{13}\sigma_{24} - \sigma_{24}\delta_{13} - \sigma_{13}\delta_{24} + 2\delta_{24}\sigma_{13} - \sigma_{13}\delta_{24} - \sigma_{24}\delta_{13})] = 0 \tag{D.7}$$

To see that $q\times\ell$ terms vanish, notice that the only angular dependence from the loop integral is on the angle between q and ℓ. Consider the integral $\int d\Omega_\ell \hat{\ell}\cdot\hat{u} f(\hat{\ell}\cdot\hat{q})$ where $f(\hat{\ell}\cdot\hat{q})$ contains the angular dependence of the loop integral and $\hat{\ell}\cdot\hat{u}$ corresponds to terms like $q\times\ell\cdot\sigma$. Rotate Ω_ℓ so that $\hat{q} = \hat{z}$ and $\phi_\ell = 0$ corresponds to the azimuthal angle of $\hat{u}$ calling these angles $\theta_{q\ell}$ and $\phi_{u\ell}$. Also define the polar angle of $\hat{u}$ as θ_{uq} Now $\hat{\ell}\cdot\hat{u} = \sin\theta_{q\ell}\cos\phi_{u\ell}\sin\theta_{uq} + \cos\theta_{q\ell}\cos\theta_{uq}$. Doing the integral $\int d\phi_{u\ell}\cos\phi_{u\ell} = 0$ so the only term that survives is proportional to $\cos\theta_{uq}$. In the spin-orbit terms, ℓ always enters as $q\times\ell\cdot\sigma = \ell\cdot(\sigma\times q)$ with $\sigma\times q$ orthogonal to q, so this contribution always vanishes.

Similarly, the contribution proportional to $\tilde{C}_0 V_{SO}$ can also be simplified by making the substitutions $2iq \times (\ell - k) \to iq \times q'$ and $2iq \times (-\ell - k') \to iq \times q'$ and using the identities in Eq. D.3. We find that

$$\begin{aligned}
\tilde{C}_0 V_{SO} \sum_{ab=\{\uparrow,\downarrow\}} & [(\sigma_{13} \cdot \sigma_{ab} - \sigma_{1b} \cdot \sigma_{a3}) iq \times q' \cdot (\sigma_{24}\delta_{ba} + \sigma_{ba}\delta_{24}) \\
& + (\sigma_{24} \cdot \sigma_{ba} - \sigma_{2a} \cdot \sigma_{b4}) iq \times q' \cdot (\sigma_{13}\delta_{ab} + \sigma_{ab}\delta_{13})] \\
& = \tilde{C}_0 V_{SO}\ iq \times q' \cdot (2\sigma_{13}\delta_{24} - 3\sigma_{24}\delta_{13} + \sigma_{13}\delta_{24} \\
& + 2\sigma_{24}\delta_{13} - 3\sigma_{13}\delta_{24} + \sigma_{24}\delta_{13}) \\
& = 0\,.
\end{aligned} \tag{D.8}$$

Thus, spin-orbit terms do not contribute to the induced interaction at leading order in V_{SO}. Up to this order, including all of the non-zero terms associated with the product $V_L \times V_R$ and performing the particle-hole loop integration, we find that the induced interaction due to the ZS diagram is given by

$$\begin{aligned}
V_{ZS}^{\text{ind}} = & -U(q)\left[(C_0^2 + 3\tilde{C}_0^2)\delta_{14}\delta_{23} - 6C_0\tilde{C}_0\delta_{13}\delta_{24})\right] \\
& - U(q)\left[(4\tilde{C}_0^2 - 2C_0\tilde{C}_0)\sigma_{13} \cdot \sigma_{24} + (2\tilde{C}_0^2 + 2C_0\tilde{C}_0)\sigma_{14} \cdot \sigma_{23})\right]
\end{aligned} \tag{D.9}$$

where

$$\begin{aligned}
U(q) & = -\frac{1}{\beta}\sum_{\ell_0}\int \frac{d^3\ell}{(2\pi)^3}\frac{1}{\ell_0 - \ell^2/2m}\frac{1}{\ell_0 - (\ell+q)^2/2m} \\
& = -\frac{m}{2\pi^2 q}\int_0^{k_F} \ell d\ell \int_{-1}^{1} \frac{d\cos\theta_{q\ell}}{\cos\theta_{q\ell} - q/2\ell} \\
& = -\frac{mk_F^2}{2\pi^2 q}\left[-\frac{q}{2k_F} + \frac{1}{2}\left(1 - \frac{q^2}{4k_F^2}\right)\log\left|\frac{1 - q/2k_F}{1 + q/2k_F}\right|\right]
\end{aligned} \tag{D.10}$$

is the positive Lindhard function.

The contribution from the ZS' diagram is obtained by switching indices 3 and 4 and by replacing q by q' in the loop integral. Explicitly,

$$\begin{aligned}
V_{ZS'}^{\text{ind}} = & -U(q')\left[(C_0^2 + 3\tilde{C}_0^2)\delta_{13}\delta_{24} - 6C_0\tilde{C}_0\delta_{14}\delta_{23})\right] \\
& - U(q')\left[(4\tilde{C}_0^2 - 2C_0\tilde{C}_0)\sigma_{14} \cdot \sigma_{23} + (2\tilde{C}_0^2 + 2C_0\tilde{C}_0)\sigma_{13} \cdot \sigma_{24})\right]\,.
\end{aligned} \tag{D.11}$$

The calculation of the momentum-dependent part of the induced potential is similar but a bit more tedious and the analytic results involves a large number of terms. To obtain useful formula with fewer terms we present results for the spin singlet and spin-triplet contributions. These will require the second and fourth moments of the Lindhard function denoted U_2 and U_4. U_2 is defined as follows:

$$\begin{aligned} U_2(q) &= -\frac{m}{2\pi^2 q}\int_0^{k_F} \ell^3 d\ell \int_{-1}^{1} \frac{d\cos\theta_{q\ell}}{\cos\theta_{q\ell} - q/2\ell} \\ &= -\frac{mk_F^4}{2\pi^2 q}\left[-\frac{q}{12k_F} - \frac{q^3}{16k_F^3} + \frac{1}{4}\left(1 - \frac{q^4}{16k_F^4}\right)\log\left|\frac{1-q/2k_F}{1+q/2k_F}\right|\right] \end{aligned} \tag{D.12}$$

U_4 is defined analagously and is given by:

$$U_4(q) = -\frac{mk_F^6}{2\pi^2 q}\left[-\frac{q}{30k_F} - \frac{q^3}{72k_F^3} - \frac{q^5}{96k_F^5} + \frac{1}{6}\left(1 - \frac{q^6}{64k_F^6}\right)\log\left|\frac{1-q/2k_F}{1+q/2k_F}\right|\right] \tag{D.13}$$

Five momentum structures appear corresponding to the five pairings of the combinations of constants given above. The momentum-dependent parts of V_L and V_R take the following form for the spin-independent terms. The spin-dependent terms are analagous.

$$\begin{aligned} V_L &\supset C_2((-\ell - k')^2 + q^2)(\delta_{13}\delta_{ab} - \delta_{1b}\delta_{a3}) + C_2'((-\ell - k')^2 - q^2)(\delta_{13}\delta_{ab} + \delta_{1b}\delta_{a3}) \\ V_R &\supset C_2((\ell - k)^2 + q^2)(\delta_{24}\delta_{ba} - \delta_{2a}\delta_{b4}) + C_2'((\ell - k)^2 - q^2)(\delta_{24}\delta_{ba} + \delta_{2a}\delta_{b4}) \end{aligned} \tag{D.14}$$

The contributions of the momentum dependence to the induced potential are:

$$\begin{aligned} \xi_a(q) &= \frac{1}{\beta}\sum_{\ell_0}\int \frac{d^3\ell}{(2\pi)^3}\Delta(\ell)\Delta(\ell+q)[2q^2 + (-\ell - k')^2 + (\ell - k)^2] \\ \xi_b(q) &= \frac{1}{\beta}\sum_{\ell_0}\int \frac{d^3\ell}{(2\pi)^3}\Delta(\ell)\Delta(\ell+q)[-2q^2 + (-\ell - k')^2 + (\ell - k)^2] \\ \xi_c(q) &= \frac{1}{\beta}\sum_{\ell_0}\int \frac{d^3\ell}{(2\pi)^3}\Delta(\ell)\Delta(\ell+q)[(-\ell - k')^2 + q^2][(\ell - k)^2 + q^2] \\ \xi_d(q) &= \frac{1}{\beta}\sum_{\ell_0}\int \frac{d^3\ell}{(2\pi)^3}\Delta(\ell)\Delta(\ell+q)[(-\ell - k')^2 - q^2][(\ell - k)^2 - q^2] \\ \xi_e(q) &= \frac{1}{\beta}\sum_{\ell_0}\int \frac{d^3\ell}{(2\pi)^3}\Delta(\ell)\Delta(\ell+q)[((-\ell - k')^2 - q^2)((\ell - k)^2 + q^2) \\ &\quad + ((\ell - k')^2 + q^2)((\ell - k)^2 - q^2)] \end{aligned} \tag{D.15}$$

$\Delta(\ell) = (\ell_0 - \ell^2/2m)^{-1}$ is the fermion propagator. After doing the loop integral, these give:

$$\begin{aligned}
\xi_a(q) &= -\frac{2mk_F^3}{3\pi^2} - (q^2 + 2k_F^2)U(q) - 2U_2(q) \\
\xi_b(q) &= -\frac{2mk_F^3}{3\pi^2} + (3q^2 - 2k_F^2)U(q) - 2U_2(q) \\
\xi_c(q) &= -\frac{mk_F^3}{\pi^2}\left(\frac{11}{15}k_F^2 + \frac{7}{12}q^2\right) - \left(k_F^4 + \frac{3}{2}q^2k_F^2 + \frac{q^4}{8}\right)U(q) \\
&\quad - \frac{3}{2}q^2U_2(q) - U_4(q) \\
\xi_d(q) &= -\frac{mk_F^3}{\pi^2}\left(\frac{11}{15}k_F^2 - \frac{3}{4}q^2\right) - \left(k_F^4 - \frac{5}{2}q^2k_F^2 + \frac{17}{8}q^4\right)U(q) \\
&\quad + \frac{5}{2}q^2U_2(q) - U_4(q) \\
\xi_e(q) &= -\frac{mk_F^3}{\pi^2}\left(\frac{22}{15}k_F^2 - \frac{q^2}{6}\right) - \left(2k_F^4 - q^2k_F^2 - \frac{7}{4}q^4\right) + q^2U_2(q) - 2U_4(q)
\end{aligned} \tag{D.16}$$

The total central induced potential in the spin triplet channel:

$$\begin{aligned}
V_{S=1}^{\text{ind}} &= -\bar{C}_0^2(U(q) - U(q')) + \bar{C}_0\bar{C}_2(\xi_a(q) - \xi_a(q')) + \bar{C}_0\bar{C}_2'(\xi_b(q) - \xi_b(q')) \\
&\quad + \bar{C}_2^2(\xi_c(q) - \xi_c(q')) + 5\bar{C}_2'^2(\xi_d(q) - \xi_d(q')) + \bar{C}_2\bar{C}_2'(\xi_e(q) - \xi_e(q'))
\end{aligned} \tag{D.17}$$

The total central induced potential in the spin singlet channel:

$$\begin{aligned}
V_{S=0}^{\text{ind}} &= \bar{C}_0^2\,(U(q) + U(q')) - \bar{C}_0\bar{C}_2(\xi_a(q) + \xi_a(q')) + 3\bar{C}_0\bar{C}_2'(\xi_b(q) + \xi_b(q')) \\
&\quad - \bar{C}_2^2\,(\xi_c(q) + \xi_c(q')) + 3\left(\bar{C}_2'^2(\xi_d(q) + \xi_d(q')) + \bar{C}_2\bar{C}_2'(\xi_e(q) + \xi_e(q')\right)\ .
\end{aligned} \tag{D.18}$$

This gives s- and p-wave central potentials:

$$\begin{aligned}
{}^1S_0 : \bar{C}_0^2\frac{mk_F}{3\pi^2}&(1 + 2\log 2) + mk_F^3[\bar{C}_0\bar{C}_2\frac{2}{3\pi^2}(5 + 4\log 2) \\
&+ \bar{C}_0\bar{C}_2'\frac{2}{5\pi^2}(7 - 4\log 2)] + mk_F^5[\bar{C}_2^2\frac{8}{315\pi^2}(277 + 96\log 2) \\
&- \bar{C}_2'^2\frac{8}{105\pi^2}(43 + 24\log 2) + \bar{C}_2\bar{C}_2'\frac{32}{105\pi^2}(37 + 6\log 2)]
\end{aligned} \tag{D.19}$$

$$\begin{aligned}
{}^3P_J : \bar{C}_0^2\frac{mk_F}{5\pi^2}&(1 - 2\log 2) + mk_F^3[\bar{C}_0\bar{C}_2\frac{2}{105\pi^2}(59 - 68\log 2) \\
&- \bar{C}_0\bar{C}_2'\frac{2}{105\pi^2}(29 + 52\log 2)] + mk_F^5[\bar{C}_2^2\frac{16}{567\pi^2}(83 - 24\log 2) \\
&+ \bar{C}_2'^2\frac{64}{567\pi^2}(34 - 3\log 2) - \bar{C}_2\bar{C}_2'\frac{16}{2835\pi^2}(523 + 204\log 2)]
\end{aligned} \tag{D.20}$$

The spin-orbit potential gives an additional contribution to the p-waves:

$$\begin{aligned}
2\bar{C}_2'V_{SO}\frac{1}{\beta}\sum_{\ell_0}\int&\frac{d^3\ell}{(2\pi)^3}\Delta(\ell)\Delta(\ell+q)[((-\ell-k')^2 - q^2)iq\times(\ell-k)\cdot(3\delta_{13}\sigma_{24} + \delta_{24}\sigma_{13}) \\
&+ ((\ell-k)^2 - q^2)iq\times(-\ell-k')\cdot(3\delta_{24}\sigma_{13} + \delta_{13}\sigma_{24})] \\
&= \bar{C}_2'V_{SO}iq\times q'\cdot(\sigma_{13}\delta_{24} + \sigma_{24}\delta_{13})\xi_f(q)
\end{aligned} \tag{D.21}$$

The function $\xi_f(q)$ is given by:

$$\xi_f(q) = -\frac{2mk_F^3}{3\pi^2} + (5q^2 - 4k_F^2)U(q) \tag{D.22}$$

This gives a contribution to the p-waves after including the ZS' diagram:

$$^3P_J : [J(J+1) - 4]\bar{C}_2' V_{SO} \frac{32mk_F^5}{945\pi^2}(43 + 24\log 2) \tag{D.23}$$

Details of the angular integration are given in the next section App. E. We calculate the contribution of the tensor interaction only to $\mathcal{O}(mk_F^3)$. The term proportional to $C_0 V_T$ gives:

$$\begin{aligned} C_0 V_T \frac{1}{\beta}\sum_{\ell_0}\int \frac{d^3\ell}{(2\pi)^3}\Delta(\ell)\Delta(\ell+q)[&-\delta_{13}\delta_{24}((-\ell-k')^2 + (\ell-k)^2) - 2q\cdot\sigma_{13}q\cdot\sigma_{24} \\ &+ (-\ell-k')\cdot\sigma_{23}(-\ell-k')\cdot\sigma_{14} + (\ell-k)\cdot\sigma_{23}(\ell-k)\cdot\sigma_{14}] \end{aligned} \tag{D.24}$$

Doing the calculation for the $\tilde{C}_0 V_T$ term gives -3 times the result for the term proportional to $C_0 V_T$ after reducing to spin singlet or triplet. The potentials in these channels after including the ZS' diagram are given by:

$$V_{S=0}^{\text{ind}} = -\bar{C}_0 V_T(2q^2 U(q) + 2q'^2 U(q')) \tag{D.25}$$

$$\begin{aligned} V_{S=1}^{\text{ind}} = \bar{C}_0 V_T\Big[&\frac{mk_F^3}{6\pi^2}(-\hat{q}\cdot\sigma_{13}\hat{q}\cdot\sigma_{24} + \hat{q}'\cdot\sigma_{13}\hat{q}'\cdot\sigma_{24}) + U(q)\left(\frac{3}{4}q\cdot\sigma_{13}q\cdot\sigma_{24}\right. \\ &\left. - \frac{1}{2}q'\cdot\sigma_{13}q'\cdot\sigma_{24} + \frac{q^2}{4}\right) - U(q')\left(\frac{3}{4}q'\cdot\sigma_{13}q'\cdot\sigma_{24} - \frac{1}{2}q\cdot\sigma_{13}q\cdot\sigma_{24} + \frac{q'^2}{4}\right) \\ &+ U_2(q)(1 + \hat{q}\cdot\sigma_{13}\hat{q}\cdot\sigma_{24}) - U_2(q')(1 + \hat{q}'\cdot\sigma_{13}\hat{q}'\cdot\sigma_{24})\Big] \end{aligned} \tag{D.26}$$

where we define the unit vector $\hat{q} = \vec{q}/|q|$. For the spin triplet, outgoing spin indices are exchanged on some terms to simplify the equations. Doing the integrals gives:

$$\begin{aligned} &^1S_0 : -\bar{C}_0 V_T \frac{16mk_F^3}{15\pi^2}(2 + \log 2) \\ &^3P_2 : -\bar{C}_0 V_T \frac{4mk_F^3}{15\pi^2}(1 - \log 2) \\ &^3P_1 : -\bar{C}_0 V_T \frac{4mk_F^3}{21\pi^2}(4 + 5\log 2) \\ &^3P_0 : \bar{C}_0 V_T \frac{2mk_F^3}{21\pi^2}(5 + 22\log 2) \end{aligned} \tag{D.27}$$

The part of the interaction proportional to V_{SO}^2 takes the form:

$$
\begin{aligned}
&-8V_{SO}^2\frac{1}{\beta}\sum_{\ell_0}\int\frac{d^3\ell}{(2\pi)^3}\Delta(\ell)\Delta(\ell+q)[(q\times(-\ell-k')\cdot\sigma_{13})(q\times(\ell-k)\cdot\sigma_{24}) \\
&\quad+\delta_{13}\delta_{24}(q\times(-\ell-k'))\cdot(q\times(\ell-k))] \\
&\quad=-\frac{2mk_F^3}{3\pi^2}(q^2(\sigma_{13}\cdot\sigma_{24}+2\delta_{13}\delta_{24})-(q\cdot\sigma_{13})(q\cdot\sigma_{24}))+U(q)[q^4\sigma_{13}\cdot\sigma_{24} \\
&\quad-q^2(q\cdot\sigma_{13})(q\cdot\sigma_{24})+2(q\times q'\cdot\sigma_{13})(q\times q'\cdot\sigma_{24})+8\delta_{24}\delta_{24}q^2k_F^2] \\
&\quad-U_2(q)[4(q^2\sigma_{13}\cdot\sigma_{24}-(q\cdot\sigma_{13})(q\cdot\sigma_{24}))+8\delta_{13}\delta_{24}q^2]
\end{aligned}
\tag{D.28}
$$

A tedious calculation gives the following contribution:

$$
\begin{aligned}
&{}^1S_0: V_{SO}^2\frac{8mk_F^5}{35\pi^2}(17+16\log 2) \\
&{}^3P_2: V_{SO}^2\frac{128mk_F^5}{4725\pi^2}(43+24\log 2) \\
&{}^3P_1: 0 \\
&{}^3P_0: V_{SO}^2\frac{64mk_F^5}{945\pi^2}(43+24\log 2)
\end{aligned}
\tag{D.29}
$$

Appendix E

Angular integrations for non-central interactions

In order to determine the contribution of an arbitrary potential given in momentum space to a given partial wave, we must make a change of basis.

$$
\begin{aligned}
V_{LSJ} &= \frac{1}{4\pi} \sum_{m_\ell m'_\ell m_s m'_s} \int d\Omega_k d\Omega_{k'} \langle J, m_j | L, m'_\ell, S, m'_s \rangle \langle L, m'_\ell | \hat{k}' \rangle \\
&\times \langle \hat{k}', S, m'_s | V | \hat{k}, S, m_s \rangle \langle \hat{k} | L, m_\ell \rangle \langle L, m'_\ell, S, m'_s | J, m_j \rangle \\
&= \frac{1}{4\pi} \sum_{m_\ell m'_\ell m_s m'_s} C^{Jm_j}_{Lm'_\ell Sm'_s} C^{Jm_j}_{Lm_\ell Sm_s} \int d\Omega_k d\Omega_{k'} Y^{*m'_\ell}_L(\hat{k}') Y^{m_\ell}_L(\hat{k}) \\
&\times \langle \hat{k}', S, m'_s | V | \hat{k}, S, m_s \rangle
\end{aligned}
\tag{E.1}
$$

where $C^{Jm_j}_{Lm_\ell Sm_s}$ are Clebsch-Gordan coefficients. When V contains non-central interactions, $m_j = m_\ell + m_s$ is conserved but m_ℓ and m_s in general are not. In the case of a central potential, m_ℓ and m_s are both conserved and V_{LSJ} depends only on L. In this case, the calculation of V_{LSJ} reduces to a standard calculation of partial waves.

$$
\begin{aligned}
V_{LSJ} &= \frac{1}{4\pi} \sum_{m_\ell m'_\ell m_s m'_s} C^{Jm_j}_{Lm'_\ell Sm'_s} C^{Jm_j}_{Lm_\ell Sm_s} \int d\Omega_k d\Omega_{k'} Y^{*m'_\ell}_L(\hat{k}') Y^{m_\ell}_L(\hat{k}) \\
&\times V(\hat{k} \cdot \hat{k}') \delta_{m_s m'_s} \\
&= \frac{1}{4\pi} \int d\Omega_k d\Omega_{k'} Y^{*m_\ell}_L(\hat{k}') Y^{m_\ell}_L(\hat{k}) V(\hat{k} \cdot \hat{k}') \\
&= \frac{1}{2} \int d\cos\theta_{kk'} P_L(\cos\theta_{kk'}) V(\cos\theta_{kk'})
\end{aligned}
\tag{E.2}
$$

Although we do include tensor interactions which in general couple different L, we neglect the effect of coupled channels. Note that V_{LSJ} is independent of m_j and so whichever m_j gives the most straightforward calculation may be used. For example, when calculating the ${}^3P_1$ potential of some interaction, it is often more convenient to calculate the $m_j = 0$ state since C^{10}_{1010} is zero and there will be fewer terms with simpler spin structure than when calculating the same interaction with $m_j = \pm 1$.

The basic recipe for doing this calculation will be illustrated with the spin-orbit spin structure but is applicable to any rotationally invariant potential. Throughout, I will use the shorthand $c = \cos\theta$, $c' = \cos\theta'$, and $c_{kk'} = \cos\theta_{kk'}$ for $\theta_{kk'} = \hat{k}\cdot\hat{k}'$ (and the same for s, s', $s_{kk'}$ but with sine instead of cosine). The relevant angular integration for the ${}^3P_2$ potential is of the form

$$\frac{1}{4\pi}\int Y_1^{*1}(\hat{k}')Y_1^1(\hat{k}) iq \times q' \cdot 2\hat{z} F(c_{kk'}) d\Omega d\Omega' \tag{E.3}$$

where $F(c_{kk'})$ is some spin-independent function that comes from the momentum integration (e.g. the Lindhard function). We want to rewrite the spin-orbit part and spherical harmonics in terms of an integral over only $c_{kk'}$. The steps to do this are

- Rewrite integral in terms of $\bar{\phi} = \phi - \phi'$. Typically, terms that cannot be rewritten this way go to zero, but this must be checked. This usually can be determined by treating F as a power series in $c_{kk'} = ss'\cos\bar{\phi} + cc'$.

- Replace $\cos\bar{\phi} = (c_{kk'} - cc')/ss'$

- Replace the $d\Omega'$ integral with an integral $dc_{kk'}d\phi_{zk'}$ where $\phi_{zk'}$ is the azimuthal angle relative to the z-axis. I.e. rotate the axes of $d\Omega'$ so that the z'-axis points in the direction of $\hat{k}$ and the x'-axis points in the direction of the z-axis. This results in the replacement $c' = cc_{kk'} + \cos\phi_{zk'}ss_{kk'}$. The $\phi_{zk'}$ integral is usually done easily.

- Typically there will be no remaining ϕ dependence (if things that go to zero were dropped earlier) so the ϕ integral just gives an overall factor of 2π. The remaining integrals are $dcdc_{kk'}$ and the dc integral can easily be done analytically. This will leave an expression of the form $\int dc_{kk'}g(c_{kk'})F(c_{kk'}$ exactly as desired.

Showing these steps for ${}^3P_2$ spin-orbit interaction

$$\frac{1}{4\pi}\int Y_1^{*1}(\hat{k}')Y_1^1(\hat{k}) iq \times q' \cdot 2\hat{z} F(c_{kk'}) d\Omega d\Omega' = -\frac{3ik_F^2}{16\pi^2}\int s^2 s'^2 \sin\bar{\phi}\, e^{i\bar{\phi}} F(c_{kk'}) d\Omega d\Omega' \tag{E.4}$$

Remembering to treat F as a power series in $\cos\bar{\phi}$, we see that only the term in the integral that goes as $\sin^2\bar{\phi}$ will survive. Doing the integral:

$$\begin{aligned}
&\frac{3k_F^2}{8\pi^2}\int s^2 s'^2(1-\cos^2\bar{\phi})F(c_{kk'})d\Omega d\Omega' \\
&\quad= \frac{3k_F^2}{8\pi^2}\int (s^2 s'^2 - (c_{kk'} - cc')^2)F(c_{kk'})d\Omega d\Omega' \\
&\quad= \frac{3k_F^2}{8\pi^2}\int (s^2 - c_{kk'}^2 + c'(2cc_{kk'}) - c'^2(s^2+c^2))F(c_{kk'})d\Omega dc_{kk'}d\phi_{zk'} \\
&\quad= \frac{3k_F^2}{8\pi}\int [2(1-c^2-c_{kk'}^2) + 4c^2c_{kk'}^2 - (1-c^2+c_{kk'}^2(-1+3c^2))]F(c_{kk'})d\Omega dc_{kk'} \\
&\quad= k_F^2\int (1-c_{kk'}^2)F(c_{kk'})dc_{kk'}
\end{aligned} \tag{E.5}$$

So, for example, the induced interaction that couples the spin-orbit and second-order p-wave potential is given by:

$$\bar{C}_2' V_{SO} k_F^2 \int (c_{kk'}^2 - 1)\left[\frac{8mk_F^3}{3\pi^2} + (8k_F^2 - 10q^2)U(q) + (8k_F^2 - 10q'^2)U(q')\right] dc_{kk'} \tag{E.6}$$

Making the substitution $\int_{-1}^{1} dc_{kk'} = \int_0^2 \bar{q}d\bar{q}$ where $\bar{q} = \hat{k}' - \hat{k}$, this integral is easily done with Mathematica, giving:

$$\bar{C}_2' V_{SO}\frac{128mk_F^5}{945\pi^2}(43 + 24\log 2) \tag{E.7}$$

Appendix F

Induced interaction between quarks

Treating quarks relativistically, the screening diagram is given by

$$\begin{aligned} V^{\text{ind}} &= g_V^2 (\bar{u}_3 \gamma_\mu u_1)(\bar{u}_4 \gamma_\nu u_2) \left(\frac{E_k + m_s}{2m_s} \right)^2 \sum_{f,c} \frac{1}{\beta} \sum_{\ell_0} \int \frac{d^3\ell}{(2\pi)^3} \\ &\times \frac{\operatorname{tr}\left[\gamma^\mu (\not{\ell} + \not{q} + m_f) \gamma^\nu (\not{\ell} + m_f)\right]}{(\ell_0^2 - \ell^2 - m_f^2)(\ell_0^2 - (\ell + q)^2 - m_f^2)} \end{aligned} \tag{F.1}$$

where $f = u, d, s$ and $c = r, g, b$ denotes the flavor and color of quarks that appear in the particle-hole loop. Since the screening diagram is enhanced by the number of flavors and colors and the other diagrams are not, we calculate only this part of the potential. We neglect anti-particle contributions by discarding the Matsubara sums that produce terms proportional to $(\exp[\beta(E + \mu)] + 1)^{-1}$, which are negligible at small temperatures. Doing the trace and noticing that $\bar{u}_3 \not{q} u_1 = \bar{u}_4 \not{q} u_2 = 0$, Eq. F.1 can be written as

$$V^{\text{ind}} = g_V^2 (\bar{u}_3 \gamma_\mu u_1)(\bar{u}_4 \gamma_\nu u_2) \left(\frac{E_k + m_s}{2m_s} \right)^2 \sum_{f,c} \int \frac{\ell d\ell d\Omega_\ell}{4\pi^3 q E_\ell} \frac{\Theta(k_{fc} - \ell)}{\cos\theta_{q\ell} - q/2\ell} (2\ell^\mu \ell^\nu - g^{\mu\nu} \vec{\ell} \cdot \vec{q}) \tag{F.2}$$

k_{fc} is the Fermi momentum of flavor f and color c with the normal subscript F suppressed for readability. Since the Fermi momentum of strange quarks is approximately the same for all colors, also suppress the color label on k_s. Expanding to zeroth order in k_s/m_s, only the $\mu = \nu = 0$ components contribute and we get:

$$V^{\text{ind}} = g_V^2 \delta_{13} \delta_{24} \frac{1}{2\pi^2 q} \sum_{f,c} \int \frac{\ell d\ell}{\sqrt{\ell^2 + m_f^2}} \frac{dc_{q\ell}}{\cos\theta_{q\ell} - q/2\ell} \Theta(k_{fc} - \ell)(2\ell^2 + 2m_f^2 - 2\ell q \cos\theta_{q\ell}) \tag{F.3}$$

Setting $m_u = m_d = 0$ and discarding components from the strange quark that are not proportional to m_s gives:

$$V^{\text{ind}} = g_V^2 \delta_{13}\delta_{24} \sum_c \left[\sum_{f=u,d} \left(-\frac{k_{fc}^2}{2\pi^2} + \frac{q^2}{2} U_0^{\text{rel}}\left(\frac{q}{k_{fc}}\right) - 2k_{fc}^2 U_2^{\text{rel}}\left(\frac{q}{k_{fc}}\right) \right) - 2U(q) \right] \tag{F.4}$$

where the mass in the Lindhard function $U(q)$ is the strange quark mass and we define relativistic dimensionless Lindhard functions in analogy with the relativistic ones (defining $\tilde{q} = q/k_{fc}$ to be distinguished from $\bar{q} = q/k_s$):

$$\begin{aligned} U_0^{\text{rel}}(\tilde{q} = q/k_{fc}) &= -\frac{1}{2\pi^2 \tilde{q}} \int d\bar{\ell} \log \left| \frac{1 - \tilde{q}/2\bar{\ell}}{1 + \tilde{q}/2\bar{\ell}} \right| \\ &= \frac{1}{2\pi^2 \tilde{q}} \left[\log \left| 1 + \frac{2}{\tilde{q}} \right| - \left(1 - \frac{\tilde{q}}{2}\right) \log \left| \frac{1 - \tilde{q}/2}{1 + \tilde{q}/2} \right| \right] \\ U_2^{\text{rel}}(\tilde{q}) &= -\frac{1}{2\pi^2 \tilde{q}} \int \bar{\ell}^2 d\bar{\ell} \log \left| \frac{1 - \tilde{q}/2\bar{\ell}}{1 + \tilde{q}/2\bar{\ell}} \right| \\ &= \frac{1}{6\pi^2 \tilde{q}} \left[\frac{\tilde{q}}{2} + \frac{\tilde{q}^3}{4} \log \left| 1 + \frac{2}{\tilde{q}} \right| - \left(1 - \frac{\tilde{q}^3}{8}\right) \log \left| \frac{1 - \tilde{q}/2}{1 + \tilde{q}/2} \right| \right] \end{aligned} \tag{F.5}$$

Analytical expressions for s- and p-wave potentials can easily be found with Mathematica or equivalent, but are long and unenlightening so we do not reproduce them here.

Bibliography

[1] W. Baade and F. Zwicky. Remarks on super-novae and cosmic rays. *Phys. Rev.*, 46:76–77, Jul 1934.

[2] A. Hewish, S. J. Bell, J. D. H. Pilkington, P. F. Scott, and R. A. Collins. Observation of a rapidly pulsating radio source. *Nature*, 217(5130):709–713, 1968.

[3] Riccardo Giacconi, Herbert Gursky, Frank R Paolini, and Bruno B Rossi. Evidence for x-rays from sources outside the solar system. *Physical Review Letters*, 9(11):439–443, 1962.

[4] B. P. Abbott et al. Gw170817: Observation of gravitational waves from a binary neutron star inspiral. *Phys. Rev. Lett.*, 119:161101, Oct 2017.

[5] V. Savchenko et al. Integral detection of the first prompt gamma-ray signal coincident with the gravitational-wave event gw170817. *The Astrophysical Journal Letters*, 848(2):L15, oct 2017.

[6] Stefano Valenti et al. The discovery of the electromagnetic counterpart of gw170817: Kilonova at 2017gfo/dlt17ck. *The Astrophysical Journal Letters*, 848(2):L24, oct 2017.

[7] E. Troja et al. The x-ray counterpart to the gravitational-wave event gw170817. *Nature*, 551(7678):71–74, 2017.

[8] K. D. Alexander et al. The electromagnetic counterpart of the binary neutron star merger ligo/virgo gw170817. vi. radio constraints on a relativistic jet and predictions for late-time emission from the kilonova ejecta. *The Astrophysical Journal Letters*, 848(2):L21, oct 2017.

[9] R. Margutti et al. The binary neutron star event ligo/virgo gw170817 160 days after merger: Synchrotron emission across the electromagnetic spectrum. *The Astrophysical Journal Letters*, 856(1):L18, mar 2018.

[10] Mia Kumamoto, Junwu Huang, Christian Drischler, Masha Baryakhtar, and Sanjay Reddy. Neutron stars with exceptionally light qcd axions. *Phys. Rev. D*, 112:043008, Aug 2025.

[11] Mia Kumamoto and Catherine Welch. Effects of landau quantization on neutrino emission and absorption. *Phys. Rev. D*, 111:063009, Mar 2025.

[12] Mia Kumamoto and Sanjay Reddy. Kohn-luttinger effect in dense matter and its implications for neutron stars. *Phys. Rev. C*, 110:025804, Aug 2024.

[13] D. G. Ravenhall, C. J. Pethick, and J. R. Wilson. Structure of matter below nuclear saturation density. *Phys. Rev. Lett.*, 50:2066–2069, Jun 1983.

[14] M. E. Caplan and C. J. Horowitz. Colloquium: Astromaterial science and nuclear pasta. *Rev. Mod. Phys.*, 89:041002, Oct 2017.

[15] Dany Page, Ulrich Geppert, and Fridolin Weber. The cooling of compact stars. *Nuclear Physics A*, 777:497–530, 2006. Special Issue on Nuclear Astrophysics.

[16] Huaiyu Duan and Yong-Zhong Qian. Rates of neutrino absorption on nucleons and the reverse processes in strong magnetic fields. *Phys. Rev. D*, 72:023005, Jul 2005.

[17] Adam Burrows, Sanjay Reddy, and Todd A. Thompson. Neutrino opacities in nuclear matter. *Nuclear Physics A*, 777:356–394, 2006. Special Isseu on Nuclear Astrophysics.

[18] William G. Newton. A taste of pasta? *Nature Physics*, 9(7):396–397, 2013.

[19] A. Y. Potekhin, J. A. Pons, and Dany Page. Neutron stars - cooling and transport. *Space Sci. Rev.*, 191(1-4):239–291, 2015.

[20] Dany Page and Sanjay Reddy. Thermal and transport properties of the neutron star inner crust. 2012.

[21] A. Y. Potekhin, G. Chabrier, and D. G. Yakovlev. Internal temperatures and cooling of neutron stars with accreted envelopes. 1997.

[22] Gilles Chabrier, Alexander Y. Potekhin, and Dmitry G. Yakovlev. Cooling neutron stars with accreted envelopes. *The Astrophysical Journal*, 477(2):L99, mar 1997.

[23] M. V. Beznogov, A. Y. Potekhin, and D. G. Yakovlev. Diffusive heat blanketing envelopes of neutron stars. *Monthly Notices of the Royal Astronomical Society*, 459(2):1569–1579, 03 2016.

[24] Mark G. Alford and Steven P. Harris. β equilibrium in neutron-star mergers. *Phys. Rev. C*, 98:065806, Dec 2018.

[25] R. N. Manchester, G. B. Hobbs, A. Teoh, and M. Hobbs. The australia telescope national facility pulsar catalogue. *The Astronomical Journal*, 129(4):1993, apr 2005.

[26] William Forman, C. Jones, L. Cominsky, P. Julien, S. Murray, G. Peters, H. Tananbaum, and R. Giacconi. The fourth uhuru catalog of x-ray sources. *Astrophysical Journal Supplement Series*, 38:357–412, 1978.

[27] Paul Demorest, Tim Pennucci, Scott Ransom, Mallory Roberts, and Jason Hessels. Shapiro Delay Measurement of A Two Solar Mass Neutron Star. *Nature*, 467:1081–1083, 2010.

[28] John Antoniadis et al. A Massive Pulsar in a Compact Relativistic Binary. *Science*, 340:6131, 2013.

[29] Emmanuel Fonseca, H. T. Cromartie, Timothy T. Pennucci, P. S. Ray, A. Yu. Kirichenko, Scott M. Ransom, Paul B. Demorest, Ingrid H. Stairs, Zaven Arzoumanian, Lucas Guillemot, Aditya Parthasarathy, Matthew Kerr, Ismael Cognard, P. T. Baker, H. Blumer, P. R. Brook, M. DeCesar, T. Dolch, F. A. Dong, E. C. Ferrara, W. Fiore, N. Garver-Daniels, D. C. Good, R. Jennings, M. L. Jones, Victoria M. Kaspi, M. T. Lam, D. R. Lorimer, J. Luo, A. McEwen, J. W. McKee, M. A. McLaughlin, N. McMann, B. W. Meyers, A. Naidu, and others. Refined mass and geometric measurements of the high-mass PSR j0740+6620. *Astrophysical Journal Letters*, 915(1):L12, 2021.

[30] I. Tews, T. Krüger, K. Hebeler, and A. Schwenk. Neutron matter at next-to-next-to-next-to-leading order in chiral effective field theory. *Phys. Rev. Lett.*, 110(3):032504, 2013.

[31] Christian Drischler, Sophia Han, James M. Lattimer, Madappa Prakash, Sanjay Reddy, and Tianqi Zhao. Limiting masses and radii of neutron stars and their implications. *Phys. Rev. C*, 103:045808, Apr 2021.

[32] Oleg Komoltsev and Aleksi Kurkela. How perturbative qcd constrains the equation of state at neutron-star densities. *Phys. Rev. Lett.*, 128:202701, May 2022.

[33] R. Somasundaram, I. Tews, and J. Margueron. Perturbative qcd and the neutron star equation of state. *Phys. Rev. C*, 107:L052801, May 2023.

[34] Oleg Komoltsev, Rahul Somasundaram, Tyler Gorda, Aleksi Kurkela, Jérôme Margueron, and Ingo Tews. Equation of state at neutron-star densities and beyond from perturbative qcd. *Phys. Rev. D*, 109:094030, May 2024.

[35] A. C. Semposki, C. Drischler, R. J. Furnstahl, J. A. Melendez, and D. R. Phillips. From chiral effective field theory to perturbative qcd: A bayesian model mixing approach to symmetric nuclear matter. *Phys. Rev. C*, 111:035804, Mar 2025.

[36] W. Weise. Nuclear chiral dynamics and phases of qcd. *Progress in Particle and Nuclear Physics*, 67(2):299–311, 2012. From Quarks and Gluons to Hadrons and Nuclei.

[37] Len Brandes and Wolfram Weise. Implications of latest nicer data for the neutron star equation of state. *Phys. Rev. D*, 111:034005, Feb 2025.

[38] Ryan Abbott, William Detmold, Marc Illa, Assumpta Parreño, Robert J. Perry, Fernando Romero-López, Phiala E. Shanahan, and Michael L. Wagman. Qcd constraints on isospin-dense matter and the nuclear equation of state. *Phys. Rev. Lett.*, 134:011903, Jan 2025.

[39] Thomas E. Riley et al. A *NICER* View of PSR J0030+0451: Millisecond Pulsar Parameter Estimation. *Astrophys. J. Lett.*, 887(1):L21, 2019.

[40] M. C. Miller et al. PSR J0030+0451 Mass and Radius from *NICER* Data and Implications for the Properties of Neutron Star Matter. *Astrophys. J. Lett.*, 887(1):L24, 2019.

[41] Serena Vinciguerra, Tuomo Salmi, Anna L. Watts, Devarshi Choudhury, Thomas E. Riley, Paul S. Ray, Slavko Bogdanov, Yves Kini, Sebastien Guillot, Deepto Chakrabarty, Wynn C. G. Ho, Daniela Huppenkothen, Sharon M. Morsink, Zorawar Wadiasingh, and Michael T. Wolff. An updated mass–radius analysis of the 2017–2018 nicer data set of psr j0030+0451. *The Astrophysical Journal*, 961(1):62, jan 2024.

[42] D.G. Yakovlev, A.D. Kaminker, O.Y. Gnedin, and P. Haensel. Neutrino emission from neutron stars. *Physics Reports*, 354(1):1–155, 2001.

[43] C. O. Heinke, P. G. Jonker, R. Wijnands, and R. E. Taam. Constraints on thermal x-ray radiation from sax j1808.4–3658 and implications for neutron star neutrino emission*. *The Astrophysical Journal*, 660(2):1424, may 2007.

[44] D. K. Galloway. Accreting neutron star spins and the equation of state. In *AIP Conference Proceedings*, volume 983, pages 510–518. American Institute of Physics, 2008.

[45] Zhongxiang Wang, Cees Bassa, Andrew Cumming, and Victoria M. Kaspi. An accurate determination of the optical periodic modulation in the x-ray binary sax j1808.4-3658. *The Astrophysical Journal*, 694(2):1115, mar 2009.

[46] B.K. Agrawal, A. Sulaksono, and P.-G. Reinhard. Optimization of relativistic mean field model for finite nuclei to neutron star matter. *Nuclear Physics A*, 882:1–20, 2012.

[47] Rudy Wijnands, Nathalie Degenaar, and Dany Page. Cooling of accretion-heated neutron stars. *Journal of Astrophysics and Astronomy*, 38(49), September 2017. Special issue on Physics of Neutron Stars and Related Objects.

[48] M. Baldo, Ø. Elgarøy, L. Engvik, M. Hjorth-Jensen, and H.-J. Schulze. $^3P_2$–$^3F_2$ pairing in neutron matter with modern nucleon-nucleon potentials. *Phys. Rev. C*, 58:1921–1928, Oct 1998.

[49] Dany Page, James M. Lattimer, Madappa Prakash, and Andrew W. Steiner. Minimal cooling of neutron stars: A new paradigm. *The Astrophysical Journal Supplement Series*, 155(2):623, dec 2004.

[50] Teruaki Enoto, Shota Kisaka, and Shinpei Shibata. Observational diversity of magnetized neutron stars. *Reports on Progress in Physics*, 82(10):106901, sep 2019.

[51] S. A. Olausen and V. M. Kaspi. The mcgill magnetar catalog*. *The Astrophysical Journal Supplement Series*, 212(1):6, apr 2014.

[52] Arthur G Suvorov and Andrew Melatos. Evolutionary implications of a magnetar interpretation for gleam-x j162759.5–523504.3. *Monthly Notices of the Royal Astronomical Society*, 520(1):1590–1600, January 2023.

[53] Andrei P. Igoshev, Sergei B. Popov, and Rainer Hollerbach. Evolution of neutron star magnetic fields. *Universe*, 7(9), 2021.

[54] R. Ciolfi. Modelling the magnetic field configuration of neutron stars. *Astronomische Nachrichten*, 335(6-7):624–629, 2014.

[55] V. Dexheimer, B. Franzon, R.O. Gomes, R.L.S. Farias, and S.S. Avancini. Magnetic field distribution in strongly magnetized neutron stars. *Astronomische Nachrichten*, 338(9-10):1052–1055, 2017.

[56] Antonios Tsokaros, Milton Ruiz, Stuart L. Shapiro, and K ōji Uryū. Magnetohydrodynamic simulations of self-consistent rotating neutron stars with mixed poloidal and toroidal magnetic fields. *Phys. Rev. Lett.*, 128:061101, Feb 2022.

[57] Andrei M. Beloborodov and Xinyu Li. Magnetar heating. *The Astrophysical Journal*, 833(2):261, dec 2016.

[58] D. J. Dean and M. Hjorth-Jensen. Pairing in nuclear systems: From neutron stars to finite nuclei. *Rev. Mod. Phys.*, 75:607–656, 2003.

[59] Mark Alford. Color-superconducting quark matter. *Annual Review of Nuclear and Particle Science*, 51(1):131–160, 2001.

[60] Steven Weinberg. A New Light Boson? *Phys.Rev.Lett.*, 40:223–226, 1978.

[61] Frank Wilczek. Problem of Strong p and t Invariance in the Presence of Instantons. *Phys.Rev.Lett.*, 40:279–282, 1978.

[62] R.D. Peccei and Helen R. Quinn. CP Conservation in the Presence of Instantons. *Phys.Rev.Lett.*, 38:1440–1443, 1977.

[63] R.D. Peccei and Helen R. Quinn. Constraints Imposed by CP Conservation in the Presence of Instantons. *Phys.Rev.*, D16:1791–1797, 1977.

[64] C. Abel et al. Measurement of the Permanent Electric Dipole Moment of the Neutron. *Phys. Rev. Lett.*, 124(8):081803, 2020.

[65] John Preskill, Mark B. Wise, and Frank Wilczek. Cosmology of the Invisible Axion. *Phys. Lett. B*, 120:127–132, 1983.

[66] L. F. Abbott and P. Sikivie. A Cosmological Bound on the Invisible Axion. *Phys. Lett. B*, 120:133–136, 1983.

[67] Michael Dine and Willy Fischler. The Not So Harmless Axion. *Phys. Lett. B*, 120:137–141, 1983.

[68] S. Navas et al. Review of particle physics. *Phys. Rev. D*, 110(3):030001, 2024.

[69] Ciaran O'Hare. cajohare/axionlimits: Axionlimits, July 2020.

[70] Anson Hook. TASI Lectures on the Strong CP Problem and Axions. *PoS*, TASI2018:004, 2019.

[71] C. B. Adams et al. Axion Dark Matter. In *2022 Snowmass Summer Study*, 3 2022.

[72] Peter W. Graham and Surjeet Rajendran. New Observables for Direct Detection of Axion Dark Matter. *Phys. Rev. D*, 88:035023, 2013.

[73] Dmitry Budker, Peter W. Graham, Micah Ledbetter, Surjeet Rajendran, and Alex Sushkov. Proposal for a Cosmic Axion Spin Precession Experiment (CASPEr). *Phys. Rev. X*, 4(2):021030, 2014.

[74] Asimina Arvanitaki and Andrew A. Geraci. Resonantly Detecting Axion-Mediated Forces with Nuclear Magnetic Resonance. *Phys. Rev. Lett.*, 113(16):161801, 2014.

[75] Asimina Arvanitaki, Amalia Madden, and Ken Van Tilburg. Piezoaxionic effect. *Phys. Rev. D*, 109(7):072009, 2024.

[76] Asher Berlin and Kevin Zhou. Discovering QCD-coupled axion dark matter with polarization haloscopes. *Phys. Rev. D*, 108(3):035038, 2023.

[77] A. A. Geraci et al. Progress on the ARIADNE axion experiment. *Springer Proc. Phys.*, 211:151–161, 2018.

[78] C. Abel et al. Search for Axionlike Dark Matter through Nuclear Spin Precession in Electric and Magnetic Fields. *Phys. Rev. X*, 7(4):041034, 2017.

[79] Seung Pyo Chang, Selcuk Haciomeroglu, On Kim, Soohyung Lee, Seongtae Park, and Yannis K. Semertzidis. Axionlike dark matter search using the storage ring EDM method. *Phys. Rev. D*, 99(8):083002, 2019.

[80] Derek F. Jackson Kimball et al. Overview of the Cosmic Axion Spin Precession Experiment (CASPEr). *Springer Proc. Phys.*, 245:105–121, 2020.

[81] Tanya S. Roussy et al. Experimental Constraint on Axionlike Particles over Seven Orders of Magnitude in Mass. *Phys. Rev. Lett.*, 126(17):171301, 2021.

[82] Deniz Aybas et al. Search for Axionlike Dark Matter Using Solid-State Nuclear Magnetic Resonance. *Phys. Rev. Lett.*, 126(14):141802, 2021.

[83] S. Karanth et al. First Search for Axionlike Particles in a Storage Ring Using a Polarized Deuteron Beam. *Phys. Rev. X*, 13(3):031004, 2023.

[84] Ivo Schulthess et al. New Limit on Axionlike Dark Matter Using Cold Neutrons. *Phys. Rev. Lett.*, 129(19):191801, 2022.

[85] Xue Zhang, Abhishek Banerjee, Mahapan Leyser, Gilad Perez, Stephan Schiller, Dmitry Budker, and Dionysios Antypas. Search for Ultralight Dark Matter with Spectroscopy of Radio-Frequency Atomic Transitions. *Phys. Rev. Lett.*, 130(25):251002, 2023.

[86] Andrew J. Winter, Tanja Marić, Viktoriya A. Balabanova, János Ádám, Glenn Randall, Arne Wickenbrock, Derek F. Jackson Kimball, Dmitry Budker, and Alexander O. Sushkov. Calibration of the Solid-State Nuclear Magnetic Resonance Search for Axion-Like Dark Matter. *Annalen Phys.*, 536(1):2300252, 2024.

[87] Mingyu Fan, Bassam Nima, Aleksandar Radak, Gonzalo Alonso-Álvarez, and Amar Vutha. First results from a search for axionlike dark matter using octupole-deformed nuclei in a crystal. 10 2024.

[88] Kfir Blum, Raffaele Tito D'Agnolo, Mariangela Lisanti, and Benjamin R. Safdi. Constraining Axion Dark Matter with Big Bang Nucleosynthesis. *Phys. Lett. B*, 737:30–33, 2014.

[89] Georg Raffelt and David Seckel. Bounds on Exotic Particle Interactions from SN 1987a. *Phys. Rev. Lett.*, 60:1793, 1988.

[90] Jae Hyeok Chang, Rouven Essig, and Samuel D. McDermott. Supernova 1987A Constraints on Sub-GeV Dark Sectors, Millicharged Particles, the QCD Axion, and an Axion-like Particle. *JHEP*, 09:051, 2018.

[91] Pierluca Carenza, Tobias Fischer, Maurizio Giannotti, Gang Guo, Gabriel Martínez-Pinedo, and Alessandro Mirizzi. Improved axion emissivity from a supernova via nucleon-nucleon bremsstrahlung. *JCAP*, 10(10):016, 2019. [Erratum: JCAP 05, E01 (2020)].

[92] Giuseppe Lucente, Leonardo Mastrototaro, Pierluca Carenza, Luca Di Luzio, Maurizio Giannotti, and Alessandro Mirizzi. Axion signatures from supernova explosions through the nucleon electric-dipole portal. *Phys. Rev. D*, 105(12):123020, 2022.

[93] Konstantin Springmann, Michael Stadlbauer, Stefan Stelzl, and Andreas Weiler. A Universal Bound on QCD Axions from Supernovae. 10 2024.

[94] Konstantin Springmann, Michael Stadlbauer, Stefan Stelzl, and Andreas Weiler. From supernovae to neutron stars: a systematic approach to axion production at finite density. *Journal of High Energy Physics*, 2025(2):138, 2025.

[95] Anson Hook and Junwu Huang. Probing axions with neutron star inspirals and other stellar processes. *JHEP*, 06:036, 2018.

[96] Reuven Balkin, Javi Serra, Konstantin Springmann, Stefan Stelzl, and Andreas Weiler. White dwarfs as a probe of exceptionally light QCD axions. *Phys. Rev. D*, 109(9):095032, 2024.

[97] Junwu Huang, Matthew C. Johnson, Laura Sagunski, Mairi Sakellariadou, and Jun Zhang. Prospects for axion searches with Advanced LIGO through binary mergers. *Phys. Rev. D*, 99(6):063013, 2019.

[98] Jun Zhang, Zhenwei Lyu, Junwu Huang, Matthew C. Johnson, Laura Sagunski, Mairi Sakellariadou, and Huan Yang. First Constraints on Nuclear Coupling of Axionlike Particles from the Binary Neutron Star Gravitational Wave Event GW170817. *Phys. Rev. Lett.*, 127(16):161101, 2021.

[99] Antonio Gómez-Bañón, Kai Bartnick, Konstantin Springmann, and José A. Pons. Constraining light qcd axions with isolated neutron star cooling. *Phys. Rev. Lett.*, 133:251002, Dec 2024.

[100] Ciaran A. J. O'Hare. Cosmology of axion dark matter. *PoS*, COSMICWISPers:040, 2024.

[101] Andrea Caputo and Georg Raffelt. Astrophysical Axion Bounds: The 2024 Edition. *PoS*, COSMICWISPers:041, 2024.

[102] Anson Hook. Solving the Hierarchy Problem Discretely. *Phys. Rev. Lett.*, 120(26):261802, 2018.

[103] Luca Di Luzio, Belen Gavela, Pablo Quilez, and Andreas Ringwald. An even lighter QCD axion. *JHEP*, 05:184, 2021.

[104] Reuven Balkin, Javi Serra, Konstantin Springmann, Stefan Stelzl, and Andreas Weiler. Heavy neutron stars from light scalars. *Journal of High Energy Physics*, 2025(2):141, 2025.

[105] Bruno S. Lopes, Ricardo L. S. Farias, Veronica Dexheimer, Aritra Bandyopadhyay, and Rudnei O. Ramos. Axion effects in the stability of hybrid stars. *Phys. Rev. D*, 106:L121301, Dec 2022.

[106] Anna L. Watts et al. Colloquium : Measuring the neutron star equation of state using x-ray timing. *Rev. Mod. Phys.*, 88(2):021001, 2016.

[107] Christian Drischler, Sophia Han, James M. Lattimer, Madappa Prakash, Sanjay Reddy, and Tianqi Zhao. Limiting masses and radii of neutron stars and their implications. *Phys. Rev. C*, 103(4):045808, 2021.

[108] C. Drischler, J. W. Holt, and C. Wellenhofer. Chiral Effective Field Theory and the High-Density Nuclear Equation of State. *Ann. Rev. Nucl. Part. Sci.*, 71:403–432, 2021.

[109] Anson Hook and Junwu Huang. Searches for other vacua. Part I. Bubbles in our universe. *JHEP*, 08:148, 2019.

[110] Reuven Balkin, Javi Serra, Konstantin Springmann, and Andreas Weiler. The QCD axion at finite density. *JHEP*, 07:221, 2020.

[111] Reuven Balkin, Javi Serra, Konstantin Springmann, Stefan Stelzl, and Andreas Weiler. Runaway relaxion from finite density. *JHEP*, 06:023, 2022.

[112] Reuven Balkin, Javi Serra, Konstantin Springmann, Stefan Stelzl, and Andreas Weiler. Density induced vacuum instability. *SciPost Phys.*, 14(4):071, 2023.

[113] P. Di Vecchia and G. Veneziano. Chiral Dynamics in the Large n Limit. *Nucl. Phys. B*, 171:253–272, 1980.

[114] Cumrun Vafa and Edward Witten. Parity Conservation in QCD. *Phys. Rev. Lett.*, 53:535, 1984.

[115] Lorenzo Ubaldi. Effects of theta on the deuteron binding energy and the triple-alpha process. *Phys. Rev. D*, 81:025011, 2010.

[116] C. Hanhart, J. R. Peláez, and G. Ríos. Quark-mass dependence of the ρ and σ mesons from dispersion relations and chiral perturbation theory. *Phys. Rev. Lett.*, 100:152001, Apr 2008.

[117] J. R. Peláez and G. Ríos. Chiral extrapolation of light resonances from one and two-loop unitarized chiral perturbation theory versus lattice results. *Phys. Rev. D*, 82:114002, Dec 2010.

[118] J. C. Berengut, E. Epelbaum, V. V. Flambaum, C. Hanhart, U. G. Meissner, J. Nebreda, and J. R. Pelaez. Varying the light quark mass: impact on the nuclear force and Big Bang nucleosynthesis. *Phys. Rev. D*, 87(8):085018, 2013.

[119] J. M. Alarcón. Brief history of the pion–nucleon sigma term. *Eur. Phys. J. ST*, 230(6):1609–1622, 2021.

[120] Lorenzo Ubaldi. Effects of θ on the deuteron binding energy and the triple-alpha process. *Phys. Rev. D*, 81:025011, Jan 2010.

[121] R.J. Crewther, P. Di Vecchia, G. Veneziano, and E. Witten. Chiral estimate of the electric dipole moment of the neutron in quantum chromodynamics. *Physics Letters B*, 88(1):123–127, 1979.

[122] Giovanni Grilli di Cortona, Edward Hardy, Javier Pardo Vega, and Giovanni Villadoro. The QCD axion, precisely. *JHEP*, 01:034, 2016.

[123] Csaba Csáki, Cem Eröncel, Jay Hubisz, Gabriele Rigo, and John Terning. Neutron Star Mergers Chirp About Vacuum Energy. *JHEP*, 09:087, 2018.

[124] Silas R. Beane and Martin J. Savage. Variation of fundamental couplings and nuclear forces. *Nucl. Phys. A*, 713:148–164, 2003.

[125] Evgeny Epelbaum, Ulf-G. Meissner, and Walter Gloeckle. Nuclear forces in the chiral limit. *Nucl. Phys. A*, 714:535–574, 2003.

[126] David B. Kaplan, Martin J. Savage, and Mark B. Wise. A New expansion for nucleon-nucleon interactions. *Phys. Lett. B*, 424:390–396, 1998.

[127] Aurel Bulgac, Gerald A. Miller, and Mark Strikman. Chiral limit of nuclear physics. *Phys. Rev. C*, 56:3307–3310, 1997.

[128] Thomas D. Cohen, R. J. Furnstahl, and David K. Griegel. Quark and gluon condensates in nuclear matter. *Phys. Rev. C*, 45:1881–1893, 1992.

[129] N. Kaiser, P. de Homont, and W. Weise. In-medium chiral condensate beyond linear density approximation. *Phys. Rev. C*, 77:025204, 2008.

[130] O. Plohl and C. Fuchs. Nuclear matter in the chiral limit and the in-medium chiral condensate. *Nucl. Phys. A*, 798:75–95, 2008.

[131] T. Krüger, I. Tews, B. Friman, K. Hebeler, and A. Schwenk. The chiral condensate in neutron matter. *Phys. Lett. B*, 726:412–416, 2013.

[132] B. D. Carlsson, A. Ekström, C. Forssén, D. Fahlin Strömberg, G. R. Jansen, O. Lilja, M. Lindby, B. A. Mattsson, and K. A. Wendt. Uncertainty analysis and order-by-order optimization of chiral nuclear interactions. *Phys. Rev. X*, 6(1):011019, 2016.

[133] D. R. Entem, N. Kaiser, R. Machleidt, and Y. Nosyk. Peripheral nucleon-nucleon scattering at fifth order of chiral perturbation theory. *Phys. Rev. C*, 91(1):014002, 2015.

[134] R. Machleidt and D. R. Entem. Chiral effective field theory and nuclear forces. *Phys. Rept.*, 503:1–75, 2011.

[135] C. Drischler, K. Hebeler, and A. Schwenk. Chiral interactions up to next-to-next-to-next-to-leading order and nuclear saturation. *Phys. Rev. Lett.*, 122(4):042501, 2019.

[136] J. Hoppe, C. Drischler, R. J. Furnstahl, K. Hebeler, and A. Schwenk. Weinberg eigenvalues for chiral nucleon-nucleon interactions. *Phys. Rev. C*, 96(5):054002, 2017.

[137] M. Dutra, O. Lourenço, S. S. Avancini, B. V. Carlson, A. Delfino, D. P. Menezes, C. Providência, S. Typel, and J. R. Stone. Relativistic mean-field hadronic models under nuclear matter constraints. *Phys. Rev. C*, 90:055203, Nov 2014.

[138] B.K. Agrawal, A. Sulaksono, and P.-G. Reinhard. Optimization of relativistic mean field model for finite nuclei to neutron star matter. *Nuclear Physics A*, 882:1–20, 2012.

[139] Gordon Baym, Christopher Pethick, and Peter Sutherland. The ground state of matter at high densities: Equation of state and stellar models. *The Astrophysical Journal*, 170:299–317, 1971.

[140] J.W. Negele and D. Vautherin. Neutron star matter at sub-nuclear densities. *Nuclear Physics A*, 207(2):298–320, 1973.

[141] Christina Gao and Albert Stebbins. Structure of stellar remnants with coupling to a light scalar. *Journal of Cosmology and Astroparticle Physics*, 2022(07):025, jul 2022.

[142] C. Alcock, E. Farhi, and A. Olinto. Strange stars. *The Astrophysical Journal*, 310:261–272, 1986.

[143] Christian Drischler, Sophia Han, James M. Lattimer, Madappa Prakash, Sanjay Reddy, and Tianqi Zhao. Limiting masses and radii of neutron stars and their implications. *Phys. Rev. C*, 103:045808, Apr 2021.

[144] Edward Witten. Cosmic Separation of Phases. *Phys. Rev. D*, 30:272–285, 1984.

[145] Ariel R. Zhitnitsky. 'Nonbaryonic' dark matter as baryonic color superconductor. *JCAP*, 10:010, 2003.

[146] Edward F. Brown, Lars Bildsten, and Robert E. Rutledge. Crustal heating and quiescent emission from transiently accreting neutron stars. *The Astrophysical Journal*, 504(2):L95, jul 1998.

[147] Edward M. Cackett, Rudy Wijnands, Jon M. Miller, Edward F. Brown, and Nathalie Degenaar. Cooling of the crust in the neutron star low-mass x-ray binary mxb 1659–29. *The Astrophysical Journal*, 687(2):L87, oct 2008.

[148] Dany Page and Sanjay Reddy. Forecasting neutron star temperatures: Predictability and variability. *Phys. Rev. Lett.*, 111:241102, Dec 2013.

[149] N. Chamel and P. Haensel. Physics of Neutron Star Crusts. *Living Rev. Rel.*, 11:10, 2008.

[150] N. Chamel, D. Page, and S. Reddy. Low-energy collective excitations in the neutron star inner crust. *Phys. Rev. C*, 87:035803, Mar 2013.

[151] Masha Baryakhtar, Marios Galanis, Robert Lasenby, and Olivier Simon. Black hole superradiance of self-interacting scalar fields. *Phys. Rev. D*, 103(9):095019, 2021.

[152] Sebastian Hoof, David J. E. Marsh, Júlia Sisk-Reynés, James H. Matthews, and Christopher Reynolds. Getting More Out of Black Hole Superradiance: a Statistically Rigorous Approach to Ultralight Boson Constraints. 6 2024.

[153] R. N. Manchester. Pulsar timing and its applications. *J. Phys. Conf. Ser.*, 932:012002, 2017.

[154] P. W. Anderson and N. Itoh. Pulsar glitches and restlessness as a hard superfluidity phenomenon. *Nature*, 256(5512):25–27, 1975.

[155] M. Ruderman. Crust-breaking by neutron superfluids and the vela pulsar glitches. *The Astrophysical Journal*, 203:213–222, January 1976.

[156] David Pines and M. Ali Alpar. Superfluidity in neutron stars. *Nature*, 316(6023):27–32, 1985.

[157] Bennett Link and Yuri Levin. Vortex pinning in neutron stars, slipstick dynamics, and the origin of spin glitches. *The Astrophysical Journal*, 941(2):148, dec 2022.

[158] N. Andersson, K. Glampedakis, W. C. G. Ho, and C. M. Espinoza. Pulsar glitches: The crust is not enough. *Phys. Rev. Lett.*, 109:241103, Dec 2012.

[159] N. Chamel. Crustal entrainment and pulsar glitches. *Phys. Rev. Lett.*, 110:011101, Jan 2013.

[160] J. Piekarewicz, F. J. Fattoyev, and C. J. Horowitz. Pulsar glitches: The crust may be enough. *Phys. Rev. C*, 90:015803, Jul 2014.

[161] T. Delsate, N. Chamel, N. Gürlebeck, A. F. Fantina, J. M. Pearson, and C. Ducoin. Giant pulsar glitches and the inertia of neutron star crusts. *Phys. Rev. D*, 94:023008, Jul 2016.

[162] R. Smoluchowski. Frequency of pulsar starquakes. *Phys. Rev. Lett.*, 24:923–925, Apr 1970.

[163] Gordon Baym and David Pines. Neutron starquakes and pulsar speedup. *Annals of Physics*, 66(2):816–835, 1971.

[164] Ashley Bransgrove, Andrei M. Beloborodov, and Yuri Levin. A quake quenching the vela pulsar. *The Astrophysical Journal*, 897(2):173, jul 2020.

[165] P. S. Negi. A starquake model for the vela pulsar. *Monthly Notices of the Royal Astronomical Society*, 366(1):73–78, 02 2006.

[166] P. S. Negi. Neutron star sequences and the starquake glitch model for the crab and the vela pulsars. *Astrophysics and Space Science*, 332(1):145–153, 2011.

[167] Biswanath Layek, Deepthi Godaba Venkata, and Pradeepkumar Yadav. Glitches due to quasineutron-vortex scattering in the superfluid inner crust of a pulsar. *Phys. Rev. D*, 107:023004, Jan 2023.

[168] E. Epelbaum, H.-W. Hammer, and Ulf-G. Meißner. Modern theory of nuclear forces. *Rev. Mod. Phys.*, 81:1773–1825, Dec 2009.

[169] Norbert Kaiser, R. Brockmann, and W. Weise. Peripheral nucleon-nucleon phase shifts and chiral symmetry. *Nucl. Phys. A*, 625:758–788, 1997.

[170] Christian Drischler. *Nuclear matter from chiral effective field theory.* PhD thesis, Technische Universität Darmstadt, Darmstadt, November 2017.

[171] J. E. Lynn, J. Carlson, E. Epelbaum, S. Gandolfi, A. Gezerlis, and A. Schwenk. Quantum monte carlo calculations of light nuclei using chiral potentials. *Phys. Rev. Lett.*, 113:192501, Nov 2014.

[172] J. E. Lynn, I. Tews, J. Carlson, S. Gandolfi, A. Gezerlis, K. E. Schmidt, and A. Schwenk. Chiral Three-Nucleon Interactions in Light Nuclei, Neutron-α Scattering, and Neutron Matter. *Phys. Rev. Lett.*, 116(6):062501, 2016.

[173] P. Maris, E. Epelbaum, R. J. Furnstahl, J. Golak, K. Hebeler, T. Hüther, H. Kamada, H. Krebs, Ulf-G. Meißner, J. A. Melendez, A. Nogga, P. Reinert, R. Roth, R. Skibiński, V. Soloviov, K. Topolnicki, J. P. Vary, Yu. Volkotrub, H. Witała, and T. Wolfgruber. Light nuclei with semilocal momentum-space regularized chiral interactions up to third order. *Phys. Rev. C*, 103:054001, May 2021.

[174] L. Coraggio, J. W. Holt, N. Itaco, R. Machleidt, L. E. Marcucci, and F. Sammarruca. Nuclear-matter equation of state with consistent two- and three-body perturbative chiral interactions. *Phys. Rev. C*, 89:044321, Apr 2014.

[175] J. W. Holt and N. Kaiser. Equation of state of nuclear and neutron matter at third-order in perturbation theory from chiral effective field theory. *Phys. Rev. C*, 95:034326, Mar 2017.

[176] Jordy de Vries, Alex Gnech, and Sachin Shain. Renormalization of *cp*-violating nuclear forces. *Phys. Rev. C*, 103:L012501, Jan 2021.

[177] U. van Kolck, J.L. Friar, and T. Goldman. Phenomenological aspects of isospin violation in the nuclear force. *Physics Letters B*, 371(3):169–174, 1996.

[178] J Gasser and H Leutwyler. Chiral perturbation theory to one loop. *Annals of Physics*, 158(1):142–210, 1984.

[179] Gu Yun-Ting, Qin Song-Mei, Zhou Li-Juan, and Ma Wei-Xing. Gasser–leutwyler coefficients of chiral lagrangian for pseudoscalar goldstone bosons in dyson–schwinger equations. *Communications in Theoretical Physics*, 50(5):1205, nov 2008.

[180] Xu Feng, Luchang Jin, and Michael Joseph Riberdy. Lattice qcd calculation of the pion mass splitting. *Phys. Rev. Lett.*, 128:052003, Feb 2022.

[181] Vincenzo Cirigliano, Maria Dawid, Wouter Dekens, and Sanjay Reddy. New class of three-nucleon forces and their implications. *Phys. Rev. Lett.*, 135:022501, Jul 2025.

[182] Martin Hoferichter, Jacobo Ruiz de Elvira, Bastian Kubis, and Ulf-G. Meißner. Matching pion-nucleon roy-steiner equations to chiral perturbation theory. *Phys. Rev. Lett.*, 115:192301, Nov 2015.

[183] Vittorio Canuto and Hong-Yee Chiu. Quantum theory of an electron gas in intense magnetic fields. *Phys. Rev.*, 173:1210–1219, Sep 1968.

[184] Lev B. Leinson and Armando Pérez. Direct urca process in neutron stars with strong magnetic fields. *Journal of High Energy Physics*, 1998(09):020, oct 1998.

[185] D. A. Baiko and D. G. Yakovlev. Direct URCA process in strong magnetic fields and neutron star cooling. *Astronomy & Astrophysics*, 342:192–200, February 1999.

[186] Victoria M. Kaspi and Andrei M. Beloborodov. Magnetars. *Annual Review of Astronomy and Astrophysics*, 55(1):261–301, 2017. First published online June 21, 2017.

[187] Pranjal Tambe, Debarati Chatterjee, Mark Alford, and Alexander Haber. Effect of magnetic fields on urca rates in neutron star mergers. *Phys. Rev. C*, 111:035809, Mar 2025.

[188] Mark G. Alford, Alexander Haber, Steven P. Harris, and Ziyuan Zhang. Beta equilibrium under neutron star merger conditions. *Universe*, 7(11), 2021.

[189] Tomoyuki Maruyama, A. Baha Balantekin, Myung-Ki Cheoun, Toshitaka Kajino, Motohiko Kusakabe, and Grant J. Mathews. A relativistic quantum approach to neutrino and antineutrino emission via the direct urca process in strongly magnetized neutron-star matter. *Physics Letters B*, 824:136813, 2022.

[190] Huaiyu Duan and Yong-Zhong Qian. Neutrino processes in strong magnetic fields and implications for supernova dynamics. *Phys. Rev. D*, 69:123004, Jun 2004.

[191] D. J. Price and S. Rosswog. Producing ultrastrong magnetic fields in neutron star mergers. *Science*, 312(5774):719–722, 2006.

[192] Kenta Kiuchi, Pablo Cerdá-Durán, Koutarou Kyutoku, Yuichiro Sekiguchi, and Masaru Shibata. Efficient magnetic-field amplification due to the kelvin-helmholtz instability in binary neutron star mergers. *Phys. Rev. D*, 92:124034, Dec 2015.

[193] M. Dutra, O. Lourenço, S. S. Avancini, B. V. Carlson, A. Delfino, D. P. Menezes, C. Providência, S. Typel, and J. R. Stone. Relativistic mean-field hadronic models under nuclear matter constraints. *Phys. Rev. C*, 90:055203, Nov 2014.

[194] H. T. Cromartie et al. Relativistic Shapiro delay measurements of an extremely massive millisecond pulsar. *Nature Astron.*, 4(1):72–76, 2019.

[195] B. P. Abbott et al. GW170817: Measurements of neutron star radii and equation of state. *Phys. Rev. Lett.*, 121(16):161101, 2018.

[196] Soumi De, Daniel Finstad, James M. Lattimer, Duncan A. Brown, Edo Berger, and Christopher M. Biwer. Tidal Deformabilities and Radii of Neutron Stars from the Observation of GW170817. *Phys. Rev. Lett.*, 121(9):091102, 2018. [Erratum: Phys.Rev.Lett. 121, 259902 (2018)].

[197] Collin D. Capano, Ingo Tews, Stephanie M. Brown, Ben Margalit, Soumi De, Sumit Kumar, Duncan A. Brown, Badri Krishnan, and Sanjay Reddy. Stringent constraints on neutron-star radii from multimessenger observations and nuclear theory. *Nature Astron.*, 4(6):625–632, 2020.

[198] Andrew Steinmetz, Martin Formanek, and Johann Rafelski. Magnetic dipole moment in relativistic quantum mechanics. *The European Physical Journal A*, 55(3):40, Mar 2019.

[199] A. Broderick, M. Prakash, and J. M. Lattimer. The equation of state of neutron star matter in strong magnetic fields. *The Astrophysical Journal*, 537(1):351–367, July 2000.

[200] I. S. Gradshteyn and I. M. Ryzhik. *Table of Integrals, Series, and Products.* Academic Press, New York, 1980.

[201] Kaushik Bhattacharya. *Elementary Particle Interactions In A Background Magnetic Field.* PhD thesis, Jadavpur University, 2004.

[202] Stuart L. Shapiro and Saul A. Teukolsky. *Black Holes, White Dwarfs, and Neutron Stars: The Physics of Compact Objects.* Wiley, New York, 1983.

[203] Elias R Most, Steven P Harris, Christopher Plumberg, Mark G Alford, Jorge Noronha, Jacquelyn Noronha-Hostler, Frans Pretorius, Helvi Witek, and Nicolás Yunes. Projecting the likely importance of weak-interaction-driven bulk viscosity in neutron star mergers. *Monthly Notices of the Royal Astronomical Society*, 509(1):1096–1108, 10 2021.

[204] Andrea Endrizzi, Albino Perego, Francesco M. Fabbri, Lorenzo Branca, David Radice, Sebastiano Bernuzzi, Bruno Giacomazzo, Francesco Pederiva, and Alessandro Lovato. Thermodynamics conditions of matter in the neutrino decoupling region during neutron star mergers. *The European Physical Journal A*, 56(1), January 2020.

[205] K. Hebeler and A. Schwenk. Chiral three-nucleon forces and neutron matter. *Phys. Rev. C*, 82:014314, 2010.

[206] S. Gandolfi, J. Carlson, S. Reddy, A. W. Steiner, and R. B. Wiringa. The equation of state of neutron matter, symmetry energy, and neutron star structure. *Eur. Phys. J. A*, 50:10, 2014.

[207] C. Drischler, R. J. Furnstahl, J. A. Melendez, and D. R. Phillips. How Well Do We Know the Neutron-Matter Equation of State at the Densities Inside Neutron Stars? A Bayesian Approach with Correlated Uncertainties. *Phys. Rev. Lett.*, 125(20):202702, 2020.

[208] Ingo Tews, Joseph Carlson, Stefano Gandolfi, and Sanjay Reddy. Constraining the speed of sound inside neutron stars with chiral effective field theory interactions and observations. *Astrophys. J.*, 860(2):149, 2018.

[209] W. Kohn and J. M. Luttinger. New mechanism for superconductivity. *Phys. Rev. Lett.*, 15:524–526, Sep 1965.

[210] C. Drischler, T. Krüger, K. Hebeler, and A. Schwenk. Pairing in neutron matter: New uncertainty estimates and three-body forces. *Phys. Rev. C*, 95(2):024302, 2017.

[211] M. Yu. Kagan. *Modern trends in Superconductivity and Superfluidity.* Springer Netherlands, 2013.

[212] D. Fay and A. Layzer. Superfluidity of low-density fermion systems. *Phys. Rev. Lett.*, 20:187–190, Jan 1968.

[213] D. Pines. Proc. xith intern. conf. on low temperature physics. In *Proc. XIth Intern. Conf. on Low temperature physics*, page 10. Academic Press of Japan, Tokyo, 1971.

[214] J.W. Clark, C.-G. Källman, C.-H. Yang, and D.A. Chakkalakal. Effect of polarization on superfluidity in low-density neutron matter. *Physics Letters B*, 61(4):331–334, 1976.

[215] A. Gezerlis, C. J. Pethick, and A. Schwenk. Pairing and superfluidity of nucleons in neutron stars. June 2014.

[216] L. P. Gorkov and T. K Melik-Barkhudarov. Contribution to the theory of superfluidity in an imperfect Fermi gas. *Sov. Phys. JETP*, 13:1018–1022, 1961.

[217] Achim Schwenk and Bengt Friman. Polarization contributions to the spin dependence of the effective interaction in neutron matter. *Phys. Rev. Lett.*, 92:082501, 2004.

[218] M. A. Baranov, A. V. Chubukov, and M. Yu Kagan. Superconductivity and superfluidity in fermi systems with repulsive interactions. *Int. J. Mod. Phys. B*, 6:2471–2497, 1992.

[219] J. González. Kohn-luttinger superconductivity in graphene. *Phys. Rev. B*, 78:205431, Nov 2008.

[220] Rahul Nandkishore, Ronny Thomale, and Andrey V. Chubukov. Superconductivity from weak repulsion in hexagonal lattice systems. *Phys. Rev. B*, 89:144501, Apr 2014.

[221] J. González and T. Stauber. Kohn-luttinger superconductivity in twisted bilayer graphene. *Phys. Rev. Lett.*, 122:026801, Jan 2019.

[222] D. V. Efremov, M. S. Mar'enko, M. A. Baranov, and M. Yu. Kagan. Superfluid transition temperature in a fermi gas with repulsion allowing for higher orders of perturbation theory. *J. Exp. Theor. Phys.*, 90(5):861–871, May 2000.

[223] Saurabh Maiti and Andrey V. Chubukov. Superconductivity from repulsive interaction. *AIP Conference Proceedings*, 1550(1):3–73, 08 2013.

[224] M Yu Kagan and AV Chubukov. Possibility of a superfluid transition in a slightly nonideal fermi gas with repulsion. *JETP Lett*, 47:614, 1988.

[225] Bengt Friman and Wolfram Weise. Neutron Star Matter as a Relativistic Fermi Liquid. *Phys. Rev. C*, 100:065807, 2019.

[226] C. J. Pethick and D. G. Ravenhall. Nuclear physics of dense matter. *Annals of the New York Academy of Sciences*, 647(1):503–509, 1991.

[227] Mark G. Alford, Jeffrey A. Bowers, Jack M. Cheyne, and Greig A. Cowan. Single color and single flavor color superconductivity. *Phys. Rev. D*, 67:054018, Mar 2003.

[228] Andreas Schmitt. Ground state in a spin-one color superconductor. *Phys. Rev. D*, 71:054016, Mar 2005.

[229] Thomas Schäfer. The Kohn-Luttinger effect in gauge theories. *Phys. Rev. D*, 74:054009, 2006.

[230] Gordon Baym, Tetsuo Hatsuda, Toru Kojo, Philip D Powell, Yifan Song, and Tatsuyuki Takatsuka. From hadrons to quarks in neutron stars: a review. *Reports on Progress in Physics*, 81(5):056902, mar 2018.

[231] Michael Buballa. Njl-model analysis of dense quark matter. *Physics Reports*, 407(4):205–376, 2005.

[232] Yifan Song, Gordon Baym, Tetsuo Hatsuda, and Toru Kojo. Effective repulsion in dense quark matter from nonperturbative gluon exchange. *Phys. Rev. D*, 100:034018, Aug 2019.

[233] Mark G. Alford, Andreas Schmitt, Krishna Rajagopal, and Thomas Schäfer. Color superconductivity in dense quark matter. *Rev. Mod. Phys.*, 80:1455–1515, 2008.

[234] Gordon Baym, Shun Furusawa, Tetsuo Hatsuda, Toru Kojo, and Hajime Togashi. New neutron star equation of state with quark–hadron crossover. *The Astrophysical Journal*, 885(1):42, oct 2019.

[235] Dima G. Yakovlev and C. J. Pethick. Neutron star cooling. *Ann. Rev. Astron. Astrophys.*, 42:169–210, 2004.

[236] Dany Page, James M. Lattimer, Madappa Prakash, and Andrew W. Steiner. Neutrino Emission from Cooper Pairs and Minimal Cooling of Neutron Stars. *The Astrophysical Journal*, 707(2):1131–1140, December 2009.

[237] J. M. Lattimer, C. J. Pethick, M. Prakash, and P. Haensel. Direct URCA process in neutron stars. *Phys. Rev. Lett.*, 66:2701–2704, 1991.

[238] Edward F. Brown, Andrew Cumming, Farrukh J. Fattoyev, C. J. Horowitz, Dany Page, and Sanjay Reddy. Rapid neutrino cooling in the neutron star MXB 1659-29. *Phys. Rev. Lett.*, 120(18):182701, 2018.

[239] Andrew Cumming, Edward F. Brown, Farrukh J. Fattoyev, C. J. Horowitz, Dany Page, and Sanjay Reddy. A lower limit on the heat capacity of the neutron star core. *Phys. Rev. C*, 95(2):025806, 2017.

[240] Jeremy W. Holt, Mamiya Kawaguchi, and Norbert Kaiser. Implementing chiral three-body forces in terms of medium-dependent two-body forces. *Front. in Phys.*, 8:100, 2020.

[241] Mia Kumamoto, Junwu Huang, Christian Drischler, Masha Baryakhtar, and Sanjay Reddy. mlkumamoto/axionns-public. Github repository, 2024.

[242] Mia Kumamoto and Catherine Welch. clwelch03/NS-landau-quantization. Github repository, 2024.

[243] Nadia Fettes, Ulf-G. Meißner, Martin Mojžiš, and Sven Steininger. The chiral effective pion-nucleon lagrangian of order p4. *Annals of Physics*, 283(2):273–307, 2000.